Eidgenössische Technische Hochschule Zürich
Swiss Federal Institute of Technology Zurich

Diss. ETH No. 23403

Direct Band Gap Germanium for Si-compatible Lasing

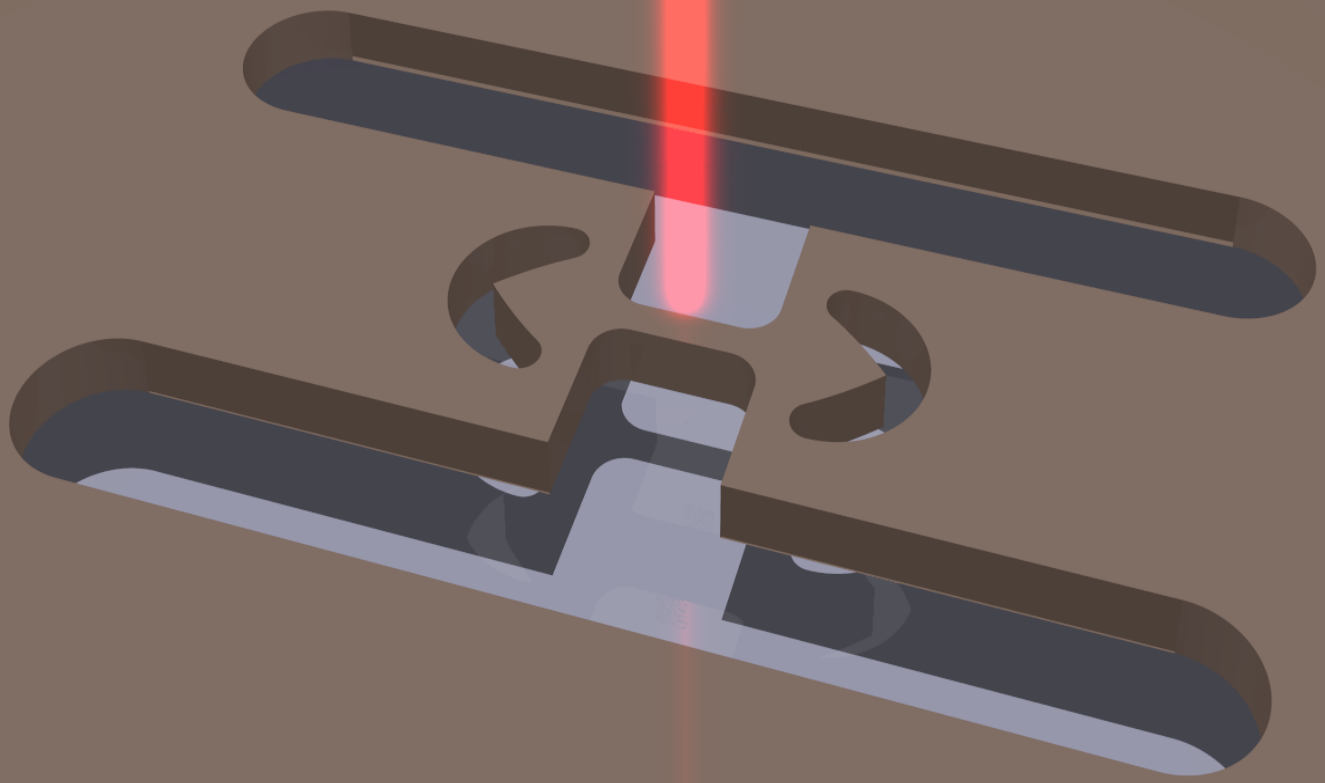

Richard Geiger

2016

DISS. ETH NO. 23403

Direct Band Gap Germanium for Si-compatible Lasing

A dissertation submitted to attain the degree of

DOCTOR OF SCIENCES of ETH ZÜRICH

(Dr. sc. ETH Zürich)

presented by

RICHARD GEIGER

Dipl.-Phys. Univ., TU München

born on 15.08.1986

citizen of Germany

accepted on the recommendation of

Prof. Dr. Jérôme Faist, examiner

Prof. Dr. Gerhard Abstreiter, co-examiner

Dr. Alexei Chelnokov, co-examiner

Dr. Hans Sigg, co-examiner

2016

'All of physics is either impossible or trivial. It is impossible until you understand it, and then it becomes trivial.'
Ernest Rutherford

To my parents.

Abstract

For several decades, an astonishing progress has been seen in the development of integrated circuits used in electronic devices. This progress was based on the miniaturization of electronic components fabricated in complementary metal-oxide-semiconductor (CMOS) technology. However, at current and future length scales, the metal interconnects constitute a bottleneck for a further increase in computing power. This bottleneck can be resolved by replacing the electrical interconnects by optical data transmission. To do so, an efficient monolithic laser source is required. Direct band gap III-V lasers offer excellent efficiencies, but it is a great challenge to integrate these on the CMOS platform. Many teams worldwide are working on overcoming the serious material incompatibilities between III-V materials and the group IV material silicon (Si). A much more attractive solution is to employ a material that intrinsically complies with Si technology such as germanium (Ge), which is nowadays already in use in silicon foundries. However, at first glance it seems unpractical to make a laser from Ge due to the unfortunate alignment of the electronic bands which form an indirect band gap. Nonetheless, it has been known since a long time that this band alignment can be modified by increasing the unit cell of the crystal or by alloying Ge with Sn. Doing either way, it is expected that the radiative recombination efficiency increases and the bands align in a direct configuration, just like the bands for III-V laser materials.

In this thesis, the optical properties of these two classes of so-called direct band gap group IV materials are investigated. To achieve the necessary unit cell deformation, tensile-strained Ge microbridges are used. These systems have been developed for this very purpose at the Paul Scherrer Institute over the last few years. A part of this development is reported in the thesis work of Dr. Martin J. Süess. For the second approach, GeSn alloys are investigated at the Paul Scherrer Institute in close collaboration with the Forschungszentrum Jülich, where the epitaxy of the alloys was developed. This collaborative work led to the demonstration of an optically pumped group IV laser. Together with the material development, this achievement has already been summarized in the thesis of Dr. Stephan Wirths.

The aim of this work is to gain insight into the physics of such direct band gap group IV semiconductors on the route towards an efficient CMOS light source and, thus, covers both systems. In the first part of this dissertation, model calculations are presented to quantify the advantageous effects of uniaxial tensile stress on the properties of Ge in terms of electron distribution and optical gain. The experimental investigation of these advantageous effects is given in the second part of this thesis, which deals with the fabrication and

optical characterization of highly strained Ge microbridges. The strained microstructures are investigated via photoluminescence spectroscopy in dependence of substrate material, strain and temperature.

The material quality plays an important role for the realization of an efficient laser. This is evidentially true for Ge layers under strain and, in particular, for the epitaxially grown GeSn alloys. Therefore, time-resolved pump-probe transmission measurements are performed to extract the carrier lifetime as well as the loss and gain properties of the investigated materials. Here, we build up on the developments during the PhD work of Dr. Peter Friedli, where the synchrotron-based pump-probe spectroscopy was developed at the infrared beamline of the Swiss Light Source. In the third part of the thesis, the time-resolved synchrotron measurements are employed to extract the carrier lifetimes for differently prepared Ge epilayers. Furthermore, the lifetime is measured for strained Ge microbridges.

Finally, the last part of this work deals with the properties of direct band gap GeSn alloys. The lasing characteristics of GeSn waveguide lasers are investigated in dependence of Sn concentration under optical excitation. Moreover, pump-probe transmission measurements are carried out to determine the carrier lifetime and the time-resolved optical gain and loss.

Zusammenfassung

Über mehrere Jahrzehnte gab es einen erstaunlichen Fortschritt in der Entwicklung integrierter Schaltkreise, die in elektronischen Geräten verbaut sind. Dieser Fortschritt konnte aufrechterhalten werden durch eine stetige Verkleinerung der elektronischen Bauteile, die basierend auf der Complementary metal-oxide-semiconductor (CMOS)-Technologie hergestellt werden. Aber bei den derzeitigen und kommenden Größenordnungen stellen die metallischen Leiterbahnen einen Engpass für eine weitere Erhöhung der Rechenleistung dar. Dieser Engpass kann überwunden werden, indem die jetzige Datenübertragung basierend auf elektrischen Strömen durch optische Datenübertragung ersetzt wird. Dafür ist eine effiziente Lichtquelle nötig, die direkt auf dem Chip aufgebracht werden kann. III-V Laser, die eine direkte Bandlücke haben, bieten exzellente Effizienzen, aber es ist eine große Hürde, diese auf der CMOS Plattform zu integrieren. Weltweit arbeiten viele Forschungsgruppen daran, die gravierenden Unverträglichkeiten der III-V-Materialien und des Gruppe IV-Materials Silizium zu überwinden. Ein viel attraktiverer Ansatz ist, ein Material zu benutzen, das inhärent mit der Silizium Technologie verträglich ist, wie z.B. Germanium (Ge), das heutzutage schon in Halbleiterwerken zum Einsatz kommt. Auf den ersten Blick wirkt es abwegig, einen Laser aus Germanium herzustellen wegen der unvorteilhalften Anordnung der elektronischen Bänder, die eine indirekte Bandlücke bilden. Allerdings ist seit langem bekannt, dass die Anordnung der Bänder durch eine Vergrößerung der Basis des Kristallgitters oder durch Legieren von Germanium mit Zinn (Sn) verändert werden kann. Es wird erwartet, dass sich dadurch die Effizienz der strahlenden Rekombination erhöht und sich die Bänder zu einer fundamental direkten Bandlücke anordnen, genau wie für die Bandstruktur der III-V Lasermaterialien.

In dieser Dissertation werden die optischen Eigenschaften dieser beiden sogenannten direkten Gruppe IV Halbleiter untersucht. Um die notwendige Vergrößerung der Kristallstrukturbasis zu erzielen, werden zugverspannte Germanium Mikrobrücken herangezogen. Diese Strukturen wurden für genau diesen Zweck über den Verlauf der letzten Jahre am Paul Scherrer Institut entwickelt. Ein Teil dieser Entwicklung ist in der Dissertation von Dr. Martin J. Süess enthalten. Um den zweiten Ansatz zu verfolgen, werden GeSn Legierungen am Paul Scherrer Institut untersucht in enger Zusammenarbeit mit dem Forschungszentrum Jülich, welches das epitaktische Wachstum der Schichten entwickelt hat. Diese gemeinschaftliche Arbeit führte zur Demonstration eines optischen angeregten Lasers. Dieser Erfolg ist zusammengefasst in der Dissertation von Dr. Stephan Wirths zusammen mit den Details über die Materialentwicklung.

Der Zweck dieser Dissertation ist es, die Kenntnis über die Physik dieser direkten Gruppe IV-Halbleiter zu erweitern auf dem Weg zur Entwicklung einer effizienten CMOS Lichtquelle, weshalb beide Systeme behandelt werden. Im ersten Teil dieser Dissertation werden Modellrechnungen präsentiert, um die vorteilhaften Effekte monoaxialer Zugverspannung auf die Eigenschaften Germaniums zu quantifizieren im Hinblick auf die Elektronenverteilung und optische Verstärkung. Die experimentelle Untersuchung dieser nützlichen Effekte wird im zweiten Teil dieser Arbeit vorgestellt, welcher sich mit der Herstellung und optischen Charakterisierung von Germaniumbrücken unter hoher Zugspannung beschäftigt. Die verspannten Strukturen werden mit Photolumineszenz-Spektroskopie in Abhängigkeit des Ausgangsmaterials, der Verspannung und der Temperatur untersucht.

Die Qualität des Materials spielt eine große Rolle bei der Entwicklung eines effizienten Lasers. Das gilt offentlichtlich für die verspannten Germaniumschichten und, im Besonderen, für die epitaktisch hergestellten GeSn Schichten. Daher werden zeitaufgelöste Pump-Probe Tranmissionsmessungen durchgeführt, um sowohl die Lebenszeit der Ladungsträger als auch die optische Verstärkung und den Verlust für die untersuchten Materialien zu bestimmen. Hierbei bauen wir auf den Entwicklungen der Dissertation von Dr. Peter Friedli auf, aus welcher der Aufbau für die Pump-Probe Spektroskopie an der Infrarot Strahllinie des Swiss Light Source Synchrotrons hervorgegangen ist. Im dritten Teil der Dissertation werden die zeitaufgelösten Synchrotron-Messungen angewandt, um die Lebenszeit der Ladungsträger für verschiedenartige Germaniumschichten zu bestimmen. Darüber hinaus wird die Ladungsträgerlebenszeit gemessen für verspannte Germaniumbrücken.

Schließlich behandelt der letzte Teil dieser Arbeit die Eigenschaften des direkten Halbleiters GeSn. Die Merkmale von GeSn Lasern werden untersucht unter optischer Anregung in Abhängigkeit der Sn-Konzentration. Ferner werden Pump-Probe Messungen durchgeführt, um die Lebenszeit der Ladungsträger zu bestimmen sowie die optische Verstärkung und den Verlust.

Contents

1 Introduction

Contents

1.1 Evolution of Moore's Law

Until the end of the 1950s, computers were large, bulky machines that consisted of hundreds or thousands of vacuum tubes. They were limited in their operations and yet required tremendous power and space [1]. In this respect, it is not surprising that at that time the CEO of IBM, Thomas Watson, presumed that *' (...) there is a world market for maybe five computers'*.

The development took a drastic acceleration after the invention of the first electronic circuits based on the semiconducting materials germanium (Ge) [2] and silicon (Si) [3]. Starting out with only a few single components per integrated function in the beginning of the 1960s, improvements led to an exponential increase in component density and already ~ 100 integrated elements per circuit in 1965. Intel co-founder Gordon Moore early recognized this exponential increase in integration density. He predicted this trend to continue in the future and anticipated the benefits and possibilities which could come along, namely *'such wonders as home computers (...), automatic controls for automobiles, and personal portable communications equipment'* [4].

The accuracy of Moore's prediction, which is widely known as 'Moore's law', is shown in Fig. 1.1, where the transistor density per single chip is shown in dependence of its year of introduction. Over a time frame of more than four decades, the number of transistors on

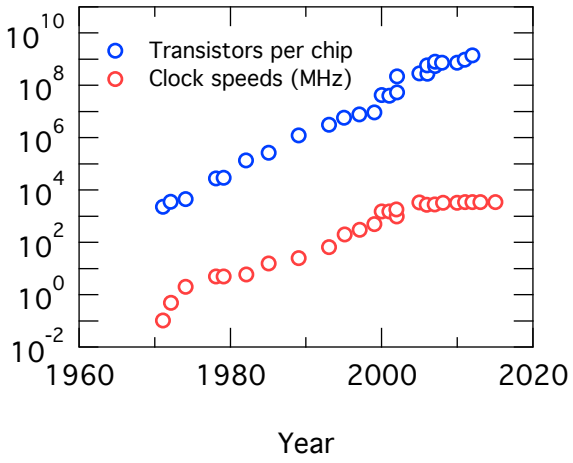

Figure 1.1: The number of transistors per chip (blue circles) followed an exponential decrease over several decades, which is widely known as Moore's law. The evolution of processor clock speeds is depicted as red circles (reproduced from [5]).

a chip could be doubled faster than every ~ 2 years such that by now, modern integrated circuits feature billions of components. The high device density together with an ever cheaper production cost per chip and the simultaneous increase in computing power led to the ubiquitous role computers play nowadays: No matter if it is at the work place e.g. in the fields of science or stock exchange, where large-scale computations are required, or in leisure time using a mobile device to gather information or enjoy entertainment - the progress in semiconductor industry has changed the way we live our lives. With the advent of the 'internet of things' [6], the digitalization will tremendously increase further, which demands further resources in terms of connectivity and computing power.

The progress in integrated circuits was driven by the scaling in device dimensions. For the year 2017, the international technology roadmap for semiconductors (ITRS), which is written by a global consortium of industrial partners, foresees the introduction of the 7 nm technology node [7]. This means that half the distance between identical features of an array, e.g. gate electrodes, are only 7 nm apart. Such device dimensions can only be reached with large investments in semiconductor technology e.g. to meet the required resolution with mass-scale and high-throughput lithography. Sooner or later, Moore's law will approach its limits and the semiconductor industry will have to find new solutions to enable future applications with ever increasing performance [5]. In Fig. 1.1, the red circles depict how the clock speed of processors has varied over the years, and it is found to have saturated in the GHz regime after the year 2000. The reason lies in the increased heat generation for reduced device dimensions. For new technology generations, the power density rises and approaches levels $> 100\,\mathrm{W/cm^2}$ similar to the power density inside a nuclear reactor [8].

Since the clock speed could not be increased further because of heating effects, multi-core architectures were introduced. This complicates the implementation of algorithms, which had to be massively parallelized [5].

In fact, a major contribution to the power consumption of integrated circuits at modern technology nodes stems from the electrical interconnects and constitutes e.g. more than 50% of the dissipated power for the 50 nm technology node [9]. The solution would be the replacement of the electrical interconnects by their optical counterparts [10]. When compared in terms of power consumption, optical interconnects outperform state-of-the-art electrical interconnects and increase in advantage with future technology nodes [11]. The advantages of photon-based signal transmission are not limited to reduced power dissipation: Optical interconnects also outperform e.g. in terms of delay time and band width, are not susceptible to effects like frequency-dependent cross-talk or impedance matching, and offer novel concepts such as wavelength division multiplexing [11–14]. Therefore, realizing data transmission via photons offers great improvements for integrated circuit performance and -power requirements and might perhaps one day be as essential on and between chips as it is already today in long-haul communications.

1.2 Towards the Implementation of CMOS Optical Interconnects

For photon-based on-chip signal transmission, several active and passive devices are needed to perform the necessary operations. An illustration of such an electronic-photonic integrated circuit is schematically shown in Fig. 1.2. The key photonic components are the light source in form of an electrically pumped laser, waveguides for light distribution, multiplexers and demultiplexers to share waveguides e.g. for light at different wavelengths, as well as modulators and photodetectors to modulate the optical signal and to convert it back into an electrical signal, respectively. In order to process the circuit within the same process line like the electronic modules, the photonic components have to be fabricated in a way which complies with the complementary metal-oxide-semiconductor (CMOS) platform. This poses additional requirements for the photonic devices e.g. in terms of material availability. To give some examples, gold or semiconductor elements from the groups III and V diffuse into silicon and may introduce fast carrier recombination centers or act as uncontrolled dopant, respectively. These elements are, therefore, not allowed in a CMOS manufacturing line [15]. But those requirements are key because only if the highly evolved CMOS technology can be used, integrated electronic-photonic circuits can be manufactured in a very large scale and, hence, at an acceptably low price per chip.

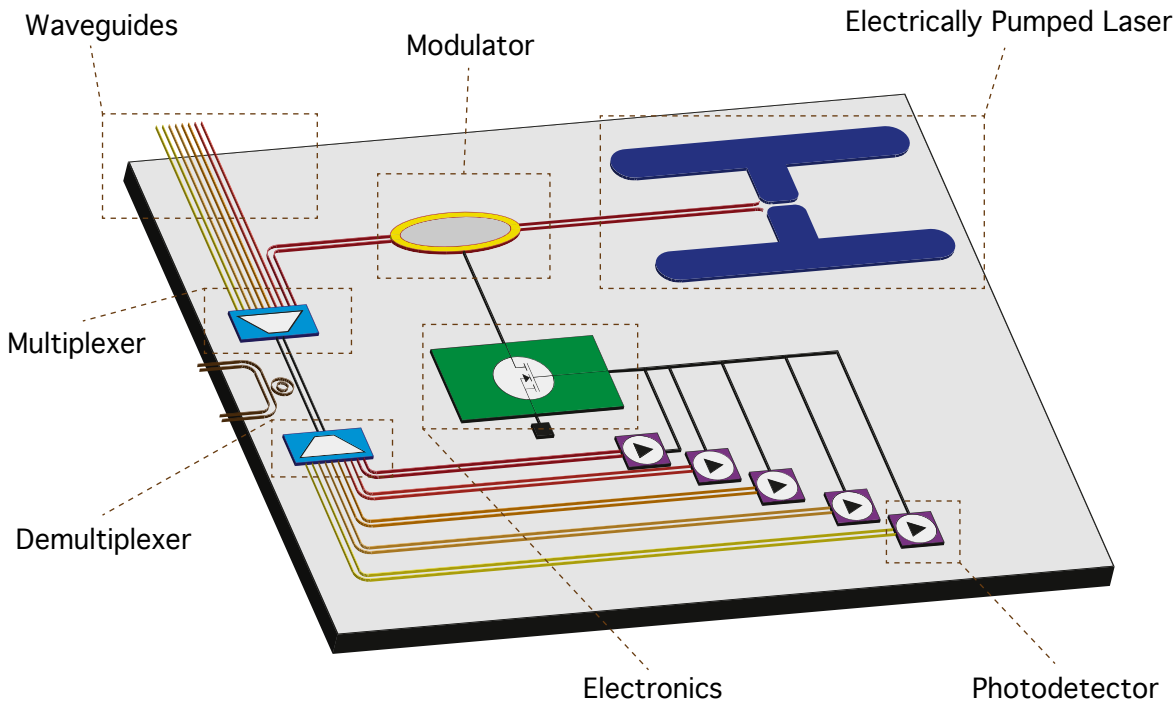

Figure 1.2: Illustration of the key components constituting an electronic-photonic integrated circuit.

Most of the necessary photonic devices have already been developed in a silicon-compatible way. The range of available CMOS compatible photonic components spans from waveguides [16–19] and multiplexers [20–23] to modulators [24–27] and photodetectors [28–32]. However, in spite of many years of research, an efficient light source that can be monolithically integrated onto Si is still missing to complete the set of required devices.

Light generation in Si is a challenging task because of its electronic band structure. In Fig. 1.3, schematic illustrations depict the cases for a direct band gap semiconductor and an indirect band gap semiconductor, respectively. In direct band gap systems, like the typical III-V laser materials InGaAs or InP, the band extrema of the conduction and valence bands in momentum- or k-space are at the center of the Brillouin zone [33]. Electrons and holes can, therefore, recombine radiatively via transitions which are direct in k-space, i.e. at the same momentum. In contrast, for an indirect semiconductor like Si, the conduction band minimum lies at a different k-vector, from where an efficient radiative recombination does not take place due to the required momentum transfer e.g. via phonon absorption or -emission. For Si, the 6-fold degenerate conduction band minimum is at the Δ-valley and has a band gap of 1.1 eV, whereas the gap for the optically active Γ states is 3.4 eV [34]. The situation is less disadvantageous for Ge where the conduction band offset ΔE_{cb} between the direct Γ states and the indirect L-valleys is only $\sim$ 140 meV [35]. Ge is a CMOS compatible material

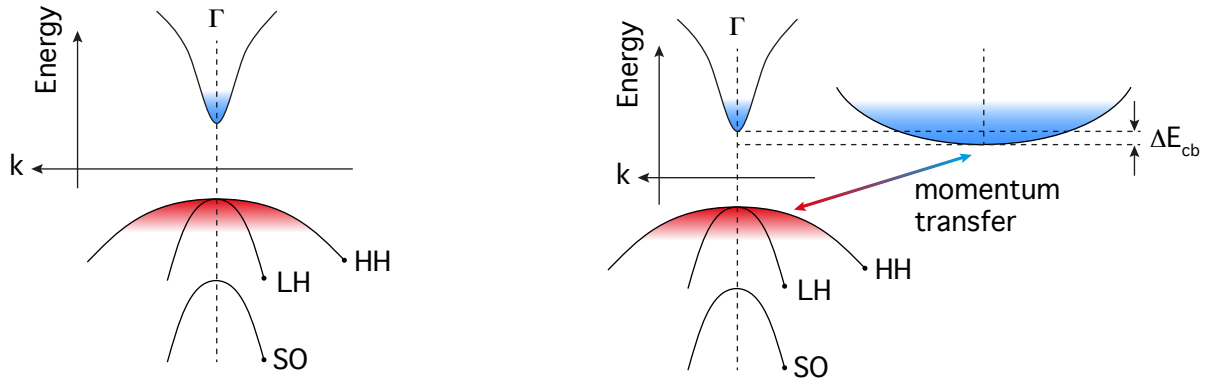

(a) Band structure of direct band gap semiconductor in momentum space.

(b) Band structure of indirect band gap semiconductor in momentum space.

Figure 1.3: Schematic illustration of electronic band structure in momentum space for (a) direct band gap semiconductor such as III-V alloys like InGaAs or InP and (b) indirect band gap semiconductor such as the group IV elements Si and Ge.

and nowadays already in use as a stressor layer for integrated circuits [36], such that the prospect to engineer Ge into a direct band gap material and, hence, into an efficient light emitter has triggered extensive research efforts.

1.3 Monolithic Approaches for Si-compatible Lasers

While several photonic components based on CMOS compatible materials could meet or even exceed the performance of their III-V counterparts, this does not hold true for the laser source. The best choice to achieve maximum performance for electronics and photonics would be the integration of state-of-the-art III-V lasers on Si. A lot of progress has been achieved for the hybrid integration of III-V lasers on Si either by heterogeneous approaches which involve bonding of epitaxial layers or dies [37–40] or by direct epitaxial growth on Si [41–45]. However, this does not meet the CMOS compatibility criterion and can, therefore, not gain from the high impact that comes along with very-large-scale integration (VLSI).

The more rewarding route is to rather take a CMOS compatible material and increase its radiative efficiency. Several attempts have been undertaken to improve light generation in Si e.g. by the introduction of Er dopants [46–48] or the creation of Si/SiO_2 nanostructures [49]. While the gain observed in Si nanocrystals could not be substantiated by a subsequent demonstration of lasing, Er suffers from limited modal gain such that ultra-high Q-factor cavities are required to achieve lasing [47]. Another approach aims to create a direct band gap by zone-folding in Si/Ge superlattices [50–52] or in a multilayer $SiGe_2Si_2Ge_2SiGe_{12}$ superstructure [53, 54]. The high demands set to epitaxy hinder the success in this approach,

as the optical properties significantly deteriorate for deviations from the nominal structure in terms of composition, thickness or interface properties [54]. Lasing in an all-Si device could be demonstrated making use of stimulated Raman scattering [55–58]. However, the need of an additional laser for optical pumping renders this approach not feasible.

Recently, intensive research effort has been focused on realizing a Si-compatible laser based on Ge. The motivation stems from the fact that the conduction band offset is much smaller than for Si, i.e. the conduction band alignment is by far less 'indirect', while Ge is a fully CMOS-compatible material. The initial approach which was proposed in 2007 at MIT is to introduce a high n-doping $N_d > 7{\times}10^{19}\,\mathrm{cm}^{-3}$ to fill the electronic states in the L-valley and, thereby, increase the population of the Γ valley. Subsequently, lasing was claimed under optical pumping for $N_d = 1{\times}10^{19}\,\mathrm{cm}^{-3}$ [59] and under electrical pumping for $N_d = 4{\times}10^{19}\,\mathrm{cm}^{-3}$ [60] with the observation of a threshold in output intensity. Since these reports in 2010 and 2012, there has only been one reproduction of the results with an intensity threshold for edge-emitting n-doped light-emitting-diodes which coincides with the breakdown of the devices [61]. On the other hand, a systematic gain-and-loss study via time-resolved pump-probe measurements revealed that the strong loss from intervalence band absorption prevents optical amplification for all injected carrier densities up to $10^{20}\,\mathrm{cm}^{-3}$ for $N_d = 1{\times}10^{19}\,\mathrm{cm}^{-3}$ [62], which is in conflict with the asserted observation of lasing. Theoretical calculations of the gain and threshold current density [63–65] under the consideration of realistic non-radiative lifetimes [66] find threshold current densities $\geq 10\,\mathrm{MA/cm}^2$, which exceeds the observed thresholds by ~ 2 orders of magnitude. As the gain/loss study and theory contradicts the claim of lasing, more research is needed to understand the observed results.

Instead of n-doping, another way to increase the emission intensity for Ge is to transform the material into a direct band gap semiconductor. By reducing the offset between Γ and L valleys, the population of electrons at the Γ valley increases such that ultimately direct band gap Ge should offer the advantageous of III-V materials while maintaining full CMOS compatibility. The application of tensile strain is predicted to be one opportunity to induce a direct band gap [63, 67]. Tensile strain can be achieved either epitaxially on a wafer scale [68, 69] but is either limited to strain $\leq 0.25\%$ or to thicknesses which are insufficient to guide an optical mode at near infrared wavelengths. Another possibility is the use of external stressor layers such as silicon nitride [70–72]. The highest strain values in sufficiently large volumes have been obtained by a top-down process which redistributes and enhances a small biaxial strain [73–75]. These type of structures will be discussed in this thesis. Furthermore, a direct band gap can be obtained when Ge is alloyed with a sufficiently high amount of Sn [76]. This prediction has recently been experimentally verified and lasing was

shown for a direct band gap GeSn alloy under optical excitation at low temperatures [77].

1.4 Outline of this Thesis

The aim of this thesis is to investigate the properties of direct band gap Ge in tensile strained Ge microstructures and GeSn alloys.

This thesis is divided into seven chapters. A short introduction and motivation for the following research was given in chapter 1. In chapter 2, the impact of tensile strain on the optical properties of Ge is modelled. The calculations focus on the electron population in the conduction band in function of strain and temperature, as well as on the gain and loss in tensile-strained Ge under varying levels of strain, n-doping and carrier injection. A method to introduce high uniaxial tensile stress in Ge by strain-redistribution is presented in chapter 3 with a special focus on fabrication. The strain-induced changes are probed by photoluminescence spectroscopy. The experimental demonstration of the crossover from indirect- to direct band gap strained Ge is shown by temperature-dependent photoluminescence measurements. In chapter 4, the non-radiative carrier lifetime is extracted by time-resolved pump-probe measurements for differently prepared Ge layers and tensilely strained Ge microstructures. The impact of the conduction band offset and the non-radiative lifetime on the properties of optically-pumped GeSn lasers is presented in chapter 5. These investigations are done by comparing the laser performance of different GeSn waveguide lasers and by time-resolved pump-probe measurements to extract the carrier lifetimes, gain and loss. Proposals for future experiments are given in chapter 6, while the summary and conclusion of the outcome of this thesis can be found in chapter 7.

2

Modelling of Uniaxially Stressed Germanium as Optical Gain Medium

Contents

In this chapter, the optical properties of strained Ge are modelled to investigate its suitability as optical gain medium. For these simulations, an 8-band k·p approach is adopted. After calculating the electronic band edges and the electron population of the Γ and L conduction band valleys in function of strain, a model to calculate the interband absorption is presented which is, subsequently, applied for the case of uniaxially stressed Ge.

2.1 Strain-Dependent Electronic Band Edges

The biggest obstacle for efficient light generation in Ge is its indirect band gap which leads to virtually all electrons residing in the L-valleys, from where an efficient radiative recombination does not take place due to the need of a phonon for momentum conservation. However, already in the 1990s theoretical work presented the idea that tensile strain can transform Ge

into a direct band gap semiconductor [67], albeit the lack of a technique to introduce such a high strain at that time.

To calculate the extrema of the electronic bands in function of strain, the band structure modelling tool nextnano^3 [78] is used where the deformation potential approach of ref. [79] is implemented. With the average valence band energy $E_{v,av} = (E_{hh} + E_{lh} + E_{so})/3$ of heavy hole (hh), light hole (lh) and split-off (so) valence bands set to zero, the Γ- and L conduction band minima as measured from $E_{v,av} = 0$ can be described as

$$E_{\Gamma,L} = \frac{1}{3}\Delta_{so} + E^0_{\Gamma,L} + \Delta E^{hyd}_{\Gamma,L}, \tag{2.1}$$

where Δ_{so} is the spin-orbit split off energy when no strain is applied, E^0_Γ and E^0_L are the Γ- and L band edges for relaxed, bulk Ge, and $\Delta E^{hyd}_{\Gamma,L}$ describes the changes of the conduction band minima due to the hydrostatic strain component:

$$\Delta E^{hyd}_{\Gamma,L} = \left(a_{c\Gamma,L} - a_v\right)(2\varepsilon_{xx} + \varepsilon_{zz}). \tag{2.2}$$

Here, $a_{c\Gamma,L}$ and a_v denote the deformation potentials for the conduction band edges at Γ and L, and for the averaged valence bands, respectively. Furthermore, ε_{xx} and ε_{zz} are the in-plane (ε_{xx}) and out-of-plane (ε_{zz}) strain components for biaxial stress or the strain components parallel (ε_{zz}) and perpendicular (ε_{xx}) to an applied uniaxial stress. The components parallel

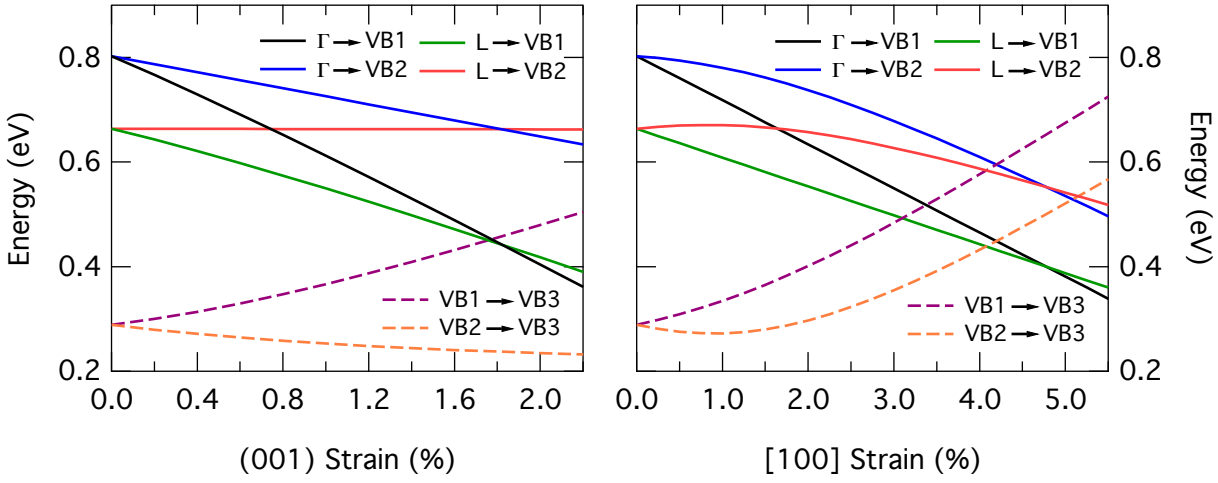

(a) Biaxial tensile stress in (001) plane.

(b) Uniaxial tensile stress along [100] direction.

Figure 2.1: Energies for interband- (solid lines) and intervalence band transitions (broken lines) in Ge for (a) biaxial tensile stress in (001) plane and (b) uniaxal tensile stress along [100] direction.

and perpendicular to the applied stress are related via the Poisson ratio ν as [80]

$$\text{biaxial stress}: \quad \varepsilon_{zz} = -\nu_{bi}\ \varepsilon_{xx} = -0.74\ \varepsilon_{xx}, \tag{2.3}$$

$$\text{uniaxial stress}: \quad \varepsilon_{xx} = -\nu_{uni}\ \varepsilon_{zz} = -0.26\ \varepsilon_{zz}. \tag{2.4}$$

Besides the modulation of the conduction band minima, strain also leads to an alteration of the valence band structure. The band edges for the three valence bands are calculated as follows:

$$E_{hh} = \frac{1}{3}\Delta_{so} - \frac{\delta E}{2}, \tag{2.5}$$

$$E_{lh} = -\frac{1}{6}\Delta_{so} + \frac{\delta E}{4} + \frac{\sqrt{\Delta_{so}^2 + \Delta_{so}\delta E + \frac{9}{4}\delta E^2}}{2}, \tag{2.6}$$

$$E_{so} = -\frac{1}{6}\Delta_{so} + \frac{\delta E}{4} - \frac{\sqrt{\Delta_{so}^2 + \Delta_{so}\delta E + \frac{9}{4}\delta E^2}}{2}, \tag{2.7}$$

$$\delta E = 2b\,(\varepsilon_{zz} - \varepsilon_{xx})\,. \tag{2.8}$$

For the strain-induced variation δE given by equation (2.8), b denotes the tetragonal deformation potential. The full list of band structure parameters used for the simulations can be found in chapter A.1.

The resulting interband- (IB) and intervalence band (IVB) transition energies are shown in Fig. 2.1 in function of a biaxial stress in the (001) plane (Fig. 2.1(a)) as well as for a uniaxial stress along the [100] direction (Fig. 2.1(b)). The solid lines depict the four interband transitions between the Γ or the L conduction band valleys into the two highest valence bands termed VB1 and VB2. Furthermore, the intervalence band transitions between either of the two top valence bands VB1 and VB2 and the lowest valence band VB3 are shown as dashed lines. Due to a mixing of the valence bands, a distinction in "heavy hole-" and "light hole" bands becomes meaningless for high strain. The ratio of effective masses m^*_{VB1}/m^*_{VB2} decreases from ~ 4.4 for relaxed Ge to ~ 1.0 at 4.0% strain along [100]. For low values of biaxial tensile stress, VB1 and VB2 are mostly "light hole-" and "heavy hole"-like, respectively, and vice versa for uniaxial tensile stress.

For both stress-loadings, a similar qualitative behavior is observed with a steady decrease in interband transition energies. Most importantly, the Γ valley shows a faster decrease in energy, such that for a strain larger than 1.8% for the biaxial case and 4.7% for the uniaxial case, Ge transforms into a semiconductor with a fundamental direct band gap, which is in good agreement with other theoretical work [75, 81–83].

As the strain increases, the IVB energies approach the energy for IB recombinations from the direct Γ valley. Eventually, the transitions are in resonance for biaxial strain just at the crossover to a direct band gap. For uniaxial stress, the resonance condition between the IB transition Γ → VB1 and the IVB transitions are reached at 3.4% (VB1 → VB2) and 4.2% (VB2 → VB3), respectively. Those direct transitions between different valence bands have been identified as the main absorption loss channel in relaxed Ge [62]. Obviously, the IVB absorption is even more of a concern for strained Ge.

2.2 Electron Statistics in Dependence of Strain and Temperature

As was shown above, tensile strain leads to a reduction in the conduction band offset $\Delta E_{cb} = E_\Gamma - E_L$, which starts out with an offset of $\sim 140\,\text{meV}$ and is, eventually, reversed when the Γ valley falls below the indirect L valleys. Therefore, the band alignment changes monotonically towards a more favorable condition for electrons to populate the Γ valley.

In Fig. 2.2, the carrier statistics in the conduction band are shown at room temperature in dependence of strain. The electron densities in the conduction band minima N_Γ and N_L are calculated by integrating the product of three-dimensional density of states and electron

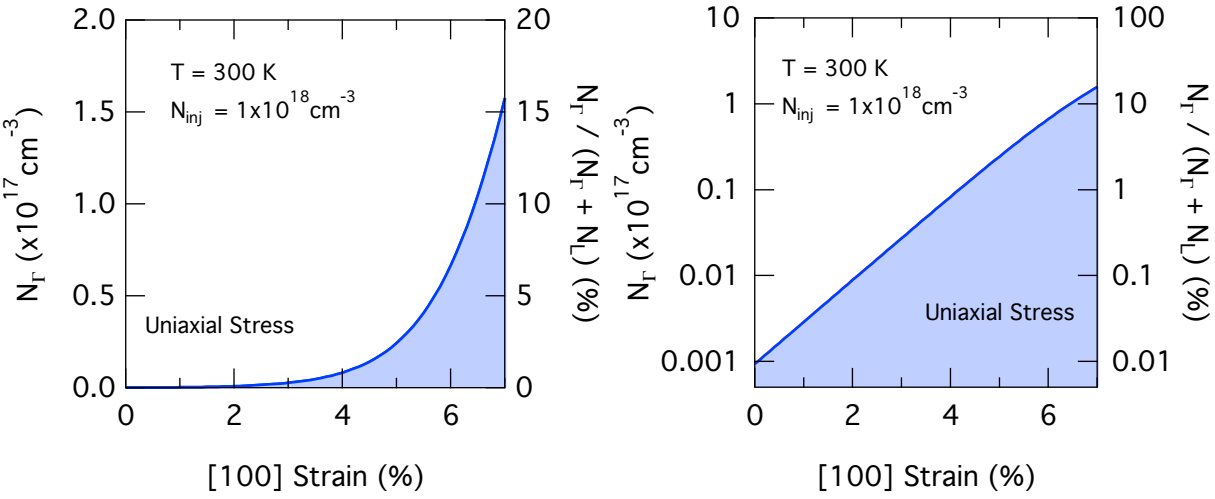

(a) Carrier density in Γ valley - linear plot.

(b) Carrier density in Γ valley - logarithmic plot.

Figure 2.2: Absolute (left ordinate) and relative (right ordinate) electron population of the Γ valley in function of [100] strain. The calculations are performed for a temperature of 300 K and an electron density of $1\times10^{18}\,\text{cm}^{-3}$ and are shown in linear (a) and logarithmic scale (b).

Fermi-function:

$$N_{\Gamma,L} = \int_0^\infty \mathrm{d}E \; \frac{1}{2\pi} \; \frac{(2m^*_{\Gamma,L})^{3/2}}{\hbar^3} \; \sqrt{E - E_{\Gamma,L}} \; \frac{1}{\exp\left(\frac{E-\mu_e}{kT}\right)+1}. \tag{2.9}$$

Here, the density of states effective masses for relaxed Ge are $m^*_\Gamma = 0.041\, m_0$ [84], and $m^*_L = \left(d^2 m^l_L m^t_L m^t_L\right)^{1/3} = 0.552\, m_0$ with the longitudinal and transverse masses $m^l_L = 1.588\, m_0$ and $m^t_L = 0.082\, m_0$ [84] and a degeneracy d of 4. Furthermore, m_0 is the electron mass in rest, $\hbar$ is the reduced Planck constant, $E_{\Gamma,L}$ are the strain-dependent band edge energies, μ_e is the electron quasi Fermi level, and k is the Boltzmann constant. For m^*_Γ, the strain-dependent mass is determined via the 8-band k·p method in nextnano^3. Due to the absence of experimental data on the strain-dependence of m^*_L, the L-effective mass is assumed to be independent of strain. This assumption is in agreement with simulations via 30-band k·p [81] or the pseudopotential method [85], which show that strain leads to an only weak reduction of the density of states at the L-valley.

From here on, the focus will be directed exclusively towards the case of uniaxial stress due to the fact that the experimental results presented in this thesis concern uniaxially stressed Ge microstructures (see chapter 3). As can be seen from the absolute and relative electron density in the Γ valley, which is plotted in Fig. 2.2 on linear (2.2(a)) and logarithmic ordinate (2.2(b)), strain leads to an exponential increase of the electron population at Γ. For an additional 2% of strain, the electron density in the Γ valley is increased by approx. one order of magnitude, as expected from Boltzmann statistics estimating $\Delta N_\Gamma / N_\Gamma \propto \exp\left(\frac{2\Delta E}{kT}\right) \sim 9.9$ with $kT = 26$ meV at room temperature and $\Delta E = 30$ meV/%. However, even at 7% strain along [100] the occupation of the Γ valley at room temperature is just slightly above 10% due to the thermally broadened Fermi distribution and the comparably small density of states at the Γ valley.

While there is a steady increase in Γ population for larger strain, no abrupt change in the electron distribution between the Γ and L levels can be seen when the crossover to a fundamental direct band gap occurs at $\sim$ 4.7%. An optical measurement such as e.g. photoluminescence (PL) spectroscopy at room temperature would, hence, not give any immediate insight into the conduction band alignment of a strained structure. However, the situation changes drastically at low temperatures when carriers thermalize into the lowest energetic states due to the reduced thermal energy kT.

The calculations in Fig. 2.2 are repeated with temperature as additional variable (see Fig. 2.3) for [100] strain between 2.0% and 6.0%. For $\varepsilon < 4.7\%$ the electrons thermalize from the Γ- into the L-states upon decreasing the temperature, and vice versa for $\varepsilon > 4.7\%$. This leads to a qualitatively opposite behavior depending on the conduction band alignment. Therefore, temperature-dependent measurements where the carrier occupation of the Γ

valley is probed (such as in PL spectroscopy) offer a reliable method to distinguish between fundamentally direct- and indirect Ge. This low-temperature approach is later used in chapter 3.4 to experimentally demonstrate the crossover towards direct band gap strained Ge.

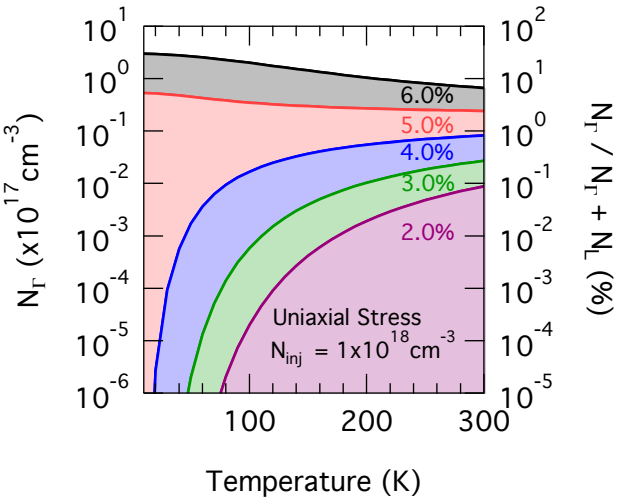

Figure 2.3: Absolute (left ordinate) and relative (right ordinate) electron population of the Γ valley for [100] strain ranging from 2.0% to 6.0% in dependence of temperature. The injected carrier density amounts to 1×10^{18} cm^{-3}.

2.3 Gain Calculations for Strained Germanium

Since the first proposal of using heavily n-doped Ge as optical gain medium [86], there has been an increased focus of theoretical work on how an efficient group IV laser can be realized. Special attention is paid to the effects and interplay of tensile strain and n-doping, where most of the work utilizes second-order perturbation theory such as the k·p approach including 6 bands [63, 82, 87, 88] or 30 bands [81], where the latter enables to describe the energy dispersion over the full *k*-space. In other approaches, the theory is based on the empirical pseudopotential method [83], density functional theory [89] or the tight-binding model [64, 90]. While mostly the effect of a biaxial tensile strain has been investigated, the recent experimental results reporting a high uniaxial tensile stress (see chapter 3 and refs. [73, 74]) triggered the consideration of uniaxial stress, as well [75, 91, 92].

In the following, a model for interband transitions in strained Ge is presented where the electronic band parameters are extracted from 8-band k·p simulations. Subsequently, the model is applied to calculate the absorption and gain in uniaxially stressed Ge in dependence of strain, injected carrier density and n-doping density. The transitions which will be investigated are schematically depicted in Fig. 2.4:

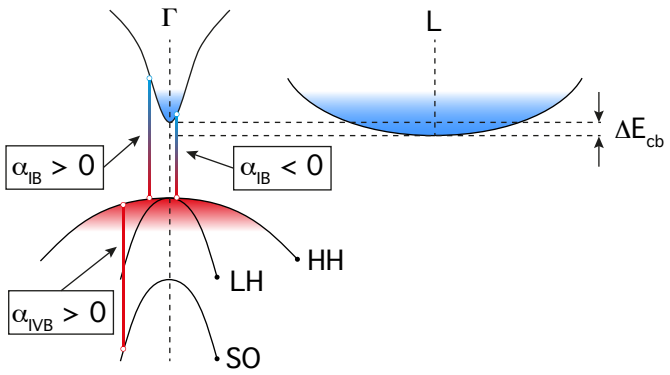

Figure 2.4: Schematic representation of the electronic band structure for relaxed Ge. The vertical transitions which are relevant for the optical properties involve either conduction- and valence band states (α_{IB}) or solely the valence bands (α_{IVB}).

On the one hand, direct transitions occur between the conduction band and the valence band. Depending on the occupation probability for the involved electron- and hole states, the interband transition can lead to a positive absorption, or to a negative absorption, which will in the following be termed gain.

On the other hand, unipolar interband transitions within the valence bands lead to a strong positive absorption, i.e. hindering the occurence of gain. The intervalence band absorption can be described by the same formalism as the interband transitions.

2.3.1 Model for Interband Absorption

For the description of interband absorption, we look at the transition of an electron between an initial energy E_i and a final energy E_f with $E_f > E_i$. To take the symmetry due to an applied strain into account, the valence band is described by a cylindrical symmetry, whereas an isotropic dispersion is assumed for the conduction band:

$$E_f = E_f^0 + \frac{\hbar^2 k_f^2}{2m_f}, \tag{2.10}$$

$$E_i = E_i^0 - \frac{\hbar^2 k_{i\parallel}^2}{2m_{i\parallel}} - \frac{\hbar^2 k_{i\perp}^2}{2m_{i\perp}}. \tag{2.11}$$

Here, E_i^0 and E_f^0 denote the valence- and conduction band extrema, m_f the electron effective mass, and $m_{i\parallel}$ and $m_{i\perp}$ the hole effective masses parallel and perpendicular to the applied uniaxial stress. The density of state effective masses are as before given as

$$m^* = \left(d^2\, m_\parallel\, m_\perp\, m_\perp\right)^{1/3}, \tag{2.12}$$

with the degeneracy d.

Furthermore, the absorption coefficient for transitions $E_i \rightarrow E_f$ derived from Fermi's golden rule reads [93]

$$\alpha_0(\hbar\omega) = \frac{\pi e^2}{n_r c \varepsilon_0 m_0^2 \omega} \int \frac{2\,\mathrm{d}^3k}{(2\pi)^3} \left|\hat{e}\cdot\mathbf{p_{if}}\right|^2 \delta\left(E_f - E_i - \hbar\omega\right)\left[1 - f_h(E_i) - f_e\left(E_f\right)\right], \tag{2.13}$$

where e denotes the elemental charge, n_r the refractive index, c the speed of light, and ε_0 the dielectric permittivity. The dipole matrix element $|\hat{e}\cdot\mathbf{p_{if}}|^2$ is determined by the orbital composition of the electronic states involved in the transition. Moreover, the Fermi functions for electrons (f_e) and holes (f_h) are defined as

$$f_e\left(E_f\right) = \frac{1}{e^{\frac{E_f-\mu_e}{kT}}+1}, \tag{2.14}$$

$$f_h(E_i) = 1 - \frac{1}{e^{\frac{E_i-\mu_h}{kT}}+1}, \tag{2.15}$$

with the quasi Fermi levels for electrons μ_e and holes μ_h defined separately.

The integral in equation (2.13) is solved using cylindrical coordinates due to the symmetry of the strained crystal, such that the equation reads after doing the integration over the azimuthal angle

$$\alpha_0(\hbar\omega) = \frac{e^2}{2\pi n_r c \varepsilon_0 m_0^2 \omega} \int \mathrm{d}k_{i\parallel} \int \mathrm{d}k_{i\perp}\, k_{i\perp} \left|\hat{e}\cdot\mathbf{p_{if}}\right|^2 \delta\left(E_f - E_i - \hbar\omega\right)\left[1 - f_h(E_i) - f_e\left(E_f\right)\right]. \tag{2.16}$$

The investigated transitions between the states described in equations (2.10) and (2.11) are direct transitions in k-space at a photon energy $\hbar\omega$, leading to the following relations due to energy- and momentum conservation:

$$\hbar\omega = E_f - E_i = E_f^0 + \frac{\hbar^2 k_f^2}{2m_f} - E_i^0 + \frac{\hbar k_{i\parallel}^2}{2m_{i\parallel}} + \frac{\hbar k_{i\perp}^2}{2m_{i\perp}}, \tag{2.17}$$

$$k_f^2 = k_{i\parallel}^2 + k_{i\perp}^2. \tag{2.18}$$

After integration over $k_{i\perp}$ and using equations (2.17) and (2.18) to express all k-vectors in terms of $k_{i\parallel}$, the absorption can be expressed as

$$\alpha_0(\hbar\omega) = \frac{e^2}{\pi n_r c \varepsilon_0 m_0^2 \omega} \frac{1}{\hbar^2}\left(\frac{1}{m_{i\perp}} + \frac{1}{m_f}\right)^{-1} \times \int_0^x \mathrm{d}k_{i\parallel} \left|\hat{e}\cdot\mathbf{p_{if}}\right|^2 \left(\frac{1}{1+\exp\left(\frac{E_i'-\mu_h}{kT}\right)} - \frac{1}{1+\exp\left(\frac{E_f'-\mu_e}{kT}\right)}\right), \tag{2.19}$$

with

$$E_f' = E_f + \frac{\hbar^2\left(k_{i\parallel}^2 + k_{i\perp}\left(k_{i\parallel}\right)^2\right)}{2m_f}, \tag{2.20}$$

$$E_i' = E_i - \frac{\hbar^2 k_{i\parallel}^2}{2m_{i\parallel}} - \frac{\hbar^2 k_{i\perp}\left(k_{i\parallel}\right)^2}{2m_{i\perp}}, \tag{2.21}$$

$$k_{i\perp}\left(k_{i\parallel}\right) = \sqrt{\frac{2}{\hbar^2}\frac{\left(\hbar\omega - \left(E_f - E_i\right)\right) - \left(\frac{1}{m_f} + \frac{1}{m_{i\parallel}}\right)k_{i\parallel}^2}{\frac{1}{m_{i\perp}} + \frac{1}{m_f}}}, \tag{2.22}$$

and the upper integration limit

$$x = \sqrt{\frac{2}{\hbar^2}\frac{\left(\hbar\omega - \left(E_f - E_i\right)\right)}{\frac{1}{m_{i\parallel}} + \frac{1}{m_f}}}. \tag{2.23}$$

Finally, a homogeneous broadening of the states is taken into account by a convolution of the absorption with a Lorentzian function of width Γ leading to the representation [93]

$$\alpha_{IB}\left(\hbar\omega\right) = \int_0^\infty \mathrm{d}E'\ \alpha_0\left(E'\right)\ \frac{\frac{\Gamma}{2\pi}}{\left(E' - \hbar\omega\right)^2 + \left(\frac{\Gamma}{2}\right)^2}\ . \tag{2.24}$$

Due to the normalization of the Lorentzian function to yield an integral value of 1, the broadening causes a decrease of peak absorption or peak gain, respectively. For the broadening, the experimentally determined value for bulk Ge ($\Gamma = 6.4$ meV [94]) is used.

To obtain the total interband absorption, equation (2.24) is evaluated for transitions between the Γ valley and the two top valence bands. The dipole matrix element is represented by the Kane energy parameter E_p as $|\hat{e}\cdot\mathbf{p_{if}}|^2 = \eta_i\frac{m_0}{2}E_p$ [95, 96] with $E_p = 26$ eV [97] and $\eta_1 = 0.75$, $\eta_2 = 0.25$ accounting for the relative strengths for transitions involving heavy hole- or light hole-like valence bands given by the selection rules for interband recombination [98]. E_p is assumed to be independent of k due to the small range of wave vectors that participate in direct recombinations [63]. Furthermore, the dipole matrix element is taken as constant in function of strain as the orbital composition of the top valence band, where the maximum gain occurs, does not couple to the strain field [99]. For light propagation along the direction of uniaxial stress, the selection rules lead to an equal strength of transverse electric- (TE) and transverse magnetic (TM) modes [98] for transitions involving the highest valence band, such that a separate consideration of both polarizations is not necessary. This is different

for biaxial strain, where the TM gain is dominating (i.e. the polarization orthogonal to the applied stress) [63].

To include strain-dependent variations of the electronic band structure, the band edges are calculated using the deformation potential description as introduced in chapter 2.1. Furthermore, the effective masses are extracted from the energy dispersion obtained via the 8-band k·p approach implemented in nextnano^3 [78]. Details about the k·p simulations including the input parameters can be found in chapter A.1.

Furthermore, phonon-assisted recombinations from the indirect L-valleys are not included in the calculations. For very high electron densities ($\geq 10^{20}$ cm^{-3}), it was found that these indirect processes can contribute up to 30% of the material gain [83]. However, as in the following the focus will not be directed towards such ultra-high electron densities which are experimentally difficult to achieve in a steady-state configuration, the gain from phonon-assisted processes is neglected. The X-valleys, which are not populated with electrons are not explicitly included in the calculations, either.

2.3.2 Calculation of Intervalence Band Absorption

In order to calculate the net optical gain and, hence, answer the question if optical amplification occurs, the parasitic losses (i.e. absorption which does not stem from interband transitions between conduction- and valence band) have to be taken into account. Processes which contribute to these internal losses are in the first place

- free carrier absorption of electrons and holes where the carriers are excited into higher states within the same band [100, 101], often referred to as Drude-type absorption,
- intervalley transitions of electrons between states in the conduction band minima at Γ, L and X [102],
- direct interband transitions for holes between the heavy hole, light hole and spin-orbit split-off valence bands [103–106].

The most severe loss channel for Ge stems from the intervalence band transitions, as recently demonstrated by pump-probe transmission experiments [62]. It was found that in weakly strained ($\varepsilon_{xx} = 0.25\%$ biaxial strain) and/or highly n-doped Ge layers on Si ($N_{dop} = 2.5 \times 10^{19}$ cm^{-3}), the IVB absorption prevents the buildup of any net optical gain despite measured interband gain of up to ~ 1000 cm^{-1}. Nevertheless, the IVB absorption has so far been rarely considered in theoretical models [83, 107]. In the following, the IVB absorption for relaxed Ge is computed and the need for experimental data is discussed.

As IVB transitions are direct transitions formally similar to a recombination between conduction- and valence band, part of the same formalism as described in chapter 2.3.1 can be applied. To derive equation (2.24) for IVB transitions, the absorption without broadening effects α_0^{IVB} is calculated in the same fashion with the final energy state being described as

$$E_f^{IVB} = E_f^0 - \frac{\hbar^2 k_f^2}{2m_f}. \tag{2.25}$$

Furthermore, the dipole matrix element $|\hat{e} \cdot \mathbf{p_{if}}|$ plays an important role in the determination of the IVB transition strength: The squared dipole matrix element for a transition between valence band states termed P_i and P_j reads

$$|\hat{e} \cdot \mathbf{p_{ij}}|^2 = |\langle P_j|\hat{e} \cdot \mathbf{p}|P_i\rangle|^2 = |\langle \sum_{n=1}^{4} \alpha_n O_n|\hat{e} \cdot \mathbf{p}| \sum_{n=1}^{4} \beta_n O_n\rangle|^2, \tag{2.26}$$

where the wave functions of both states P_i and P_j are expressed as a superposition of the four orbital basis functions $|S\rangle$ with s-like symmetry and $|X\rangle$, $|Y\rangle$ and $|Z\rangle$ with p-like symmetry [95]. Due to symmetry arguments, the only non-vanishing contributions are obtained when the momentum-operator $\mathbf{p}$ is applied between an s-like and a p-like orbital function as [98]

$$\begin{aligned} &|\langle X|p_x|S\rangle|^2 = |\langle Y|p_y|S\rangle|^2 = |\langle Z|p_z|S\rangle|^2 \\ &= |\langle S|p_x|X\rangle|^2 = |\langle S|p_y|Y\rangle|^2 = |\langle S|p_z|Z\rangle|^2 = \frac{m_0}{2} E_p. \end{aligned} \tag{2.27}$$

A transition between two valence bands can, hence, only occur if a mixing with the conduction band takes place because the valence bands are generally described by p-type orbitals. Therefore, the squared dipole matrix element between two valence band states for a polarization along $\hat{k}$ reads as

$$\begin{aligned} |\hat{e_k} \cdot \mathbf{p_{ij}}|^2 &= \frac{1}{2}\left(|\langle \alpha_k K|p_k|\beta_s S\rangle|^2 + |\langle \alpha_s S|p_k|\beta_k K\rangle|^2\right) \\ &= \frac{1}{2}\left(\alpha_k^2\beta_s^2 + \alpha_s^2\beta_k^2\right)\frac{m_0}{2} E_p = P_{ij}\frac{m_0}{2} E_p, \end{aligned} \tag{2.28}$$

where α_k, β_k denote the $|K\rangle$-like composition of states P_i and P_j with $|K\rangle \ \epsilon \ \{|X\rangle, |Y\rangle, |Z\rangle\}$, and α_s, β_s are the compositional portions of the $|S\rangle$ orbitals. The composition of the valence band states is extracted from 8-band k·p simulations via nextnano^3 [78] which calculates the eigenfunctions of the strained Hamiltonian matrix.

In Fig. 2.5, the resulting dimensionless transition strengths P_{ij} summed over all polarizations are plotted in function of wave vector k for transitions between all three subbands. In contrast to the dipole matrix element for interband transitions, which is maximum at $k = 0$,

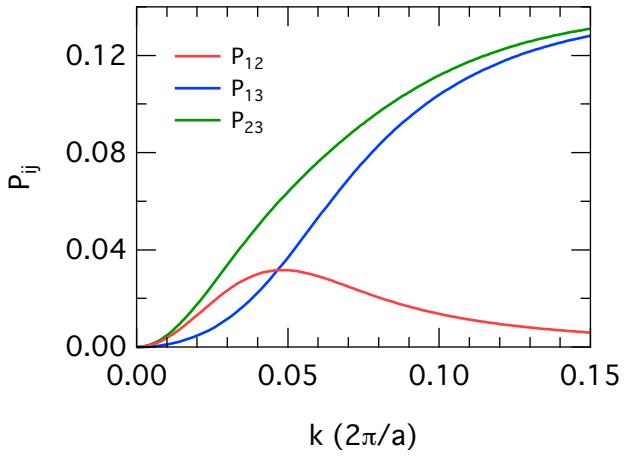

Figure 2.5: Strength of dipole matrix element for intervalence band transitions between all subbands in relaxed Ge obtained from 8-band k·p approach.

there is no interaction with the basis wave function $|S\rangle$ which leads to a vanishing transition strength at the center of the Brillouin zone. Instead, there is a local maximum in dipole matrix element for transitions between the heavy hole and light hole band, whereas the strength of transitions with the split off-band being involved is a monotonically increasing function. It is, therefore, immediately evident from Fig. 2.5 that large hole densities lead to an increased intervalence band absorption. The results are in very good agreement with [108], where the transition strengths are determined with a similar 8-band k·p model.

As a next step, the model is used to calculate the IVB absorption in relaxed, intrinsic Ge for hole densities between 1×10^{19} cm^{-3} and 1×10^{20} cm^{-3}. For these simulations, the average of TE and TM polarization is calculated. Furthermore, the level broadening γ_{ij} between two valence bands i and j is taken as reported in [108], where γ was determined for p-doped $Ge_{0.98}Sn_{0.02}$ alloys by fitting an IVB model to experimental ellipsometry data. The level broadening is obtained for the three IVB transitions with a linear dependence on the hole density N_h as:

$$\gamma_{12} = 29.7 \text{ meV} + 0.27 \text{ meV} \frac{N_h}{10^{18} \text{ cm}^{-3}}, \tag{2.29}$$

$$\gamma_{13} = \gamma_{23} = 24.1 \text{ meV} + 1.41 \text{ meV} \frac{N_h}{10^{18} \text{ cm}^{-3}}. \tag{2.30}$$

Expressed as a k-vector via $k_{ij}^{\gamma} = \sqrt{2\, m_{ij}^{*}\, \gamma_{ij}}/\hbar$ with the reduced effective masses $1/m_{ij}^{*} = 1/m_i^{*} + 1/m_j^{*}$, the broadening constants for unpumped, intrinsic Ge relate to $k_{12}^{\gamma} = 0.015$ $(2\pi/a)$, $k_{13}^{\gamma} = 0.018$ $(2\pi/a)$, and $k_{23}^{\gamma} = 0.012$ $(2\pi/a)$. While the hole-dependent increase in broadening for transition VB1→VB2 is negligible, the broadening for transitions with VB3 involved increases from 24.1 meV to ∼ 100 meV for a hole density of $5{\times}10^{19}$ cm^{-3}.

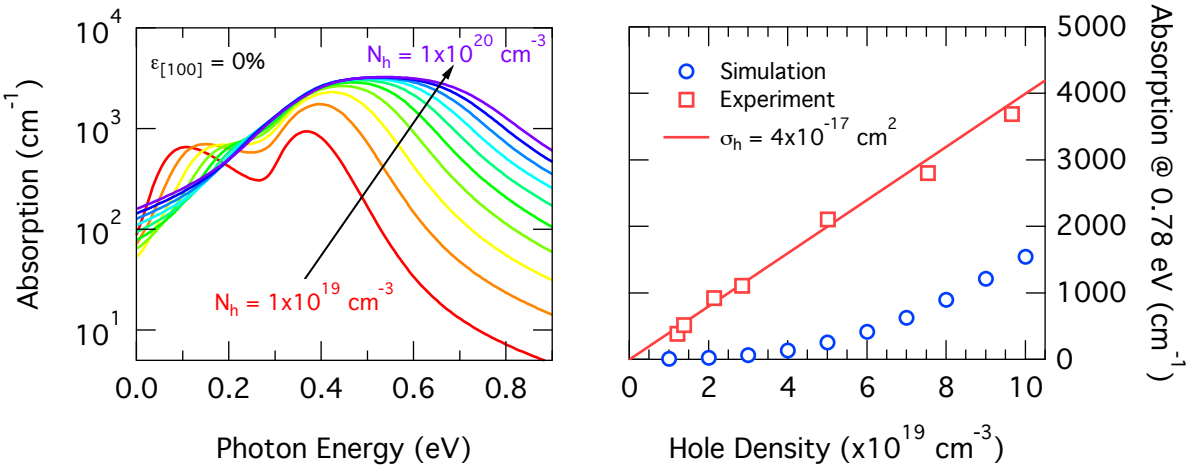

(a) Calculated intervalence band absorption spectra for relaxed Ge.

(b) Absorption at 0.78 eV in function of hole density comparing experiment (red squares) [62] and model (blue circles).

Figure 2.6: (a) Calculated intervalence band absorption spectra for relaxed Ge at hole densities between 1×10^{19} cm^{-3} and 1×10^{20} cm^{-3}. (b) In contrast to the experimental absorption at 0.78 eV reported in [62] (experimental data shown as red squares, and the resulting linear cross-section model with $\sigma_h = 4\times10^{-17}$ as red line), the simulated absorption does not yield a satisfactory agreement with an underestimation by > 1500 cm^{-1}.

The resulting IVB absorption spectra for relaxed Ge are shown on a logarithmic scale in Fig. 2.6(a). At $N_h = 1\times10^{19}$ cm^{-3}, two resonances can be distinguished which are related to VB1→VB2 and VB1→VB3 transitions. Despite the larger dipole matrix element, the VB2→VB3 transition is much weaker due to the smaller density of states and is, therefore, not observable as long as the two top valence bands are degenerate. For an increase in carrier density, the VB1→VB3 transition leads to a rise in absorption which spans an increasingly wider spectral range due to the filling of VB1 and the hole density-dependent broadening parameter. The absorption due to transitions between the two top valence bands VB1→VB2, instead, decreases in intensity. This is attributed to a stronger filling of VB2, such that the density of free states which can take part in a transition is decreased.

In order to compare the modelling to experimental data, the absorption at 0.78 eV is shown in function of the hole density in Fig. 2.6(b), which allows a direct comparison with the experimental data from ref. [62]. The data from [62] are, therefore, also shown in the figure. The IVB absorption was experimentally obtained by pump-probe transmission measurements and yielded a linear dependence on the hole density as $\alpha_{IVB}(0.78\,\text{eV}) = \sigma_h N_h$ with the hole cross-section $\sigma_h = 4\times10^{-17}$ cm^2 for the range from $N_h = 1\times10^{18}$ cm^{-3} to 1×10^{20} cm^{-3}.

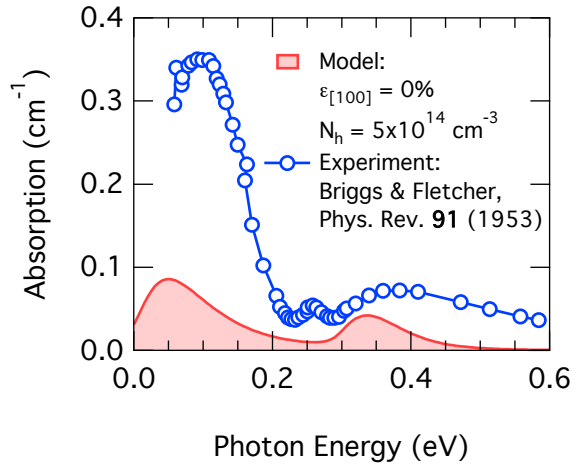

Figure 2.7: Calculated IVB spectrum at $N_h = 5 \times 10^{14}$ cm^{-3} (red, filled area) in comparison to experimental data from [100] (blue circles).

However, the results from the simulation show a linear increase only at densities above 6×10^{19} cm^{-3}. The cross-section obtained from a fit to the data at large N_h leads to $\sigma_h = 3.1 \times 10^{-17}$ cm^2, which is in good agreement with the experimental value from [62]. Consequently, the underestimated increase in absorption at lower hole densities causes a discrepancy of 1500 cm^{-1} in absorption coefficient which proves the model in this state to be insufficient to accurately describe the loss due to IVB.

In addition, the calculated IVB absorption spectrum at a hole density of $N_h = 5{\times}10^{14}$ cm^{-3} is shown in Fig. 2.7 in comparison to the experimental data from Briggs and Fletcher [100]. From the experiments, the VB1→VB2 absorption is found to be the dominating transition. Furthermore, the data shows two more distinct maxima associated to VB2→VB3 transitions at $\sim$ 0.26 eV and VB1→VB3 transitions with the peak at $\sim$ 0.37 eV, which is in agreement with other experimental work on p-doped Ge [104, 109, 110]. In contrast, the model underestimates the absorption between heavy hole- and light hole bands by approximately a factor of 3.5. While Drude-type intraband absorption becomes important towards low energy due to its scaling with λ^2 [95], the corresponding absorption of the order of $\sim 5{\times}10^{-3}$ cm^{-1} estimated with the electron cross-section $\sigma_e = 4{\times}10^{-18}$ cm^2 and the energy dispersion from [62] is too low to make up for the difference [110]. Moreover, the spectral features for the transitions into VB3 are not well reproduced qualitatively or quantitatively, either.

Comparisons of the IVB absorption model with experimental results under low (see Fig. 2.7) or high excitation $> 10^{19}$ cm^{-3} (see Fig. 2.6(b)) revealed strong deviations between the calculations and the experiments. The IVB transition strengths P_{ij} do not seem to be reliably reproduced from the 8-band k·p simulations. This discrepancy might be due to the fact that for the 8-band k·p, only the coupling of the lowest conduction band with the

valence bands is explicitly included [111]. A better description of the orbital mixing could possibly be achieved when the coupling of additional, higher-order conduction bands are explicitly taken into account as e.g. in a 14-band [112] or a 30-band [81, 113] k·p approach. Furthermore, the influence of the hole density plays an important role determining the peak absorption and spectral width due to the hole density-dependent lifetime broadening [108], which might even differ for carriers introduced either by p-doping or by optical or electrical injection.

As a matter of fact, previous attempts to describe intervalence band absorption in III-V alloys, Ge or GeSn [108–110, 114, 115] based on k·p theory or first-principle quantum theory did only deliver a precise description of experimental data after the introduction of fitting parameters. Typically, three free parameters allow for the independent determination of relative absorption strength, lifetime broadening and k-dependent variation of the dipole matrix element. For Ge under tensile strain, there are no reports on experimental investigation of IVB absorption yet. Therefore, there is a strong incentive to deliver experimental data on the intervalence band absorption in strained Ge to allow the improvement of existing modelling of IVB transitions.

2.3.3 Description of Loss Function

Due to the lack of accuracy for the above introduced model for IVB transitions, the loss will be described in the following by the experimentally determined electron- and hole absorption cross sections $\sigma_e = 4{\times}10^{-18}$ cm^2 and $\sigma_h = 4{\times}10^{-17}$ cm^2 from [62]. Taking into account the spectral dependence, the loss-related absorption follows as:

$$\alpha_{loss}(\hbar\omega) = \left(N_e^{tot}\,\sigma_e + N_h^{tot}\,\sigma_h\right) \times \left(1 + 1.56\,(0.775 - \hbar\omega/\mathrm{eV})\right), \tag{2.31}$$

with N_e^{tot} and N_h^{tot} denoting the total electron- and hole carrier density, respectively. In this loss-function, the absorption due to IVB transitions and Drude-like free carrier absorption of electrons and holes are included.

It should be stressed that the experimental data which the loss function is based on was obtained for Ge layers with only a small biaxial tensile strain. Therefore, the change in absorption due to strain for free carrier absorption and, in particular, intervalence band absorption is not accounted for. Hence, there might exist situations where the net gain is drastically reduced due to IB and IVB transitions falling into resonance.

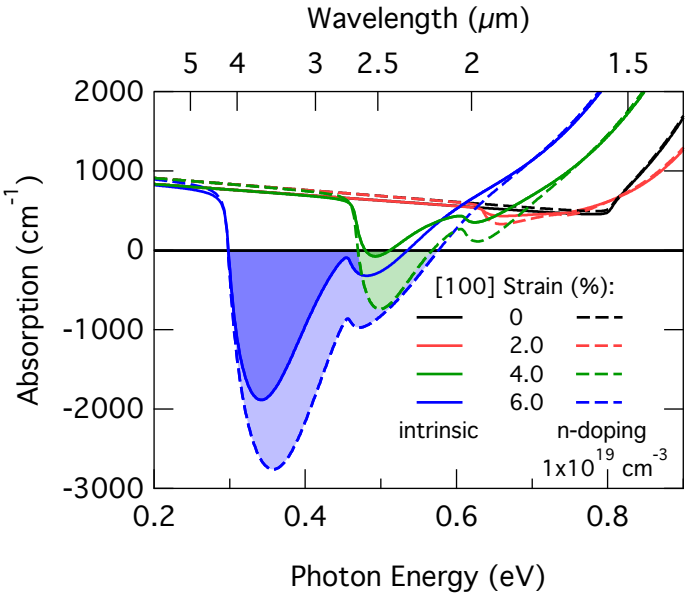

Figure 2.8: Absorption including interband transitions and free carrier loss for [100] strain between 0% and 6.0% at an injected carrier density of 1×10^{19} cm^{-3}. Solid lines depict intrinsic Ge, whereas the broken lines show the absorption at an n-type doping of 1×10^{19} cm^{-3}.

2.3.4 Gain in Uniaxially Stressed Germanium

After having investigated the advantageous effects of tensile strain on the electron population in the Γ valley (see chapter 2.2), the total absorption coefficient $\alpha_{tot} = \alpha_{IB} + \alpha_{loss}$ related to interband absorption and parasitic free carrier absorption is investigated in the following. In Fig. 2.8, the absorption is plotted for [100] strain ranging from 0% up to 6% at an injected carrier density of 1×10^{19} cm^{-3}. The calculations are performed for intrinsic Ge (solid lines) as well as for an n-type doping of 1×10^{19} cm^{-3}.

Looking at the absorption for intrinsic, relaxed Ge (black, solid curve), it can be seen that even below the absorption edge at ∼ 0.8 eV, there is a significant absorption due to Drude-type and IVB transitions which increases linearly for lower energies. Above the band gap, IB absorption leads to a steep increase in absorption. No significant reduction in absorption due to material gain can be observed around the band gap, indicating the insufficient electron population of Γ states for relaxed Ge.

For a tensile strain of 2% (red, solid line), the occurrence of material gain is clearly visible in form of a decrease in absorption around the red-shifted band gap region. However, the gain is not sufficient yet to overcome the losses such that in total, a positive absorption remains over the full band width. This changes, however, at a strain of 4% (green, solid line), where the absorption is reduced over a spectral width of ∼ 200 meV due to interband transitions including both two top valence bands. Moreover, the gain associated with the

highest VB exceeds the optical losses such that at the minimum absorption at 0.49 eV, the absorption amounts to -75 cm^{-1}, i.e. net gain or optical amplification.

The effect is further increased for a larger strain, as can be seen for the absorption at 6% strain (blue, solid line) where the net gain increases up to nearly 1900 cm^{-1} due to the once more increased population of electrons at the Γ valley. Furthermore, there is now also a net gain from transitions of electrons into the second valence band, as well, which increases the band width of optical amplification up to $\sim$ 230 meV.

In contrast to optical injection of carriers, adding additional electrons by n-type doping increases the total density of electrons without increasing the number of holes, which constitutes the largest factor of absorption losses. Obviously, an increase in n-type doping improves the gain characteristics because all negative effects are neglected. In particular, n-doping leads to an increase in lifetime broadening [116], which will reduce the obtained peak gain values depending on the amount of doping density. Furthermore, the non-radiative carrier lifetime decreases (see e.g. chapter 4 or [66]) such that high steady-state carrier densities require a stronger excitation and, therefore, reduce the efficiency. Hence, the simulation results shown for n-doped Ge only represent an upper bound of gain which might be achieved in an ideal case, which will not prevail in reality.

The dashed curves in Fig. 2.8 show the absorption under consideration of a doping density of 1×10^{19} cm^{-3}, which can technologically be reached via several epitaxy techniques without a doping-induced deterioration of the luminescence intensity [117–121]. For strain values up to 2.0%, no crucial improvement due to the doping can be observed as the absorption stays $>$ 500 cm^{-1}. At higher strain, doping leads to more essential quantitative changes with an increase in net gain from 75 cm^{-1} to 730 cm^{-1} for 4.0% strain (green lines) and from 1900 cm^{-1} to 2750 cm^{-1} for 6.0% strain (blue lines). Therefore, n-doping is a useful tool to further increase the optical gain in strained Ge especially at high strain values as long as the material quality can remain comparable to intrinsic material.

A more detailed view on the dependence of the minimum absorption, i.e. negative net gain, in dependence on strain and injected carrier density is offered in Fig. 2.9, where the minimum absorption is shown for the cases of (a) intrinsic Ge, (b) $N_{dop} = 5\times10^{18}$ cm^{-3} and (c) $N_{dop} = 1\times10^{19}$ cm^{-3}.

For intrinsic Ge (c.f. Fig. 2.9(a)), transparency (i.e. the internal losses being equalized by interband optical gain, $\alpha_{tot} = \alpha_{IB} + \alpha_{loss} = 0$) can be achieved for strain values below the crossover to a direct band gap. At a minimum of 3.8% strain, transparency is reached at an injection of $N_{inj} = 3.8 \times 10^{19}$ cm^{-3}. Under an assumption of cavity losses of $\sim$ 200 cm^{-1} as for a distributed feedback (DFB) cavity with 14 grating periods (see chapter 3.2.3 and [122]), the lasing onset could be achieved at 4.0% strain and $N_{inj} = 3.3 \times 10^{19}$ cm^{-3}. High injection

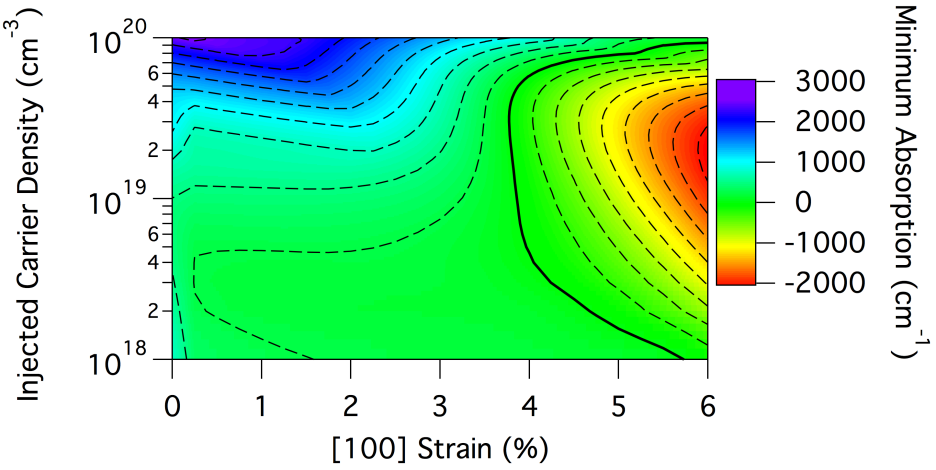

(a) Intrinsic Ge.

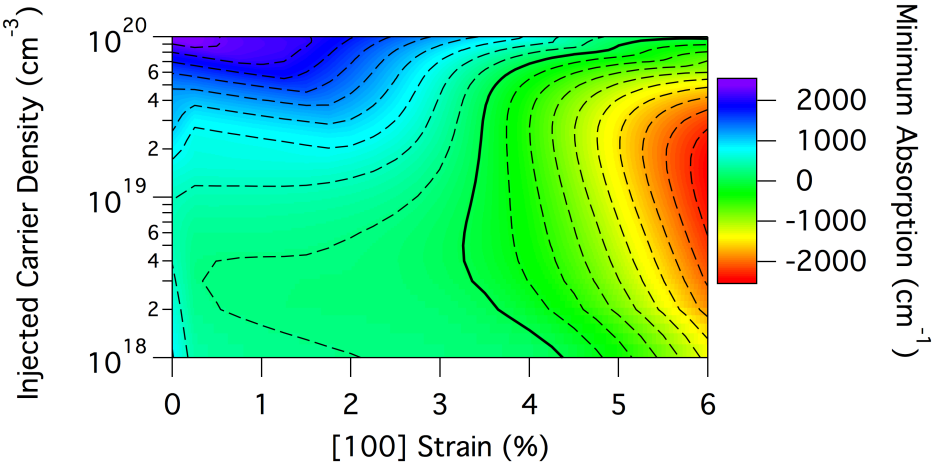

(b) $N_{dop} = 5{\times}10^{18}$ cm^{-3}.

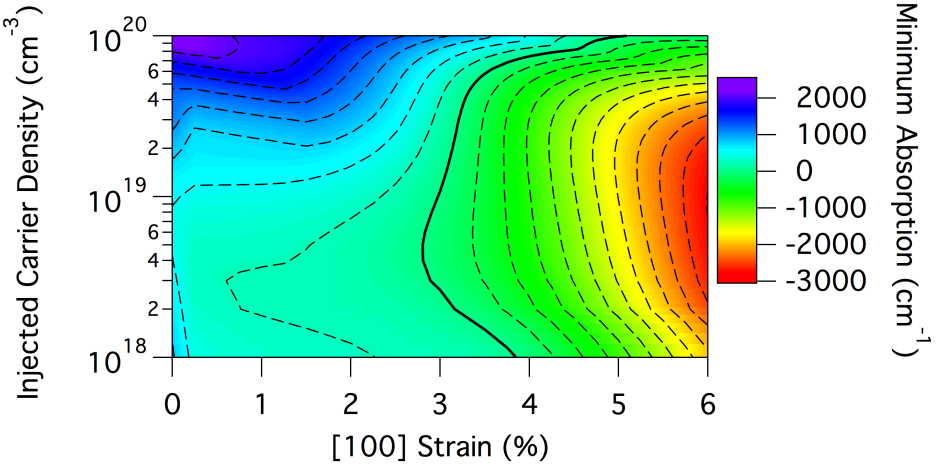

(c) $N_{dop} = 1{\times}10^{19}$ cm^{-3}.

Figure 2.9: Contour plots of the minimum total absorption in function of injected carrier density and [100] strain. The n-doping density amounts to (a) no doping, (b) $5{\times}10^{18}$ cm^{-3}, and (c) $1{\times}10^{19}$ cm^{-3}, respectively. The dashed contour lines show the change in absorption in increments of 250 cm^{-1}, while the solid line corresponds to the transparency condition where $\alpha_{tot} = 0$.

densities $> 1 \times 10^{19}$ cm^{-3} are required to reach lasing in intrinsic Ge if the strain is not surpassing 4.7%, while for direct band gap Ge with $\varepsilon > 5\%$, transparency can be reached for carrier densities in the low 10^{18} cm^{-3}.

The improvements in gain by n-doping are discussed for the case of a doping density of $N_{dop} = 1{\times}10^{19}$ cm^{-3} (see Fig. 2.9(c)) as the effects are more pronounced compared to $N_{dop} = 5{\times}10^{18}$ cm^{-3}: In contrast to intrinsic Ge, transparency is reached at 2.8% strain for $N_{inj} = 4 \times 10^{18}$ cm^{-3}. The reduction of the required steady-state carrier density is an important figure-of-merit to achieve reasonable current densities for electrically pumped lasers. As an example, to inject a steady-state carrier density of $N_{inj} = 4 \times 10^{18}$ cm^{-3} for a 1 µm thick Ge layer with a non-radiative carrier lifetime of 5 ns (see chapter 4), a current density of ~ 10 kA/cm^2 is required. As a comparison, state-of-the-art quantum dot-based III-V lasers on Si [44, 123] operate at sub-kA/cm^2 threshold current densities. Therefore, to realize an efficient Ge laser with threshold current densities that can compete with III-V alternatives, the strain for intrinsic Ge should exceed 5% to operate at carrier densities in the low 10^{18} cm^{-3} or smaller. Nevertheless, n-type doping is an attractive approach to relax the requirements for strain, such that a net gain of > 250 cm^{-1} can be achieved with a doping density of $N_{dop} = 1 \times 10^{19}$ cm^{-3} and a steady-state carrier density of $< N_{inj} = 4 \times 10^{18}$ cm^{-3}.

The spectral variation of the absorption in function of strain is shown at an injection density of $N_{inj} = 5 \times 10^{18}$ cm^{-3} for intrinsic Ge (Fig. 2.10(a)) and for n-doped Ge with $N_{dop} = 1 \times 10^{19}$ cm^{-3} (Fig. 2.10(b)). For intrinsic Ge, transparency is reached starting from $\sim 4.0\%$, while at 5.0% strain the net gain width spans ~ 100 meV from 380 meV to 480 meV. The gain stems exclusively from direct interband transitions into the top valence band.

Transparency is already reached at 3.0% strain for the n-doped Ge. At a strain of 1.0% above the transparency threshold, the net gain spectral width reaches 100 meV comparable to the intrinsic case. However, from 4.7% strain and onwards, the high-energy shoulder indicates that negative absorption is also achieved for interband transitions where VB2 is involved, which leads to an additional increase in spectral gain width.

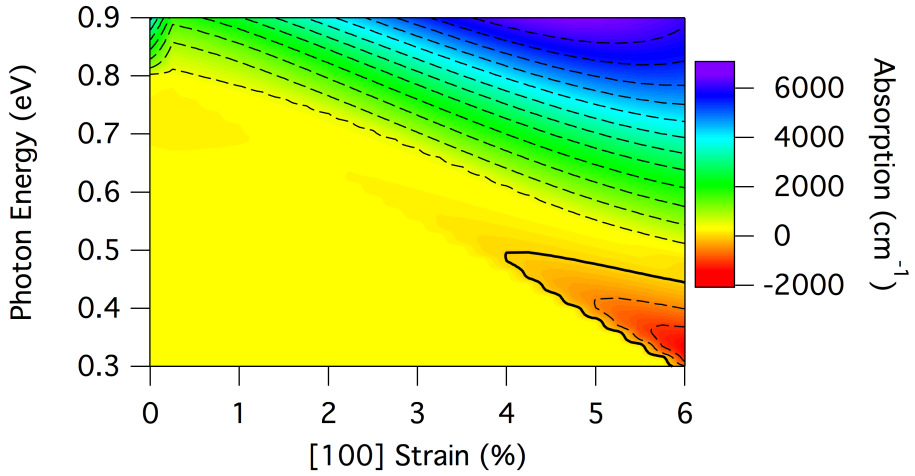

(a) Intrinsic Ge.

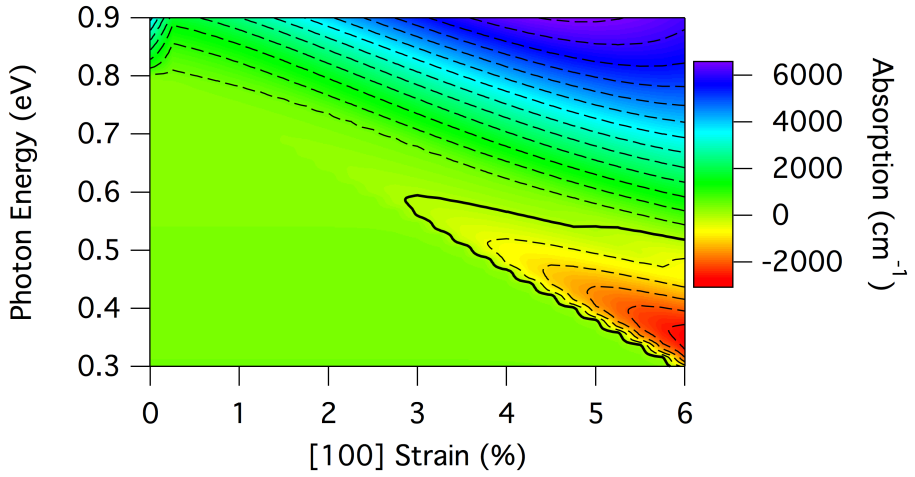

(b) $N_{dop} = 1{\times}10^{19}$ cm^{-3}.

Figure 2.10: Contour plots of the total absorption in function of [100] strain and photon energy for an injected carrier density of $5{\times}10^{18}$ cm^{-3}. The simulations are conducted for (a) intrinsic Ge and (b) Ge with n-doping density of $1{\times}10^{19}$ cm^{-3}, respectively. The dashed contour lines illustrate the change in absorption in increments of 500 cm^{-1}, while the solid line corresponds to the transparency condition where $\alpha_{tot} = 0$.

2.4 Summary

The optical properties of Ge were modelled in function of tensile strain. The commonly used deformation potentials yield that for a uniaxial tensile stress, 4.7% strain along the [100] direction is required to achieve a degeneration of the Γ valley with the L valleys such that at an even higher strain, Ge turns into a group IV semiconductor with a fundamental direct band gap. We showed that the reduction of the offset between the Γ- and L states leads to a steady increase in electron population at Γ, from where an efficient radiative recombination can take place. For decreasing temperatures, the Γ valley population decreases for $\varepsilon_{[100]} < 4.7\%$ or increases for $\varepsilon_{[100]} > 4.7\%$, which makes temperature-dependent measurements an adequate tool to distinguish between fundamentally direct and indirect band gap Ge.

Furthermore, the optical absorption in Ge has been calculated in dependence of strain, n-type doping and the optically induced steady-state carrier density. The absorption was derived from Fermi's golden rule and was fed with strain-dependent band edges and effective masses obtained via 8-band k·p theory. It was shown that optical amplification is obtained in intrinsic Ge at carrier densities in the low 10^{18} cm^{-3} when the strain exceeds the crossover strain of $\varepsilon_{[100]} = 4.7\%$. However, by adding n-doping of 1×10^{19} cm^{-3}, this condition can be relaxed to $< 3.0\%$.

The description of interband absorption has, moreover, been adopted for the case of intervalence band transitions. IVB transitions represent the main internal loss channel to be overcome to achieve optical amplification. The k-dependent momentum dipole matrix elements were extracted from the same k·p theory. The model failed to accurately describe the IVB absorption. Generally, the hole absorption cross-section was found to be smaller than experimentally determined. This is in accordance with literature where additional free parameters were introduced into the k·p theory because of this shortcoming. Instead of such a post-analysis, absorption data from experiments was used which was, however, determined for the case of only slightly strained Ge. Because of the lack of experimental data, the state lifetime broadening and the decrease in carrier lifetime due to n-doping was not included in the model, as generally done in recent literature.

2.5 Compendium

The aforementioned results provide the theoretical background that guides the path towards efficient room temperature lasing based on strained Ge. The use of an n-type doping of 1×10^{19} cm^{-3} greatly relaxes the required strain to achieve optical amplification. However, a significant decrease of the carrier lifetime for n-doped Ge, as will be shown later in

chapters 4.4 and 4.5, may cancel out the mentioned effect.

As the k·p simulations did not provide reasonable results for the absorption loss from intervalence band absorption, experimental values as interpolated from only slightly strained Ge had to be used. The loss contribution might, hence, be underestimated. It should be noted that the calculations are done under the assumption of quasi-equilibrium, i.e. the population of electrons in the Γ and L conduction band valleys is described by one common quasi Fermi level. This is a commonly used assumption, which will nevertheless be questioned when the photoluminescence emission intensity for strained Ge is discussed (see chapter 3.6), as well as for the extracted gain from time-resolved pump-probe measurements of optically-pumped direct band gap GeSn (see chapter 5.5.2).

3

Uniaxially Stressed Direct Band Gap Germanium

Contents

In this chapter, the method to locally induce a high uniaxial stress by redistribution of a small, biaxial strain is described. After a short introduction of the concept, the fabrication technology is presented in detail. The strain-induced

changes of the electronic bands in Ge are investigated by means of photoluminescence spectroscopy. The performances of two different substrates under high strain - germanium on silicon-on-insulator *vs.* germanium-on-insulator - are compared. With the superior germanium-on-insulator platform, the transition of germanium towards a direct band gap semiconductor is evidenced by temperature-dependent photoluminescence measurements.

Parts of this chapter were published in a similar form as:

M. J. Süess and R. Geiger *et al.*, Analysis of enhanced light emission from highly strained germanium microbridges. *Nature Photonics* **7**, 466-472 (2013).

3.1 Concept of Strain Enhancement

Generally, methods to introduce strain rely either on the deposition on a substrate with a different lattice constant [124–128] or on strain-transfer by external stressor layers, where silicon nitride (SiN) takes on a prominent role due do its compatibility with CMOS processing [70–72, 129–136]. However, epitaxial strain is only applicable for small layer thicknesses before plastic relaxation sets in, which prevents to achieve a high strain for layers thick enough to be interesting for optical applications [137], while the approach with external stressor layers faces challenges with strain-homogeneity and, possibly, limitations towards reaching high strain [132].

In contrast to above mentioned methods, strain can be induced with high homogeneity even for thick layers when applying a simple redistribution of strain by geometrical patterning. The basic principle of this approach is depicted in Fig. 3.1: The top plane of a face-centered cubic lattice is shown in Fig. 3.1(a). The layer is under a homogeneous biaxial tensile strain $\varepsilon_L > 0$ with the lattice constant $a_{L,\parallel} = (1+\varepsilon_L)\, a_0$ along the in-plane directions, where a_0 is the unperturbed lattice constant. When the layer is released from its underlying substrate, the lattice releases the tensile stress and reduces its lattice constant to a_0. The way to use this restoring force for stress-redistribution is schematically shown in Fig. 3.1(b): Here, the lattice is patterned into a 'microbridge'-geometry with a central, narrow 'constriction', which is symmetrically surrounded by larger 'pads' with increased cross-sections. As explained above, the pads relax upon release from the substrate creating a uniaxial force as indicated by the arrows pointing outwards. This force leads to a strong uniaxial tensile stress in the constriction with lattice constants $a_{C,\parallel} = (1+\varepsilon_C)\, a_0$ parallel to the applied stress and $a_{C,\perp} = (1-\nu\varepsilon_C)\, a_0$ perpendicular to the stress, with the Poisson ratio ν determining the

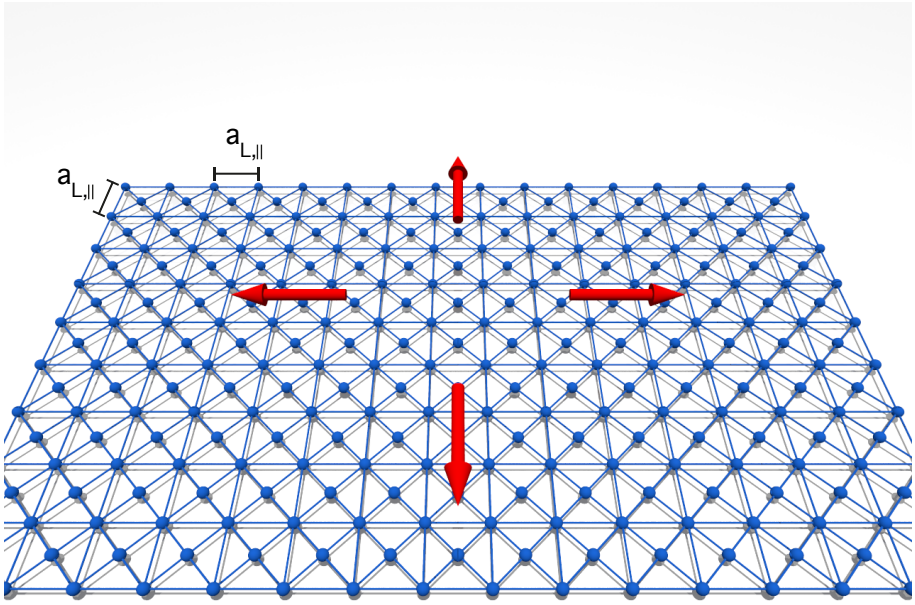

(a) Biaxially stressed face-centered cubic lattice.

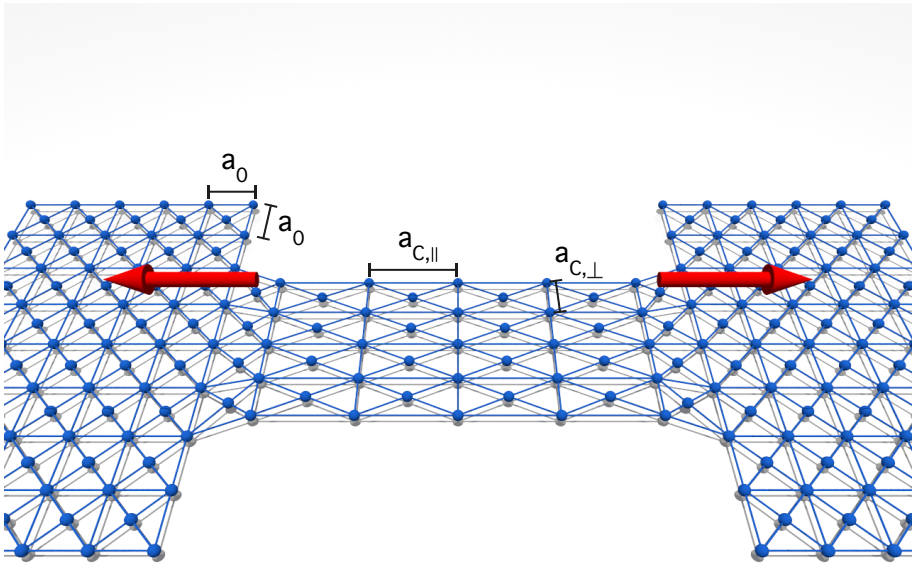

(b) Uniaxially stressed face-centered cubic lattice after patterning of biaxially stressed layer into microbridge-geometry and subsequent release from the underlying substrate.

Figure 3.1: Schematics of strain redistribution by patterning of a biaxially strained layer. After processing the layer into a structure with a narrow, central cross-section and larger, outer cross-sections, the biaxial stress redistributes after the layer is released from the underlying substrate into a high uniaxial stress indicated by the red arrows pointing along the uniaxial force direction.

reduction in width and thickness of the constriction.

According to Hooke's law, the strain in the constriction ε_C is inversely proportional to the width-ratio of constriction and pad, while the acting force is largely determined by the length of the pads, such that the strain in the constriction can readily be tuned by solely changing the geometrical dimensions [73, 138]. Therefore, any strain can be achieved by appropriately tuning the structure with the limiting parameter being the yield strength of the material. This approach is independent of the overall structure's length scale, which makes the technique suitable for strain enhancement on the nanoscale e.g. for nanoelectronic applications like strained Si nanowires [139] as well as for optoelectronic applications on micron sizes as covered in this thesis for the case of strained Ge as optical gain material.

In Fig. 3.2, the strain redistribution is shown in a more detailed and quantitative way obtained from finite element modelling with COMSOL multyphysics. In the left panel, the strain component along <100> is plotted for the case of a suspended germanium-on-insulator (GeOI) structure with a prestrain of $\varepsilon_{xx} = \varepsilon_L = 0.16\%$. We can see that the small prestrain is released in the pads, whereas in the constriction a strain of $\varepsilon_{xx} = 3.0\%$ builds up, which

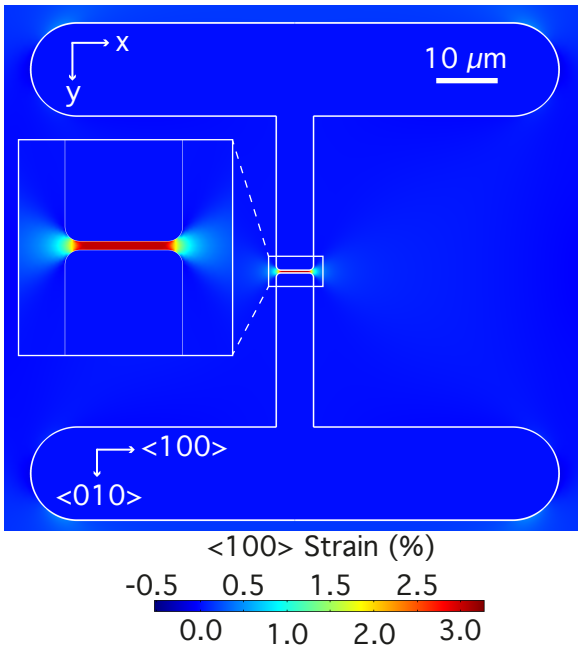

(a) Two-dimensional map of longitudinal strain ε_{xx} in suspended GeOI microbridge.

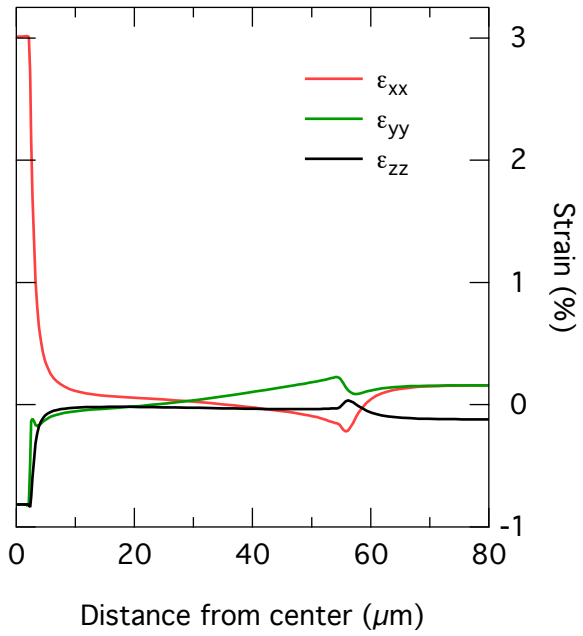

(b) Strain components in principle directions for linescan in x-direction at center of structure.

Figure 3.2: Finite-element COMSOL modelling of longitudinal strain in a suspended GeOI microbridge. After selective release of the structure from the substrure, the prestrain relaxes in the pads which leads to a high strain $\varepsilon_{xx} = 3.0\%$ in the central constriction.

corresponds to an enhancement factor $EF = \varepsilon_{xx}/\varepsilon_L = 18.8$. The strain in the constriction shows a high homogeneity along the bridge-direction. For more details on how design parameters like the fillet radius or the underetched length influence the strain distribution, the reader may refer to the PhD thesis of Martin J. Süess, ETH Zürich [138].

A linescan along x-direction at y = 0 is shown in Fig. 3.2(b) with the strain components along x, y, and z plotted in red, green and black, respectively. For a distance > 70 µm from the center, where the Ge layer is rigidly connected to the underlying substrate, the biaxial strain $\varepsilon_{xx} = \varepsilon_{yy} = \varepsilon_L$ is conserved. In contrast, uniaxial stress along [100] is apparent in the constriction as can be seen from the positive strain along x-direction and the two identical compressive strain contributions for y- and z-directions perpendicular to the applied uniaxial stress. At at a distance of ~ 55 µm from the center, the end of the underetched part leads to strain variations in all main directions right at the transitions between released- and non-released Ge. The strain-relaxed pads bend upwards, causing a variation in strain along the pad length.

The principle of strain redistribution is shown here for the case of transforming a small biaxial stress into a large uniaxial stress. However, the approach is not limited to the uniaxial case, but can also be used in a similar way to realize a large strain-enhanced biaxial strain [138]. The use of biaxial strain has the advantage that a direct band gap is already expected for 1.8% strain compared to 4.7% for strain along [100] (see chapter 2).

The biaxial structure bears, however, some limitations compared to the uniaxial case. The systematic simulation study in [138] shows that the maximum von Mises stress σ_{vM} appears at the corner of the etch windows and is at least 2.4× larger than the biaxial stress σ_{bi} in the center of the structure. The von Mises stress is a scalar stress which takes into account the full stress tensor to allow the comparison of stress states under different loadings. For a material with yield strength σ_y, a biaxially strain-enhanced structure will, therefore, not reach a higher strain than $\sigma_{bi} = \sigma_y/2.4$. Using high-quality germanium-on-insulator (GeOI) material, biaxial stress of 1.6 GPa [140] and 2.7 GPa [141] could be realized, corresponding to biaxial strain of 1.1% and 1.9%, respectively.

A typical resonator geometry, which fits the symmetry of the biaxially strained structure would be a microdisk cavity. As long as the inner strained region is still connected to the outer area via the pads, such a cavity-type is not compatible with the strain-enhancing geometry. Bonding the strained layer to the underlying substrate might be a viable solution such that the outer area can be disconnected and, hence, a circular circumference can be defined as recently attempted by Sukhdeo *et al.* [142]. But as long as an efficient bonding process is not developed, which keeps the induced strain over the whole area, additional steps to restore strain-homogeneity are required [142]. In our opinion, the need of an additional step to

deposit an external stressor layer takes the advantage of strain-redistribution over straining microdisks directly with external silicon nitride stressor layers [70, 130].

In contrast, for uniaxially stressed bridges the pads do not prevent efficient cavity integration, as either the constriction can be patterned directly with distributed feedback gratings [122, 143] or the pads can be patterned to provide feedback from distributed Bragg reflectors [144, 145].

3.2 Fabrication of Strained Ge Microbridges

3.2.1 Starting Material

To apply above described strain-redistribution technique, two prerequisites have to be met:

1. The layer must be under biaxial tensile stress.
2. A process needs to be available to release the structure from its underlying substrate.

For the case of Ge directly grown on Si, a biaxial tensile strain of up to 0.25% can be achieved due to the difference in thermal expansion coefficients. Typically, Ge is deposited in a two-step growth scheme, where a thin, nearly fully relaxed layer grown at low temperature ($\sim$ 400°C) serves as a seed layer followed by high temperature-deposition ($\sim$ 750°C) of Ge [146]. After cooling to room temperature following the high-temperature growth [147] or thermal annealing cycles to reduce the density of threading dislocations [148], the in-plane lattice constant of Ge is increased compared to its relaxed value due to the larger thermal

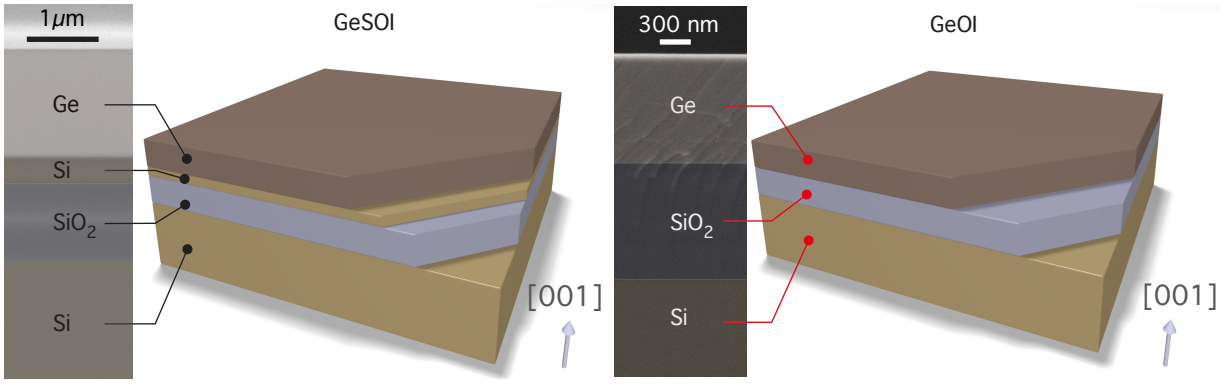

(a) GeSOI layer stack.

(b) GeOI layer stack.

Figure 3.3: Schematics and cross-sectional scanning-electron-microscope images of GeSOI and GeOI substrates.

expansion coefficient with respect to Si, leaving the Ge epilayer with a small biaxial tensile strain.

To selectively underetch the Ge layer, the underlying Si could e.g. be removed by wet chemical etching in potassium hydroxide (KOH) which only etches the Si. Such structures were successfully fabricated, but only with a strain up to $\approx 1\%$ [73]. Better control is offered when using the silicon-on-insulator (SOI) platform, which is the standard for silicon photonics applications due to the favorable waveguiding offered by the large refractive index contrast between silicon and silicon dioxide [149, 150]. On SOI, the buried oxide can readily be removed selectively via hydrofluoric acid (HF).

The strained microbridges presented in this work are processed on two different substrates, which are schematically depicted in Fig. 3.3: Structures referred to as 'GeSOI' are fabricated from Ge layers directly grown on SOI via low-energy plasma-enhanced chemical vapor deposition (LEPECVD) at L-NESS, Como (Italy) [151]. The silicon device layer has a thickness of 340 nm, with a buried oxide of 1.0 µm below. Germanium-on-insulator (GeOI) substrates shown on the right side of Fig. 3.3 are fabricated at CEA-LETI, Grenoble (France) [144]. The process flow for the GeOI material is shown in Fig. 3.4:

After the growth of 2.5 µm Ge on Si via reduced-pressure chemical vapor deposition (RPCVD) and thermal annealing cycles to reduce the density of threading dislocations, the layer is capped with a 2 nm Si passivation layer and 200 nm plasma-enhanced chemical-vapor-deposited SiO_2. Then, H^+ implantation is performed to create a defect layer, which is later on required for wafer splitting. Subsequently, the Ge layer is bonded onto an oxidized Si handle wafer where annealing of the bonded stack leads to splitting at the previously created

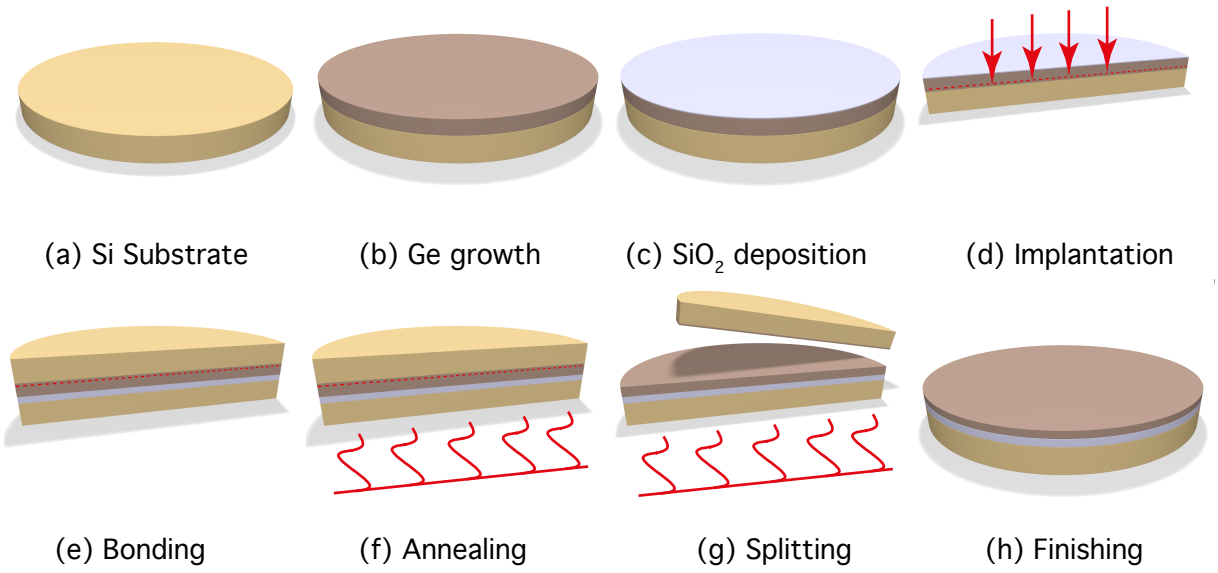

Figure 3.4: Schematics of GeOI process flow.

defect region. Finally, chemical mechanical polishing (CMP) is used to reduce the surface roughness. The final substrate consists of a stack of 1.0 µm high quality Ge on 1.1 µm SiO_2 processed on 200 mm Si.

As the defective Ge/Si interface is on the top of the stack after bonding and splitting, it is readily accessed and removed via CMP, which significantly reduces the dislocation density [152–154]. In chapter 4.4, it will be shown that the highly defective Ge/Si interface is the main limiting factor for the non-radiative lifetime. The superior mechanical quality of GeOI over GeSOI is evidenced by the higher strain values reached by strain-redistribution (see chapter 3.3.4). These examples emphasize the crucial importance of high material quality for the realization of a strained Ge laser. The development of integrated mid-infrared photonics can profit even further from GeOI due to Ge's increased transmission window compared to Si [155].

3.2.2 Process Flow for Microbridge Fabrication

The process flow to fabricate strained Ge bridges from either GeSOI or GeOI base material is schematically shown in Fig. 3.5: Electron-beam lithography is used to define the geometry in polymethylmethacrylat (PMMA) resist. This pattern is transferred into a chrome hard mask of typically 30 nm by dry etching using chlorine gas. Then, the Ge layer is patterned via dry-etching in an inductively-coupled reactive-ion-etching tool from Oxford Instruments using an $SF_6/C_4F_8/O_2$ gas mixture. If a thinner Ge device layer is desired e.g. to allow optical confinement in growth direction only for the fundamental mode, then the layer can be thinned either by dry-etching using the same $SF_6/C_4F_8/O_2$ process or by wet-etching in H_2O_2. For the process flow of a thinned Ge device layer with a typical thickness of 400 nm, the chrome hard mask may be omitted when the bridge structure is defined. Subsequently, to allow the pads to relax, the underlying buried oxide is selectively removed with hydrofluoric acid (HF). The underetching can be performed with liquid HF as well as with HF in the gas phase, where the latter has the advantage that no capillary forces are acting during the process such that breaking due to an additional strain caused by bending of the structures can be prevented.

For the reactive-ion-etching step, the Bosch-process is used to pattern the 1-2 µm thick Ge layers of the GeSOI substrate. Fast, cyclically alternating steps of etching and passivating at 10°C using SF_6 and C_4F_8 lead to well defined, steep sidewalls (see Fig. 3.6(a)). The SF_6/C_4F_8 gas flows during etching and passivation are 100/4 and 4/100 sccm, respectively. The RF and ICP powers are set to 13 W and 600 W. Each etch cycle leads to an etch front with rectangular shape, which results in a certain roughness at the sidewalls of the constriction. Especially at the highly strained parts, a smooth surface is crucial as roughness might lead

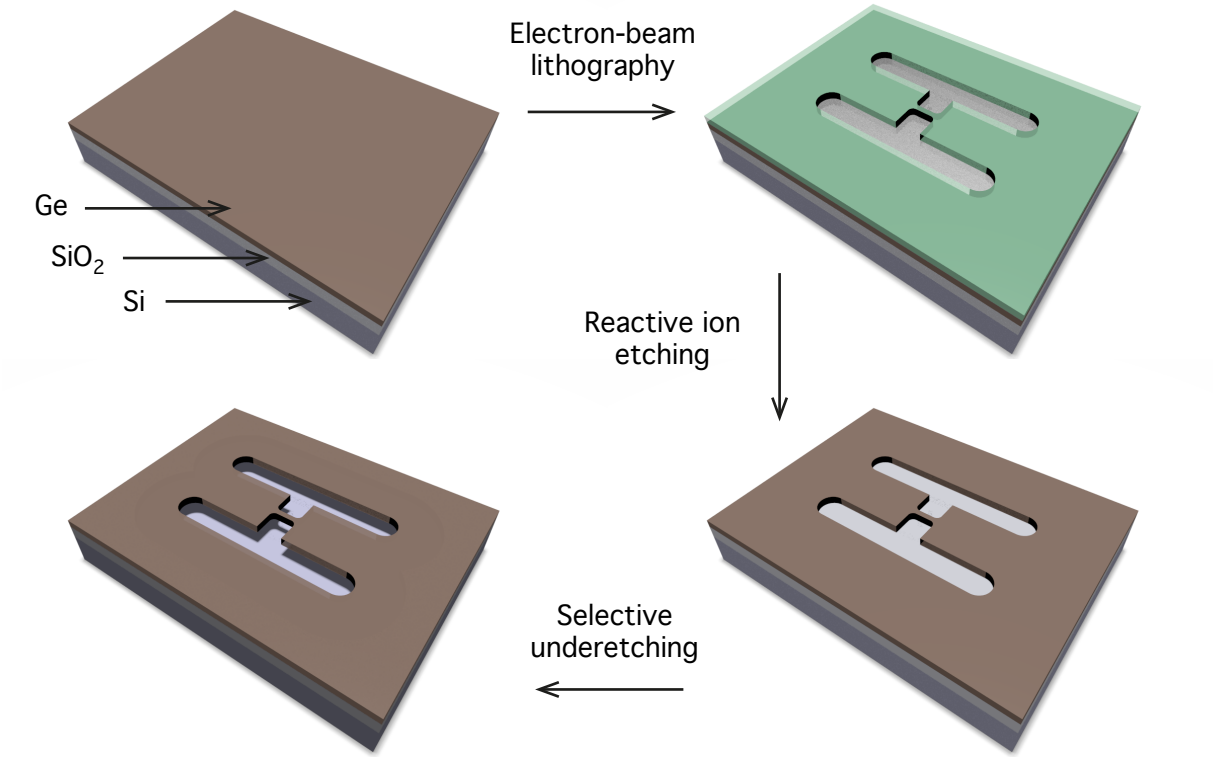

Figure 3.5: Process flow for fabrication of suspended germanium-on-insulator microbridges.

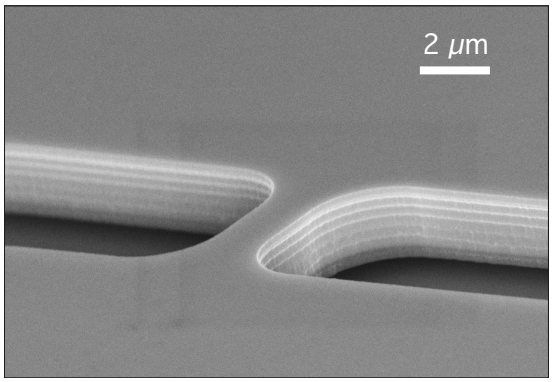

(a) Bosch process with cyclically alternating steps of etching and passivation at SF_6/C_4F_8 gas ratios 100/4 and 4/100.

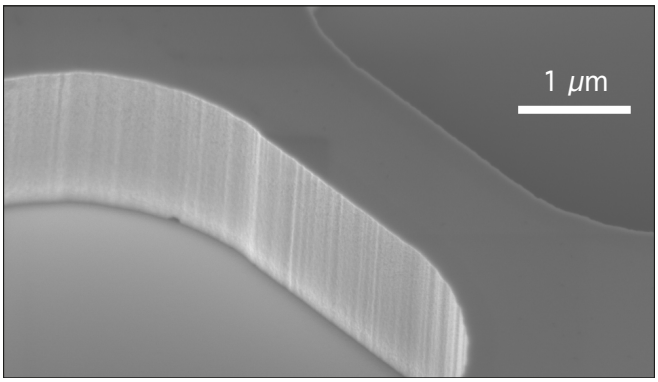

(b) One-step dry-etching with simultaneous flow of $SF_6/C_4F_8/O_2$ at 40/66/5 sccm.

Figure 3.6: Dependence of sidewall roughness on dry etching process parameters. While the Bosch process shown in (a) leads to a triangular shape for each etch cycle, the one-step process in (b) creates vertical sidewalls with a decreased roughness.

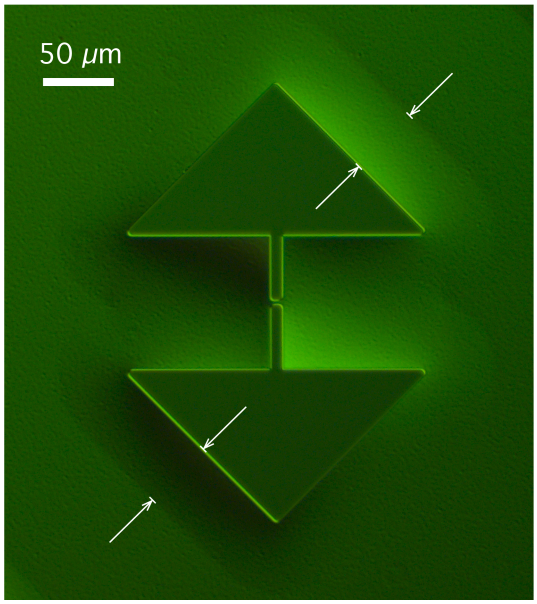

Figure 3.7: Optical micrograph of an underetched GeSOI microbridge. The image is taken in difference interference contrast mode, where the underetched area is visible by the contrast to the non-underetched Ge laser. The borders of the underetched length L are indicated by the white arrows.

to stress-concentration such that the yield-stress is reached causing failure of the structure. Therefore, latest generations of devices are etched at 0°C using a one-step process with simultaneous flow of SF_6, C_4F_8 and O_2, which yields a significantly improved quality of the etched fronts in terms of surface roughness (see Fig. 3.6(b)). The gas flow is set to $SF_6/C_4F_8/O_2 = 40/66/5$ sccm with RF and ICP powers of 30 W and 600 W, respectively.

Using GeSOI or GeOI offers an easy way to selectively remove the underlying buried oxide via HF either in liquid or gaseous aggregate. In Fig. 3.7, a microscope image of a GeSOI structure is shown after underetching in liquid HF. The image is taken in difference interference contrast - mode (DIC) with a 20× objective, such that the underetched region can nicely be made visible in order to clarify that the pads of a structure have been fully released.

3.2.3 Integration of Optical Microcavity

To realize a laser based on highly strained Ge, a cavity has to be integrated into the strain-redistribution approach such that optical feedback is provided. Special attention has to be paid that any additional patterning of the layer does not lead to a relaxation of the strain. In the following, two approaches are presented with particular emphasis towards fabrication issues.

Distributed Feedback Cavity

Ge only provides optical gain under a large tensile strain. An optimum design would, therefore, keep the optical mode within the highly strained region to reach a large modal overlap with the gain material. A possible solution which satisfies this condition is shown in Fig. 3.8 where the sidewalls of the microbridge are patterned into gratings. This distributed feedback (DFB)-type of cavity was designed by Christopher Bonzon at ETH Zürich. The mode profile of the targeted 5^{th} order lateral mode is shown in Fig. 3.8(a) as obtained by finite element modelling (FEM) with COMSOL. The simulation was performed by Esteban Marín at Paul Scherrer Institute for a 1 µm thick Ge layer suspended in air. A quality-factor Q of 17000 is computed for the mode centered at 0.60 eV (= 2050 nm). By scaling the cavity dimensions, the resonance can be shifted towards higher or lower energies.

In Fig. 3.8(b), the longitudinal strain along [100] is computed via FEM simulations for a

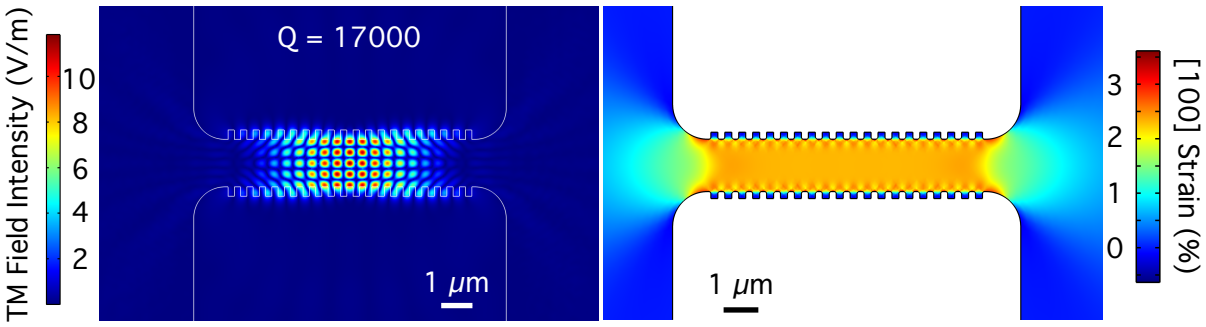

(a) FEM simulation of TM mode profile for DFB cavity with Q-factor of 17000.

(b) FEM simulation of strain along [100] for DFB cavity.

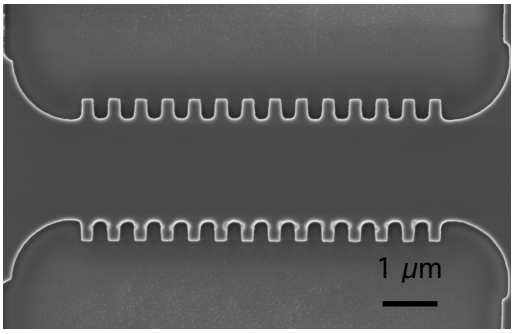

(c) Top-view SEM image of GeOI DFB cavity.

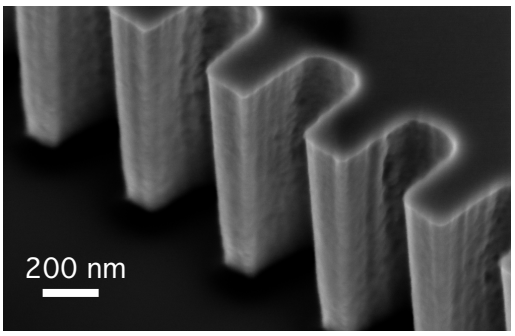

(d) Tilted-view close-up SEM image of DFB cavity grating.

Figure 3.8: Optical and mechanical finite-element simulations of a 5^{th} order distributed feedback (DFB) cavity show that a high Q-factor of 17000 can be achieved while the strain in the constriction is preserved. To process such structures on 1 µm thick GeOI, good control over the dry etching is required to fabricate the small, high aspect ratio structures.

corrugated bridge structure. Most importantly, the strain in the constriction does not relax due to the patterned sidewalls. The grating itself is not under any strain due to the free surfaces. However, an increase in stress is found between the etched parts of the grating due to the variation in width of the constriction. The stress concentrated at the bridge sidewalls is larger than the stress in the center of the constriction and might lead to a higher vulnerability of the DFB cavities to fracture compared to non-corrugated bridges.

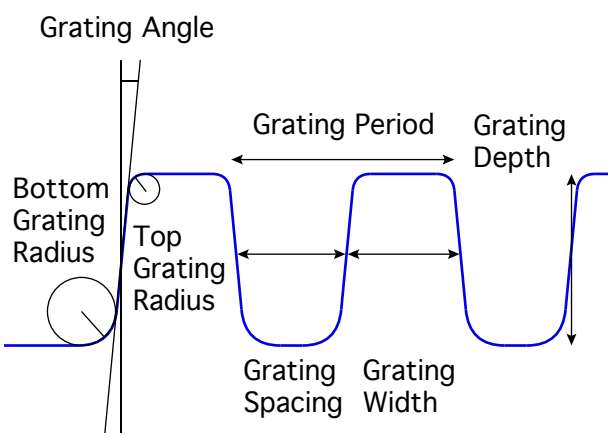

(a) Terminology of sources for Q-factor drop due to deviations from nominal DFB design.

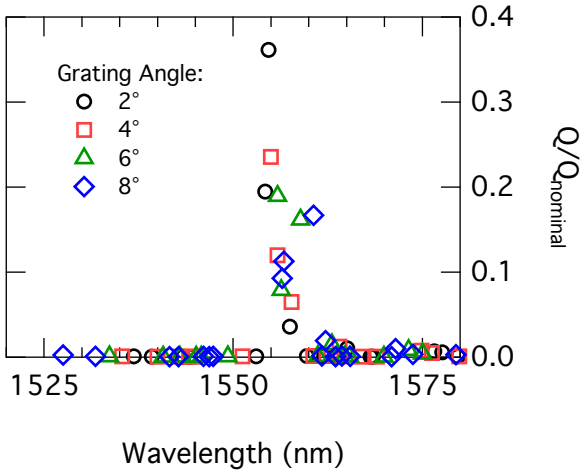

(b) Q-factor in dependence of grating angle.

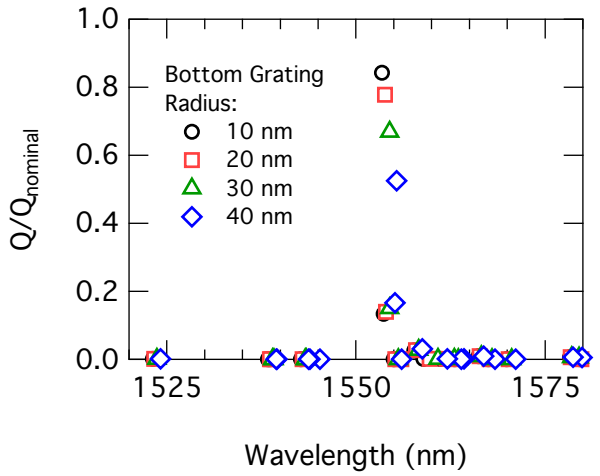

(c) Q-factor in dependence of bottom grating radius.

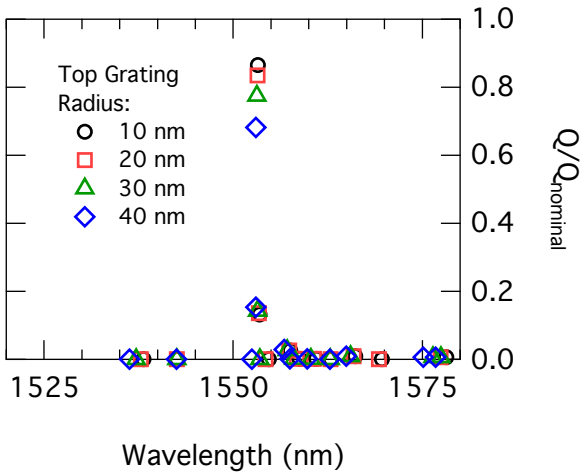

(d) Q-factor in dependence of top grating radius.

Figure 3.9: Imperfections during the fabrication of DFB cavities lead to a substantial decrease of the Q-factor. The drop in Q due to certain variations is calculated in (b) - (d), where the various sources for deviations from the nominal design are given in (a). The study was performed by Esteban Marín [156].

For the fabrication of DFB cavities with smooth surfaces, a well-controlled dry etching process is crucial to etch the high aspect-ratio structures into the 1 µm thick Ge layer. Typically, the grating period is of the order of ∼ 600 - 800 nm. In Figs. 3.8(c) and 3.8(d), scanning electron microscope images are shown in top- and tilted view for a DFB cavity after dry etching and removal of the Cr hard mask. The one-step recipe described above is used for the processing. In the top view image, a slight damage of the Ge layer can be seen at certain parts of the lower grating due to an undercut of the Cr hard mask. An increased roughness is also observed in the tilted view image for surfaces which are close to the sidewall defining the central bridge.

In contrast to the rectangular shape of the grating defined for the mode simulations, the resulting gratings differ from the ideal case to some extent. In Fig. 3.9(a), the possible types of deviations are illustrated. For each of these parameters, a deviation from the ideal, rectangular case leads to a drop in Q-factor. This is exemplarily shown in Figs. 3.9(b)-3.9(d) for the impact of the grating angle, the bottom grating radius and the top grating radius, respectively. The FEM simulations were performed by Esteban Marín at Paul Scherrer Institute for DFB cavities in SOI with a resonance around 1550 nm [156]. The plots show the relative Q-factor Q/Q_{nominal} for varying one of the parameters while keeping all other at the optimum value. Q_{nominal} is calculated for the case of perfectly rectangular gratings. It can be seen that variations in the grating angle of 8°, which are the case for the processed GeOI structure, reduce the Q-factor by nearly an order of magnitude. Furthermore, rounding of the grating leads to a reduction to < 0.6 and < 0.7 for a 40 nm radius at the bottom or top of the grating, respectively.

A better control over the resulting grating shape can be achieved when the Ge is thinned

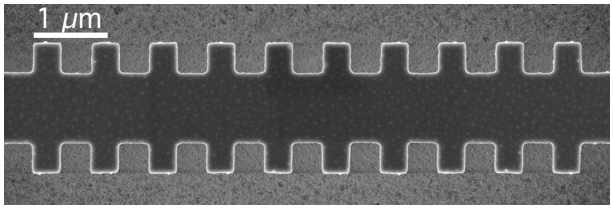

(a) Top-view SEM image of a DFB cavity processed on thinned GeOI.

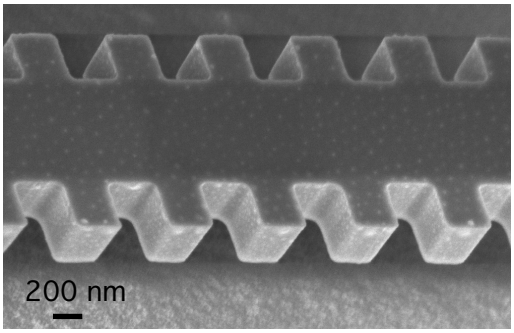

(b) Tilted-view SEM image of a DFB cavity processed on thinned GeOI.

Figure 3.10: Thinning of the GeOI layer facilitates to process DFB cavities with significantly less deviations from the nominal design (a) and improved surface roughness (b). The presented structure was fabricated from Thomas Zabel at Paul Scherrer Institute.

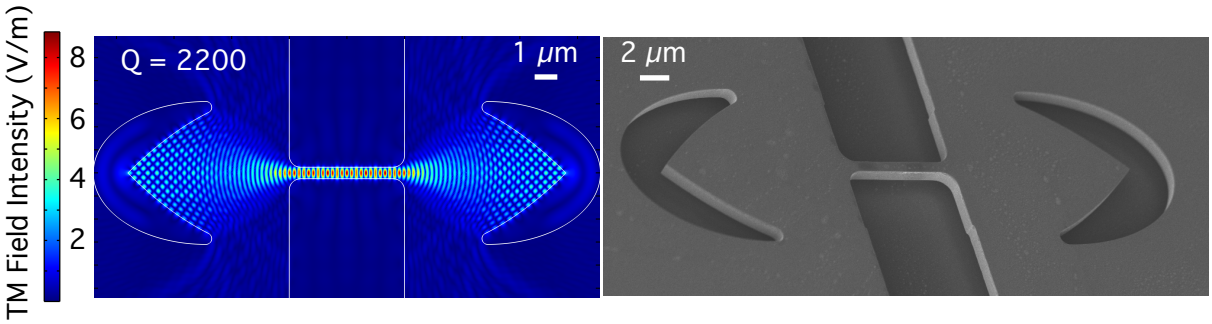

(a) Simulated field strength for cornercube cavity with a TM mode showing a Q-factor of 2200.

(b) Tilted-view scanning electron micrograph of suspended cornercube cavity.

Figure 3.11: Reflectors can be introduced into the pads of a microbridge to provide optical feedback without a relaxation of the strain in the constriction. A simulated TM mode of such a cornercube cavity is shown in (a). A tilted-view SEM image of a fabricated GeOI cornercube cavity is presented in (b).

to $\sim$ 400 nm before the cavity is patterned. The results can be seen in Fig. 3.10, where top- and tilted-view SEM images are shown for a DFB cavity after HF underetching processed on thin GeOI. As a third-order mode was targeted, the width of the constriction is reduced. The fabrication and imaging was performed by Thomas Zabel at Paul Scherrer Institute. Due to the reduction of the aspect ratio and the omission of the Cr hard mask, the definition of the grating is significantly closer to the ideal case. The gratings feature no angle, and the bottom angle could be reduced to $<$ 50 nm. Furthermore, all etched surfaces show the same low roughness and no damages are found at the top surface of the grating. With the process on thinned GeOI, maximum strain levels exceeding 3% could be achieved.

Cornercube Cavity

A different approach to combine the microbridge approach with an optical microcavity is shown in Fig. 3.11 in form of a 'cornercube' design. The design was proposed by Christopher Bonzon at ETH Zürich and optimized by Esteban Marín at Paul Scherrer Institut. In contrast to the DFB cavity, the cornercube design has the advantage that the constriction is not altered, i.e. no additional stress increase occurs compared to structures without cavity. To define the cavity, two parabolic mirrors are etched into both pads. For a sufficient distance between mirrors and constriction, the strain in the bridge is not reduced. As the etch windows defining the reflectors are large, there is no additional technological complexity in fabricating the structures.

The ease in fabricating the multi-mode cavity comes at the prize of reduced optical prop-

erties. The optical field for a TM mode simulated by Esteban Marín is shown in Fig. 3.11(a). The mode features a *Q*-factor of 2200, which is significantly less than for the DFB cavity. Furthermore, for one round trip the mode propagates most of the time in unstrained material where there is no gain. If charge carriers are injected in the unstrained areas, the propagation leads to strong losses.

An SEM image of an underetched cornercube cavity is shown in tilted-view in Fig. 3.11(b). The processing and imaging was done by Thomas Zabel at Paul Scherrer Institute. The cavity is processed on 1 µm thick GeOI substrate. High strain is achieved using the cornercube approach, with a maximum Raman shift of -6.2 cm^{-1} corresponding to a strain of 3.3%. Photoluminescence measurements on cornercube cavities will be shown in chapter 3.5.

3.2.4 Extension of Concept to Enhanced Substrate Material

The strain-redistribution approach relies on the selective underetching of a tensilely pre-strained layer. As shown before, Ge directly grown on SOI or GeOI offer this possibility due to the buried oxide layer. After processing, structures are suspended in air which leads to disadvantageous thermal properties and a susceptibility for heating under e.g. optical excitation [73, 145]. Researchers at Stanford University extended on our work and introduced a novel substrate to reduce the vulnerability to heating effects. Instead of bonding Ge onto an oxidized Si wafer as for GeOI production, Ge is transferred onto Si featuring two dielectric layers, namely a thick layer of SiO_2 and a 25 nm thin layer of Al_2O_3 [145, 157]. To release the Ge layer, the Al_2O_3 is etched selectively in liquid KOH. The deliberate choice of a liquid etchant is taken in order to make use of capillary forces to stick the Ge layer to the underlying

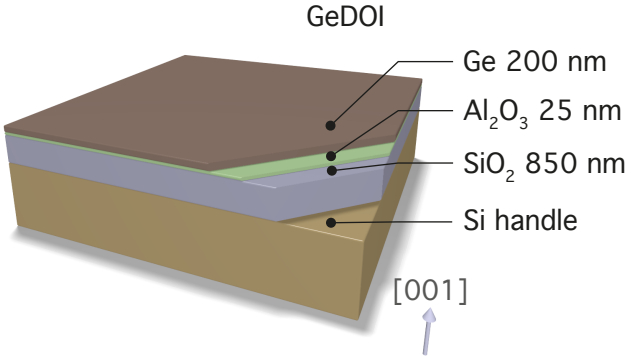

Figure 3.12: Schematic illustration of 'Germanium-on-dual-insulator' substrate. After selectively etching the Al_2O_3 layer using a liquid etchant, capillary forces bring the Ge layer into contact with the underlying SiO_2. Therefore, an improved heat transport can be achieved while remaining a high refractive index contrast.

SiO_2. Therefore, a thermal contact is made to the buried oxide layer which improves the thermal transport compared to a structure which is suspended. At the same time, a large refractive index contrast is maintained to assure mode confinement within the Ge.

Following this approach, the Stanford group successfully stuck strained structures to the underlying structures where the strain remained. For the strain generation, they adopted our strain-enhancement technique to reach 2.3% strain under uniaxial loading in a DBR-type optical cavity [145] and 1.1% strain under biaxial loading [140].

3.3 Room-Temperature PL Spectroscopy on Strained Ge Microbridges

3.3.1 Experimental Setup

To probe the changes in electronic band structure in function of strain, Ge is investigated by means of photoluminescence spectroscopy (PL). For the PL measurements, electron-hole pairs are optically generated by an external laser pulse with an energy typically far above the direct band gap energy. Subsequently, the carriers that recombine radiatively after thermalization into the lowest energetic states are investigated by measuring the spectrum of the emitted photons.

The first of the two setups, which is used for PL spectroscopy in this work is schematically depicted in Fig. 3.13. The sample is excited with a diode-pumped solid-state laser operating in continuous-wave mode at a wavelength of 532 nm, which corresponds to an energy of 2.33 eV. The laser is focused onto the sample surface using a commercial inverted microscope with a 50× objective featuring a numerical aperture (NA) of 0.8. For the excitation, an reduced NA of 0.2 of the objective is used, resulting in an excitation spot size of ~ 1 µm. The emitted signal is collected with the same objective using the full NA and is focused into a 400 µm multimode fiber, which couples the signal into a Bruker Fourier-transform infrared (FTIR) spectrometer. After the FTIR, the signal is detected by a liquid-nitrogen cooled InSb detector with 500 µm diameter from Electro-Optical Systems, Inc. The InSb detector is equipped with a short pass filter for suppression of dark current. Additionally, a long pass filter is needed to prevent the detection of scattered light from the excitation laser. The PL spectra are recorded in step-scan mode using standard lock-in technique to increase the signal-to-noise ratio.

However, the sensitivity of the commercial microscope ranges only down to ~ 0.56 eV $\hat{=}$ 2.2 µm such that highly-strained microbridges cannot be measured in that configuration. Therefore, a second setup is used where only reflective optics is installed, resulting in

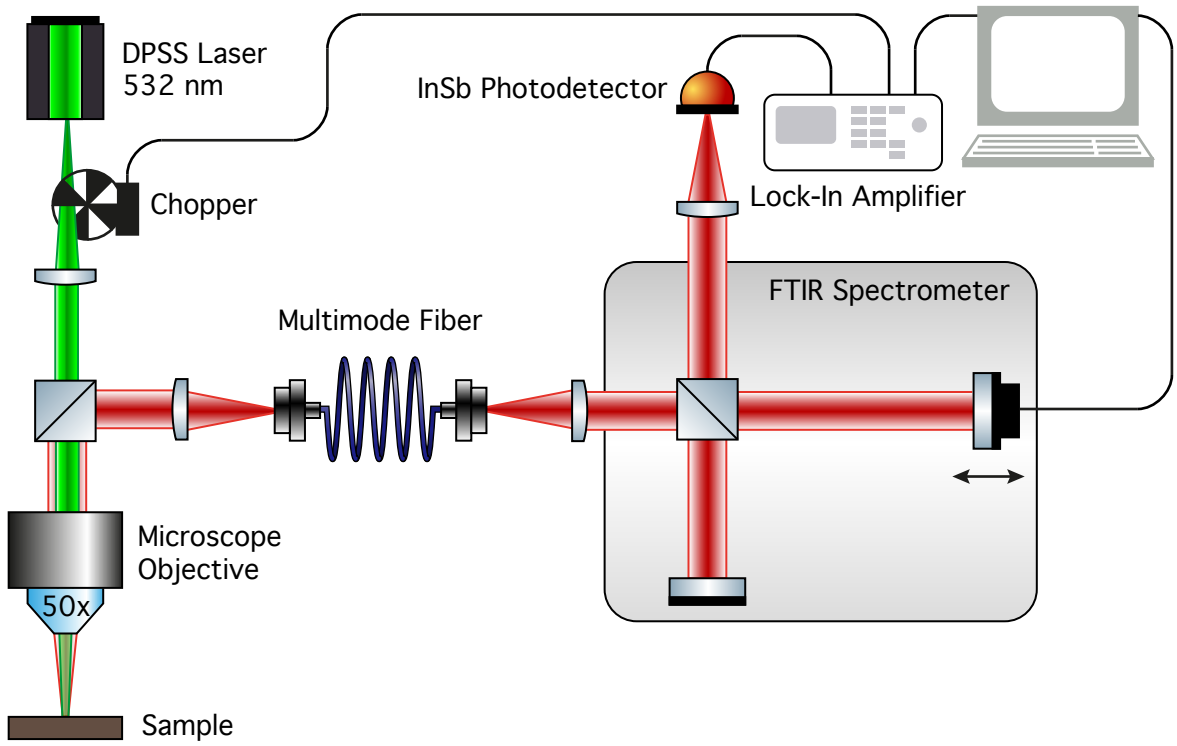

Figure 3.13: Schematic drawing of one experimental setup used for photoluminescence spectroscopy measurements.

broadband sensitivity. In contrast to the setup described above, the all-metal optics setup is equipped with a 15× Schwarzschild objective (NA = 0.4) and the coupling into an FTIR spetrometer is realized via free-space propagation instead of fiber coupling. Furthermore, an InSb detector with 250 µm diameter detection area from Teledyne Judson Technologies is used, which does not feature an internal filter, increasing the sensitivity down to ~ 0.25 eV $\triangleq$ 5.0 µm. Due to the reduced numerical aperture, the excitation spot size increases to typically $\sim$ 7 µm. To increase the signal-to-noise ratio, the angle of acceptance of the detector is reduced to $\sim 10°$ to match the detection solid angle to the irradiated solid angle given by the NA and magnification of the Schwarzschild objective and the used optics, respectively.

3.3.2 Strain-Dependent Emission Characteristics

PL spectra of strained GeSOI bridges recorded at room-temperature with the 50× microscope objective are shown in Fig. 3.14(a). The microbridges are excited locally in the center of the constriction where the maximum strain is obtained, with an excitation power density which is approximated to 850 kW cm^{-2}. All structures have identical dimensions for the constriction with 6 µm in length and 2 µm in width, and a fillet rounding radius of 2 µm.

The constriction is set to fixed length scales for the whole set of samples such that a change in emission intensity due to a change of the strained volume is avoided. To change the tensile strain in the constriction, the pad dimensions have been varied. The resulting strain is measured via Raman spectroscopy, where the power-dependent shift is extrapolated to zero excitation power in order to obtain the heating-corrected Raman shift [158]. A maximum shift of $\Delta\omega = -4.8$ cm^{-1} is obtained for the structure with the largest pads, which translates into a longitudinal strain along [100] of 3.1% when the linear Raman-strain-correlation is used [73], which is an accurate description of the strain-induced Raman shift up to a maximum strain of $\sim 3\%$:

$$\varepsilon_{[100]} = -\Delta\omega/154 \text{ cm}^{-1}. \tag{3.1}$$

It was recently found that for higher strain, the strain cannot be extracted from the Raman shift via the linear relationship [159]. Comparisons of Raman measurements with strain determined via x-ray diffraction measurements yield the following, non-linear relationship:

$$\varepsilon_{[100]} = -0.588\,\text{cm}\ \Delta\omega - 0.0072\,\text{cm}^2\ \Delta\omega^2. \tag{3.2}$$

Two effects are apparent when comparing the emission spectra depicted in Fig. 3.14(a) in dependence of strain:
First, an increase in strain leads to a reduction in the direct band gap which manifests in a decreased emission energy in Fig. 3.14(a). In Fig. 3.14(b), the band gap energies from the spectra in (a) are extracted and plotted as a function of strain together with a theoretical prediction obtained from deformation potential theory (red line, see chapter 2). A fair agreement is obtained between model and experiment.

Second, an increase in strain not only shifts the direct band gap to lower energies, but as a more important feature the L-valleys decrease even faster in energy, such that the separation between Γ- and L-states decreases (see chapter 2). Therefore, the population of electrons in the Γ valley increases which leads to a rise in radiative recombination. In Fig. 3.14(d), the integrated emission intensities from the spectra in (a) are shown in function of strain and normalized to the intensity for the unpatterned GeSOI layer. Up to a strain of 2.6%, the intensity is monotonically increasing with a maximum enhancement in integrated intensity of 20× at 2.6% compared to the unpatterned layer.

The red line shows the calculated integrated emission intensity based on a model which takes into account the strain-dependent band edges and effective masses and the joint-density-of-states (JDOS) of dipole-allowed transitions. For the calculation of the spontaneous emission rate R_{sp}, the conduction- and valence bands are assumed to be isotropic and

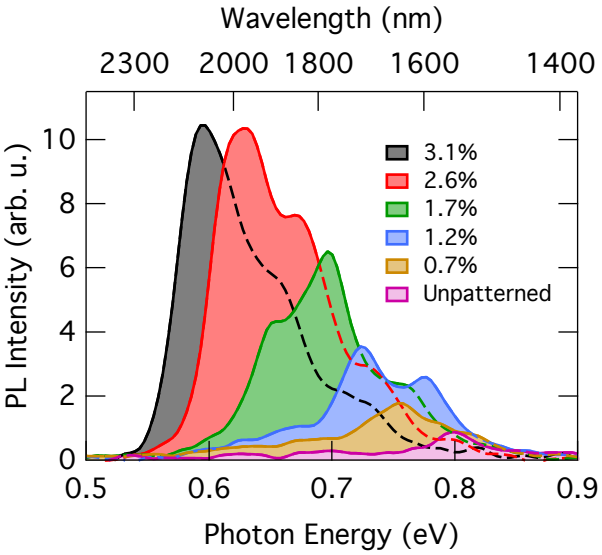

(a) Room-temperature PL spectra from GeSOI bridges with varying strain[1].

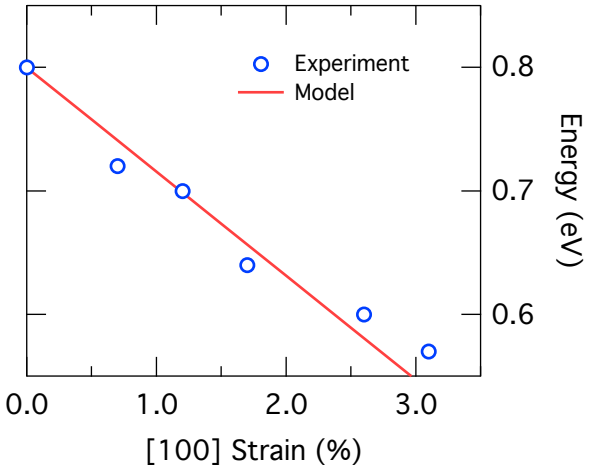

(b) Extracted band gap in dependence of strain.

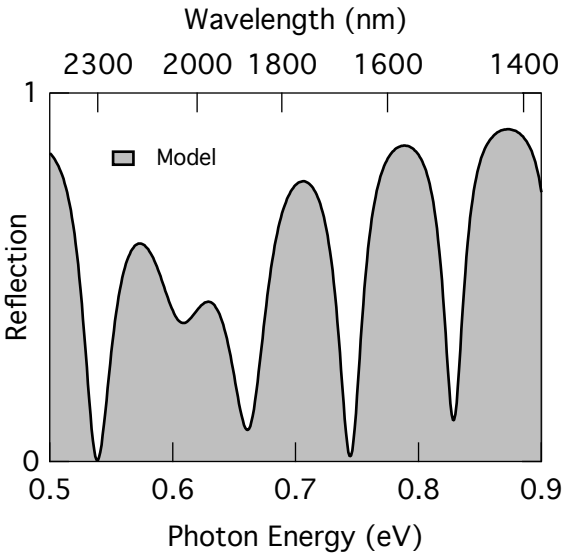

(c) Calculated reflection from suspended GeSOI layer stack.

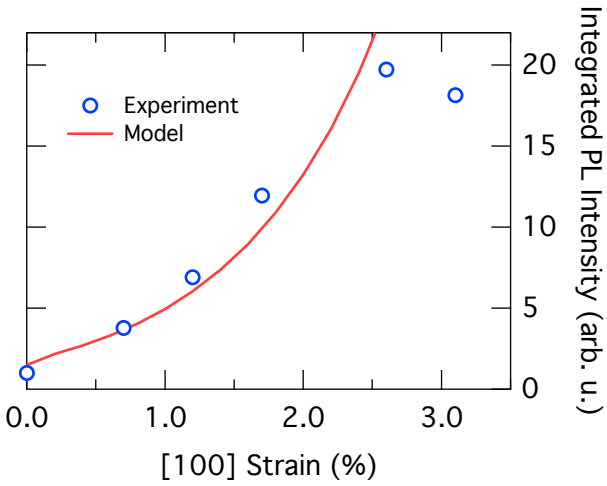

(d) Integrated PL intensity in function of strain from experiment (blue circles) and R_{sp} model (red line).

Figure 3.14: Room-temperature PL of GeSOI microbridges. With an increase in strain, the emission is found to decrease in energy as well as increase in intensity in accordance with simulations. Due to the strong Fabry-Perot interferences, contributions from the two valence bands cannot be resolved.

[1]The strain is determined from Raman shifts via equation (3.1).

parabolic, such that R_{sp} can be written as:

$$\begin{aligned} R_{sp}(E) \propto\ & E_p^{vb1}\, f_e\left(E'_{cb1}\right) f_h\left(E'_{vb1}\right)\left(\frac{1}{m_{cb}^{-1}+m_{vb1}^{-1}}\right)^{3/2}\sqrt{E-\left(E_{cb}^0-E_{vb1}^0\right)} \\ +\ & E_p^{vb2}\, f_e\left(E'_{cb2}\right) f_h\left(E'_{vb2}\right)\left(\frac{1}{m_{cb}^{-1}+m_{vb2}^{-1}}\right)^{3/2}\sqrt{E-\left(E_{cb}^0-E_{vb2}^0\right)}, \end{aligned} \tag{3.3}$$

$$E'_{cbi} = E_{cb}^0 + \frac{\left(m_{cb}^{-1}+m_{vbi}^{-1}\right)^{-1}}{m_{cb}}\left(E-\left(E_{cb}^0-E_{vbi}^0\right)\right), \tag{3.4}$$

$$E'_{vbi} = E_{vbi}^0 - \frac{\left(m_{cb}^{-1}+m_{vbi}^{-1}\right)^{-1}}{m_{vbi}}\left(E-\left(E_{cb}^0-E_{vbi}^0\right)\right). \tag{3.5}$$

Here, the band edges E_{cb}^0 and E_{vb}^0 and the effective masses m_{cb} and m_{vb} of the Γ conduction band and the two top valence bands are obtained from 8-band k·p calculations implemented in the simulation tool nextnano^3 [78]. Details about the k·p simulations can be found in the appendix (chapter A.1). Furthermore, f_e and f_h denote the electron- and hole quasi-Fermi-levels, respectively, whereas E_p describes the dipole matrix element. For the case of uniaxial stress and normal incidence-detection, a ratio of $E_p^{vb1}/E_p^{vb2} = 3/5$ is obtained for polarizations parallel and perpendicular to the applied stress by considering the selection rules for interband transitions. For simplicity, the model shown here does not take strain-dependent changes of the relative transition strengths into account.

With above introduced model, the integrated emission intensity is calculated for a constant charge carrier density of $1 \times 10^{19}\mathrm{cm}^{-3}$ estimated for 850 kW cm^{-2}, 1.4 µm layer thickness, 1.4 ns carrier lifetime and including reflection losses at the surface. A good agreement is obtained for a strain up to 2.6%. However, the emission for the bridge with 3.1% strain is lower in intensity than for the 2.6% structure, which does not follow the theoretical prediction and stops the trend of a continuously increasing emission strength. The reason for the drop might be related to the spectral sensitivity of the setup, which reaches its limit at ∼ 0.56 eV.

The splitting of the valence bands should be well resolvable in the PL measurements as long as the strain is not too large and the carrier density is not too low such that both valence bands can be populated with holes. However, the large contrast in refractive index between Ge and air leads to a modulation of the emission spectra due to multiple interference within the suspended layer stack. Therefore, the predictions for the strain-dependent valence band splitting cannot be tested in this configuration. A possible solution to the problem is to lay the structures down onto the underlying Si substrate to reduce the refractive index contrast e.g. by making use of capillary forces after wet chemical etching [160].

To visualize that the modulation of the PL spectra in Fig. 3.14(d) stems from Fabry-Perot oscillations, the broadband-reflection of an identical GeSOI layer stack is calculated

and shown as a comparison in Fig. 3.14(c). The reflection can be calculated using the transfer-matrix-method as described in the appendix (c.f. chapter A.2). We see that the periodicity of the minima in reflection nicely matches with the oscillations seen in the emission spectra, where slight differences from device to device are attributed to variations in the layer thickness.

After the Ge microbridges are selectively released from the substrate, heat transport from the narrow constriction is only possible laterally into the pads with larger cross section. The suspended structures are, therefore, more likely to heat up under optical pumping, especially under continous-wave optical excitation at energies far above the band gap. As an increased temperature leads to a decreased band gap and can, therefore, be mistaken for a shift due to tensile strain, PL measurements in function of excitation power are performed on a bridge with 3.1% strain. The normalized spectra, which are recorded at the all-metal optics setup, are shown in Fig. 3.15 for excitation power densities ranging from 100 up to 770 kW cm^{-2}. From the inset, we find a red-shift which amounts to $\sim$ 20 meV. The variation in band gap energy is empirically described by the Varshni equation [161]:

$$E_g = E_g^0 - \frac{aT^2}{T+b}. \tag{3.6}$$

With $E_g^0 = 0.88$ eV [162], $a = 4.774 \times 10^{-4}$ K^{-1} and $b = 235$ K [163], a temperature increase by 50 K is estimated from the 20 meV band gap narrowing, which is by a factor of

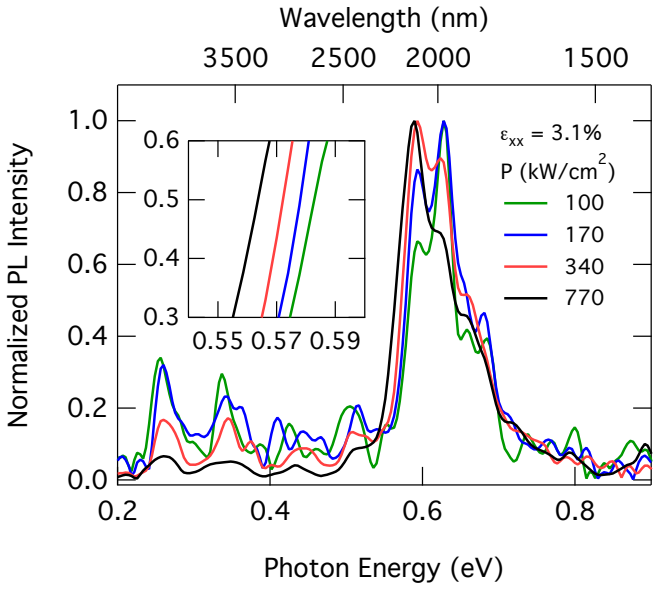

Figure 3.15: Excitation-dependent emission spectra from a GeSOI bridge with 3.1% strain[2]. The inset shows the heating-induced red-shift being limited to $\sim$ 20 meV.

[2]The strain is determined from the Raman shift via equation (3.1).

two smaller than calculated by finite element modeling [73]. Therefore, the observed red shifts can safely be attributed to the influence of strain, as the shift due to heating is by a factor of ten smaller.

3.3.3 Ambipolar Carrier Drift due to Strain Gradient

To examine the carrier transport along the strained Ge bridge, PL measurements are performed where the local excitation of sub-micrometer spot size is placed in varying distances from the center of the structure.

In Fig. 3.16(d), a two-dimensional strain map of the investigated GeSOI microbridge with a strain of 2.6%[3] is shown. The white, broken circles depict the excitation positions, which are displaced from the region with the maximum strain by up to 4.5 µm, whereas the detection area is kept unaltered on the center of the bridge. The resulting normalized emission spectra can be seen in Fig. 3.16(a). When the center of the structure is excited at 850 kW/cm^2 (X = 0 µm, i.e. the part with maximum strain is directly excited), the maximum of the emission is obtained at the lowest energy of the spectrum at $\sim$ 0.64 eV. For larger distances between the highly strained area and the excitation spot, the intensity at 0.64 eV decreases approximately linearly (c.f. Fig. 3.16(b)). When the constriction is excited 4.5 µm away from the center, the strain in the excited area amounts to $\sim$ 0.5 - 0.7%, such that an emission at 0.64 eV cannot stem from the directly excited part of the structure (c.f. Fig. 3.14). The emission at 0.64 eV can, hence, only originate from the central part with a strain of 2.6%, meaning that a considerate part of the electrons and holes drifts into the center before recombining there radiatively.

The reason for the efficient ambipolar transport of carriers into the central part of the constriction can be seen in Fig. 3.16(c), where the band alignment along the constriction is shown at Y = 0 µm. The band edges are computed with the deformation potential approach implemented in nextnano^3 [78], with the exact strain tensor as obtained from finite element COMSOL modelling as input for the band structure simulation. Due to the strain gradient along the bridge with the maximum strain in the center, a type-I band alignment is obtained, which means that electrons and holes are spatially confined at the same position. The simulated band offsets between the center (X = 0 µm) and the pad (X = 6 µm) amount to 112, 47 and 75 meV for the Γ-, L- and top valence band, respectively. Therefore, the strain-induced electric field along the length of the bridge leads to an efficient drift of carriers into the region with the highest strain and, hence, the highest radiative recombination efficiency. For structures with a larger maximum strain, the effect should increase due to a

[3] The strain is determined from the Raman shift via equation (3.1).

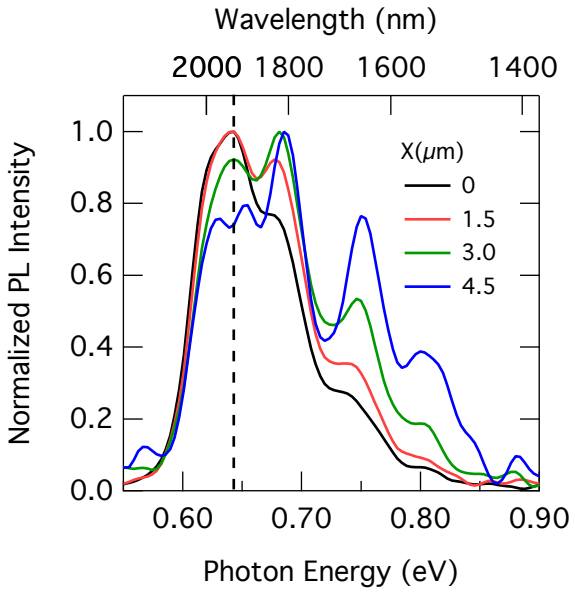

(a) Normalized emission detected at center of bridge for excitation X µm away from center (see Fig. 3.16(d)).

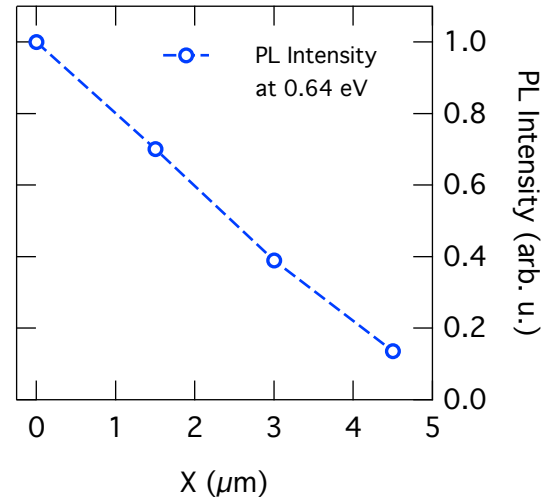

(b) PL intensity at 0.64 eV corresponding to emission from region with maximum strain for locally varying excitation.

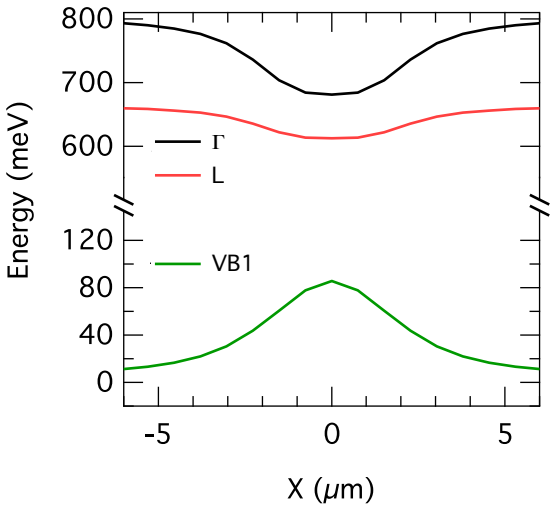

(c) Band alignments calculated via deformation potential theory showing a type I - band alignment along the length of the bridge.

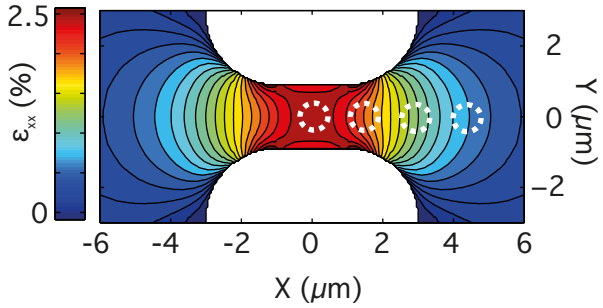

(d) Two-dimensional strain map of microbridge with indication of excitation positions.

Figure 3.16: PL emission spectra for 2.6% strain[4] detected at the center of the bridge for locally varying excitation position. Due to a type-I band alignment along the length of the bridge, there is a drift of carriers into the highly strained constriction, which leads to emission from the central part of the bridge even for local excitation on the pad.

[4]The strain is determined from the Raman shift via equation (3.1).

stronger strain-gradient. The same carrier collection effect has been recognized as well in ref. [74] from the investigation of so-called pseudo-heterostructure GeOI nanowires.

In conclusion, the strain-gradient along the bridge leads to a type-I confinement and, therefore, to an ambipolar drift of carriers, which additionally increases the charge carrier density at the region with the highest strain. This drift of carriers is advantageous for laser injection schemes where the gain-volume would be the central, strained part of the microbridge.

3.3.4 Comparison of GeSOI and GeOI Microbridges

As discussed in chapter 3.1, the strain-enhancement technique is in principle not limited to a certain achievable maximum strain as long as the yield stress of a material is not exceeded. For the GeSOI microbridges presented above, the maximum strain that could be achieved is 3.1%. With this 3.1% strain, the conduction band offset between the Γ- and L-states is reduced by $\sim$ 90 meV from 140 meV to 50 meV according to deformation potential theory. However, there is the incentive to reach even higher strain as the optical properties improve further when getting closer to a fundamental direct band gap.

For thick germanium layers directly deposited on silicon, the large difference in lattice constant leads to a highly defective interface because the strain is released by the creation of dislocations [146]. In chapter 4, the defective interface is shown to be the limiting reason for the non-radiative lifetimes. But as will be shown experimentally here, the defects are also the restricting factor for the achievable maximum strain. To that end, strained microbridges based on germanium-on-insulator layers are fabricated, where the defective interface is removed within the process as has been discussed above. In Fig. 3.17(a), room temperature PL spectra are shown for GeOI bridges with 6 µm × 500 nm constriction and varying pad lengths for an excitation density of $\sim$ 18 kW cm^{-2} at 532 nm. The strain measured via Raman spectroscopy amounts to a maximum of 3.6% using equation (3.2), which exceeds the maximum strain achieved in GeSOI. Similarly as for the GeSOI bridges at lower strain values, where the emission was red shifted with respect to the unpatterned germanium layer, the emission energy for the GeOI bridges decreases with increasing strain down to $\sim$ 0.45 eV for 3.6% strain. The further decrease in conduction band offset is evidenced by the steady increase in PL intensity with increasing strain, as the population of states in the Γ valley increases.

Strained microbridges made from GeOI do not only feature longer carrier lifetimes (c.f. chapter 4) and are mechanically stronger than their counterpart made from GeSOI, but they are also more efficient emitters. This is because the strain is more homogeneous and, therefore, the volume relevant for emission is larger.

A direct comparison of the PL emission between a GeOI and a GeSOI structure is shown in Fig. 3.17(b). The two microbridges fabricated from different substrate material have a similar strain which is apparent due to the equal emission energies measured under identical conditions.

However, the GeOI structure (grey, filled area) shows an integrated intensity which is $\sim 14\times$ stronger than for GeSOI (red, filled area, scaled by $5\times$ for clarity), even though the constriction in the GeSOI case has a volume $2.8\times$ larger than for GeOI (with an increase by a factor 2 in area and 1.4 due to different layer thicknesses). This overall efficiency increase of $14\times2.8 \sim 40$ is largely explained by the strain profile along the growth direction shown for both cases in Fig. 3.18(a). For GeOI (top panel), the strain is homogeneous along constriction-length (i.e. x-direction) as well as along the growth-direction (i.e. z-direction) with a maximum strain of 3.0%. The situation is very different for GeSOI because of the 340 nm thick silicon layer below the germanium layer. Due to the difference in stiffness between Ge and Si, the Ge layer bends upwards after being released. The bending leads to an increase in strain when compared to a GeOI structure with nominally identical dimensions, which can reach up to an additional 33% for the optimal Si thickness [73, 138]. However, the increase

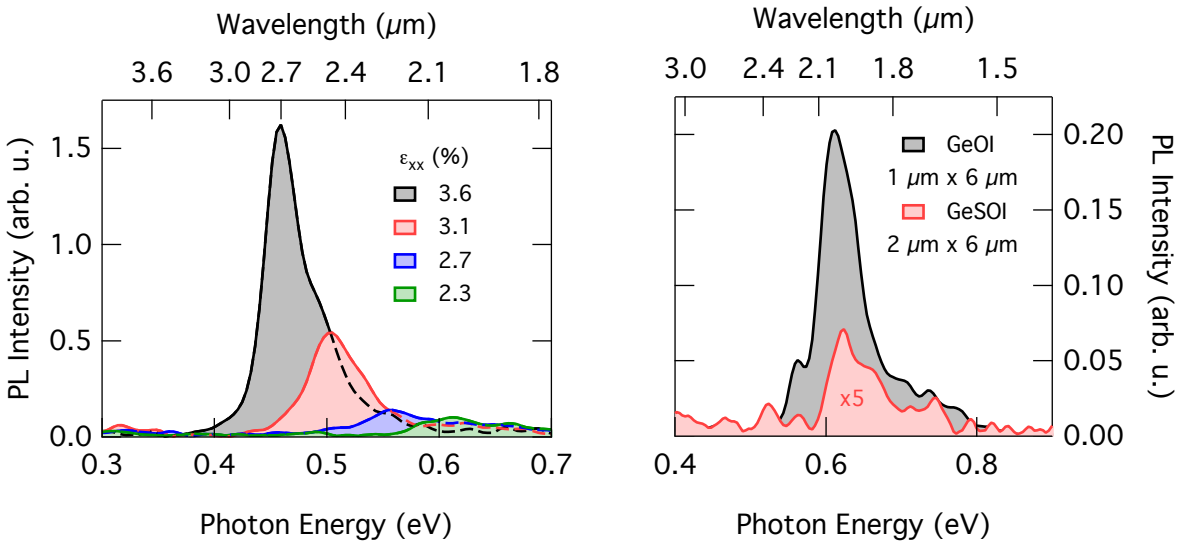

(a) Room temperature PL spectra from GeOI bridges with varying strain[5].

(b) Comparison of emission from GeSOI and GeOI bridge at comparable strain under identical experimental conditions.

Figure 3.17: Room-temperature PL spectra of Ge microbridges. For GeOI and GeSOI bridges under similar strain, GeOI shows a significantly stronger emission intensity even for a smaller constriction volume.

[5]The strain is determined from Raman shifts via equation (3.2).

in strain comes at the price of a largely inhomogeneous strain distribution along z-direction.

In Fig. 3.18(b), the homogeneity in strain is visualized in terms of how large the volume under a certain amount of strain is. Due to the bending, for GeSOI the maximum strain of 3.0% is obtained only in a small fraction of the total structure. Hence, the volume under 3.0% strain for GeOI is 11.5× larger than for GeSOI albeit the difference in layer thickness and constriction width. The measured PL emission does not only reflect the strained volume, but also depends on the carrier lifetime (see chapter 4).

In summary, bridges fabricated on GeOI reach strain values up to 3.6%, significantly surpassing the maximum strain achieved in GeSOI due to the improved mechanical strength of the starting material. At a comparison between the emission intensity of GeOI and GeSOI bridges at a similar strain, the GeOI structure shows a superior efficiency by ∼ 40× due to an improved spatial homogeneity in strain and longer non-radiative lifetimes. The large uniformity in strain within a large volume is essential to obtain a mode propagating with a large overlap with the gain medium.

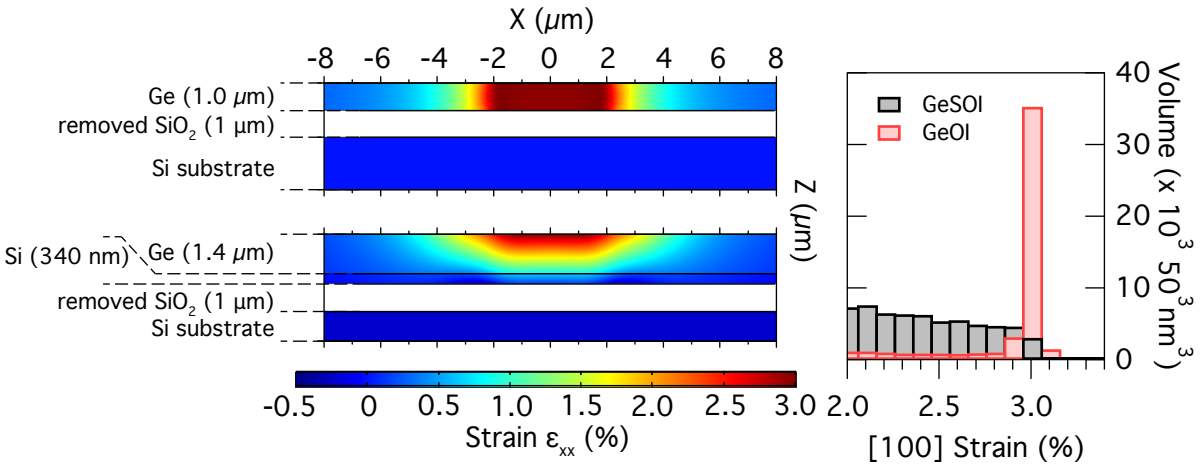

(a) Cross-sectional view of strain through center of GeOI (top) and GeSOI (bottom) microbridge.

(b) Histogram showing volume in function of strain.

Figure 3.18: (a) Cross-sectional view of ε_{xx} strain for GeOI (top) and GeSOI (bottom) microbridges of identical dimensions obtained by finite-element modelling. Due to bending in the GeSOI case, the maximum strain is increased at the top surface of the constriction. (b) Histogram depicting the volume of a microbridge in function of strain.

3.4 Experimental Demonstration of Direct Band Gap Germanium

According to literature, strain values around the transition point to direct band gap Ge have been achieved for biaxial strain via silicon nitride stressors [70], pressurized membranes [164–166], or epitaxy on InGaAs [125]. Record values of strain have been obtained in only 200 nm thin GeOI nanowires using above introduced strain-enhancement technique [75]. However, no report on optical spectroscopy for the supposedly direct band gap GeOI nanowires is given [75]. The available PL data on the biaxially strained structures are performed at room temperature [70, 164]. As there is no abrupt change in optical properties at the crossover to a fundamental direct band gap, luminescence data at 300 K in function of strain do not give a reliable indication on whether the structure is fundamentally indirect or direct. Instead, PL measurements at low temperature can provide the necessary information as only the lowest energetic states are populated. In that case, the direct gap emission should either increase or freeze out, as recently demonstrated for direct band gap GeSn [77]. The low-temperature data shown for 10 nm thick Ge layers epitaxially strained on InGaAs with a biaxial strain up to 2.33% revealed a strong emission at 1670 nm [125]. However, at such a high strain and low temperature an emission wavelength of ≈ 3 µm would be expected, creating doubts about the origin of the detected emission.

In the following, temperature-dependent PL measurements are presented on differently strained GeOI microbridges. A qualitatively different behavior is found for samples with either more or less than $\sim 4.0\%$ strain. As will be shown in the following, this is attributed to the transition from indirect- to direct band gap Ge. The argumentation consists of three parts:

(i) the temperature-dependent strain evolution,

(ii) the modelling of temperature-dependent PL emission,

(iii) the experimental temperature-dependent PL results.

3.4.1 Temperature-Dependent Mechanical Strain Simulations

The strain in the constriction of a microbridge $\varepsilon_C = \varepsilon_L \times EF$ depends on the biaxial prestrain in the layer ε_L and the enhancement factor EF given by the structure's geometrical dimensions. So far, the strain has been tuned by adjusting EF. In general, this is achieved e.g. by extending the length of the pads. Another approach to increase ε_C is to increase the biaxial prestrain ε_L,

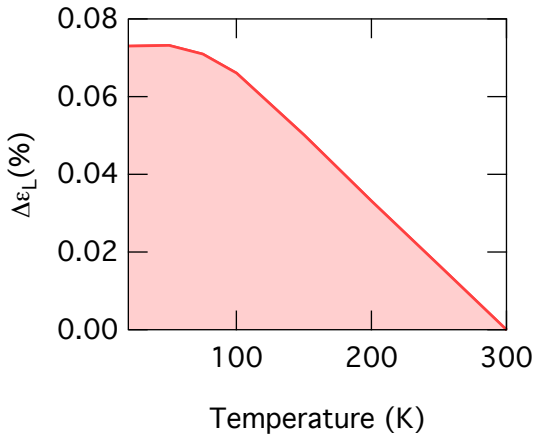

(a) Temperature-dependent increase in biaxial strain $\Delta\varepsilon_L$ for a Ge layer on Si given in absolute units.

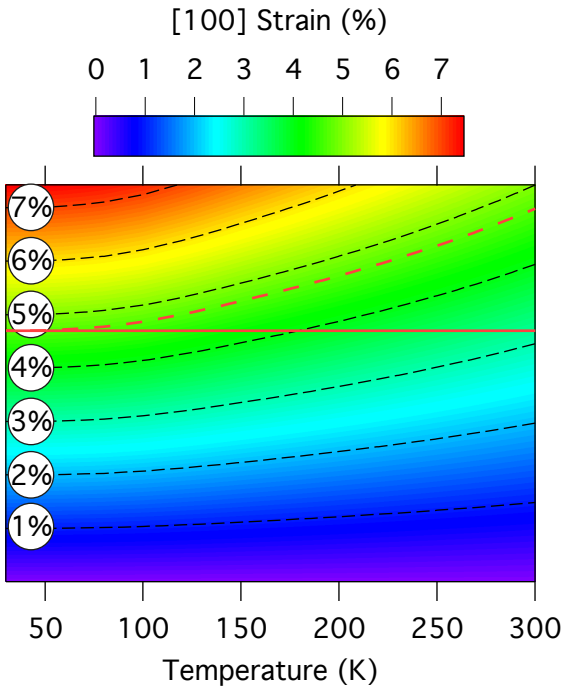

(b) Finite-element simulation of temperature-dependent strain enhancement in Ge microbridges. The red, broken line indicates a strain of 4.7%, which can be reached at 50 K for a structure with 3.2% strain at room temperature (see red, full line).

Figure 3.19: Finite-element modelling of temperature-dependent strain enhancement. By cooling from room temperature to 50 K, the strain can be increased by > 45%, such that a strain of 4.7% at 50 K can be reached for a microbridge with a strain of 3.2% at 300 K.

where already small changes can lead to a large change in maximum strain in the constriction due to the enhancement by EF.

For Ge on Si, the biaxial tensile prestrain originates from the difference in thermal expansion coefficients occuring after cooling from high temperature during growth or annealing to room temperature. By cooling to temperatures below 300 K, this difference increases and, thus, increases the prestrain even further. To investigate the cooling-induced strain variation, FEM modelling is performed using the thermal expansion coefficients of Si [167] and Ge [168] as well as the temperature-dependence of the elastic constants [169]. In Fig. 3.19(a), the absolute increase in biaxial tensile strain $\Delta\varepsilon_L$ is shown in function of temperature. In the temperature range between 300 K and $\sim$ 100 K, the increase in strain is linear with temperature. This rise in strain saturates at $\sim$ 100 K. When zero Kelvin is reached, a maximum increase in strain of $\sim$ 0.07% is obtained. The GeOI substrates used in this work have a typical biaxial prestrain of 0.16% at 300 K such that at 50 K a biaxial strain of 0.24% is reached representing a relative increase in strain of more than 40%.

The evolution of [100] strain with temperature is shown as contour plot in Fig. 3.19(b). The broken, red line depicts 4.7% strain, which is predicted as crossover to fundamentally direct band gap Ge (see chapter 2). The strain for a given structure relates to a horizontal line in the plot. As an example, the full, red line depicts a microbridge with 3.2% strain under ambient conditions. When the temperature is decreased to 30 K, the strain in the device reaches 4.7%. Therefore, temperature can be used as tool to deliberately and reversibly fine-tune the strain of a given structure and investigate characteristic parameters in dependence of strain on one and the same device.

3.4.2 Modelling of Temperature- and Strain-Dependent Emission Intensities

Besides the increase in strain, cooling to low temperatures also leads to a thermalization of electrons into the lowest energy states available in the conduction band. This effect is exploited to distinguish between a fundamentally direct- and indirect band gap as recently done for GeSn [77]. If the conduction band alignment is indirect, i.e. if the L-valleys are at a lower energy than the Γ states, then the carriers will increasingly populate the L-valleys from where there is no efficient radiative recombination. Therefore, it is expected that the direct gap luminescence will vanish for Ge with a fundamentally indirect band gap. In contrast, in direct band gap Ge the thermalization leads to a redistribution of carriers into the Γ valley which yields an increased emission signal. The increase flattens out once all the electrons are located at Γ.

For a quantitative assessment of the expected temperature-dependent emission, the integrated spontaneous emission intensity is calculated in function of temperature for Ge

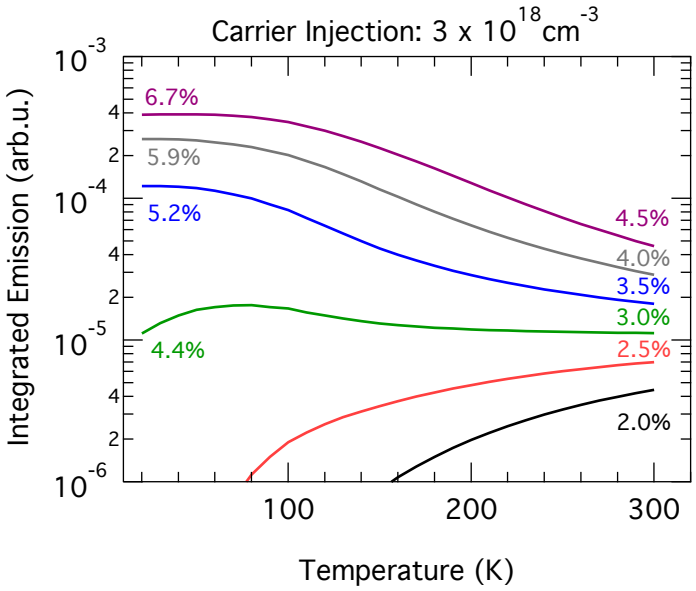

Figure 3.20: Calculated integrated emission intensity in dependence of temperature for Ge bridges with varying strain. If a fundamental direct band gap cannot be reached, the direct gap emission vanishes, whereas the intensity increases for structures, where the band alignment is inverted at low temperatures.

microbridges with room temperature strain between 2.0% and 5.0% (see Fig. 3.20). The model is introduced in chapter 3.3.2. The joint-density-of-states of dipole-allowed interband transitions is calculated under the assumption of isotropic, parabolic bands with strain-dependent band edges and effective masses from nextnano[3]. The conduction band offset between Γ- and L-states is assumed to not change with temperature, i.e. the same Varshni-parameters are considered for both valleys. Additionally, the temperature-dependent increase in strain as shown in Fig. 3.19 is taken into account.

The calculations are done for an injected carrier density of $3{\times}10^{18}$ cm^{-3}, without the carrier diffusion from the pad regions into the highly strained constriction (see chapter 3.3.3) taken into account. Two different regimes are found:

i) For $\varepsilon < 3.0\%$, the integrated direct gap emission steadily decreases because the direct gap crossover cannot be reached, such that at low temperature only the L states are populated.

ii) For $\varepsilon > 3.0\%$, cooling leads to an increase in spontaneous emission as for low-temperatures Ge turns into a direct band gap material such that a decrease in temperature increases the electrons at the Γ valley.

Therefore, photoluminescence measurements at low temperature are the method of choice to

distinguish between fundamentally direct- and indirect semiconductors as a clear indication about the conduction band alignment is provided.

3.4.3 Low-Temperature PL Measurements

In Fig. 3.21(a), PL spectra for a bridge with 3.6% longitudinal strain at 300 K are shown for different temperatures. The bridges are optically excited in continuous-wave at 532 nm over an area of ~ 7 µm diameter with an excitation density of 18 kW/cm^2. The strain is determined via power-dependent Raman spectroscopy [158], where a heating-corrected Raman shift of -6.7 cm^{-1} is obtained.
From the red-shift of the emission peak with decreasing temperature, it is apparent that the strain increases upon cooling as predicted by above introduced model. Therefore, the band gap narrowing due to tensile strain overcompensates the typically obtained blue-shift. To validate the strain-extrapolation for low temperatures, the direct band gap energy E_{gap} is extracted for various samples with different room temperature strain by fitting the PL peak with a simple model describing the spontaneous radiative efficiency $R(E)$ of a bulk material as [170]

$$R(E) \propto \sqrt{E - E_{gap}} \exp\left(\frac{E}{kT}\right), \tag{3.7}$$

where k is the Boltzmann constant and T is the temperature. The band gaps are extracted at different temperatures and shifted towards their value at 300 K via Varshni's formula [171]:

$$E_{gap}(T) = E_{gap}(0) - \frac{aT^2}{T+b}. \tag{3.8}$$

Here, $E_{gap}(0) = 0.88$ eV [162], $a = 4.774\times10^{-4}$ 1/K [163] and $b = 235$ K [163]. The results are shown in Fig. 3.21(b) for a series of samples with room temperature strain between 1.9% and 3.6%. The band gaps extracted for different structures at the same strain yield a good agreement between each other, which confirms that the strain-extrapolation seems to be accurate. It should be noted that the microbridges show no sign of degradation. In particular, the PL emission remains at the same intensity over time even after several cooling cycles with the same maximum strain being reached. According to the extrapolation of the room-temperature strain conversion via equation (3.2), the highest strain at low temperature corresponds to 5.4%, which is the largest longitudinal [100] strain achieved up to date. For a comparison, the Raman data taken at 300 K as well as the strain from the linear- and non-linear conversion at 300 K and the respective extrapolations for 20 K are summarized in table 3.1.

Additionally, the red, broken line in Fig. 3.21(b) shows the shift in direct band gap energy obtained from a tight binding model developed at CEA LETI, which was previously applied to

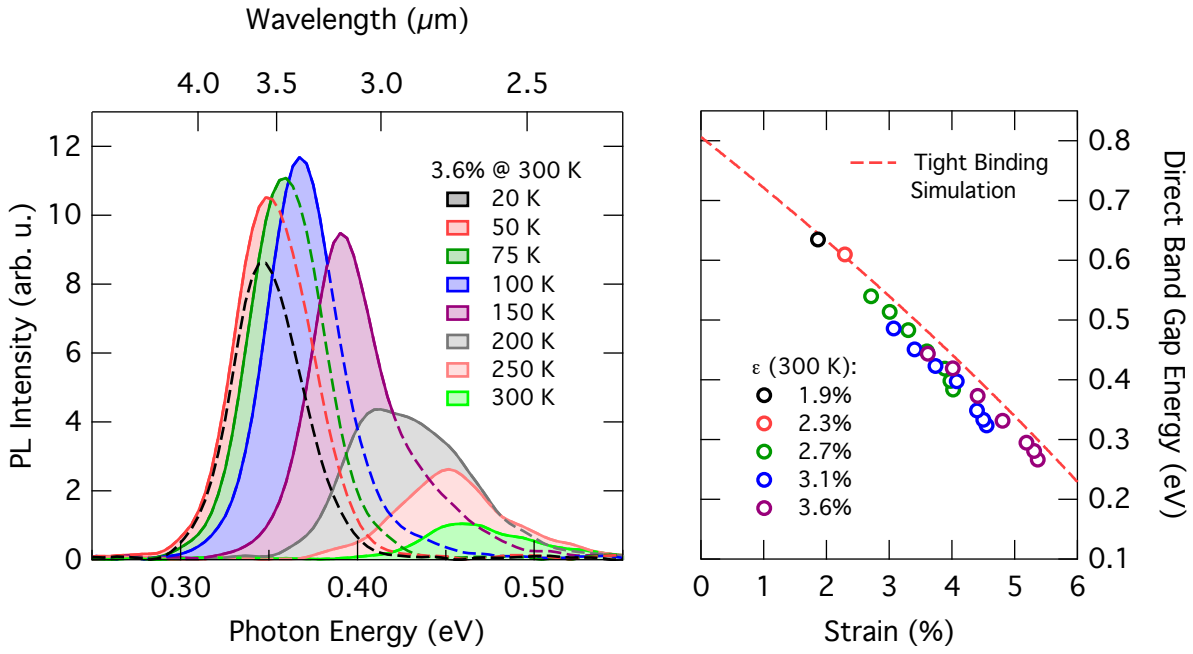

(a) Temperature-dependent PL spectra for a GeOI microbridge with a uniaxial strain of 3.6%[6] at 300 K.

(b) Extracted direct band gap energies in function of strain.

Figure 3.21: PL measurements in function of temperature. The red-shift for lower temperatures (a) and the consistency for the extracted band gaps from different samples (b) prove the applicability of the above introduced strain-extrapolation for low temperature measurements.

biaxially strained Ge [90]. This model reproduces ab initio calculations over a wide range of deformations and predicts, in particular, a slight bowing of band gap energy at large uniaxial strain, which is found to be in good agreement with the experimental data.

The intensities integrated over the PL peak for the set of strained GeOI bridges are shown in Fig. 3.22 in logarithmic representation in function of temperature. For any temperature, a larger strain leads to a larger emission intensity due to the more favorable conduction band alignment, which leads to an increased population of the direct Γ valley. When the temperature decreases from 300 K to 200 K, the intensity increases for all bridges independent on strain although for strain $< 3\%$, the model predicts a monotonic decrease in intensity. This discrepancy between experiment and model is attributed to the diffusion of carriers from the pads into the highly strained region, where they contribute to the emission intensity at maximum strain (see chapter 3.3.3). This effect is illustrated in Fig. 3.23. Due to the relative dimensions of constriction (6 µm length, 500 nm width) and the excitation spot size

[6]The strain is determined from Raman shifts via equation (3.2).

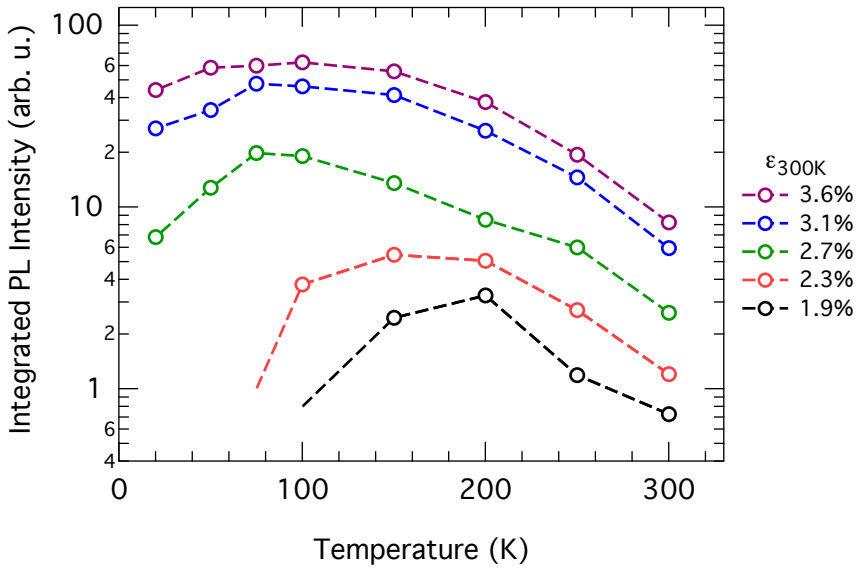

Figure 3.22: Integrated PL intensities in dependence of temperature for microbridges with room-temperature strain[7] varying between 1.8% and 3.6%.

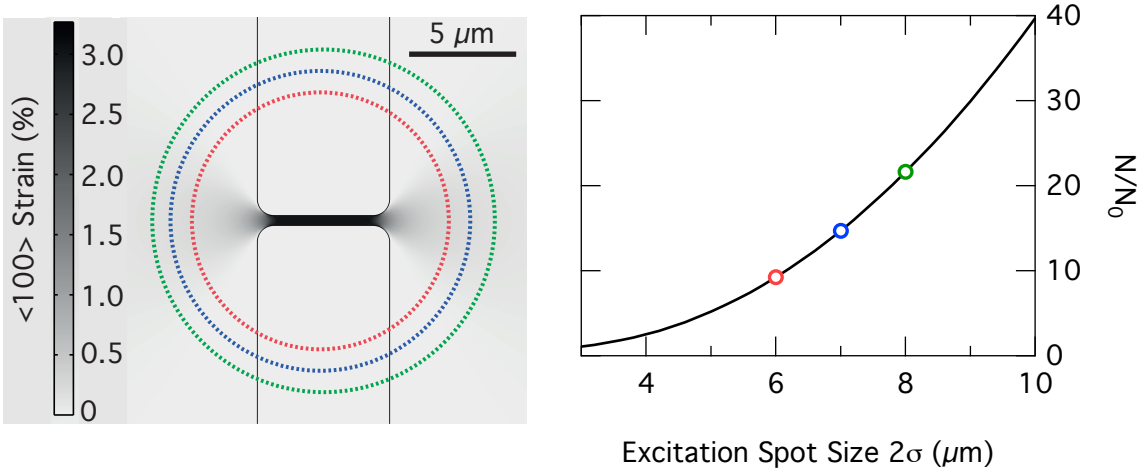

(a) <100> strain map of a suspended GeOI bridge. The circles give the $1/e^2$ limits of Gaussians with $2\sigma = 6$ (red), 7 (blue) and 8 (green) µm, respectively.

(b) Increase in carrier density in homogeneously strained area in function of excitation spot size due to diffusion of carriers.

Figure 3.23: Influence of ambipolar carrier diffusion into highly strained constriction. The red, green and blue circles in (a) depict the $1/e^2$ limit of Gaussian spots with widths of $2\sigma = 6.0$, 7.0 and 8.0 µm, respectively. In (b), the excited area weighted with a symmetric, two-dimensional Gaussian is normalized to the homogeneously strained area of 4.5 µm × 500 nm.

[7]The room temperature-strain is determined from Raman shifts via equation (3.2).

which is estimated to a width of $2\sigma \sim 7$ µm, the structure is excited over an area which is considerably larger than the strained part. This is schematically depicted in Fig. 3.23(a), where the red, blue and green broken lines visualize the $1/e^2$ limits of Gaussian excitation spots with a width of $2\sigma = 6.0$, 7.0 and 8.0 µm, respectively. In the PL data taken at 300 K, the extension of the excitation spot beyond the constriction can nicely be seen by the emission peak slightly below 0.8 eV, which is assigned to radiative recombinations in the unpatterned part of the layer (c.f. Fig. 3.24(a)). Therefore, the emission from the highly strained part is divided into contributions of electron-hole pairs which are created directly in the constriction, and carriers which diffuse and drift into the central part. The latter is not included in the model, but effectively leads to an increased charge carrier density. In Fig. 3.23(b), the relative increase in charge carrier density due to diffusion is estimated. The excitation spot is assumed to be a circularly symmetric Gaussian distribution with a width parametrized as σ. Compared to the area $A_0 = 4.5$ µm × 500 nm with constant strain, the total excited area weighted with the two-dimensional Gaussian is ∼ one order of magnitude larger. Hence, the carrier density can increase up to 10× due to diffusion assuming that all carriers reach the constriction. The collection efficiency is expected to be stronger for lower temperatures due to an increase in carrier mobility [172, 173].

To come back to Fig. 3.22, the emission intensities for the bridges with 1.9% and 2.3% start to decrease for temperatures below 200 K. At 150 K, the emission of all bridges can still be detected (see Fig. 3.24(b)), while at 20 K the PL intensity for the two smallest strains, which account to 2.7% and 3.3% with the strain enhancement being considered, vanish (c.f. Fig. 3.24(c)). This observation is in accordance with the model, where the direct gap emission freezes out for strain too low to reach the crossover to a fundamental

Raman 300 K $\Delta\omega$ (cm^{-1})	$\varepsilon_{[100]}$ (%) 300 K equation (3.2)	$\varepsilon_{[100]}$ (%) 300 K equation (3.1)	$\varepsilon_{[100]}$ (%) 20 K equation (3.2)	$\varepsilon_{[100]}$ (%) 20 K equation (3.1)
−3.3	1.9	2.1	2.8	3.2
−4.1	2.3	2.6	3.4	3.9
−4.9	2.7	3.2	4.0	4.7
−5.6	3.1	3.6	4.5	5.4
−6.7	3.6	4.3	5.4	6.4

Table 3.1: Raman shifts and [100] strain at 300 K and 20 K for GeOI microbridges. The strain values at 300 K are obtained either by linear (equation (3.1)) or non-linear (equation (3.2)) strain-shift conversion, whereas the low temperature values are extrapolated from FEM modelling.

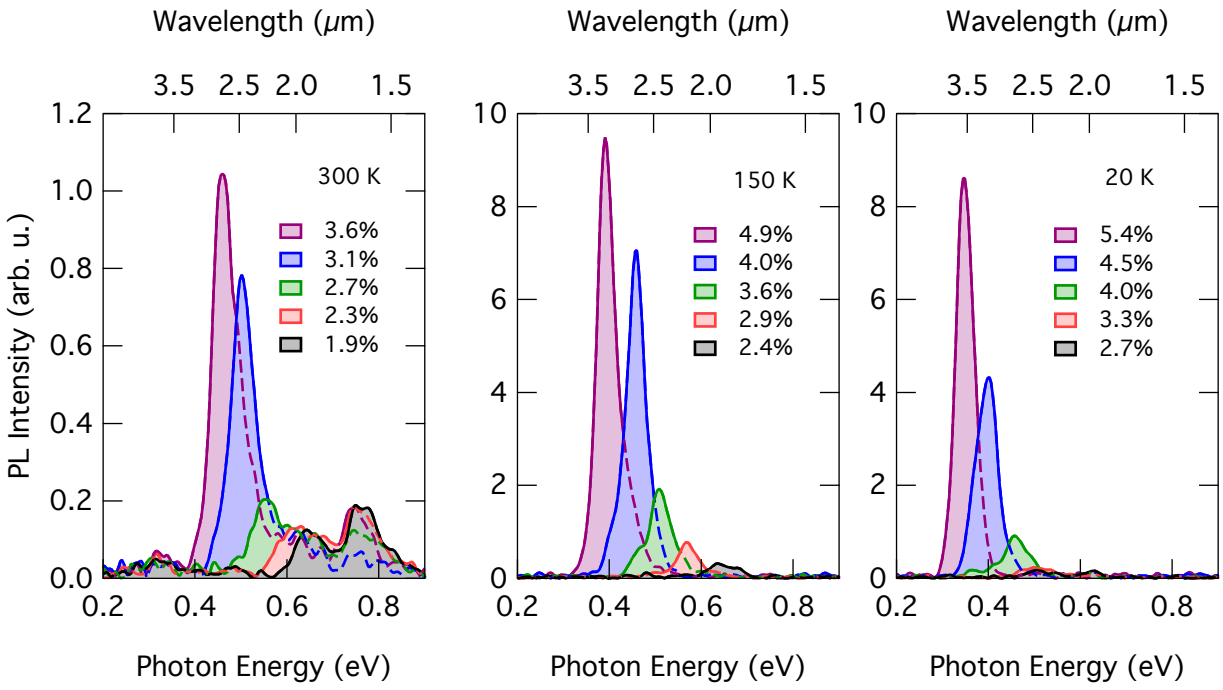

(a) $T = 300$ K. (b) $T = 150$ K. (c) $T = 20$ K.

Figure 3.24: PL measurements in dependence of strain[8] at different temperatures for an excitation density of 18 kW/cm^2.

direct gap. In contrast, there is still a strong emission at 20 K for strain values of 4.0%, 4.5% and 5.4% at an excitation density of 18 kW/cm^2. Moreover, when the excitation density is decreased to 5 kW/cm^2 (see Fig. 3.25) - which corresponds to a steady state carrier density of 6×10^{17} cm^{-3} with a lifetime of 5.0 ns and neglecting carrier diffusion - the PL signal for 5.4% and 4.4% can still be clearly detected, whereas the emission intensity for 4.0% drops below the noise limit. The bridge at 4.0% is, hence, ascribed to be close but yet below the transition towards a direct band gap Ge. On the other hand, the structures with 4.5% and 5.4% strain are found to have a fundamental direct band gap. Therefore, the crossover of elemental Ge towards a fundamental direct band gap is for the first time experimentally confirmed to occur for a [100] longitudinal tensile strain between 4.0% and 4.5%. The required crossover strain seems to be slightly lower and, hence, more favorable than anticipated by most predictions [75, 88, 92].

Strikingly, the integrated intensities for the two direct band gap devices not only flatten out as expected, but the intensity slightly decreases when the temperature decreases below 75 K, which is not in accordance with the theory. One might question the assumption of similar Varshi-shifts for Γ- and L-valley such that the alignment at lower temperatures is less

[8]The room temperature-strain is determined from Raman shifts via equation (3.2).

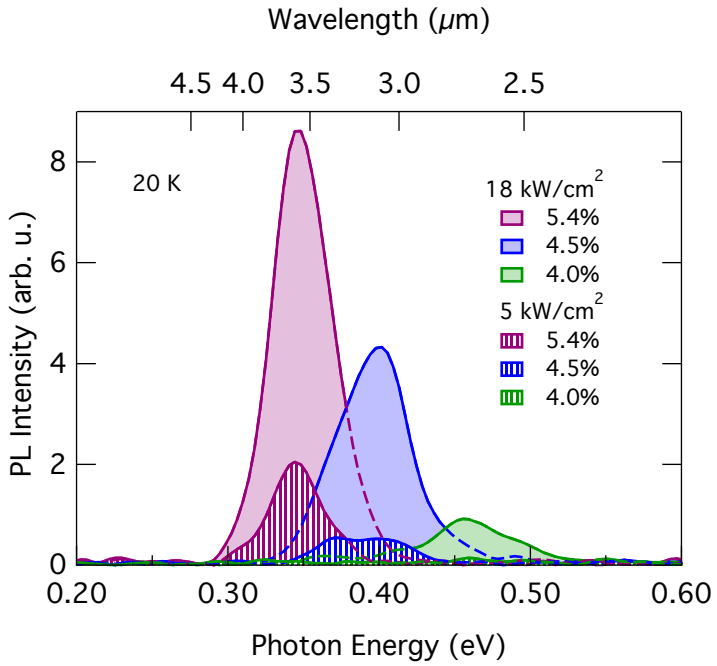

Figure 3.25: Power-dependent PL spectra at 20 K. Due to a strong emission at 20 K and a low excitation density of 5 kW/cm^2, microbridges with $>$ 4.5% strain are identified as fundamental direct band gap Ge.

favorable than at 300 K. But at such low temperatures the band edge variations are too small to explain the observed effect.

A more likely explanation is connected to the efficiency of intervalley scattering (IVS) from the L-valley into the Γ valley. For the case of a GeOI bridge with a fundamental direct band gap, the carriers diffusing from the pads into the strained region relax into the L valley after photogeneration and need to transfer in k-space from the L- into the Γ states. For GaAs, the transfer rate of this phonon-assisted process was found to decrease by approximately a factor of three between 300 K and 30 K [174]. Due to the near-degeneracy of the Γ- and L-valleys in the strained Ge, the IVS phonon bottleneck is expected to be even more constraining than in GaAs, which may explain that in spite of the long non-radiative lifetime, the occupation of Γ at low temperature seems not to be in thermal equilibrium with the L valley. Once the separation between Γ- and L valleys is more than a typical phonon energy with the Γ states $\sim$ 30 meV below the L-states, the bottleneck should disappear. This is in accordance with the highest strained sample and a decline of less than 30%, where we can estimate a conduction band offset $\Delta E_{cb} = E_\Gamma - E_L = -40$ meV following a linear extrapolation as

$$\Delta E_{cb} = 140 \text{ meV}\left(1 - \frac{5.40\%}{4.25\%}\right) = -40 \text{ meV} \tag{3.9}$$

with the crossover to a direct band gap taken at 4.25%.

3.5 Spectroscopy on Strained Microbridges with Integrated Microcavity

To realize a laser based on highly strained Ge, the gain material has to be incorporated into an optical cavity. Ge microbridges featuring the cornercube cavity introduced in chapter 3.2.3 were processed by Thomas Zabel at Paul Scherrer Institute. Raman spectroscopy yields a Raman shift of -6.0 cm^{-1}, which translates into a strain of 3.3% according to equation 3.2. The PL spectra shown in Fig. 3.26(a) were recorded by Esteban Marín at Paul Scherrer Institute with a spectral resolution of 1 meV. The measurements were performed at 50 K, such that the strain in the microbridge increases to 4.9%, i.e. above the transition towards direct band gap Ge. Optical injection of charge carriers is delivered in continuous-wave at the excitation wavelength of 532 nm. The emission spectra are strongly modulated with a free spectral range (FSL) of $\sim$ 3 meV. The FSL translates into a cavity length L_c of $\sim$ 50 µm via $L_c = \frac{c}{2n_r\Delta\nu}$, where c is the speed of light, $n_r = 4$ is the refractive index of Ge, and $\Delta\nu = 7.8{\times}10^{11}$ s^{-1} is the FSR. The thus obtained cavity length is in accordance with the geometry of the cornercube design.

For an increase in excitation density from 6 kW/cm^2 to 13 kW/cm^2, the integrated intensity increases by $\sim 9\times$, with a pronounced relative increase between 0.35 and 0.36 eV. In Fig. 3.26(b), the spectrum at 6 kW/cm^2 is shown in a close-up on one of the spectral peaks. The loaded Q-factor is extracted by a Lorentzian fit to the data and amounts to 530. The determination is limited by the resolution of the measurement, such 530 represents the lower bound for the Q-factor.

The dependence of the Q-factor in function of the excitation density is shown in Fig. 3.27 for several resonances. The Q-factors decrease with increasing pump power, which indicates additional losses. Lasing characteristics such as a distinct linewidth narrowing (i.e. increase in Q-factor) or a rapid intensity increase for a single cavity mode are not observed. This might be attributed to the insufficient population of the Γ states under CW excitation: For an excitation density of 13 kW/cm^2, the steady-state carrier density is estimated to $\sim 1{\times}10^{18}$ cm^{-3}. At 50 K and 5% tensile strain, less than 10% of the total electron density populates the Γ states, which is further reduced due to the heating caused by the CW excitation. Furthermore, the excitation energy is far above the band gap of relaxed Ge, which leads to unwanted absorption in the unstrained volume. For increased carrier densities, reduced heating and reduced absorption in the unstrained Ge, the optical excitation should be performed in pulsed mode at an excitation wavelength of 1.5 µm or longer, such that no carriers are generated

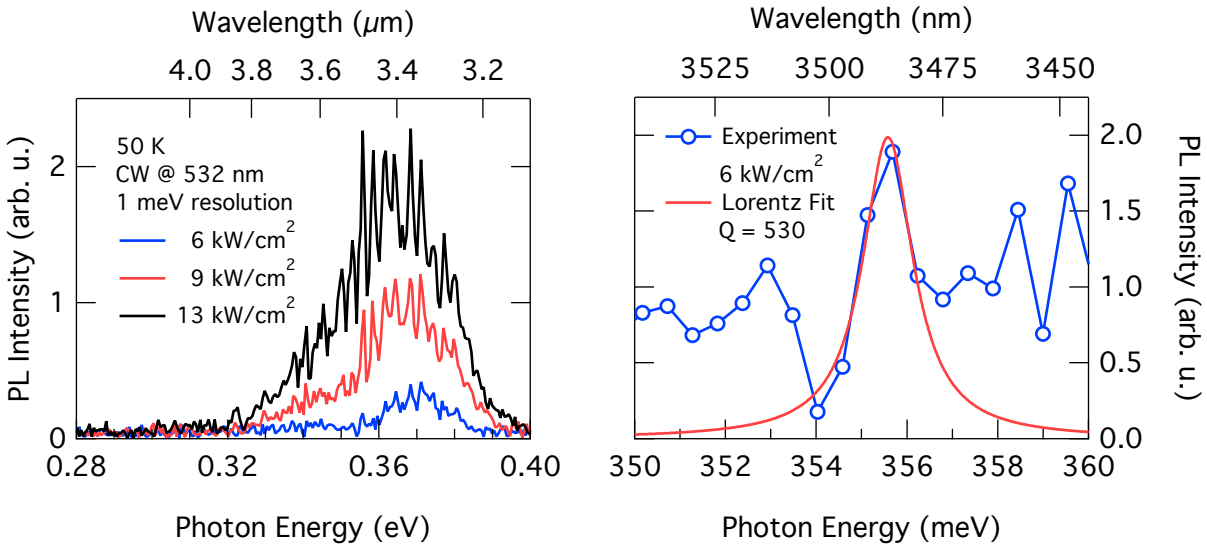

(a) PL spectra for bridge with cornercube cavity at 50 K.

(b) Lorentzian fit to a single emission peak at 6 kW/cm^2. A Q-factor of 530 is extracted.

Figure 3.26: (a) High-resolution PL spectra of a microbridge with cornercube cavity under 4.9% strain for excitation densities between 6 and 13 kW/cm^2. (b) A Lorentzian fit to a single peak taken under 6 kW/cm^2 excitation density reveals a Q-factor of 530 limited by the resolution of the measurement.

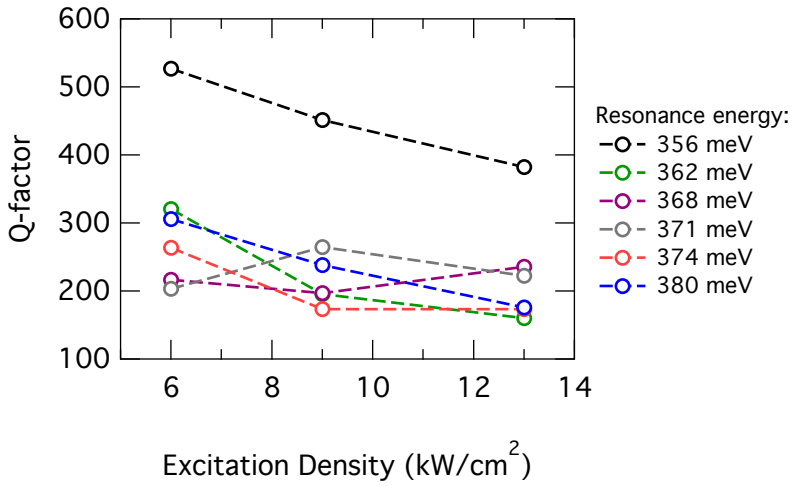

Figure 3.27: Experimentally determined Q-factors in function of excitation density. An indication for lasing such as a distinct increase in Q-factor is not observed.

within the relaxed Ge.

3.6 Efficiency of PL Emission from Strained Microbridges

For a GeOI microbridge under a tensile strain of 3.6%, the PL signal measured at room temperature for a continuous-wave excitation density of 18 kW/cm^2 amounts to a detector photocurrent of $I_{exp} = 5{\times}10^{-12}$ A. The estimation of the expected photocurrent I_{th} consists of three parts:

(i) the spontaneous radiative emission rate R_{sp} of strained Ge,

(ii) the collection efficiency of the setup η_{col},

(iii) the transmission efficiency through the microfocus setup η_{MF}.

The spontaneous radiative emission rate R_{sp} is determined by the steady-state carrier density of the Γ states N_Γ and the spontaneous radiative decay time τ_r as $R_{sp} = N_\Gamma/\tau_r$. The total carrier density is obtained as

$$N_{tot} = \frac{P_{exc}\,\tau_{nr}}{E_{ph}\,d}. \tag{3.10}$$

For the excitation density $P_{exc} = 18$ kW/cm^2, the non-radiative lifetime $\tau_{nr} = 5$ ns as obtained from pump-probe measurements, the excitation energy $E_{ph} = 2.33$ eV (i.e. 532 nm) and the layer thickness $d = 1.0$ µm, we obtain $N_{tot} = 2 \times 10^{18}$ cm^{-3}. At 300 K and 3.6% strain, $x_\Gamma \sim 0.5\%$ of the total carrier density populates the Γ states. The radiative recombination time τ_r is extracted from the modelled spontaneous emission rate in [63]. There, R_{sp} is calculated for biaxially strained Ge close to a fundamental direct band gap at $N_{tot} = 1{\times}10^{18}$ cm^{-3}, from which a radiative recombination time $\tau_r \sim 2$ ns is deduced. With the volume of the constriction $V_c = 6.0$ µm $\times$ 0.5 µm $\times$ 1.0 µm, this leads to a radiative emission rate of

$$R_{sp} = \frac{N_{tot}\,x_\Gamma\,V_c}{\tau_r} = 1.5 \times 10^{13}\ \mathrm{s}^{-1}. \tag{3.11}$$

The emission from the Ge layer is only partially collected by the Schwarzschild objective. The collection angle is determined by the numerical aperture $NA = 0.4$ as $\alpha_{NA} = \arcsin(NA) = 23.5°$. The angle α_{INT}, which corresponds to the internal angle of acceptance, is calculated from Snell's law via $n_{Ge} \times \sin(\alpha_{Ge}) = n_{Air} \times \sin(\alpha_{Air})$. With $\alpha_{Air} = \alpha_{NA}$ and the refractive indices $n_{Ge} = 4$ and $n_{Air} = 1$, we obtain $\alpha_{INT} = 5.7°$. For a spatially isotropic emission, the ratio of photons collected by the Schwarzschild optics η_{col} can be calculated by integration over the solid angle Ω_{INT} as

$$\eta_{col} = \frac{\Omega_{INT}}{\Omega_{tot}} = \frac{2\pi\,(1-\cos(\alpha_{INT}))}{4\pi} = 2.5 \times 10^{-3}, \tag{3.12}$$

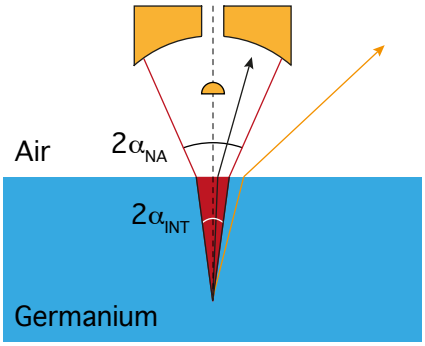

Figure 3.28: Illustration of the collection efficiency for PL measurements. The acceptance angle of the Schwarzschild objective amounts to $\alpha_{NA} = 23.5°$, which translates into an internal angle of $\alpha_{INT} = 5.7°$. Only photons emitted in the Ge layer under an angle $\alpha < \alpha_{INT}$ are detected by the objective (black path).

where Ω_{tot} is the full solid angle.

To determine the transmission efficiency through the microfocus setup η_{MF}, the detector photocurrent is calibrated using a black body emitter of known temperature and emission area. The thus obtained efficiency is found as $\eta_{MF} = 2.75 \times 10^{-2}$.

The expected photocurrent I_{th} is then calculated as

$$I_{th} = e\, R_{sp}\, \eta_{col}\, \eta_{MF} = 1.6 \times 10^{-10}\ \mathrm{A}, \tag{3.13}$$

where e is the elemental charge. Strikingly, the estimated photocurrent is $> 30\times$ larger than the measured photocurrent I_{exp}. The observation suggests that either the electron density at Γ seems to be smaller than assumed in the quasi-equilibrium estimation, or the recombination time τ_r seems to be much longer than estimated.

A possible explanation attributes the reduced electron density at Γ to a bottleneck for intervalley electron scattering from Γ into L as schematically illustrated in Fig. 3.29. In the PL measurements, the electrons are optically injected far above the band gap. After the generation, a fast phonon-assisted thermalization distributes the electrons into the conduction band minima. These processes are described by the intravalley scattering time τ_{Intra} for relaxation within the Γ valley and the intervalley scattering time τ_{Inter} for relaxation into the L states. Due to the significantly larger density of states, the scattering process into the L valleys is dominant. After the thermalization, the electrons either recombine radiatively or non-radiatively on time scales τ^{Γ}_{rec} and τ^{L}_{rec}, or they are scattered between the conduction band minima described by $\tau_{\Gamma L}$ and $\tau_{L\Gamma}$.

During the thermalization, virtually all electrons scatter into the L-valley due to the large density of states, such that the scattering time $\tau_{L\Gamma}$ is crucial for the steady-state carrier

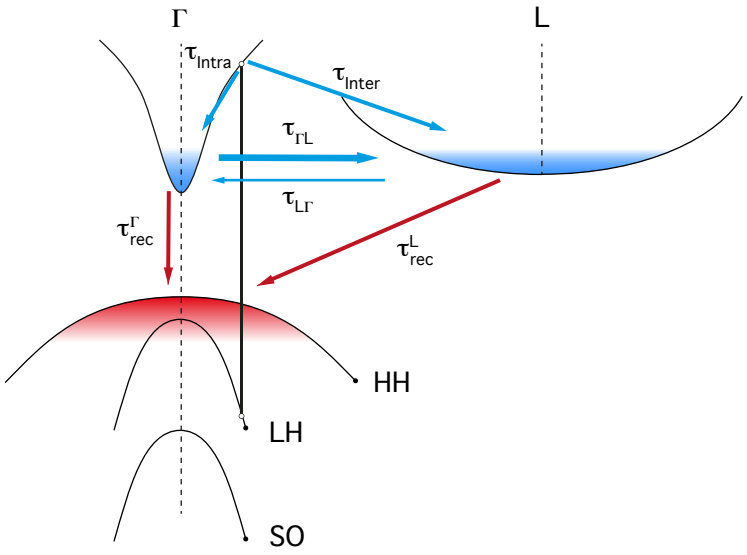

Figure 3.29: Illustration of electron scattering processes in direct band gap Ge after generation far above the band gap. The steady-state density in the Γ valley is determined by several intra- and intervalley scattering processes within the conduction band (blue arrows) and interband recombinations (red arrows).

density at Γ. To calculate the electron populations N_Γ and N_L at the Γ and L-valley minima, the following coupled rate equations need to be solved:

$$\frac{dN_\Gamma}{dt} = \frac{G}{\tau_{Intra}} - \left(\frac{1}{\tau_{\Gamma L}} + \frac{1}{\tau^\Gamma_{rec}}\right) N_\Gamma + \frac{1}{\tau_{L\Gamma}} N_L, \tag{3.14}$$

$$\frac{dN_L}{dt} = \frac{G}{\tau_{Inter}} - \left(\frac{1}{\tau_{L\Gamma}} + \frac{1}{\tau^L_{rec}}\right) N_L + \frac{1}{\tau_{\Gamma L}} N_\Gamma, \tag{3.15}$$

where G is the generation rate. Unfortunately, only two of those time constants have so far been experimentally determined: $\tau^L_{rec} = 5$ ns (see chapter 4.5) and $\tau_{Inter} \sim 0.2$ ps - 1.0 ps [175, 176]. According to theoretical modelling of intervalley scattering times [177], the scattering time $\tau_{L\Gamma}$ for transitions into Γ is expected to be ∼ 2-3 orders of magnitude larger than $\tau_{\Gamma L}$. A scattering time $\tau_{L\Gamma}$ in the ns range and longer would contribute to a reduced electron density at Γ compared to the quasi-equilibrium approximation. However, experiments are needed to prove this speculation.

Besides time-resolved pump-probe measurements with a time-resolution in the fs - ps range, where the scattering processes can directly be observed, PL measurements at resonant excitation might give an insight about the hypothesis of slow L→ Γ scattering rates. When the charge carriers are resonantly excited directly into the Γ minimum, the PL efficiency should be significantly enhanced.

3.7 Summary

In this chapter, we described our technique to redistribute a small biaxial tensile strain to yield a high, uniaxial tensile stress by geometrical patterning. The changes on the electronic band structure were investigated by room temperature photoluminescence spectroscopy, where a red shift in emission energy and an increase in emission intensity was demonstrated for the first time at such high strain values. Moreover, we showed an efficient drain of carriers generated in the outer, relaxed Ge regions into the center of the strained constriction.

Microbridges processed on GeSOI or GeOI substrates were compared to exemplify the superior properties of GeOI concerning yield strength and strain homogeneity. Using the high-quality GeOI platform, room-temperature strain values up to 3.6% corresponding to a Raman shift of -6.7 cm^{-1} were achieved.

By measuring the emission from strained GeOI microbridges in function of temperature, cooling below 300 K led to a further increase in tensile strain due to the difference in thermal expansion coefficients up to a maximum strain of 5.4%, which is the largest [100] strain obtained to date. On the other hand, lower temperatures induce a thermalization of electrons into the lowest conduction band valleys, which enables to distinguish between a direct or indirect conduction band alignment. Due to a strong direct gap emission at low temperature and at low excitation densities, GeOI bridges with a longitudinal strain of 4.5% or more could be identified as elemental Ge with a fundamental direct band gap. Therefore, the transition towards direct band gap Ge could be experimentally determined to occur between 4.0% and 4.5% [100] strain, which is slightly more favorable than widely anticipated.

Direct band gap Ge microbridge structures were processed including a cavity design based on reflectors via etched Ge/air facets. The signature of the cavity was observed by a strong modulation of the PL emission signal, featuring cavity modes with Q-factors > 530. Under continuous-wave excitation, no indication of lasing was observed.

An investigation of the quantitative emission intensity of strained GeOI microbridges revealed that the measured signal is $\sim 30\times$ weaker than anticipated. Possibly, L$\rightarrow\Gamma$ scattering rates are too slow to populate the conduction band minima as described by the quasi-equilibrium approximation.

3.8 Compendium

Here, we developed the key ingredients to realize a laser, which includes the fabrication of the gain material (in this case direct band gap Ge) and the cornercube optical cavity. Using the high-quality GeOI substrates, strain values exceeding 5.0% were reached at low temperatures,

which surpasses the experimentally determined crossover towards fundamentally direct band gap Ge. Such direct band gap Ge bridges were combined with an optical microcavity without a relaxation of the strain.

A setback was experienced which could pose a serious challenge to achieve optically pumped lasing in particular for non-resonant excitation conditions. At low temperature, the decrease in PL emission intensity upon cooling of direct gap microbridges raises the question about the efficiency of electron intervalley scattering into the Γ valley. A similar mechanism would explain the unexpectedly low emission efficiency for strained Ge. The electron transfer from the L states into the Γ valley will be discussed again in chapter 5.5.2 when the gain evolution in direct band gap GeSn is analyzed.

4

Charge Carrier Lifetimes in Ge Layers and Microbridges on Si

Contents

This chapter is devoted to investigations concerning the material quality of Ge epilayers in terms of their carrier decay time. After a short discussion on the importance of the non-radiative lifetime for the efficiency of Ge-based light emitters, a method for the extraction of the excess carrier decay time via pump-probe transmission experiments is presented together with the underlying theoretical aspects. Thereafter, differently prepared Ge layers directly deposited on Si as well as high-quality GeOI substrates are examined in terms of the carrier decay times. Furthermore, the technique is applied to extract the carrier lifetimes in strained microbridges on GeSOI and GeOI.

Parts of this chapter were published in a similar form as:

R. Geiger *et al.*, Excess carrier lifetimes in Ge layers on Si. *Applied Physics Letters* **104(6)**, 062106 (2014).

4.1 Impact of Non-Radiative Lifetime on Γ-Valley Population

In chapter 3, the effect of uniaxial stress on the electronic band structure of Ge was shown to considerably improve the optical emission properties: With an increase in strain, the conduction band offset between the Γ- and L-valleys decreases such that the carrier concentration in the Γ states rises and, hence, the radiative recombination rate increases. From the comparison between strained structures either made from Ge on SOI or from GeOI, where GeOI features a significantly reduced dislocation density, it is apparent that the improvement in material quality is directly correlated to the yield stress [178] and, therefore, leads to larger achieved strain levels for GeOI with up to 5.4% corresponding to a Raman shift of 9.9 cm^{-1}.

However, a starting material of high quality is not only important with respect to mechanical stability, but also concerning its optical properties. As a measure for the optical quality of a material, the non-radiative decay time of excess charge carriers τ_{nr} serves as an important indicator, because this time directly relates to the steady-state carrier density and, hence, to the carriers at the Γ states. As an illustration of this relation, the electron population of the Γ valley is calculated in dependence of τ_{nr} in Fig. 4.1.

As a test case, uniaxially stressed Ge with a longitudinal strain of 4.0% is examined, where the band edges and effectives masses are taken from the calculations in chapter 2. The total carrier density N_{tot} is computed for a constant generation rate $G = 5{\times}10^{26}$ cm^{-3} s^{-1}, which corresponds to optical pumping of a micron-thick Ge layer with 5 mW power at 532 nm excitation wavelength on a 5 µm spot, i.e. 25 kW/cm^2. As the Ge is still fundamentally indirect and, therefore, has the majority of electrons residing in the indirect L-valleys, the steady-state carrier density N_{tot} is determined by the non-radiative decay time τ_{nr} associated e.g. to Shockley-Read-Hall-type (SRH) recombinations and Auger-recombinations with a corresponding decay time $\tau_{Auger} = \left(\gamma N_{tot}^2\right)^{-1}$, where γ is the Auger recombination coefficient. The total carrier density follows when solving equation (4.1) for N_{tot}.

$$N_{tot} = G \times \tau_{eff} = G \times \left(\frac{1}{\tau_{nr}} + \frac{1}{\tau_{Auger}}\right)^{-1} = G \times \left(\frac{1}{\tau_{nr}} + \gamma N_{tot}^2\right)^{-1}. \tag{4.1}$$

The steady-state carrier density in the Γ valley is shown in Fig. 4.1 in function of the non-radiative decay time τ_{nr} for an Auger coefficient, which was experimentally determined as

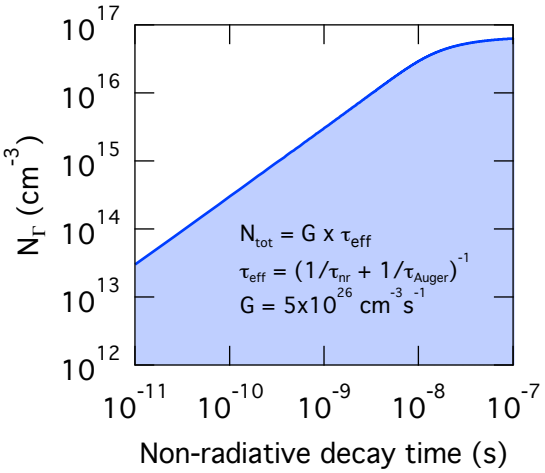

Figure 4.1: Influence of the non-radiative charge carrier decay time τ_{nr} on the electron population at the Γ valley. The simulation is done for Ge under 4.0% longitudinal strain and a constant carrier generation rate G = $5{\times}10^{26}$ $cm^{-3}s^{-1}$.

$\gamma = 5.0 \times 10^{-31}$ cm^6s^{-1} (see chapter 4.4). As long as the total carrier density is not limited by Auger recombinations, there is a linear increase in electrons populating the Γ valley. This means, that an increase in τ_{nr} by 10× leads to an increase in N_Γ by 10×, which is equivalent to an increase in tensile strain by 2.0% (see chapter 2.1).

With this simple model, it is demonstrative that not only the conduction band offset, but also the non-radiative lifetime is an important parameter in determining the optical properties of strained Ge light emitters and is most significant for the modelling of lasing threshold densities. The next chapter delivers the first systematic investigation of non-radiative carrier lifetimes in Ge layers on Si as well as for strained Ge microbridges.

4.2 Synchrotron-Setup for Infrared Pump-Probe Spectroscopy

In the 1950s, the carrier lifetime in Ge was thoroughly investigated. In general, mostly electrical techniques were applied to understand the lifetime-dependence on parameters such as e.g. temperature, doping-density or dopant material [179–182]. In that time, the subject of examination was always bulk Ge. Later, new techniques emerged to extract the decay time including photoconductivity or microwave reflection measurements, where especially surface treatments of bulk Ge was of great scientific interest [183–187]. However, due to the interest in the use of Ge devices in CMOS technology, the focus of research has shifted from bulk Ge to Ge layers epitaxially grown directly on Si. In contrast to bulk Ge, Ge epilayers on Si feature a highly defective interface if the film is thick enough for plastic strain relaxation to set in [188]. Therefore, it is necessary to provide new experiments to determine the lifetime

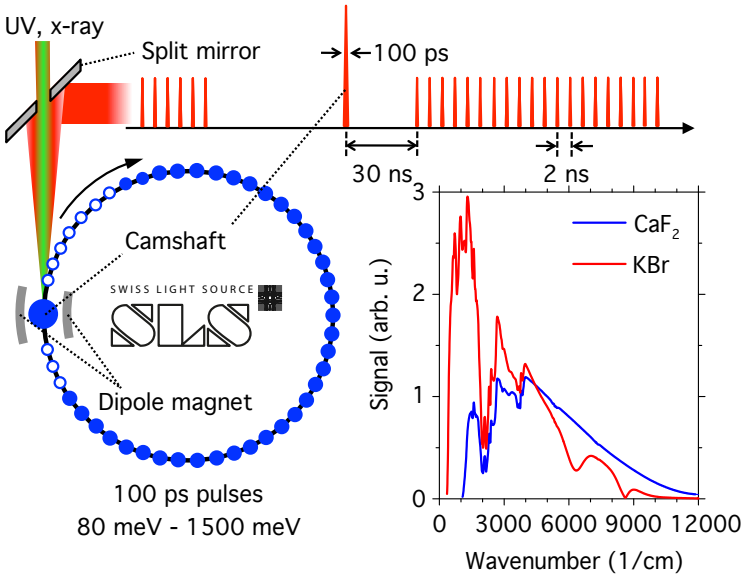

Figure 4.2: Schematics of synchrotron-based generation of 100 ps short, broadband infrared pulses (adapted from [197]).

for epitaxial Ge layers.

Only recently, the investigation of Ge epilayers has gained more attention. Reports of carrier lifetimes have been provided by means of photocurrent measurements [189, 190], time-resolved photoluminescence spectroscopy [191–194], microwave reflection [195] or laser-based pump-probe transmission measurements [196] with a clear focus on the effect of the dislocation density.

In the following, an experimental approach is presented based on broadband pump-probe transmission measurements, where the carrier decay time is extracted by measuring the carrier-induced refractive index dynamics. The spectroscopy is performed at the X01DC infrared beamline at the Swiss Light Source synchrotron (SLS) at the Paul Scherrer Institute [197]. A schematic representation of the infrared-generation is shown in Fig. 4.2. In a storage ring, electrons are propagating along their circular path in discrete bunches. Each time the electrons are deflected from their route and, hence, accelerated in a certain direction, they emit a broadband radiation, from which the low energy part is filtered by a split mirror. The obtained spectral range covers energies from approximately 80 meV up to 1500 meV, i.e. from the visible spectrum up to 15 µm. Due to the electrons orbiting in discrete bunches, pulsed radiation is provided, which offers the possibility for time-resolved measurements with 100 ps resolution [197, 198].

The synchrotron radiation is transported to a microfocus setup via reflective optics, where a 15× Schwarzschild-type reflective objective focuses the light onto the sample surface to a spot size below 25 µm. Subsequently, an identical objective focuses the collected transmission

onto a fast InSb detector with a detection area of 100 µm. To generate charge carriers, the sample is optically excited over a spot size of approx. 35 µm with 100 ps long pulses at 1064 nm from a 1 kHz Nd:YAG laser. An electronic delay is used to vary the time between the monochromatic pump and the broadband synchrotron probe. With its 100 ps time resolution, the system is especially well suited to measure electron dynamics [62, 66, 199], where the broadband probe of high brillance offers the investigation of processes in semiconductors occuring above and below band gap at the same time. For more details on the synchrotron setup, the reader may refer to ref. [198].

4.3 Modelling of Broadband Transmission under Optical Excitation

In chapter 3.3.2, the reflection of a GeSOI layer is calculated for a broad spectral range using the transfer-matrix-method. The obtained spectrum is strongly dependent on the refractive indices of the layer stack. When Ge is optically excited to generate a charge carrier density N_c, the excess charge carriers change the refractive index of the layer as $\Delta n_r \propto -N_c/E^2$ [200, 201]. For a transmission through a Ge epilayer, this means that the distinct Fabry-Perot pattern shifts with a linear dependence on the carrier density, which makes the dynamics of the refractive index a convenient tool to extract the time-dependent charge carrier density using the above introduced synchrotron-based pump-probe setup.

To establish a relation for the conversion of the observed peak-shift between pumped and unpumped transmission to a charge carrier density, the transmission is modelled under inclusion of the free carrier influence on the refractive index via the Drude model [201]. Therefore, the real part of the refractive index n_r is parametrized using an empirical description, which was determined for Ge in dependence of temperature and wavelength [202] including the carrier plasma contribution [95, 203] as

$$n_r(\lambda, T) = \sqrt{\varepsilon(N_c, \lambda) + \frac{L(T)}{\lambda^2}\left(2.5381 + 1.8260 \times 10^{-3}\, T + 2.8888 \times 10^{-6}\, T^2\right)} \tag{4.2}$$

$$\begin{aligned} L(T) = \exp\{-3\,[&5.790 \times 10^{-6}(T-293) + 1.768 \times 10^{-9}(T-293)^2 \\ &- 4.562 \times 10^{-13}(T-291)^3]\} \end{aligned} \tag{4.3}$$

$$\begin{aligned} \varepsilon(N_c, \lambda) &= \varepsilon_\infty\left(1 - \frac{\omega_p^2}{\omega^2}\right) = \varepsilon_\infty\left(1 - \frac{N_c e^2}{\varepsilon_0 m^* \omega^2}\right) \\ &\text{with } \omega = \frac{2\pi c}{\lambda} \text{ and } \omega_p^2 = \frac{N_c e^2}{\varepsilon_0 m^*}. \end{aligned} \tag{4.4}$$

Here, λ is the wavelength in µm, T is the temperature in K, c the vacuum speed of light,

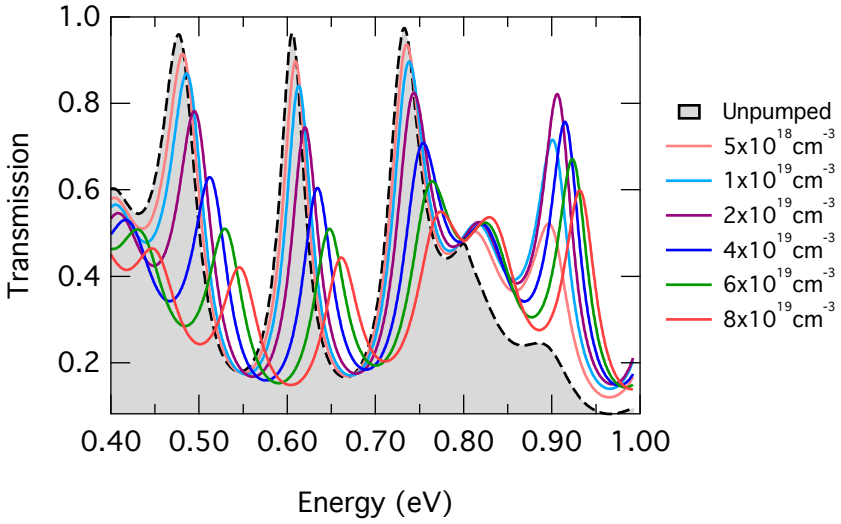

Figure 4.3: Modelled transmission through GeOI layer stack for charge carrier densities between $5{\times}10^{18}$ cm^{-3} and $8{\times}10^{19}$ cm^{-3}. The change in refractive index due to an increased charge carrier density leads to a shift of the Fabry-Perot oscillations towards higher energies. The change in absorption due to injected charge carriers (i.e. intervalence band absorption, free carrier absorption, interband absorption and interband gain) from chapter 2.3.4 have been included.

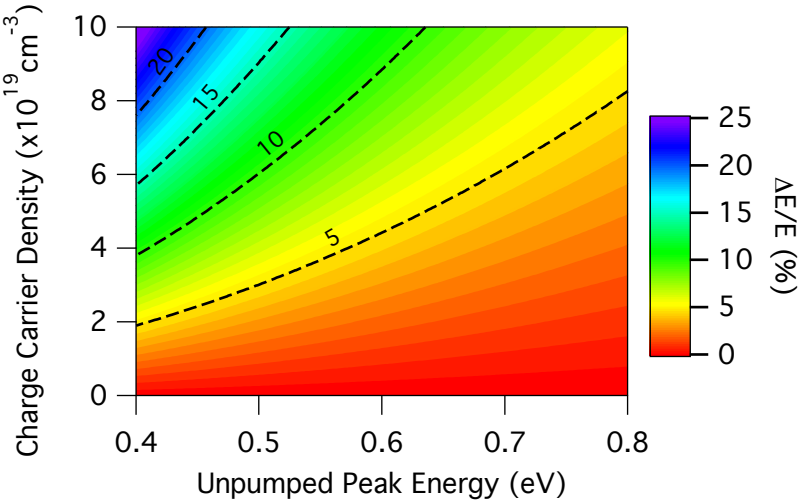

Figure 4.4: Relative peak shift $\Delta E/E$ in dependence of peak energy E and injected charge carrier density N_c following the phenomenologically determined dependence $\Delta E/E = \frac{4.3182{\times}10^{-22}}{E(\mathrm{eV})^2} \times N_c \ \left(\mathrm{cm}^{-3}\right)$.

ε_0 and ε_∞ the vacuum and high frequency permittivity, respectively, and m^* the effective mass. The plasma resonance ω_p is well below 0.35 eV for carrier densities up to 10^{20} cm^{-3} such that the high-frequency approximation $\omega^2 \gg \omega_p^2$ is used for the dielectric function [204]. The plasma mass is taken as 0.08 m_0, obtained from the reduced mass of L-valley effective mass of conductivity and the hole mass for an equilibrium filling of heavy hole- and light hole states [62]. Due to the smaller mass for electrons in the Γ valley compared to the L-valley mass, the described effects are stronger once the tensile strain is sufficiently high to distribute a significant amount of electrons into the Γ conduction band states.

In Fig. 4.3, the model is used to calculate the transmission through a GeOI substrate with a 1 µm Ge layer on a micron thick buried oxide for carrier densities ranging up to 8×10^{19} cm^{-3}. The absorption α due to intraband-, interband- and intervalence band transitions from chapter 2.3.4 is taken into account by introducing the imaginary part κ of the refractive index, which is related to the absorption as $\alpha = 4\pi\kappa/\lambda$ [95], where λ is the wavelength in vacuum. The influence of κ on the real part of the refractive index as determined by the Kramers-Kronig relations [204] is neglected. The shift of the distinct oscillation maxima can nicely be seen, with stronger effects for a larger carrier density and smaller photon energies.

From Fig. 4.3, the relative peak shifts $\Delta E/E$ are phenomenologically extracted in dependence of the injected charge carrier density N_c yielding the conversion

$$\Delta E/E = \frac{4.3182 \times 10^{-22}}{E\,(\mathrm{eV})^2} \times N_c \left(\mathrm{cm}^{-3}\right), \tag{4.5}$$

which is shown as contour plot in Fig. 4.4, with E being the unpumped peak energy in eV, ΔE the shift between pumped- and unpumped peak energy in eV, and N_c the charge carrier density in cm^{-3}, respectively. In the following, equation (4.5) will be used to translate experimentally obtained peak shifts to an absolute charge carrier density.
In contrast to a previous approach, where the charge carrier density was extracted from the minimum in mid-infrared reflection at the plasma frequency ω_p [62], the dependence on carrier density N_c is linear for the near-infrared transmission instead of following a square root law, such that a higher sensitivity for the detection of small carrier densities is achieved.

4.4 Comparison of Differently Prepared Ge Layers on Si

For bulk Ge, the charge carrier lifetimes are well known and can reach the order of hundreds of microseconds [186]. However, with the highly defective Ge/Si interface, high-temperature annealing cycles to reach a biaxial tensile strain, or n-type doping to improve the radiative recombination rate, the properties of technologically interesting Ge layers might differ significantly from the results obtained for bulk Ge. Therefore, in the following the carrier

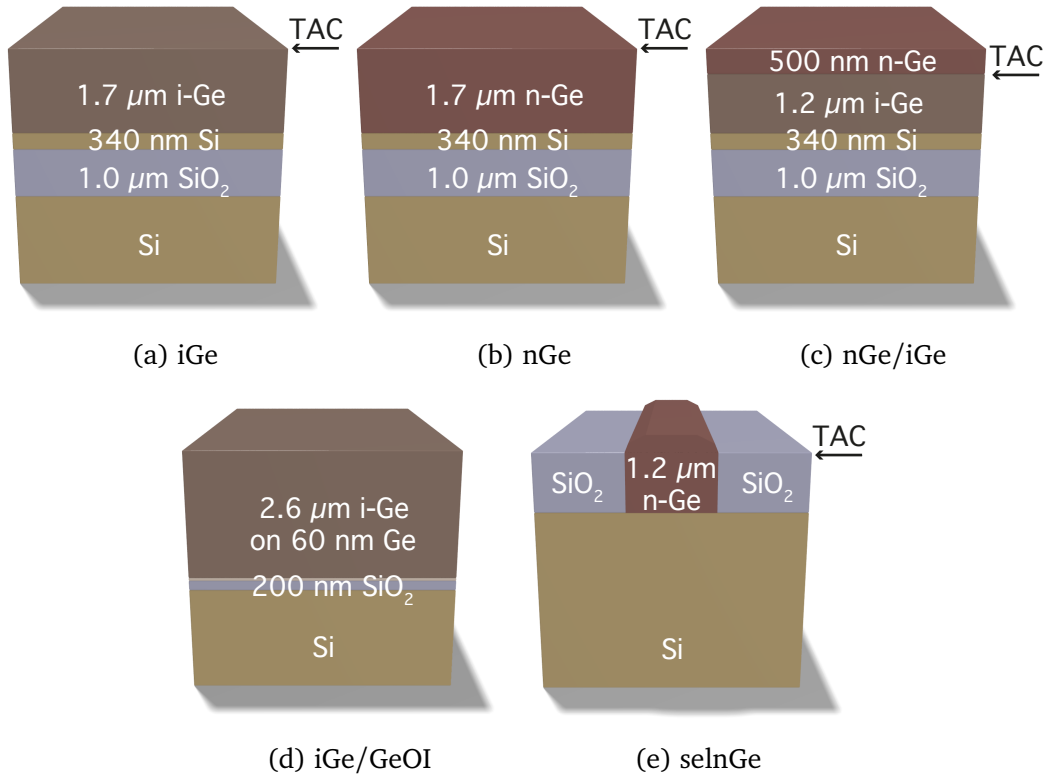

(a) iGe (b) nGe (c) nGe/iGe

(d) iGe/GeOI (e) selnGe

Figure 4.5: Schematic cross-sectional profiles of investigated layer stacks and indication, if and at which point thermal annealing cycling (TAC) was performed.

lifetime is extracted for differently prepared Ge epilayers via the previously introduced pump-probe transmission spectroscopy.

The cross-sectional profiles of the investigated samples are schematically shown in Fig. 4.5. Samples iGe, nGe and nGe/iGe feature 1.7 µm of Ge grown by LEPECVD on SOI at L-NESS laboratory in Como [151] with no intentional doping (iGe), in-situ phosphorus doping at a nominal concentration of $N_D = 1{\times}10^{19}$ cm^{-3} over the full layer thickness (nGe), or 500 nm n-doped Ge at the same doping concentration on 1.2 µm intrinsic Ge (nGe/iGe). After growth (iGe and nGe) or after the growth of the intrinsic layer (nGe/iGe), in-situ thermal annealing cycles (TAC) are performed to reduce the threading dislocation density (TDD). The TACs typically consist of 6 cycles between 600°C and 800°C with 150 s and 120 s to ramp up and ramp down the temperature, respectively, after which the TDD is reduced by approximately two orders of magnitude to $\sim 10^7$ cm^{-2} as verified by defect etching [205].

Furthermore, sample iGe/GeOI features a 2.6 µm layer of Ge deposited by LEPECVD on a commercial germanium-on-insulator substrate (IQE Silicon Compounds Ltd.) with a 60 nm Ge device layer on 200 nm buried oxide, while sample selnGe is a 1.2 µm Ge layer from MIT (Boston, USA) which is selectively grown between SiO_2 trenches via ultra-high vacuum chemical vapor deposition (UHVCVD) with an in-situ phosphorus doping of

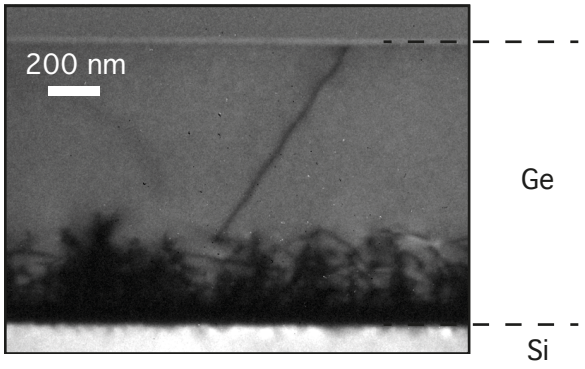

Figure 4.6: Transmission electron micrograph of the interface of a Ge layer grown on Si. Due to the large lattice mismatch between Ge and Si, the interface is highly defective. The imaging was performed by Martin J. Süess at ETH Zürich.

$N_D = 8 \times 10^{18}$ cm^{-3} [206] followed by TAC.

Despite the TAC, which leads to annihilation of threading dislocations, the typically performed two-step growth of Ge on Si (with a low temperature step to accommodate the large lattice mismatch by plastic relaxation, followed by high-temperature deposition of Ge resulting in a layer of high crystallinity), the interface between Ge and Si remains with a vast amount of defects. In Fig. 4.6, a transmission electron micrograph taken from Martin J. Süess at ETH Zürich shows the Ge/Si interface of sample iGe, where a region of $\sim$ 300 nm from the interface is containing the major density of dislocations.

In Fig. 4.7(a), the transmission through sample iGe is shown at an excitation density of 30 MW/cm^2 before (filled, grey area) and after excitation (solid lines) for delay times between pump and probe pulse up to 5.0 ns. Due to the strong contrast in refractive index, distinct Fabry-Perot (FP) oscillations modulate the signal with a shift in peak energy dependent on the carrier density as discussed in chapter 4.3. The numbers in the graph indicate the order i of the FP peaks. To illustrate the free carrier-like dispersion of the refractive index, the relative peak shifts $\Delta E/E$ are plotted over $1/n_r^2E^2$ in Fig. 4.7(b). A linear relation is obtained with the slope being larger for shorter times, i.e. for larger carrier densities, which is as expected by theory. For a larger delay time, the decrease in carrier density is inferred by the decrease in slope, validating that the carrier decay is probed. In contrast, heating of the sample would increase the refractive index (see equation (4.2)) and not show the $1/E^2$-dependence.

Due to the broadband coverage of the synchrotron infrared radiation, the injection-dependent transmission can be examined for energies above to far below the direct band gap. Near and above the direct gap energy of $\sim$ 0.8 eV, bleaching is observed. Below the band gap, the transmission is drastically decreased due to valence interband absorption and, to a

smaller extent, free carrier absorption [62]. These parasitic processes prevent any net gain and optical amplification to set in. This observation holds true for all investigated samples at all excitation densities and supports the previous observation that Ge with such a low strain and an n-doping level up to 2.5×10^{19} cm^{-3} does by far show no net gain [62]. In the meanwhile, this observation has been confirmed by other work with even higher strain ($\varepsilon_{[100]} > 2.3\%$) [145].

To quantitatively specify the observed intervalence band absorption, the Drude model introduced before is fitted to the spectrum at maximum overlap between pump and probe pulse (i.e. $\Delta t = 0$), which means at the maximum carrier density. Therefore, the layer thicknesses as well as the charge carrier density serve as fitting parameters. Additionally, the intervalence band absorption α_{IVB} is introduced via the imaginary part of the refractive index κ as $\alpha_{IVB} = 4\pi\kappa/\lambda$. As above, the absorption is not included in the real part of the refractive index via the Kramers-Kronig relations. For the assumption of the intervalence band absorption being linearly dependent on energy [62], a very satisfactory agreement can be found for a carrier density of $N_c = 5.5 \times 10^{19}$ cm^{-3} and an absorption coefficient of 2610 cm^{-1} at 0.8 eV. This absorption coefficient is in good agreement with the electron- and hole absorption cross-sections of 4×10^{-18} cm^{-2} and 4×10^{-17} cm^{-2} from Carroll *et al.* [62], which yield $\alpha_{IVB} = 2420$ cm^{-1} at the aforementioned carrier density. Due to the neglection of optical bleaching and refractive index changes due to gain [200], the good agreement between model and experiment is limited to the sub-band gap part of the spectrum.

With the excitation wavelength at 1064 nm, the 1/e penetration depth amounts to 1.15 µm [82], such that the investigated Ge layers are not pumped over the full thickness. Nevertheless, a homogeneous distribution of charge carriers for the typically less than 2 µm thick layers can be assumed, as with a diffusion coefficient of $D = 103$ cm^2/s [207], an electron can diffuse over a length of 1 µm in less than 100 ps, which is below the time resolution of the pump-probe setup. Bleaching of the Ge layer further increases the penetration depth.

The investigated Ge layers feature only a small, thermally induced biaxial tensile strain of less than 0.2%. Due to the given conduction band alignment, >99% of the electrons are residing in the L-valleys (see chapter 2.2). From the L-states, radiative recombinations with holes at the Γ Brilluoin zone center need an additional phonon for momentum conservation, which leads to long radiative lifetimes for this type of three particle process. Virgilio *et al.* calculated the radiative lifetime for the L-states to be of the order of ∼ 1 ms, 6 orders of magnitude longer than for the Γ states, which feature a radiative lifetime of the order of nanoseconds [63]. The experimentally determined lifetime τ_{exp} depends on the electron

population as

$$\tau_{exp} = \left(\frac{N_\Gamma}{\tau_\Gamma} + \frac{N_L}{\tau_L}\right)^{-1} = \left(\frac{N_\Gamma}{\tau_r} + \frac{N_L}{\tau_{nr}}\right)^{-1}. \tag{4.6}$$

As the recombination from the L-valleys is determined by non-radiative recombination, the experiments yield the non-radiative decay time τ_{nr}. Due to the small population of the Γ

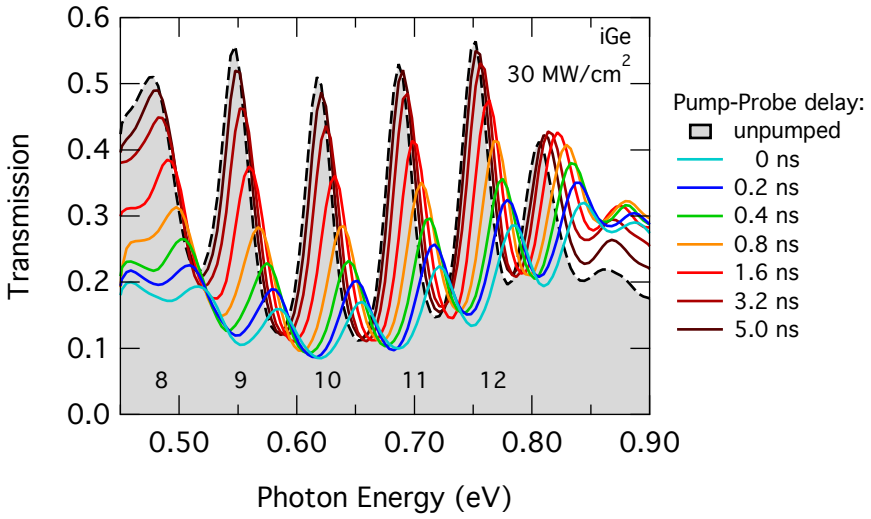

(a) Broadband transmission spectra through sample iGeSOI at an excitation density of 30 MW/cm^2. Owing to the refractive index-modulation in dependence of the excess carrier density, the oscillations shift in energy.

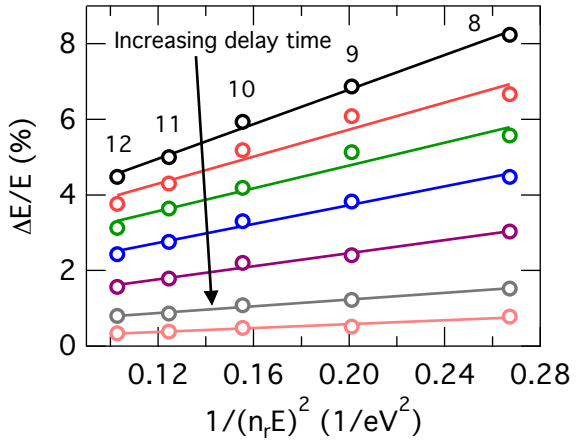

(b) Validation of the free carrier-like dispersion of the refractive index.

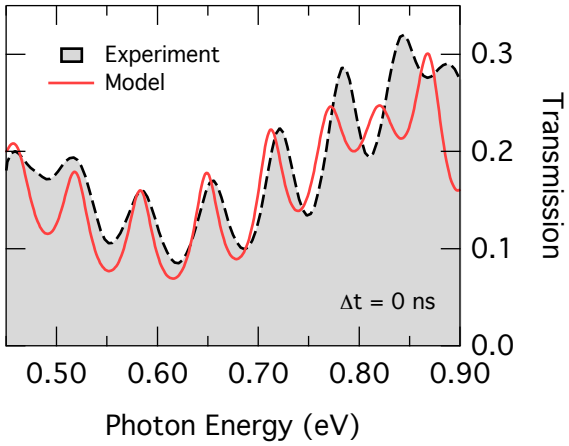

(c) Transmission for $\Delta t = 0$ and model taking into account the change in refractive index and parasitic absorption from a phenomenological model (see text).

Figure 4.7: Infrared pump-probe transmission spectra for sample iGeSOI.

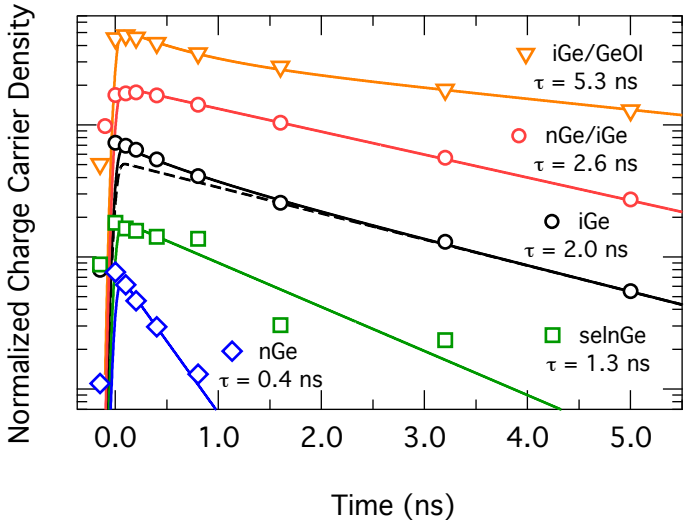

Figure 4.8: Charge carrier densities normalized to unity at $t = 0$ for differently prepared Ge layers on Si. The spectra have been offset for clariy.

states, no information on the radiative lifetime τ_r can be extracted, which determines the decay from the Γ states when $\tau_{nr} > \tau_r$.

The peak shifts in dependence of time are plotted for all investigated layers in Fig. 4.8. For clarity, the spectra are normalized to unity at $t = 0$ and offset with respect to each other. The corresponding decay times are determined by a fit $G(t)$ to the data which takes into account the $2\sigma = 100$ ps pump pulse as well as one or two exponential decays with time constant τ_i as

$$G(t) = \int_{-\infty}^{\infty} \mathrm{d}T \left[A \times \Theta(t-T) \times \exp\left\{-\frac{T^2}{\sigma^2}\right\} \times \left(\sum_{i=1}^{1,2} \exp\left\{-\frac{t-T}{\tau_i}\right\} \right) \right]. \tag{4.7}$$

Here, A is a scaling factor to account for the intensity of the excitation, and Θ is the Heaviside step function. The obtained decay times are given in Fig. 4.8.

For sample iGe, a decay time of 2.0 ns is found. However, a single exponential decay does not yield a satisfactory agreement with the data (black, broken line) due to a second, fast decay with a time constant of 600 ps. This fast decay is only seen for high excitation densities and is, therefore, attributed to Auger recombination. In Fig. 4.9, the time-dependent carrier densities for sample iGe are plotted for two different excitation densities. The data is used to extract the lifetime τ and the Auger recombination coefficient γ by solving

$$N_c(t) = N_0 \left(\exp\left\{-\frac{t}{\tau_{Auger}}\right\} + \exp\left\{-\frac{t}{\tau}\right\} \right) = N_0 \left(\exp\left\{-t\gamma N_c^2(t)\right\} + \exp\left\{-\frac{t}{\tau}\right\} \right). \tag{4.8}$$

Both decays are well described by an Auger recombination coefficient of 5.0×10^{-31} cm^6/s, which is a factor of 2 to 3 larger compared to literature values obtained under low excitation

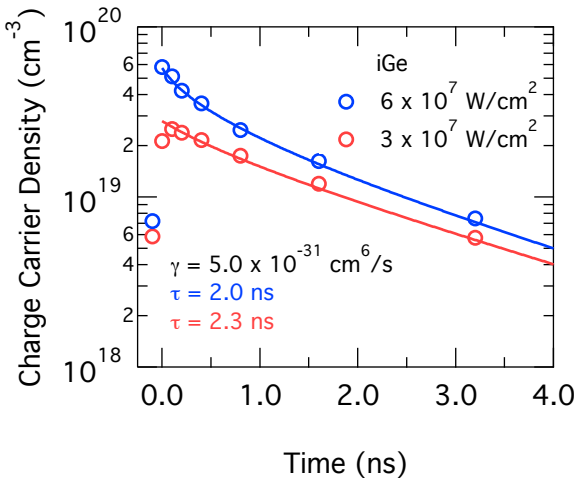

Figure 4.9: Carrier decay time for sample iGe under two different excitation densities. For the higher excitation density, a fast decay can be seen for high carrier densities, which does not occur for the lower excitation. The fast decay is ascribed to Auger recombination and can be nicely fit with an Auger recombination rate of 5.0×10^{-31} cm^6/s.

[208], but approximately one order of magnitude lower than the Auger recombination rate obtained under carrier saturation condition [62]. For the latter method, processes higher than second order might play a role, which could explain the deviation. Furthermore, the non-radiative lifetime is not largely affected by the intensity of excitation considering the experimental time resolution of 0.1 ns.

Coming back to Fig. 4.8, a short decay of only 400 ps is found for sample nGe, which also holds true for long delay times where the carrier density is too low for three-particle processes like Auger recombination to play a significant role. Furthermore, TEM analysis and etch pit density counting reveal a TDD of $\sim 3\times10^{-7}$ cm^{-2} similar to sample iGe, such that an increase in dislocation density cannot explain the deviation in decay time. However, atom probe tomography performed by Martin J. Süess at ETH Zürich shows that the average density of phosphorus dopant atoms (P) of 2.7×10^{19} cm^{-3} is exceeded in several zones by two orders of magnitude (see Fig. 4.10). These enriched zones seem to preferentially form along threading dislocations, as they are predominantly found when the volume below an etch pit is probed. The rapid decay of sample nGe is, hence, ascribed to the aggregation of P atoms during the annealing, as the solubility limit of phosphorus might be exceeded especially in the region close to the surface [209].

For sample selnGe, the rapid decay is not observed even though it went through similar annealing cycles. Instead, the decay is described by a time constant of 1.3 ns. The improved behavior is ascribed to a lower dopant density of 8×10^{18} cm^{-3}, which might be low enough to prevent dopant aggregation.

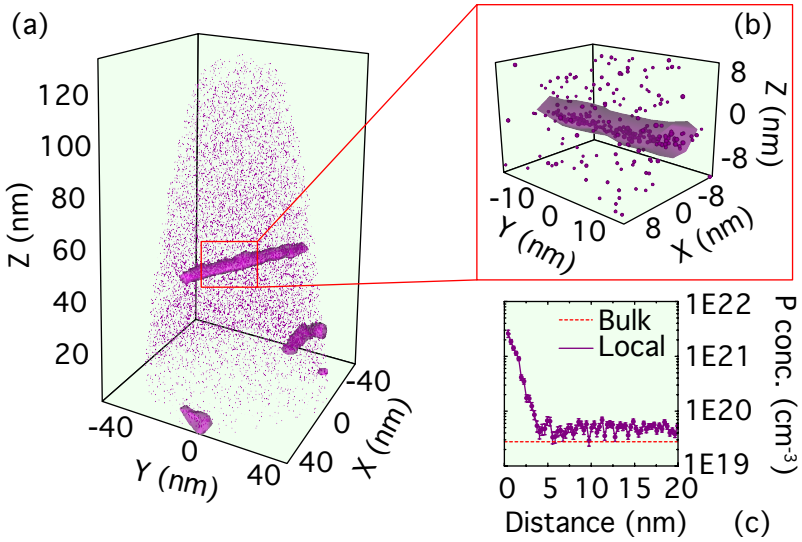

Figure 4.10: Atom probe tomography (ATP) reconstruction of sample nGe. To highlight the accumulation of P atoms, iso-concentration surfaces are displayed at 2×10^{20} cm^{-3}. The doping enrichment seems to occur along a dislocation line. Compared to the bulk doping level (2.7×10^{19} cm^{-3}), a concentration difference of two orders of magnitudes is found for the accumulation center (2.5×10^{21} cm^{-3}). The ATP was performed by Martin J. Süess.

Sample nGe/iGe is grown in two steps with the TAC after deposition of the intrinsic layer, such that a high-quality n-doped layer with a low TDD can be obtained without the occurrence of dopant accumulation. Indeed, the decay time is found as 2.6 ns, significantly exceeding the performance of sample nGe. However, the decay time decreases to 0.9 ns after rapid thermal annealing (RTA) consisting of 3 cycles with 25 s at 800°C, which suggests that a similar dopant-enrichment process might take place during RTA as for sample nGe during TAC.

To discuss the decay times τ with respect to the layer thickness d, the lifetimes can be normalized to obtain the surface recombination velocity (SRV) as $s \cong d/\tau$, which is a good approximation for the case where the SRV of one surface is dominating [210]. In table 4.1, the SRV is given together with the layer thickness and respective decay times for all samples.

Comparing the SRV of samples iGe (s=850 m/s) and nGe/iGe (s=660 m/s), the selectively doped sample shows a reduction by approx. 30%. This can be partially attributed to a lower TDD of 9×10^{6} cm^{-2} compared to 3×10^{7} cm^{-2} for iGe [211]. Furthermore, the doping scheme introduces a built-in field for sample nGe/iGe, which helps to keep the photoexcited electrons away from the defective Ge/Si interface, giving an indication that the lifetime is predominantly limited by the Ge/Si interface.

For the selectively grown n-doped Ge layer (selnGe), a SRV of 920 m/s is obtained. This

Sample	Ge thickness (μm)	Decay time (ns)	Surface recombination velocity (m/s)
iGe	1.7	2.0	850
nGe	1.7	0.4	-*
nGe/iGe	1.7	2.6	660
selnGe	1.2	1.3	920
iGe/GeOI	2.6	5.3	490

*The decay of sample nGe is not described by a surface recombination.

Table 4.1: Experimentally determined surface recombination velocities.

SRV is very close to the value obtained for iGe grown via LEPECVD, which is another sign that the limiting recombination process is related to an interface.

Finally, the most conclusive evidence for the Ge/Si interface to be the main limitation for the non-radiative lifetimes comes from the investigation of iGe/GeOI, where defects at the interface are drastically reduced [152]. The observed SRV of 490 m/s is, indeed, the lowest for the investigated set of samples. However, surface recombination velocities of unpassivated bulk Ge are still much larger [185]. The difference might be connected to microcracks and vacancies created by the ion-implantation step during the SmartCut^{TM} process [212, 213]. Furthermore, the interface between the GeOI device layer and the LEPECVD overgrown Ge may also contribute to the decay. Unfortunately, the Ge layer from the bare GeOI substrate without that interface is only 60 nm thick such that the decay time falls below the 100 ps time resolution and, furthermore, no multiple interference pattern occurs.

To exclude the decay being attributed to carrier diffusion out of the probed area rather than their non-radiative decay, the measurements are repeated with larger excitation- and detection spot sizes (200 μm and 100 μm, respectively) where in-plane carrier diffusion can safely be neglegted. The resulting decay times match with the results obtained with the microfocus setup. Furthermore, a diffusion into the substrate is prevented by the band offset between Ge and Si or SiO_2 and can, hence, be excluded, as well.

With the results obtained, there now exist new experimental data which can be used to estimate non-radiative carrier lifetimes for the modelling of Ge lasers on Si. As an example, a Ge laser cavity may have the waveguide dimensions of 0.5 μm in thickness and 2.0 μm in width. With a SRV of 660 m/s, which is the lowest value for any Ge epilayer directly grown on Si in this work, the non-radiative decay time for the aforementioned laser cavity can be estimated to 0.8 ns. Therefore, an injected current density of 100 kA/cm^2 is required to achieve an excess carrier density of 10^{19} cm^{-3}. This current density is almost two orders

of magnitude higher than predicted by a previous simulation [214]. The discrepancy is due to the fact that for modelling efforts, carrier lifetimes for bulk Ge are widely being used [64, 65, 86, 215, 216], even though it has been shown here that there is a significant deviation between lifetimes in bulk Ge and Ge epilayers on Si, which should be taken into account for a reliable prediction of Ge-based laser performance.

To further improve the carrier lifetimes in Ge epilayers, several approaches can be followed such as the passivation of surfaces or the use of heterostructures, which keeps the carriers away from decay time-limiting surface and interface regions. One successful approach to increase the quality of Ge layers is the removal of the defective Ge/Si interface as done for GeOI. This high-quality material will be examined in the following.

4.5 Thickness-Dependent Lifetime of High-Quality GeOI

In the previous chapter, it was shown that the highly defective Ge/Si interface is the main limiting factor for the non-radiative carrier lifetime in Ge epilayers on Si. Therefore, GeOI showed the longest carrier decay times due to the removal of the Ge/Si interface during the fabrication process. Sample iGe/GeOI investigated in the measurements is a GeOI substrate with an only 60 nm thin device layer suitable for electronic applications, which is overgrown by a thick Ge layer by LEPECVD. Therefore, the properties might differ from the thick GeOI layers fabricated at CEA LETI via SmartCut^{TM} technology (see chapter 3.2).

In Fig. 4.11(a), pump-probe transmission spectra are presented for the base GeOI material consisting of a 1 µm intrinsic Ge device layer on buried oxide. The same features as for Ge layers on Si are found, with a distinct shift in Fabry-Perot oscillations as well as a strong absorption loss and bleaching. As before, no signature of optical amplification is observed. Even after 9 ns delay time between pump and probe pulse, there is still a significant shift between pumped and unpumped peak maxima, indicating that a substantial amount of charge carriers is still present in the system.

The extracted charge carrier densities following equation (4.5) are plotted in Fig. 4.11(b) for micron-thick layers of intrinsic Ge (blue circles) as well as n-doped Ge (red circles). For the n-doped sample, phosphorus dopants were introduced by ion implantation at a nominal concentration of $N_D = 1 \times 10^{19}$ cm^{-3} followed by thermal annealing [144]. The time-dependent carrier densities are fitted with the non-radiative decay time τ and the Auger recombination coefficient γ as the free fitting parameters, yielding $\gamma = 4 - 5 \times 10^{-31}$ cm^6/s in perfect agreement with measurements on GeSOI layers, and non-radiative carrier lifetimes of 5.0 ns (intrinsic GeOI) and 1.3 ns (n-doped GeOI).

To decouple bulk and surface/interface effects, the decay time is measured for a series

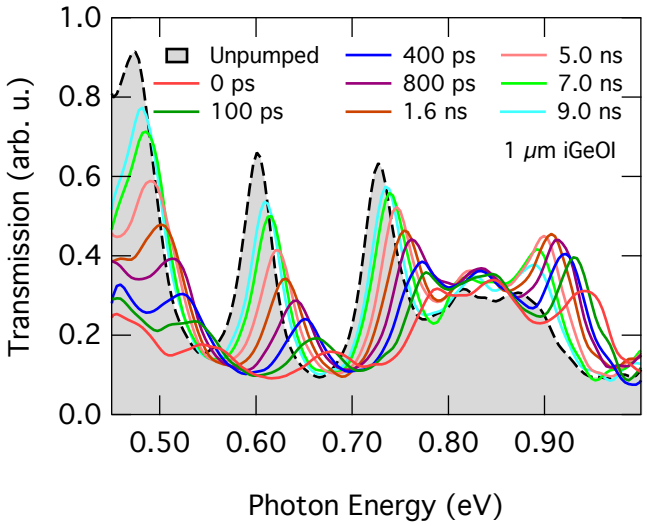

(a) Pump-probe transmission for 1 µm GeOI.

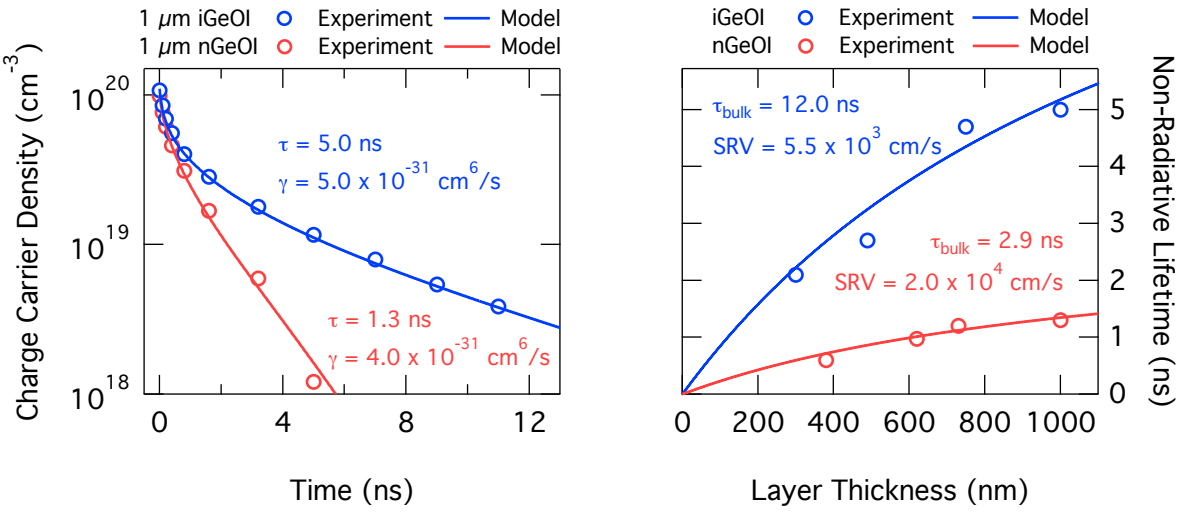

(b) Carrier decay for 1 µm intrinsic (blue) and n-doped (red) GeOI with modelled decay function, where the Auger recombination coefficient and the carrier lifetimes serve as fitting parameters.

(c) Thickness-dependent decay time for intrinsic (blue) and n-doped (red) GeOI. The quality of the n-doped material seems to be severely affected by the ion implantation.

Figure 4.11: Analysis of non-radiative lifetime in GeOI. From the Fabry-Perot shifts induced by a carrier density-dependent change in refractive index (a), the lifetime and the Auger coefficient are experimentally determined for micron-thick intrinsic and n-doped GeOI (b). Futhermore, the surface recombination velocity and the bulk-lifetimes are extracted by analyzing the thickness-dependent carrier decay (c).

of samples with varying layer thickness d. To reduce the thickness, the 1 µm Ge layers are thinned at CEA LETI by reactive ion etching using SF_6, Ar and CHF_3 chemistry. In Fig. 4.11(c), the decay times τ are shown in function of layer thickness for intrinsic (blue circles) and n-doped (red circles) GeOI. The thickness-dependent data are accurately described by [192, 210, 217]

$$\frac{1}{\tau} = \frac{1}{\tau_{bulk}} + \left(\frac{d}{2s} + \frac{d^2}{\pi^2 D} \right)^{-1}, \tag{4.9}$$

where τ_{bulk} is the bulk lifetime, s is the surface recombination velocity, and D is the diffusion constant taken as $D = 100$ cm^2/s [207]. Apparently, the thinning by reactive ion etching does not significantly affect the surface recombination velocity because the data are nicely described by a constant SRV, which might be due to an effective passivation of surface states by methyl groups [218].

For the intrinsic GeOI, a bulk lifetime of 12.0 ns and a SRV of 5500 cm/s are obtained. Hence, the layer with a thickness of 1 µm and a decay time of 5.0 ns shows a lifetime which is roughly as long as for the overgrown GeOI substrate, even though the thickness for sample iGe/GeOI is 2.5× thicker, which indicates the superior material quality of the optical GeOI substrate. Furthermore, the lifetime without any surface recombination yields $\tau_{bulk} = 12.0$ ns, meaning that even longer decay times may be achieved by proper surface treatments [184, 219–221]. The high quality - quantified in terms of the non-radiative carrier lifetime - together with the mechanical stability, which led to the observation of a fundamental direct band gap for highly strained Ge microbridges (see chapter 3.4.3), demonstrates the potential of high-quality, thick GeOI substrates as platform for Si-compatible integrated photonics.

On the other hand, there is an obvious negative effect of the n-doping via ion implantation on the material quality evidenced by an approximately fourfold decrease in charge carrier lifetime and a fourfold increase in surface recombination velocity. The quality loss is ascribed to lattice defects generated by the implantation process [222–224]. This degradation is in accordance with photoluminescence measurements comparing ion-implanted n-doped Ge with in-situ n-doped Ge, where the emission intensity for the implanted sample is significantly weaker [225].

The two cases, where n-doped samples showed a significantly worse material quality in terms of carrier decay lifetimes - either due to dopant aggregation or due to implantation damages - serve as a good example for the general trade-off, which has to be made: On the one hand, n-type doping is theoretically expected to increase the optical gain [92]. On the other hand, it is not a trivial task to achieve a doping in the range $> 1{\times}10^{19}$ cm^{-3} while keeping the non-radiative carrier lifetime in an acceptable range e.g. due to non-activated

dopant atoms [226, 227].

4.6 Lifetimes of Strained Ge Microbridges

4.6.1 GeSOI Microbridges

When a fundamental direct band gap is induced in Ge via strain-redistribution, the final structure differs from the starting substrate material due to a large induced tensile stress and additionally introduced surfaces via reactive ion etching (see chapter 3). To investigate any effects on the optical material quality, the carrier decay times are extracted for Ge microbridges following the same approach as for the unprocessed substrates.

In Fig. 4.12, SEM images of the investigated GeSOI microbridges are shown. In order to exceed the synchrotron probe spot of $\sim$ 10 µm, the dimension of the constriction is 20 µm in length and 3 µm in width. The length of the constriction is much larger than usual and limits the obtained maximum strain to 1.4%. Strained bridges are processed from sample iGe and sample nGe/iGe (see chapter 4.4).

The transmission through a strained constriction without (grey, filled area) and with optical excitation (colored, solid lines) is shown in Fig. 4.13(a), with the unpumped transmission through the pad shown in the inset. In contrast to the pad-transmission, which features Fabry-Perot oscillations related to the suspended Ge layer thickness, the pattern changes

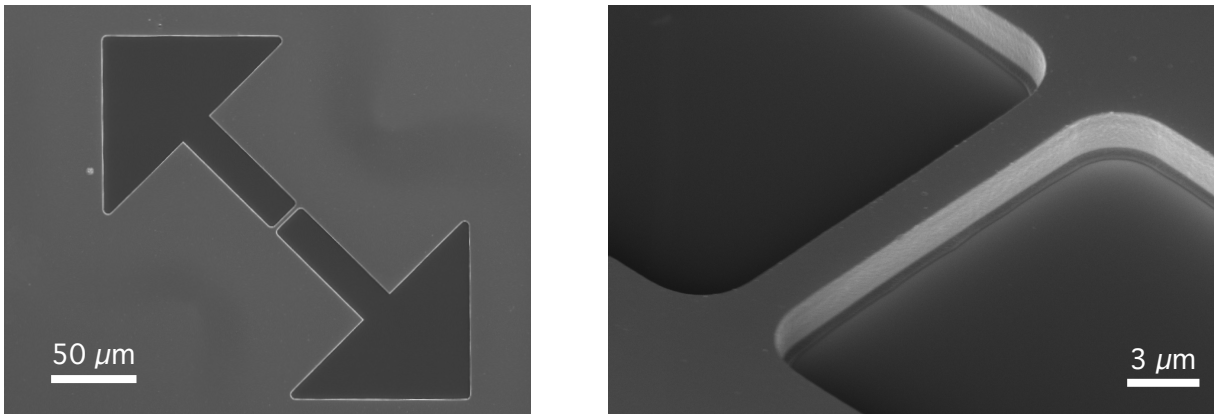

(a) Scanning electron microscope image of a suspended GeSOI microbridge with 20 µm constriction length.

(b) Close up of the constriction of an investigated GeSOI microbridge before underetching.

Figure 4.12: Scanning electron microscope images of GeSOI microbridges. The constriction length of the bridges was increased to 20 µm such that only the strained part of the structure was probed in synchrotron-based transmission measurements.

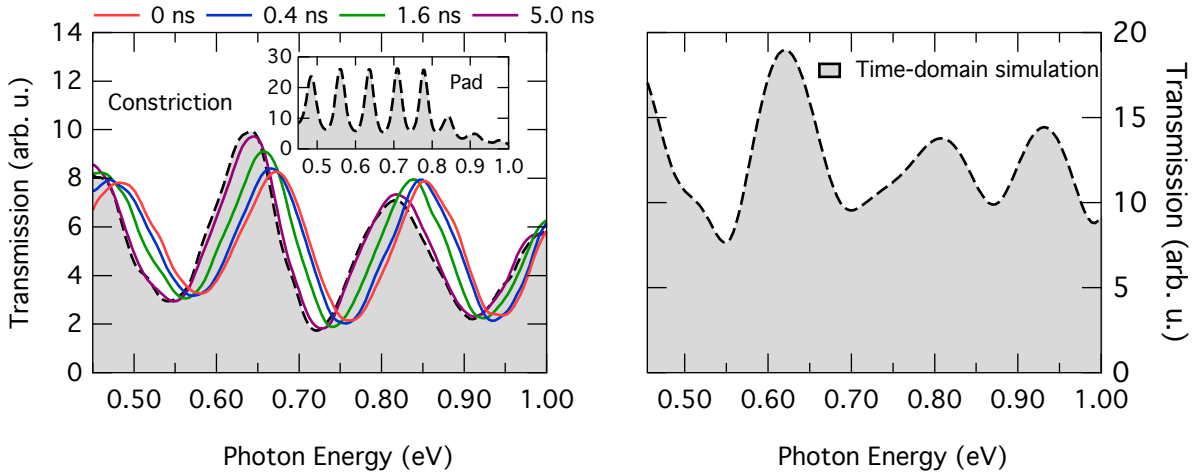

(a) Broadband pump-probe transmission through iGeSOI microbridge. The inset shows the unpumped transmission through the suspended pad.

(b) Simulation of spectrally resolved transmission through iGeSOI constriction via a time-domain solver. The simulation was performed by Christopher Bonzon.

Figure 4.13: Transmission through the suspended constriction of an iGeSOI microbridge. A distinct difference in the oscillation pattern can be seen in comparison to the transmission through a suspended pad as shown in the inset. The change in the transmission characteristics is well reproduced by time-domain simulations shown in (b).

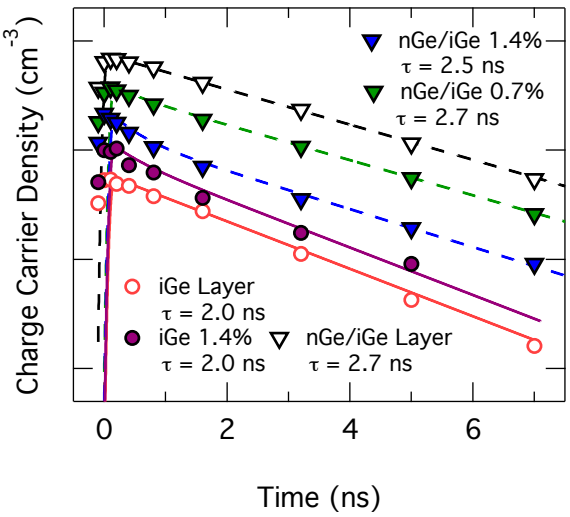

Figure 4.14: Carrier decay times for iGeSOI and nGe/iGeSOI blanket layers (open symbols) and strained microbridges with up to 1.4% longitudinal strain (filled symbols). The curves are offset for clarity.

significantly when the constriction is probed. The change in oscillation pattern is due to diffraction and complex, anomalous coupling of the infrared probe to the smaller-sized suspended constriction. The experimental spectrum can be reproduced with satisfactory agreement by a time-domain simulation using the CST microwave studio software package, when the transmission of a broadband source is detected after the transmission through the geometry under investigation. The time-domain simulation was performed by Christopher Bonzon from ETH Zürich. Most importantly, the increased complexity of the transmission spectra does not prevent the extraction of the carrier decay times following the same procedure as introduced above.

The obtained decay times for the unprocessed parts of the iGe and nGe/iGe layers (open symbols) as well as for strained, suspended microbridges (filled symbols) are shown in Fig. 4.14. As shown previously (see chapter 4.4), the highly-defective Ge/Si interface is the main limiting factor for the carrier lifetime, leading to longer decay times for nGe/iGe (2.7 ns) than iGe (2.0 ns) due to an internal built-in field, which keeps electrons away from the interface.

For the processed microbridges, there is no difference in lifetime compared to the unprocessed layer within the 100 ps accuracy given by the experimental time resolution. Therefore, neither the additionally introduced surfaces nor the tensile stress lead to a faster carrier decay with respect to the unprocessed layer, indicating that the high crystalline quality is maintained under strain. For the additional surface from reactive ion etching, the process chemistry which includes C_4F_8 might lead to a passivation of the surface such that no effect in decay time is observable, as the SRV connected to the highly defective Ge/Si interface significantly exceeds the one associated to the etched facets.

4.6.2 GeOI Microbridges

For strained microbridges processed on GeOI substrates, the carrier decay times are extracted via synchrotron-based transmission measurements, as well. For these experiments, the structures are designed with a length of 8 µm and a width of 1 µm. The carrier-decay measured on the pad (red circles) and on the constriction (blue circles) for a bridge with 1.6% strain are shown in Fig. 4.15. Similar as for the structures on GeSOI, there is virtually no change in lifetime between the pad (4.1 ns) and the constriction (3.8 ns), which strongly indicates passivated etched facets after the processing as there is now no highly-defective Ge/Si interface.

Interestingly, the Auger recombination coefficients are obtained as 5.0×10^{-31} cm^6/s for the pad and 3.0×10^{-31} cm^6/s for the constriction. However, the Auger coefficient is expected to increase for strained Ge due to the dependence on band gap and effective

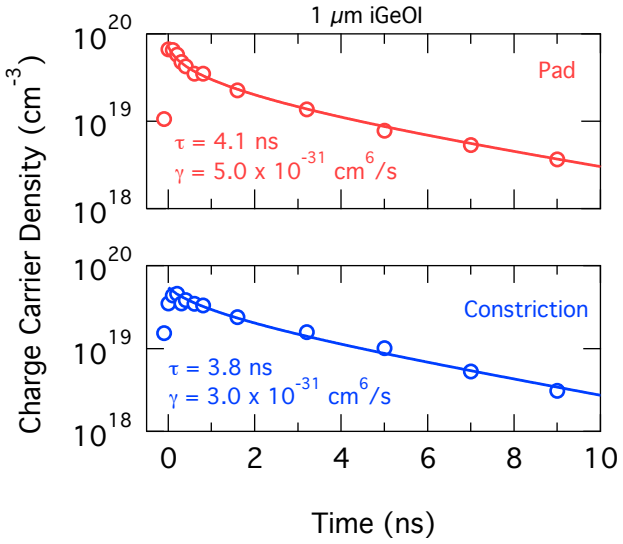

Figure 4.15: Time-dependent charge carrier densities (circles) and modelled carrier decay (solid lines) for iGeOI pad (red) and strained microbridge (blue) with 1.6% longitudinal strain.

masses [228–230], which might pose challenges for the efficiency of direct band gap group IV lasers due to the short Auger recombination times. Nevertheless, more experimental results are needed to gain more information on the Auger coefficient in dependence on strain, especially for larger strain when considerably more electrons populate the Γ states and can, hence, undergo direct Auger processes.

4.7 Outlook

As shown above, time-resolved pump-probe experiments are a powerful tool to investigate gain and carrier decay dynamics in Ge layers on Si. As the technological part to achieve a direct band gap in strained Ge has been reached, more effort can be put towards the investigation of gain, loss and carrier lifetime under strain. In the following, additional experiments are proposed, which tackle key questions concerning the effects of strain and n-doping:

So far, only a limited number of experiments was performed on strained microbridges. The strain in the investigated structures was not exceeding 2.0%, such that technologically interesting strain values in the range of $> 4.0\%$ could not be investigated. The effect of such a high strain on the carrier decay time remains, therefore, an open question. Large constrictions enable to make sure that only carriers in the strained volume are probed, but high strain values are then difficult to achieve. A solution for this drawback would be to decrease the constriction length and cover the non-strained part with a chrome layer, such

that carriers are optically excited only within the constriction. Apart from that, optical excitation at longer wavelengths leads to the same effect if the pump energy is too low to generate charge carriers in the relaxed Ge.

With a decrease in band gap and effective masses, Auger recombination becomes an increasingly important material parameter. As shortly discussed above, the Auger recombination rate γ is, therefore, expected to increase for an increasing tensile strain. For direct band gap Ge, the achievable steady-state carrier density might be Auger-limited at significantly lower carrier densities compared to relaxed Ge. While no substantial increase in γ could be observed at a strain of 1.6%, a larger statistics and especially measurements on structures with higher strain are required to confirm or contradict the observations.

To reach net gain in Ge layers under a small, thermal tensile strain $< 0.25\%$, theoretical work finds that n-doping densities $> 6{\times}10^{19}$ cm^{-3} are required [63]. At such high dopant concentrations, epitaxy has to overcome challenges regarding solid solubility and out-diffusion of the dopant atoms [231]. Due to recent progress in chemical vapor deposition epitaxy, new regimes of activated doping levels could be achieved with $> 6{\times}10^{19}$ cm^{-3} using in-situ doping with high order precursor gas [120], and $\sim 1{\times}10^{20}$ cm^{-3} using phosphorus δ-doping layers [232, 233]. Pump-probe measurements could be used to extract the influence of the high doping on the lifetime and to determine the doping-dependent gain and loss to further deepen the understanding of the underlying physics for highly n-doped Ge.

4.8 Summary

In this chapter, the charge carrier lifetimes in Ge epilayers were extracted via synchrotron-based time-resolved infrared pump-probe transmission spectroscopy. The optically generated charge carrier density results in a distinct shift of the strong Fabry-Perot interferences due to a change in refractive index, which is probed for the extraction of the carrier decay time.

By a comparison of differently prepared Ge layers, it was shown that the highly defective Ge/Si interface is the main limiting factor for the non-radiative carrier lifetimes, with the carrier decay for Ge epilayers on Si differing significantly from results for bulk Ge. Therefore, the best quality in terms of carrier decay time is achieved for GeOI fabricated via SmartCut^{TM} technology, which already showed superior mechanical properties, as well. From the investigation of the carrier lifetime in function of layer thickness, a bulk lifetime of 12.0 ns was extracted.

The impact of n-type doping via ion implantation was found to significantly decrease the charge carrier lifetime by a factor of four associated to a damage of the crystal during the implantation process. But also in-situ n-doping as shown for sample nGe grown on SOI via

LEPECVD has a detrimental effect when the dopant atoms populate the threading dislocation lines.

Finally, the effect of patterning the Ge layer into a suspended microbridge structure was investigated. It was found that neither the additionally introduced etched facets nor a tensile strain of up to 1.6% significantly alter the recombination dynamics, proving that the high crystalline quality is maintained under strain when induced using our strain enhancement technology. Within the strain values that were reached for the analyzed structures, no increase in Auger recombination coefficient was obtained despite the theoretical prediction that a decreased band gap leads to faster Auger recombination rates. In fact, the opposite is observed for the one measured case.

4.9 Compendium

The carrier lifetime measurements reveal that the best choice of material is intrinsic GeOI. On another positive note, the reactive ion etching used here does not degrade the material quality in terms of carrier lifetime. In contrast, the lifetime for n-doped Ge layers was found to decrease, which questions the advantage of n-doping to enhance the material gain as theoretically discussed in chapter 2.3.

In the following chapter, the pump-and-probe analysis is applied to direct band gap GeSn alloys showing a decay time which is one order of magnitude faster than for the Ge.

5

Investigation of Temperature-Limitation for Optically Pumped GeSn Lasers

Contents

In this chapter, direct band gap GeSn alloys are examined to understand the limitation of lasing to temperatures $\leq$ 90 K and the high threshold excitation density as reported in [77]. To quantify the role of the conduction band alignment as well as the defective GeSn/Ge interface, the performance of underetched Fabry-Perot waveguide cavities with different Sn concentrations and, hence, varying offset between Γ and L-valleys is analyzed. Time-resolved pump-probe transmission measurements are performed to investigate the temperature-dependent non-radiative lifetime and to quantify the material gain.

Parts of this chapter were published in a similar form as:

S. Wirths and R. Geiger *et al.*, Lasing in direct-bandgap GeSn alloy grown on Si. *Nature Photonics* **9(2)**, 88 (2015).

5.1 Introduction

Alloying Ge with α-Sn is a viable approach to engineer a direct band gap semiconductor from group IV materials. After the first prediction of direct band gap behavior for GeSn at a sufficiently high Sn concentration [76], several research groups investigated the molecular beam epitaxy (MBE) of GeSn in the 1980s and 1990s [234–238]. Due to the challenges epitaxy is facing such as the low solid solubility of $< 1\%$ for Sn in Ge [239] or the large lattice mismatch between Sn and Si (17%) and Ge (15%), it was not before the early 2000s that device-grade layers could be synthesized via chemical vapor deposition (CVD) [240]. Nowadays, high-quality GeSn layers are available based on MBE [241–243] or CVD growth [244–248], triggered by the interest in GeSn for CMOS-compatible optical devices in the mid-infrared [155] such as light-emitting diodes [249–252] or photodetectors [253–255], and the possible application for next-generation electronics [128, 256, 257]. For a recent review on the developments in GeSn epitaxy, the reader may refer to [258]. Compared to tensilely strained Ge as presented above, GeSn alloys offer a bulk volume material with a direct band gap, which simplifies device design compared to the microbridge approach. On the other hand, achieving different conduction band alignments on the same wafer and waveguiding of the direct gap emission in the bulk material are advantageous for tensile-strained Ge and the GeOI platform, respectively, due to the top-down patterning approach.

In general, a compressive strain builds up in coherently grown GeSn on Ge or Si. As the compressive strain increases the offset $\Delta E_{cb} = E_\Gamma - E_L$ between Γ and L valleys, it hampers to reach a direct band gap and shifts the crossover to a higher Sn amount [259]. Recently, the Forschungszentrum Jülich achieved a break through in synthesizing direct band gap GeSn layers of high crystalline quality. GeSn layers were grown thick enough to induce plastic strain-relaxation [107, 260]. Due to an advantageous strain-relaxation mechanism when GeSn is deposited on Ge, dislocations seem to predominantly protrude into the Ge virtual substrate (VS) rather than into the GeSn epilayer which, therefore, remains of high quality. Based on this premise, GeSn layers with Sn contents up to 14 at.% were obtained with a low density of non-radiative recombination centers in the active material [77, 261, 262].

At the Paul Scherrer Institute, a detailed spectroscopic study has been performed on these layers. It could be shown via temperature-dependent photoluminescence (PL) mea-

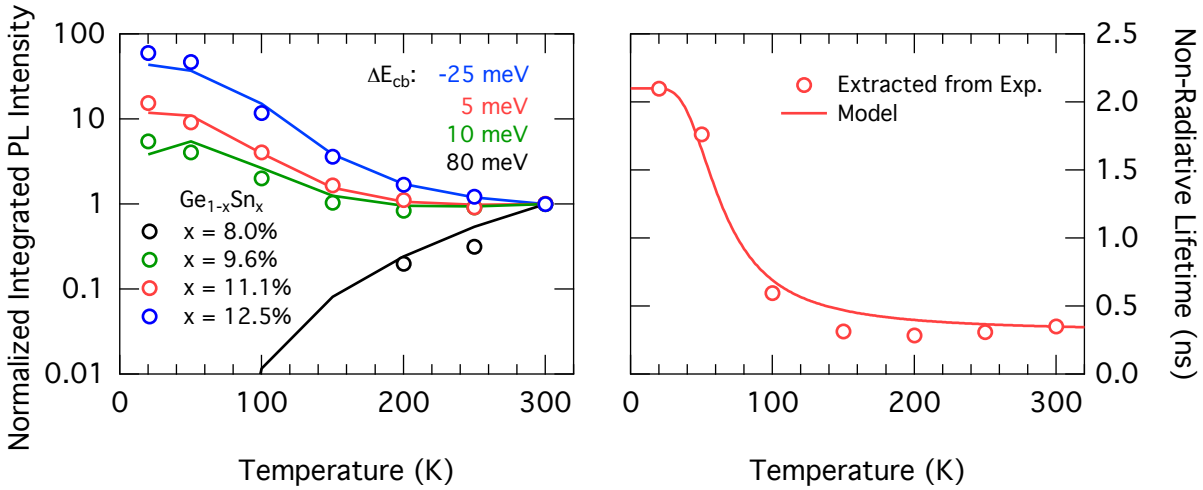

(a) T-dependent integrated direct gap emission (circles) and modelled spontaneous emission intensity (solid line).

(b) Non-radiative lifetime extracted from PL measurements (circles) and modelled T-dependence (solid line).

Figure 5.1: Temperature-dependent PL on GeSn layers with $x_{Sn} = 8.0\% - 12.5\%$ allows the extraction of the conduction band alignments (a) and the non-radiative decay time τ_{nr} (b). From modelling the spontaneous emission intensity to the experimental data, a fundamental direct band gap of $\Delta E_{cb} = -25$ meV is found for $Ge_{0.875}Sn_{0.125}$. The rapid decay in τ_{nr} for increasing temperature is well described by carrier-capture from Shockley-Read-Hall-like mid-gap states.

surements similar to the approach in chapter 3.4.3 that GeSn becomes a direct band gap group IV semiconductor. The experimental data is shown in Fig. 5.1(a). The integrated PL intensity is shown for a set of 4 samples with Sn concentration x_{Sn} between 8.0% and 12.5%. The solid lines show the calculated emission intensity based on the following modelling procedure: The spontaneous radiative emission R_{sp} is calculated based on the model introduced in chapter 3.3.2, which takes into account the joint-density-of-states of dipole-allowed transitions between isotropic, parabolic bands, and the quasi Fermi-levels are calculated in dependence of temperature. The conduction band offset ΔE_{cb} for each sample is a free fitting parameter. Furthermore, the non-radiative carrier lifetime τ_{nr} is adjusted at each temperature to yield the best fit to the data, where τ_{nr} is assumed to be identical for all investigated alloys. The solid lines in Fig. 5.1(a) show the results of the recursive fitting procedure yielding a very good agreement with the experimental data and a fundamental direct band gap of $\Delta E_{cb} = -25$ meV for an alloy with 12.5% Sn and -0.7% strain. The crossover was interpolated to occur at a Sn content of $\sim$ 9% for a relaxed lattice [77].

For alloys with an only slightly indirect conduction band alignment, i.e. $\Delta E_{cb} = 5-10$ meV, decreasing the temperature leads to an increase in emission intensity even though the con-

duction band minimum for those epilayers is determined by the L-valleys. This is attributed to a distinct increase in the non-radiative carrier lifetime τ_{nr}, which is plotted in Fig. 5.1(b), leading to an increased steady-state carrier density. An increase in emission intensity for lower temperatures can, therefore, not serve as the exclusive argument to prove the occurrence of a fundamental direct band gap. Similarly, an argument based only on the emission line width as presented in [263] - which may be governed by Sn-inhomogeneity or the strain-dependent valence band alignment - is not sufficient, either. In [263], Ghetmiri *et al.* claim a fundamental direct band gap at 10% Sn and -1.2% biaxial strain without a significant increase in emission intensity upon cooling, despite the identification of an epilayer with 9.6% Sn and -0.4% strain as fundamentally indirect in the analysis of PL measurements presented here.

The T-dependent lifetime extracted from the PL measurements is well described by a model for carrier capture by mid-gap defect states as

$$\tau_{nr} = \left(\frac{1}{\tau_0} + \frac{1}{\tau_{SRH}} \right)^{-1}, \tag{5.1}$$

where τ_0 describes the lifetime at low temperatures, and τ_{SRH} is the time associated with the capture of a charge carrier by a Shockley-Read-Hall-like mid-gap state, which has the following temperature dependence [170]:

$$\tau_{SRH} = A \times \left(1 + \cosh\left(\frac{\Delta E_T}{kT} \right) \right), \tag{5.2}$$

where ΔE_T is the difference between the trap level energy E_T and the intrinsic Fermi level, k is the Boltzmann constant, and A is a factor to scale the lifetime at 300 K to the lifetime obtained from the modelling.

As expected for a direct band gap material, lasing was demonstrated for $Ge_{0.875}Sn_{0.125}$ under pulsed optical pumping at 1064 nm after patterning the layer into Fabry-Perot waveguide cavities. A high threshold peak excitation density of 325 kW/cm^2 was required to start lasing action at 20 K. This is shown in Fig. 5.2(a), where the modal gain is extracted at 20 K by the variable stripe length method (red circles) and the calculated mirror losses of the Fabry-Perot cavities (blue squares). Furthermore, at the highest available excitation density of 1000 kW/cm^2, lasing could be achieved up to a maximum temperature of 90 K. In Fig. 5.2(b), the edge emitted spectra are shown at different temperatures, which demonstrates that at 100 K only spontaneous emission is detected indicated by the drop in intensity by more than 2 orders of magnitude and a significant increase in spectral width. Strikingly, the temperature regime where lasing cannot be reached anymore coincides with the significant drop in carrier lifetime as obtained by the PL analysis.

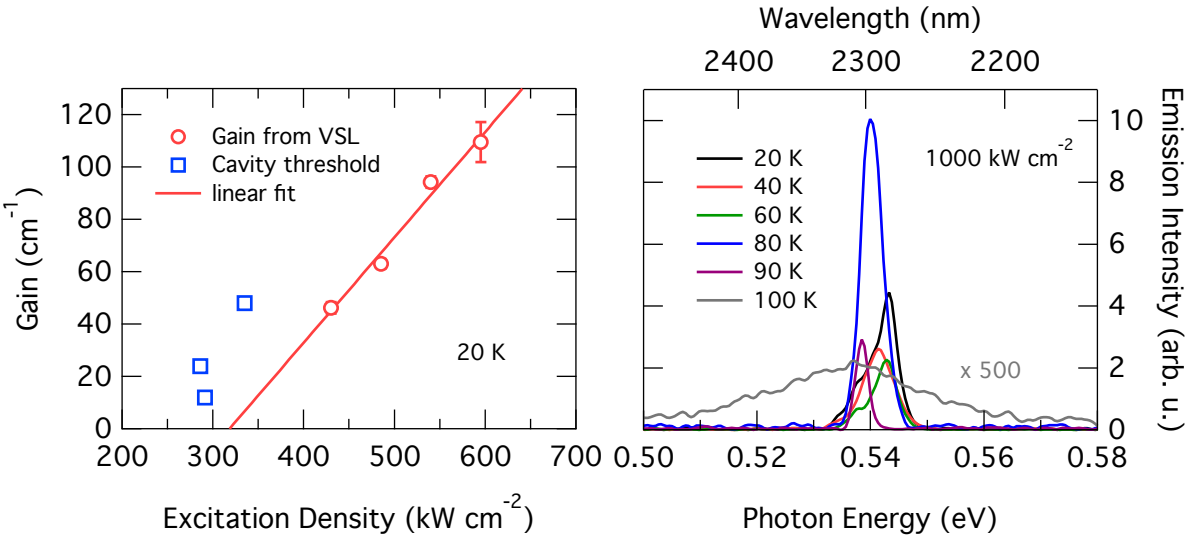

(a) Gain from variable stripe length method and treshold from cavities with different length.

(b) Lasing spectra at 1000 kW/cm^2 in function of temperature.

Figure 5.2: (a) The modal gain for $Ge_{0.875}Sn_{0.125}$ at 20 K is shown as determined via the variable stripe length (VSL) method (red circles) and from the threshold of Fabry-Perot cavities of different length (blue squares). A threshold excitation density of 325 kW/cm^2 is obtained. (b) Lasing spectra for temperatures between 20 K and 100 K at 1000 kW/cm^2. Above 90 K, the device does not lase anymore as indicated by the significant drop in intensity and the large increase in spectral width.

The high threshold and the limitation of lasing to low temperatures are in strict contrast to theoretical predictions, which anticipate the above material to easily exceed operation temperatures of 300 K [260]. In Fig. 5.3, the contour plot shows the minimum of total absorption α_{tot} in function of injected carrier density and temperature for direct band gap $Ge_{0.875}Sn_{0.125}$. The calculation is based on the model introduced in chapter 2.3, with effective masses and valence band splitting taken from [77]. The conduction band alignment is set to -25 meV as determined experimentally. Due to the lack of experimental data on the injection-dependent parasitic absorption, the electron- and hole cross sections for Ge are used with their respective dispersion [62], which might underestimate the absorption loss. It is found that at temperatures below 50 K, injected carrier densites in the order of 10^{16} cm^{-3} are sufficient to reach transparency, i.e. $\alpha_{tot} = 0$. For an increase in temperature to 100 K, the threshold carrier density N_{thr} increases rapidly because the probability for electrons to populate L-states increases with increasing thermal energy. The increase flattens out once the majority of electrons occupies the L-valleys. Nevertheless, the threshold carrier density at 300 K is still in the low 10^{18} cm^{-3} and, hence, in a range which should be experimentally

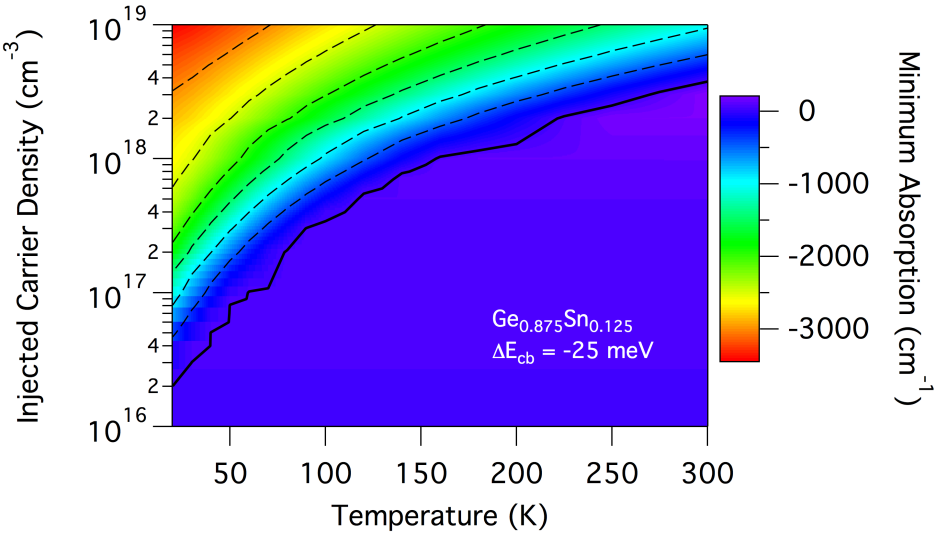

Figure 5.3: Modelling of the minimum total absorption α_{tot} in funtion of injected carrier density and temperature for direct band gap GeSn. The solid, black line shows when the transparency condition is met, i.e. $\alpha_{tot} = 0$, while the dashed lines depict the decrease of α_{tot} in decrements of 500 cm^{-1}.

accessible under optical pumping.

Reaching room-temperature lasing is clearly the next big milestone towards the realization of a practical group IV light emitter. In order to achieve this next step, a good understanding is required on what causes the high threshold and the limitation of lasing to low temperature. In the following, the role of the most essential material parameters are investigated, which are the conduction band offset and the non-radiative lifetime. First, the influence of non-saturated surface states is investigated by a comparison of surface passivated and non-passivated laser devices. Then, the lasing characteristics in dependence of temperature will be examined for devices with different Sn concentration to address the role of the conduction band offset ΔE_{cb}. In the last part of the chapter, time-resolved pump-probe measurements on GeSn layers will be presented to extract the non-radiative carrier lifetime and the dynamics of optical gain and -loss.

5.2 Influence of Surface Passivation

For the investigation of surface passivation effects, the same epilayer as for the first demonstration of lasing is used [77]. The GeSn alloy is grown at the Forschungszentrum Jülich in an industry-compatible AIXTRON 200 mm reduced-pressure CVD reactor using the precursors Ge_2H_6 and $SnCl_4$ [77, 107, 246, 264]. The epilayer with a Sn-content of 12.5% is deposited

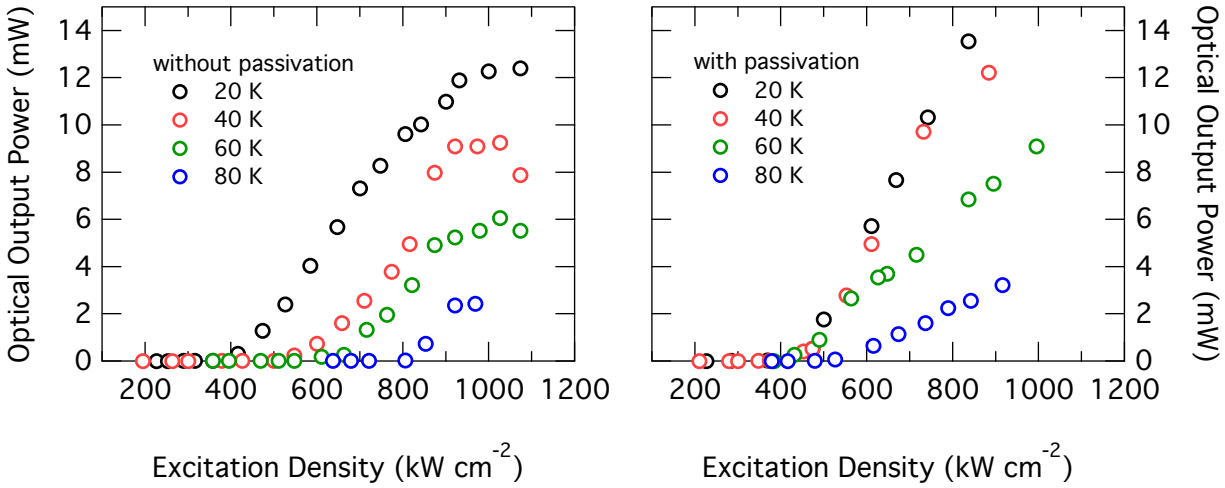

(a) L-L-plots for unpassivated $Ge_{0.875}Sn_{0.125}$ waveguide cavity.

(b) L-L-plots for passivated $Ge_{0.875}Sn_{0.125}$ waveguide cavity.

Figure 5.4: Comparison of temperature-dependent L-L characteristics for (a) unpassivated and (b) passivated $Ge_{0.875}Sn_{0.125}$. The passivation layer is 10 nm Al_3O_2 deposited by atomic layer deposition, which was followed by a forming gas anneal.

on a 2.7 µm thick Ge virtual subtrate (VS), where the Ge buffer is weakly tensilely strained by 0.16% at room temperature. Due to the GeSn layer thickness of 560 nm, which exceeds the limit for strain-relaxation, only a weak compressive strain of −0.6% is observed. Electron beam lithography and anisotropic reactive ion etching are employed to process the epilayer into Fabry-Perot cavities with 5 µm width and 1 mm length as schematically shown in Figs. 5.6 (i) and (ii). Dry etching generally leads to an increase in defect density at the surface [265], which affects the non-radiative carrier lifetime and, thus, the achievable steady-state carrier density. An effective countermeasure is to passivate the device after the etching, e.g. by the deposition of 10 nm Al_2O_3 which is known to reduce the amount of non-saturated interface states [266, 267]. Whereas the GeSn laser devices in [77] were dry etched at Paul Scherrer Institute using $SF_6/C_4F_8/O_2$ chemistry, which provided a surface passivation by the C_4F_8, the Fabry-Perot cavities investigated here are processed at the Forschungszentrum Jülich using a dry etch based on Cl_2/Ar with an optional subsequent surface passivation by atomic layer deposition of Al_2O_3 and forming gas annealing [267].

In Fig. 5.4, the light-in versus light-out (L-L) characteristics are shown for a passivated and an unpassivated device in dependence of temperature. The excitation density refers to the incident, external radiation density. The samples are cooled in a liquid helium cold-finger cryostat and optically excited with a pulsed Nd:YAG laser emitting pulses of ∼ 5 ns length at a wavelength of 1064 nm with a repetition rate of 17 kHz. The excitation laser is focused

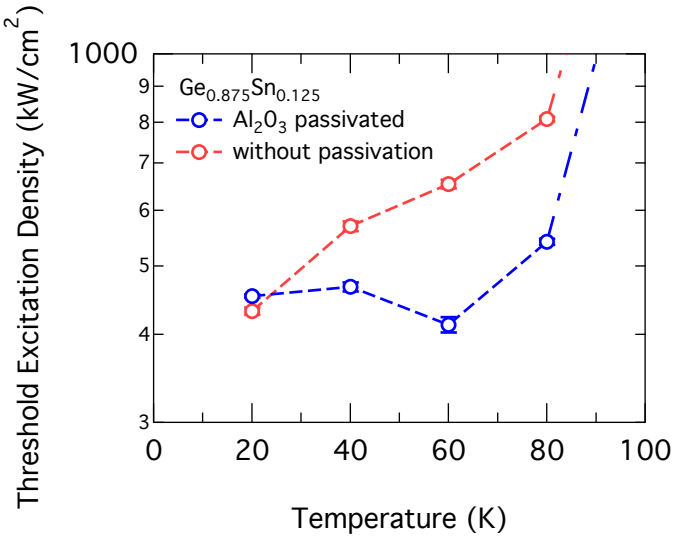

Figure 5.5: Temperature-dependent variation of excitation density at lasing onset for passivated (blue circles) and unpassivated (red circles) $Ge_{0.875}Sn_{0.125}$ waveguide cavity.

with a cylindrical lens onto a variable slit which is imaged 1:1 onto the waveguide surface by a biconvex lens resulting in a well-defined pump beam of $\sim$ 10 µm width and $>$ 1 mm length. The light emitted from the waveguide facet is collected with a 15× Schwarzschild objective (see chapter 3.3.1) and spectrally analyzed with an FTIR equipped with a liquid-nitrogen-cooled InSb detector. The setup is the same as used for the investigations reported in [77].

As can be seen in Fig. 5.5, no improvement due to the passivation is found at 20 K in terms of threshold density, which shows that the carrier density is not limited by surface recombinations at this temperature. However, the properties of the two devices differ significantly in their temperature-dependent behavior. While the threshold for the passivated device is pinned to $\sim$ 450 kW/cm^2 for temperatures $\leq$ 60 K, the threshold for the device without passivation increases steadily with increasing temperature. Neither of the two devices reaches lasing at 100 K.

The comparison between the two waveguide cavities shows that unsaturated surface states introduce a temperature-dependent increase in threshold carrier density due to a decrease in non-radiative lifetime, which is successfully suppressed by an Al_2O_3 passivation layer. At T $>$ 80 K, a steep increase in threshold density prevents to reach lasing even for the passivated device. This limiting process is likely to be caused by non-radiative recombination at the GeSn/Ge interface and features a much stronger temperature sensitivity than observed for the surface states.

5.3 Engineering of Fabry-Perot Waveguides by Selective Underetching

For GeSn epitaxy, the use of a Ge VS facilitates to synthesize high-quality epilayers. On the other hand, laser devices suffer e.g. from the small refractive index contrast between GeSn and Ge, which leads to a small modal overlap with the GeSn gain material. In the following, the process flow to fabricate selectively underetched GeSn waveguide cavities will be presented. The selective removal of the Ge VS results in enhanced performance, which will be discussed in terms of the improved optical confinement and the strain relaxation. Such second-generation GeSn Fabry-Perot cavities will be presented from epilayers with different Sn content such that the lasing characteristics can be investigated in function of the conduction band offset ΔE_{cb}.

5.3.1 Device Processing

A schematic of the process flow for underetched FP waveguides as developed at the Forschungszentrum Jülich is shown in Fig. 5.6. The epilayer is first patterned via electron beam lithography and Cl_2/Ar dry etching into ridge waveguides with 10 µm width and 1 mm length as discussed in the previous chapter. After definition of the waveguides, the Ge VS is selectively removed in an isotropic CF_4 dry etch, which leaves the GeSn unaltered due to the formation of a thin, passivating layer of SnF_x [268]. As final step, the whole device is conformally coated with a 10 nm Al_2O_3 passivation layer by atomic layer deposition. In Fig. 5.7, an SEM image is shown for a 10 µm wide $Ge_{0.9}Sn_{0.1}$ FP waveguide cavity with an undercut of 3.7 µm.

Underetched FP cavities are processed from 4 different GeSn epilayers with a Sn concentration between 8.5% and 14.0% termed samples A - D. All investigated devices with their respective Sn content, thickness, strain and undercut are listed in table 5.1.

Sample	Sn concentration (at.%)	Thickness (nm)	Strain (%)	Undercut (µm)
A	8.5	800	−0.2	3.7
B	10.0	800	−0.3	3.7
C	12.5	560	−0.4	4.3
D	14.0	350	−0.5	2.6

Table 5.1: List of investigated samples and their Sn concentration, layer thickness, biaxial strain, and undercut, respectively.

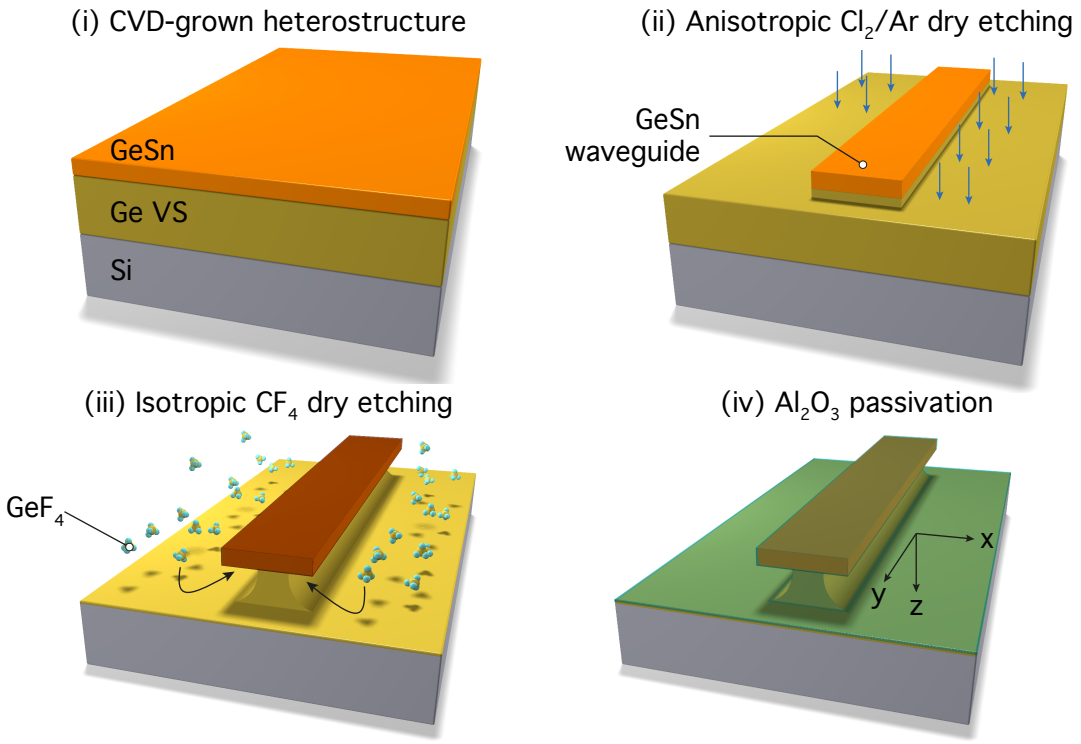

Figure 5.6: Schematic process flow for the fabrication of underetched GeSn Fabry Perot waveguide cavities executed at the Forschungszentrum Jülich.

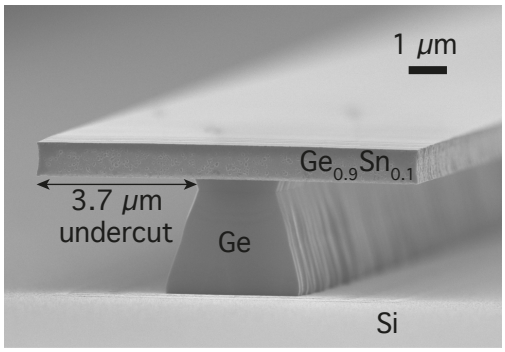

Figure 5.7: Scanning electron microscope image of the facet of a GeSn Fabry-Perot waveguide cavity with 3.7 μm undercut.

5.3.2 Modal Overlap

Guiding a light wave at a wavelength > 2.0 μm within a thin, Ge-buffered GeSn layer poses some challenges due to the small refractive index contrast between Ge and GeSn. At ~ 3.0 μm, the refractive index for an alloy with 12.5% Sn content (sample C) was determined

by ellipsometry as $n_{GeSn} \sim 4.2$ [77, 264] compared to $n_{Ge} \sim 4.0$ [269]. For a large mode confinement Γ between the optical mode and the GeSn, thicknesses > 300 nm are required.

In Fig. 5.8(a), the field intensity of the fundamental transverse electric (TE) mode is shown for a 10 µm wide and 560 nm thick ridge waveguide. This is the configuration for the first generation of GeSn lasers [77]. As the heavy hole-like valence band determines the top of the valence band structure for biaxially, compressively strained GeSn, TE gain is dominating [270]. The mode has been calculated using the 2D plane-wave expansion method presented in [271, 272] with the geometrical dimensions, the refractive indices n_{GeSn} = 4.2, n_{Ge} = 4.0, n_{Si} = 3.4, n_{Air} = 1.0, and the mode wavelength of 2.3 µm (∼ 0.54 eV) as input parameters. For these conditions, a confinement factor of 60% is calculated, indicating that a large portion of the mode is propagating within the Ge VS.

By the selective removal of the Ge, the situation changes drastically (see Fig. 5.8(b)): For an undercut of 4.3 µm, the increased refractive index contrast between GeSn and air over the large underetched length leads to a strong confinement in the GeSn epilayer in form of a second-order lateral mode. The confinement factor increases to 96% such that the mode is nearly fully travelling within the GeSn layer. Therefore, the underetched FP waveguide cavities should see a relative increase in modal gain by at least 60%. Since the propagation in the Ge VS is not loss-free owing to the carriers, which are excited within the Ge VS, the gain enhancement is expected to be even larger. It should be noted that for sample D, the confinement factor according to the modelling amounts to only ∼ 24% due to the insufficiently deep undercut and the smaller epilayer thickness.

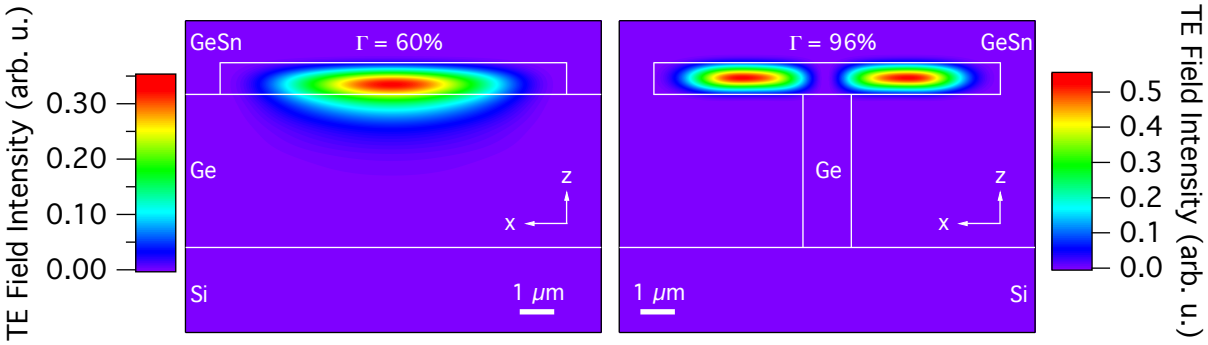

(a) TE mode profile for GeSn ridge waveguide without underetching.

(b) TE mode profile for underetched GeSn ridge waveguide.

Figure 5.8: Improvement of modal overlap with $Ge_{0.875}Sn_{0.125}$ gain medium by selective removal of Ge virtual substrate. Due to the increased refractive index contrast, the confinement factor Γ increases from 60% to 96%.

5.3.3 Strain Relaxation

Despite the layer thickness-induced plastic strain-relaxation, there still remains a compressive strain in the layers which increases the conduction band offset ΔE_{cb} and, hence, decreases the population of electrons at the Γ states compared to a relaxed layer. A decrease in compressive strain is, therefore, always of benefit for the optical properties [259]. The strain at half of the GeSn layer thickness is calculated for a $Ge_{0.875}Sn_{0.125}$ waveguide (WG) via finite-element COMSOL modelling, where the stiffness constants are linearly interpolated using the values for Ge and Sn listed in table 5.2. The strain tensor components along the main stress directions are shown in Fig. 5.9(a) for a line scan perpendicular to the waveguide direction. Without the underetching (dashed lines), a biaxial compressive strain occurs in the center of the waveguide, whereas the strain component in x-direction can relax towards the WG edges due to the introduced free surfaces. After underetching, the situation changes into a uniaxial compressive stress at the edges of the waveguide, where the optical field intensity is maximum. The maximum in compressive hydrostratic strain remains to appear

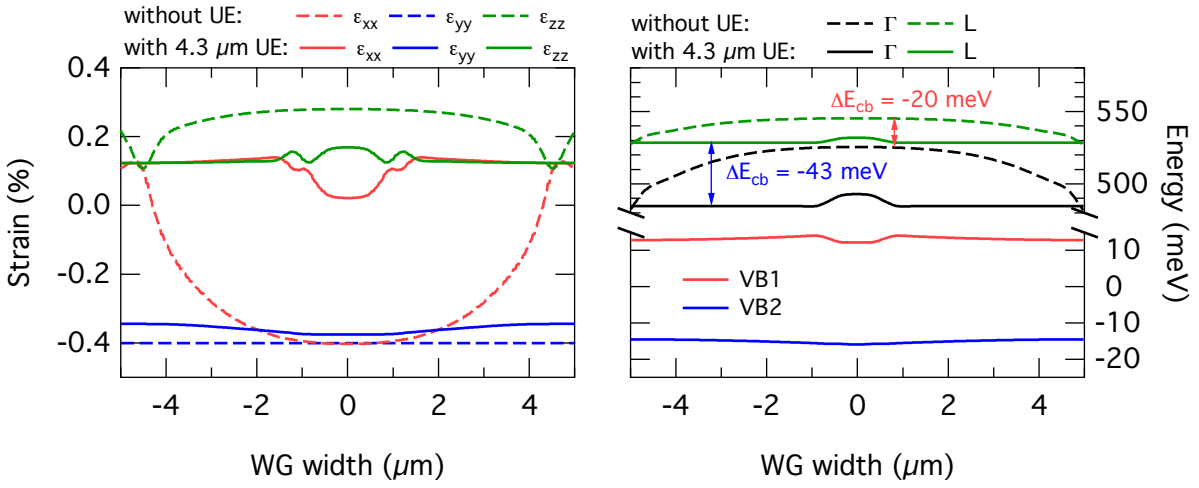

(a) Strain in main stress directions from FEM simulations for underetched (solid lines) and non-underetched (dashed lines) $Ge_{0.875}Sn_{0.125}$ ridge waveguide.

(b) Band edges from deformation potential calculations for underetched (solid lines) and non-underetched (dashed lines) $Ge_{0.875}Sn_{0.125}$ ridge waveguide.

Figure 5.9: The selective removal of the Ge VS leads to strain-relaxation in the undercut GeSn ridge waveguide. The strain tensor components along the main stress directions are shown in (a) for $Ge_{0.875}Sn_{0.125}$ along a linescan perpendicular to the waveguide direction before (dashed lines) and after the underetching (solid lines). The resulting band alignment computed with interpolated deformation potentials is shown in (b). The offset between Γ and L valleys increases by 23 meV at the positions of maximum mode intensity.

in the center of the waveguide.

To investigate the resulting electronic band alignment, the band edges are calculated with NextNano[3] using linearly interpolated deformation potentials and the spatially varying strain tensor as obtained from COMSOL. Furthermore, the positions of the unstrained band edges are calculated in dependence of the Sn concentration x_{Sn} as [277]

$$E_{\Gamma,L}^{GeSn} = E_{\Gamma,L}^{Ge}\,(1-x_{Sn}) + E_{\Gamma,L}^{Sn}\,x_{Sn} - b_{\Gamma,L}\,x_{Sn}(1-x_{Sn}). \tag{5.3}$$

Whereas the bowing parameter for the L-valley b_L is taken from literature [276], the bowing parameter for the Γ valley b_Γ is calculated to reproduce the crossover towards direct band gap GeSn at 9% as extrapolated from the experiment in [77]. For the non-underetched WG, these parameters lead to a conduction band offset of ΔE_{cb} = -20 meV (see Fig. 5.9(b)), which is slightly less advantageous as experimentally determined [77]. Owing to the strain-decrease by underetching, the absolute value of ΔE_{cb} increases to 43 meV at the positions where the mode intensity is maximum. This increase of $\sim kT$ at room temperature is, hence, expected to be significant. Furthermore, the strain-variations perpendicular to the waveguide direction lead to a barrier of $\sim$ 10 meV height for electrons in the Γ valley.

In conclusion, the strain-relaxation induced by the undercut causes an increase in electron population for the Γ states. Together with the enhanced mode confinement, this is expected to improve the performance of the laser devices as is discussed in the next chapter.

	Ge	Ref.	**Sn**	Ref.
C_{11} (GPa)	129	[80]	69	[273]
C_{12} (GPa)	48	[80]	29	[273]
C_{44} (GPa)	67	[80]	36	[273]
$a_{c\Gamma}$ (eV)	−10.41	[274]	−6.00	[273]
a_{cL} (eV)	−4.35	[274]	−2.14	[273]
a_v (eV)	1.24	[273]	1.58	[273]
E_Γ (eV)	0.80	[162]	−0.42	[275]
E_L (eV)	0.66	[162]	0.14	[275]
b_Γ (eV)	1.61		determined from [77]	
b_L (eV)	0.68		[276]	

Table 5.2: List of stiffness constants, deformation potentials and band gap energies at 300 K, which are linearly interpolated for the calculation of the strain tensor and the band alignment, besides the unstrained band edges where a bowing described by b_Γ and b_L is taken into account.

5.4 Lasing Characteristics

The underetched FP waveguide lasers are investigated under pulsed optical pumping as described earlier for the passivated WG device. First, the impact of the waveguide engineering is investigated by a comparison of an underetched device and a waveguide laser without undercut. Then, the temperature-dependent properties of underetched FP lasers with Sn concentration between 8.5% and 12.5% are examined.

In Fig. 5.10(a), the light-in versus light-out curves for underetched and non-underetched $Ge_{0.875}Sn_{0.125}$ waveguides are shown at 20 K. The waveguides are 1 mm long and have widths of 10 µm (underetched device) and 5 µm (without undercut). As expected, the improved electronic and optical properties lead to a reduction in threshold excitation density. The threshold decreases by approximately a factor of 2 from $\sim$ 400 kW/cm^2 for the waveguide without underetching to $\sim$ 200 kW/cm^2 for the device featuring an undercut. The deviation from a linear increase in output intensity which can be observed for the underetched WG at excitation densities $\gtrsim$ 700 kW/cm^2 is ascribed to shot-to-shot fluctuations of the pulsed excitation source, which features a binary distribution. Therefore, the second onset is attributed to an excitation power which is sufficient that also the weaker pulses lead to lasing.

The effect of strain-relaxation on the gain medium is apparent when the emission spectra of the two lasers are compared as shown in Fig. 5.10(b). For the undercut device, the lasing peak shifts by $\sim$ 20 meV towards lower energy. From the deformation potential calculation, a red-shift of 40 meV is predicted. The deviation might result from the oversimplification of linearly interpolating the deformation potentials of Ge and Sn. Furthermore, the external differential quantum efficiency (EQE), which is determined by the slope of the increasing output above threshold, increases by $\sim$ 2.3×. This difference is solely attributed to the increase in performance due to the selective underetching as a similar collection efficiency is found for both devices. This can be seen in Fig. 5.11, where the spatial far-field power-distribution is calculated for both waveguide lasers by Fourier-transformation of the respective near-field distributions [96]. The green area indicates the range of angles which are detected by the Schwarzschild optics, yielding coupling efficiencies of $\eta = 45\%$ (no undercut) and $\eta = 38\%$ (undercut). In light of the analysis in ref. [77], we thus obtain an EQE of $\sim$ 3.5% for the underetched waveguide.

The superior performance of the underetched WG has to be ascribed to several aspects, where certainly the most important ones are the increase in energy difference between the Γ and L-states, and the increased modal overlap with the GeSn. The increased mode confinement is especially helpful as mode propagation within the Ge VS contributes to high absorption loss because the 1064 nm excitation source also generates carriers in the Ge. An

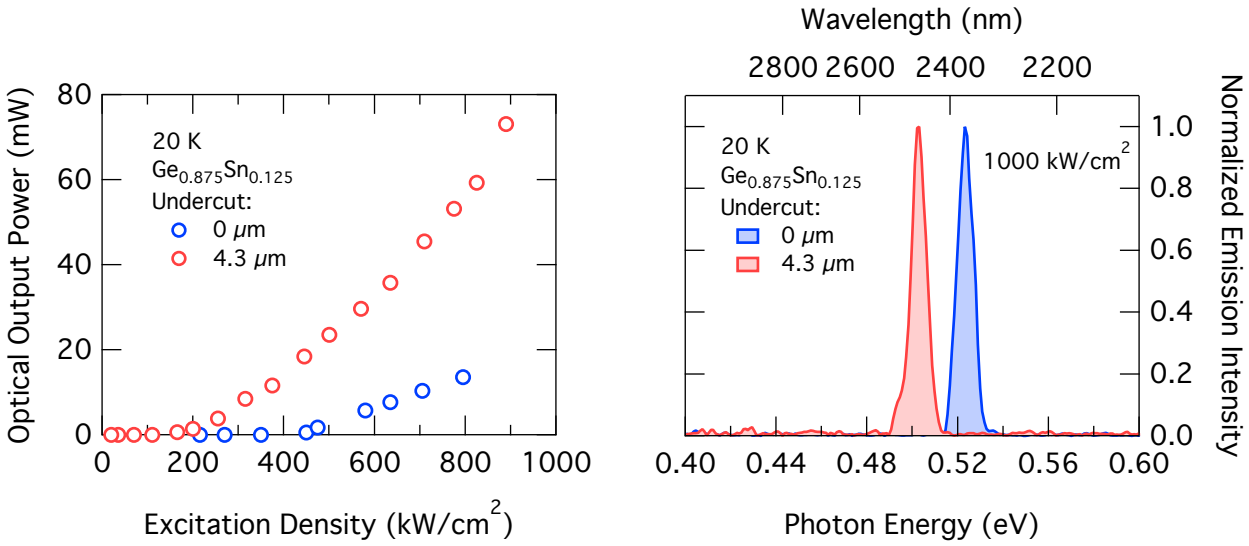

(a) L-L-plot for undercut (red) and non-undercut (blue) $Ge_{0.875}Sn_{0.125}$ cavity at 20 K.

(b) Normalized edge emission spectra for $Ge_{0.875}Sn_{0.125}$ cavity with (red) and without (blue) undercut.

Figure 5.10: (a) Light-in versus light-out plots for underetched and non-underetched $Ge_{0.875}Sn_{0.125}$ waveguides. The improved device properties lead to a reduction in threshold density by a factor of 2 for the undercut waveguide. (b) The strain-relaxation induced by the underetching is evident by the red-shifted lasing peak for the undercut waveguide cavity. The spectra are recorded at 20 K for an excitation density of 1000 kW/cm^2.

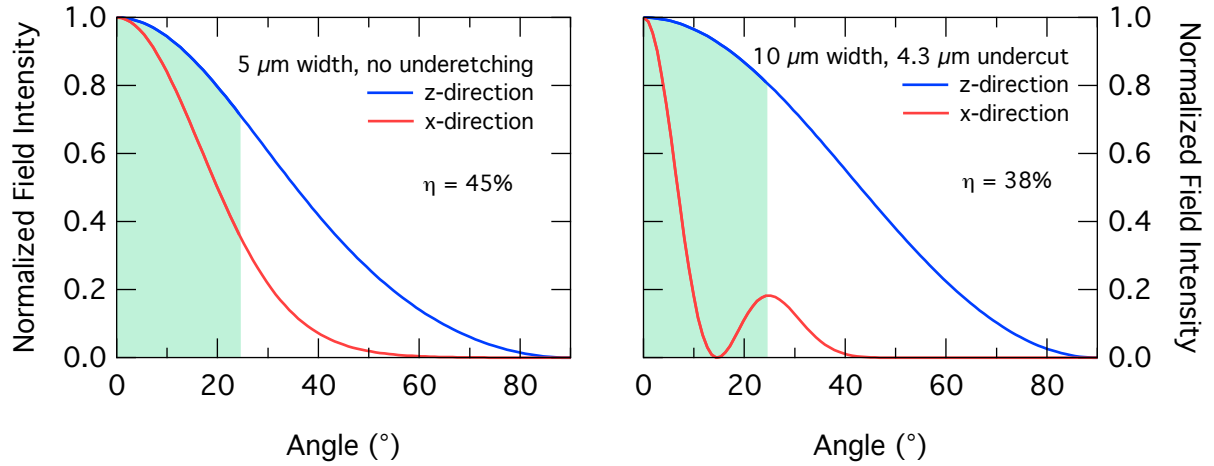

(a) Far-field intensity for non-underetched WG.

(b) Far-field intensity for underetched WG.

Figure 5.11: Simulation of far-field emission for (a) 5 µm wide, non-underetched waveguide and (b) 10 µm wide, underetched waveguide. The field intensity is shown along (blue) and perpendicular (red) to the growth direction. The green area shows the emission detected by the Schwarzschild objective amounting to 45% (no underetching) and 38% (with underetching), respectively.

advantageous effect might also stem from a better charge confinement within the GeSn once the Ge is removed. On the other hand, increased surface roughness due to the isotropic Ge etch might lead to additional waveguide losses. In total, the advantages clearly prevail the disadvantages of the undercut as evident by the enhanced perfomance.

For the investigation of the temperature-dependent laser characteristics, underetched and surface passivated waveguides with different Sn concentration are compared. This enables to compare identical devices with the conduction band offset ΔE_{cb} as the sole difference. In Figs. 5.12(a) and 5.12(b), the L-L characteristics are shown for samples A ($x_{Sn} = 8.5\%$) and C ($x_{Sn} = 12.5\%$) in function of temperature. When the small strain is neglected, the conduction band offsets ΔE_{cb} are calculated with equation (5.3) to 7 meV and −50 meV, respectively. Strikingly, despite the large difference in the conduction band alignment, the threshold excitation density is very similar for both devices at 20 K. This can partially be attributed to a $\sim 2.5\times$ longer non-radiative carrier lifetime for sample A (see chapter 5.5.1), and to the fact that at high carrier densities, the advantage of having a direct band gap system becomes less significant. As an example, for the aforementioned conduction band offsets, the Γ electron density at 25 K and an injected carrier density of 1.0×10^{17} cm^{-3} is calculated as 5.9×10^{-13} cm^{-3} for indirect gap sample A, and $> 9.9\times10^{16}$ cm^{-3} for direct gap sample C. The Γ carrier density is calculated with the model introduced in chapter 5.1. In contrast, at 25 K and an injected carrier density of 2.0×10^{19} cm^{-3}, Γ electron densities of 2.1×10^{17} cm^{-3} and 5.1×10^{17} cm^{-3} are obtained. Therefore, the conduction band alignment does not play a role in determining the lasing threshold due to the large required carrier densities.

The temperature-dependent threshold densities for samples A and C are shown in Fig. 5.12(c). While the threshold is identical at low temperature as discussed above, the increase in threshold starts for sample A for T > 40 K, while the threshold for sample C starts to increase after T > 60 K. Both curves increase following a similar exponential behavior. An abrupt increase for T > 80 K, which is indicated by the dash-dotted line, limits to reach lasing at the achievable pump densities < 1000 kW/cm^2 for sample A, similar to what was observed for the non-underetched, passivated waveguide cavity. For sample C, the exponential increase continues up to 135 K.

In Fig. 5.12(d), the maximum temperature T_{max} where lasing is achieved is shown together with the modal overlap for each device in function of Sn concentration. A linear increase in T_{max} with increasing Sn content is found despite for sample D with $x_{Sn} = 14\%$. The latter is attributed to the decreased modal overlap of 24% leading to larger absorption losses as most of the mode is confined within the Ge, which is a significant loss factor as soon as the Ge is optically pumped [62]. For samples A to C, the increase in T_{max} amounts to $\sim$ 14 K

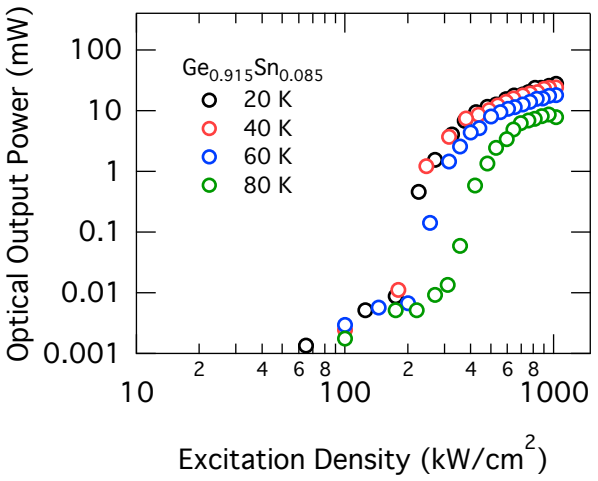

(a) L-L plot for undercut $Ge_{0.915}Sn_{0.085}$ waveguide cavity in function of temperature.

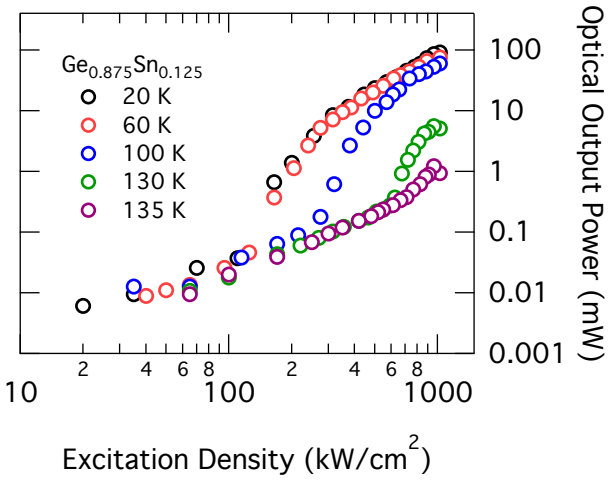

(b) L-L plot for undercut $Ge_{0.875}Sn_{0.125}$ waveguide cavity in function of temperature.

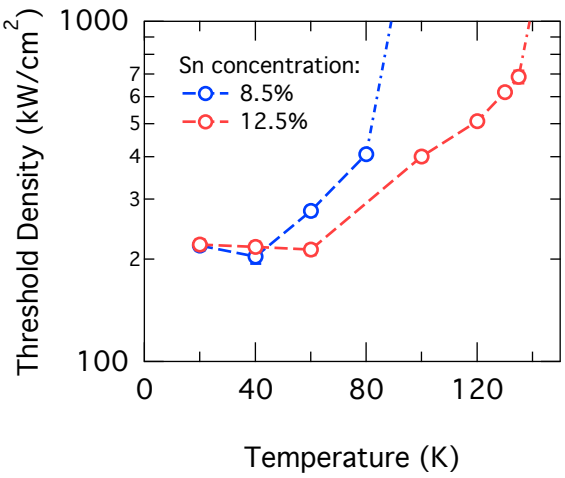

(c) T-dependent threshold density for sample A (blue circles) and sample C (red circles).

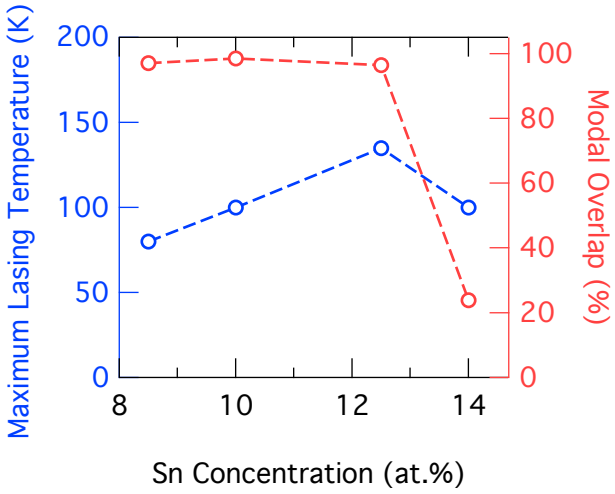

(d) Maximum lasing temperature (blue circles) and mode confinement factor (red circles) for samples A-D in function of the Sn content.

Figure 5.12: The light-in versus light-out characteristics for samples A and C are shown in dependence of temperature in (a) and (b), respectively. While there is no difference in excitation threshold density at 20 K, the maximum operation temperature increases with increasing Sn concentration (d). The trend does not follow for sample D ($x_{Sn} = 14\%$) due to the insufficient modal overlap. The temperature-dependent threshold excitation densities are plotted in (c) for samples A and C.

per 1% Sn. By extrapolation, this predicts that a Sn content of $> 24\%$ is needed to reach room temperature lasing, which significantly exceeds current possibilities of high-quality GeSn epitaxy.

In summary, the underetching of FP waveguide cavities significantly improved the lasing characteristics of GeSn lasers due to an increase in conduction band offset ΔE_{cb} and an improved mode confinement. The undercut reduces the threshold density at 20 K by $\sim 50\%$, but there still remains a relatively high threshold excitation density of ~ 200 kW/cm^2 at 20 K. With an increase in ΔE_{cb}, a gradual yet slow increase of 14 K/1% Sn in maximum lasing temperature T_{max} is observed.

5.5 Pump-Probe Measurements on GeSn Layers

5.5.1 Determination of Carrier Lifetime

To investigate the carrier lifetimes with respect to temperature and conduction band alignment, time-resolved pump-probe transmission measurements are performed as described in chapter 4.2. In contrast to those room temperature experiments, the optical excitation is set up collinear with the synchrotron probe beam to facilitate the use of a cryostat for sample cooling. Due to the spatial resolution, which is currently ~ 20 µm, the measurements are so far restricted to blanket GeSn layers such that the underetched waveguide structures with undercut dimensions in the range below 4 µm could not be investigated.

Broadband transmission spectra through the virtual substrate material which consists of a 2.7 µm Ge layer on Si are shown in Fig. 5.13(a) for pump-probe delay times Δt up to 7.0 ns. As described in chapter 4.4 for a 1.7 µm Ge layer on Si, a strong decrease in transmission due to valence interband absorption and bleaching for energies above the direct gap at 0.8 eV are observed. For longer times Δt, the oscillation maxima approach the unpumped values in terms of energy and transmission due to the decay in charge carrier density. As the Ge is deposited directly on a Si handle wafer, the interference maxima are less pronounced compared to the Ge layers grown on SOI due to the smaller contrast in refractive index. After growth of thick GeSn epilayers on such a Ge VS, plastic strain-relaxation leads to a high density of dislocations which mostly protrude into the Ge layer [77]. To probe the effect of strain relaxation on the non-radiative carrier decay time, pump-probe transmission is measured on a $Ge_{0.875}Sn_{0.125}$ layer with a thickness of 220 nm (c.f. Fig. 5.13(b)).

The carrier decay time is extracted from the time-dependent decay of differential transmission $\Delta T/T$, which is linearly dependent on the charge carrier density [62]. In Fig. 5.13(c), the extracted differential transmission is shown for the Ge VS and the GeSn/Ge layer stack.

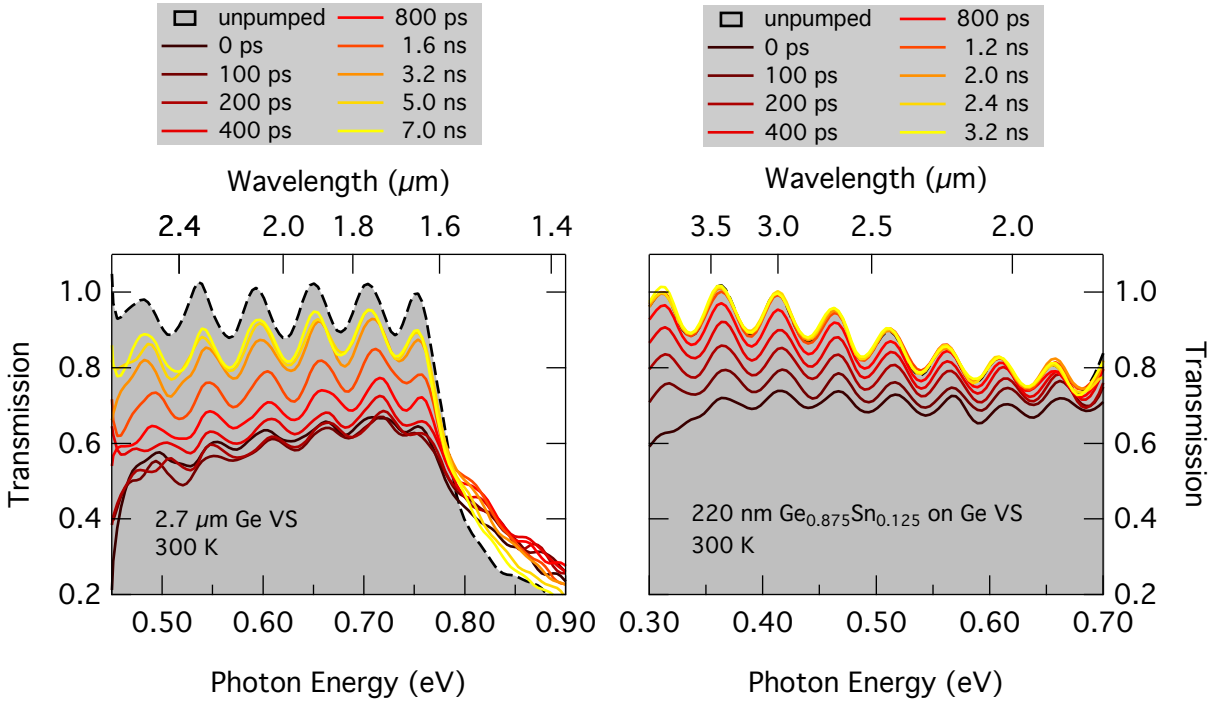

(a) Pump-probe transmission spectra for 2.7 µm Ge VS on Si at 300 K.

(b) Pump-probe transmission spectra for 220 nm $Ge_{0.875}Sn_{0.125}$ on Ge VS at 300 K.

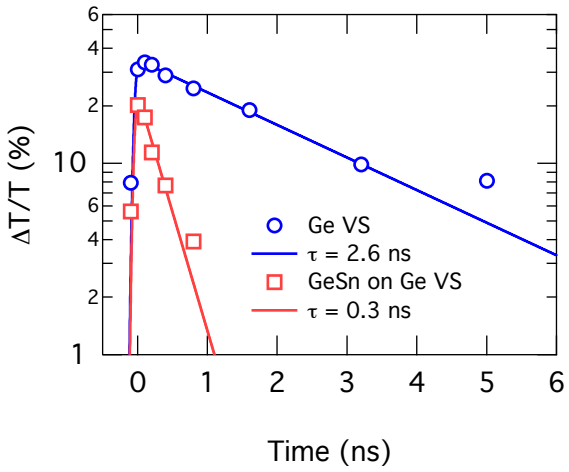

(c) Non-radiative decay times extracted from the relative change in transmission. The obtained lifetimes amount to 2.6 ns (Ge VS) and 0.3 ns (GeSn).

Figure 5.13: Broadband transmission spectra taken at 300 K are shown for varying pump-probe delay times for (a) 2.7 µm Ge virtual substrate (VS) on Si, and (b) 220 nm $Ge_{0.875}Sn_{0.125}$ on Ge VS. The decay times extracted from the relative change in transmission are shown in (c). Due to the defects introduced by plastic strain relaxation, the carrier lifetime reduces drastically from 2.6 ns for Ge VS to 0.3 ns for GeSn/Ge.

The decay times which are extracted from an exponential fit to the data are obtained as 2.6 ns for Ge and 0.3 ns for GeSn/Ge. For the optical excitation at 1064 nm, only ∼ 50% of the pump pulse is absorbed within the GeSn under the assumption of an absorption coefficient of $3{\times}10^4$ cm^{-1} and neglecting bleaching effects, which would lead to a further reduced absorption coefficient. Hence, we expect that more than 50% of the carriers are optically created within the Ge VS. The dislocation density induced by plastic strain-relaxation manifests in a short non-radiative decay time, which is reduced by ∼ a factor of 10 compared to the bare Ge VS. No decay component with a longer time constant is found for GeSn on Ge VS, thus both the carriers in the Ge VS as well as in the GeSn have a short lifetime. These results seem to confirm that the carrier lifetimes for GeSn at room temperature are of the order of a few hundred picoseconds in accordance with the lifetime estimated from the analysis of temperature-dependent PL measurements (see chapter 5.1).

Low-temperature pump-probe transmission spectra for the unprocessed layers of samples A and C, i.e. 800 nm $Ge_{0.915}Sn_{0.085}$ and 560 nm $Ge_{0.875}Sn_{0.125}$, are shown in Fig. 5.14. Here, the major part of the excitation pulse is absorbed in the GeSn due to the increased thickness of the epilayers. With an absorption coefficient of $3{\times}10^4$ cm^{-1} at 1064 nm and neglecting bleaching effects, the ratio of absorbed excitation power is estimated to 90% for sample A and 80% for sample C, respectively. Hence, the observed carrier dynamics should largely originate from carriers generated within the GeSn.

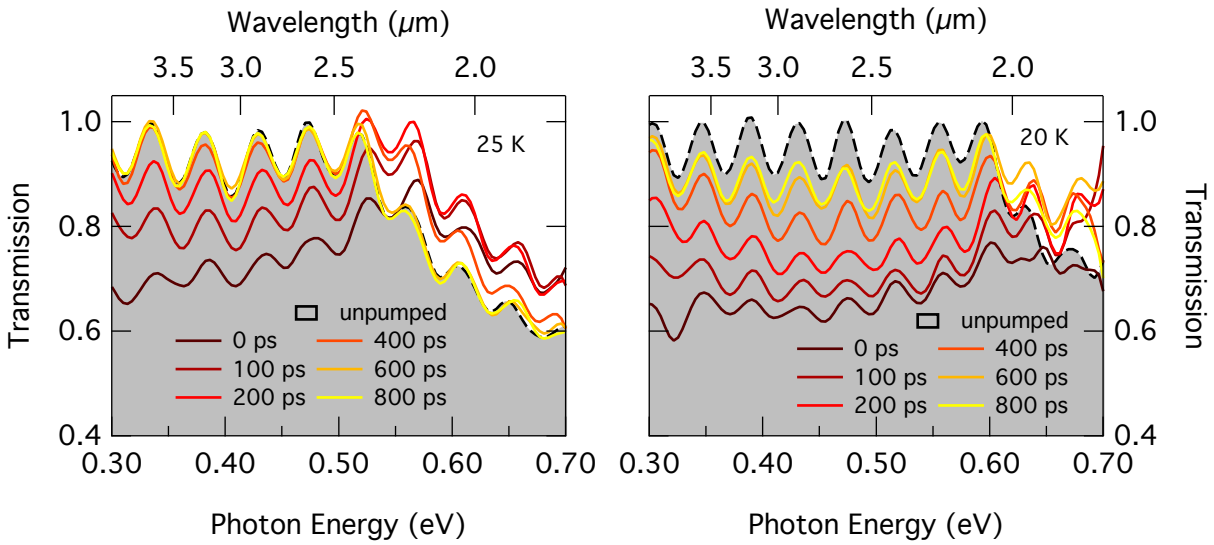

(a) Pump-probe transmission spectra for 560 nm $Ge_{0.875}Sn_{0.125}$ at 25 K.

(b) Pump-probe transmission spectra for 800 nm $Ge_{0.915}Sn_{0.085}$ at 20 K.

Figure 5.14: Pump-probe transmission spectra at low temperature for (a) $Ge_{0.875}Sn_{0.125}$ and (b) $Ge_{0.915}Sn_{0.085}$. The peak excitation density amounts to ∼ 10 MW/cm^2.

As for the measurements before, the spectra show a distinct decrease in transmission due to pump-induced absorption. For sample C, a strong bleaching is observed for transmission > 0.5 eV and a significant gain as evidenced by the spectral increase in transmission at energies just above the direct gap. Between 200 ps and 400 ps, the unpumped transmission is overcome indicating optical amplification, i.e. the material gain exceeds the pump-induced losses. Net gain is not observed for any carrier density for the indirect band gap sample A. Gain and bleaching will be investigated in more detail in chapter 5.5.2. Here, the decay times are extracted to investigate possible differences in dependence of Sn concentration and temperature.

The decay time is extracted from the time-dependent differential transmission $\Delta T/T$. The choice for the transmission rather than the phase-shift of the Fabry-Perot interference pattern as done for Ge/SOI and GeOI (see chapter 4) is motivated in Fig. 5.15. The left panel shows the relative energy shift of local maxima or minima extracted from the spectrum for $Ge_{0.915}Sn_{0.085}$ at 20 K shown in Fig. 5.14(b), while the right panel shows the differential transmission extracted for the same set of local extrema. The data based on the spectral peak extrema yields a large scattering of data due to the small refractive index contrast and the small shift in the range of $< 1\%$. Fitting each data set individually with an exponential decay function, the averaged decay time is obtained with a relative error of $> 50\%$ as (570 ± 300) ps. On the other hand, extracting the relative change in transmission yields much more reproducible data when the decay for different Fabry-Perot extrema are compared. The lifetime is obtained with a relative error of less than 10% as (445 ± 30) ps. Therefore, for the following lifetime investigations the decay will be extracted from the differential transmission due to the superior accuracy.

The extracted time-resolved differential transmission is shown in Fig. 5.16 for samples A and C at 300 K and 25 K or 20 K, respectively. At room temperature, the decay times are extracted as (470 ± 15) ps for sample A and (260 ± 35) ps for sample C. The longer lifetime for sample A can partially be attributed to the difference in layer thickness d: When the lifetimes are translated into the surface recombination velocity (SRV) s as $s \sim d/\tau$ [210] under the assumption of the GeSn/Ge interface being the dominating interface, the SRVs at 300 K are obtained as $s_A \sim (170 \pm 5) \times 10^3$ cm/s and $s_C \sim (215 \pm 29) \times 10^3$ cm/s for samples A and C, respectively. The lower SRV for sample A indicates a better GeSn/Ge interface quality, which is expected due to the reduced compressive strain and, hence, lower dislocation density induced by plastic relaxation. Similarly obtained SRVs for Ge epilayers directly deposited on Si [66] are a factor of 2-4 smaller, which indicates room for improvements for GeSn/Ge interface engineering.

At low temperatures, the non-radiative lifetime for sample A does not show a variation

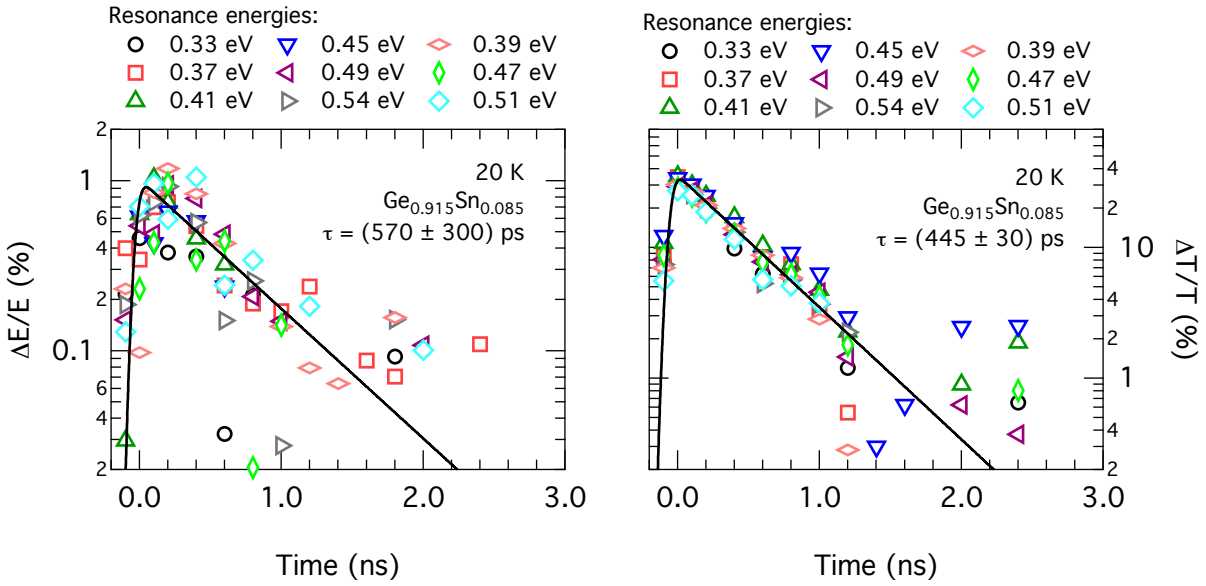

(a) Relative energy shift of spectral extrema in function of time. The lifetime is obtained with a relative error of ∼ 50% due to the large scattering in experimental data.

(b) Relative decrease in differential transmission of spectral extrema in function of time. The decay time is determined with a relative error of < 10%.

Figure 5.15: The charge carrier decay may be extracted from (a) the shift in energy of local maxima and minima, or (b) the reduction of the transmission below the direct band gap. The approaches probe either the real or imaginary part of the refractive index, respectively which are linearly dependent on the charge carrier density. Both cases are compared for $Ge_{0.915}Sn_{0.085}$ at 20 K. Using the $\Delta T/T$-approach delivers the lifetime with a superior accuracy.

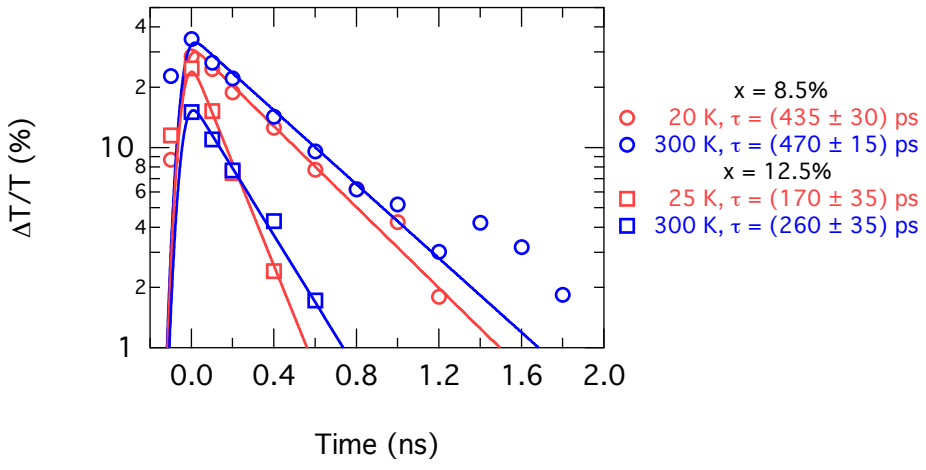

Figure 5.16: Extraction of carrier decay time from time-resolved differential transmission $\Delta T/T$ for $Ge_{0.915}Sn_{0.085}$ (circles) and $Ge_{0.875}Sn_{0.125}$ (squares) at room temperature (blue markers) and 20 K or 25 K (red markers), respectively.

within the accuracy of the experiment with $\tau_{20K} = (435 \pm 30)$ ps. For sample C, the decay time obtained at 25 K yields $\tau_{25K} = (170 \pm 35)$ ps, which is shorter than the decay time measured at room temperature. This observation is in strong contradiction to the temperature-dependent behavior extracted from PL measurements where cooling to 20 K led to an increase in lifetime by one order of magnitude. This deviation might be connected to the different carrier concentration regimes which both experiments are performed under. While for the PL measurements, the continuous-wave optical excitation is ~ 10 kW/cm^2 and, thus, generates carrier densities in the low 10^{17} cm^{-3}, the 100 ps pulses with a peak power of 10 MW/cm^2 create carrier densities of $\sim 10^{20}$ cm^{-3}. One might argue that due to the high carrier densities, Auger recombination is the main electron-hole recombination path. The Auger recombination time depends on the carrier density N_c as $\tau_{Auger} = \left(\gamma_{Auger}\, N_c^2\right)^{-1}$ with the Auger coefficient γ_{Auger}. Since, in spite of the carrier decay being followed for one order of magnitude, no carrier-dependence can be seen in the dynamics, merely Auger recombination cannot be the reason for the short lifetime.

From this lifetime measurement, the threshold carrier density for the direct band gap GeSn lasers at 25 K is estimated to $\sim 2{\times}10^{18}$ cm^{-3}. This still leaves a discrepancy of two orders of magnitude between experiment and predictions from theory, such that the short carrier lifetime cannot fully account for the high threshold carrier densities to reach lasing at low temperatures.

5.5.2 Material Gain and Loss Extraction

In the following, the focus is directed towards the temperature-dependent behavior of gain and bleaching for direct band gap GeSn. In Fig. 5.17, pump-probe transmission spectra for $Ge_{0.875}Sn_{0.125}$ are shown for a peak excitation density of 10 MW/cm^2 for temperatures between 25 K and 200 K. At 25 K, a substantial material gain is observed which manifests in an increased transmission around the direct gap at $\sim$ 0.50 eV - 0.60 eV. For pump-probe delay times of 200 ps and 400 ps, the material gain exceeds the unpumped transmission in a narrow spectral range due to a rapid decay in pump-induced absorption. From 0.5 eV to 0.7 eV, a strong bleaching of the direct gap absorption is observed up to a decay time of 400 ps. Gain and bleaching rapidly drop and at 600 ps, all carriers in the system have recombined, such that the transmission returns to its unpumped state. For increasing temperatures, the bleaching decreases rapidly while only minor variations are observed for the carrier-induced absorption.

Strikingly, for 50 K and 75 K no optical amplification is observed even though lasing could be achieved in non-underetched waveguide cavities under optical pumping. This discrepancy is ascribed to absorption losses in the Ge VS and the different modal overlap between the

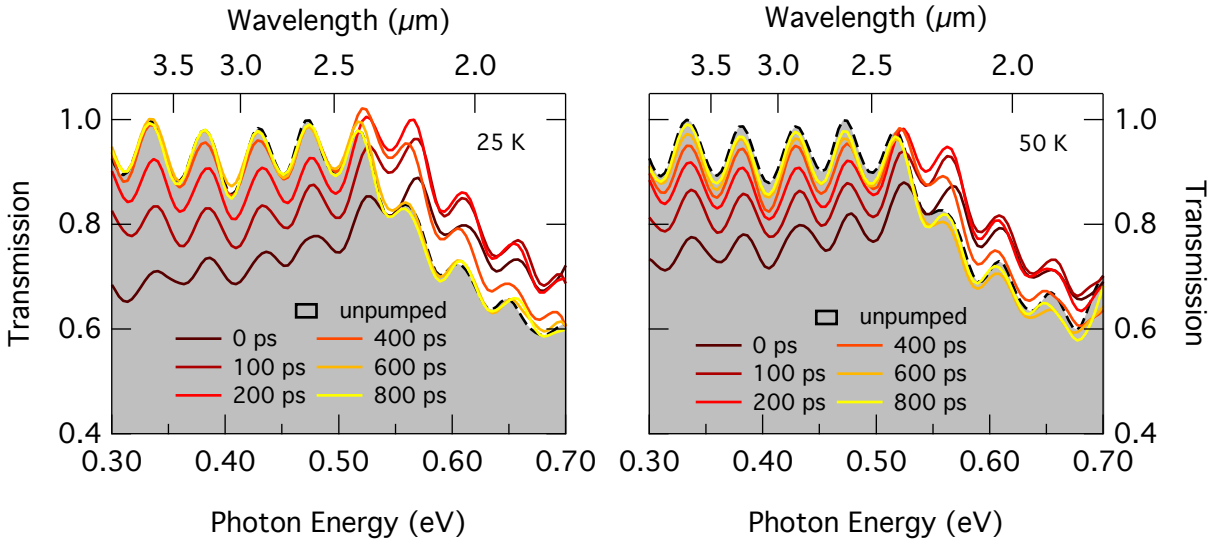

(a) Pump-probe spectra of sample C at 25 K.

(b) Pump-probe spectra of sample C at 50 K.

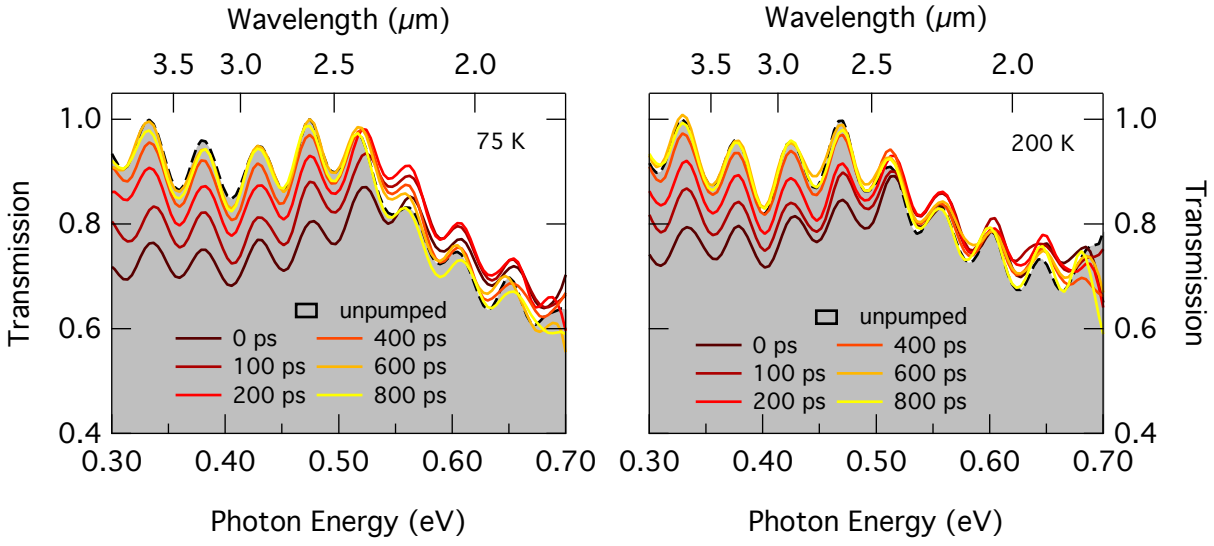

(c) Pump-probe spectra of sample C at 75 K.

(d) Pump-probe spectra of sample C at 200 K.

Figure 5.17: Broadband pump-pump transmission spectra for $Ge_{0.875}Sn_{0.125}$ at temperatures between 25 K and 200 K. The measurements are performed for an excitation density of 10 MW/cm^2.

propagation along the Fabry-Perot waveguide cavity and the normal incidence transmission measurements. For the mode propagation along the non-underetched waveguide cavity, the modal overlap with the GeSn was calculated as $\Gamma = 60\%$. The remaining 40% propagate within the Ge VS such that the total modal gain for the waveguide propagation α_{tot}^{WG} amounts to

$$\alpha_{tot}^{WG} = \Gamma\ \alpha_{GeSn} + (1-\Gamma)\ \alpha_{Ge} = 0.6\ \alpha_{GeSn} + 0.4\ \alpha_{Ge}, \tag{5.4}$$

where α_{GeSn} and α_{Ge} are the absorption for GeSn and Ge, respectively. In contrast, for the normal incidence measurement the absorption loss in Ge is more significant as the total absorption is determined as

$$\alpha_{tot}^{NI} = \frac{d_{GeSn}}{d_{GeSn}+d_{Ge}}\,\alpha_{GeSn} + \frac{d_{Ge}}{d_{GeSn}+d_{Ge}}\,\alpha_{Ge} = 0.17\,\alpha_{GeSn} + 0.83\,\alpha_{Ge}, \tag{5.5}$$

where d_{GeSn} and d_{Ge} denote the GeSn and Ge layer thicknesses.

In Fig. 5.18, the transmission through $Ge_{0.875}Sn_{0.125}$ is modelled via the transfer-matrix-method including injection-related contributions to the real and imaginary part of the refractive index. The absorption loss α_{IVB} is taken from the experimental data at $\Delta t = 200$ ps where the maximum gain or bleaching is observed independent of temperature. The loss function α_{IVB} is assumed to be the same at all temperatures and its dispersion is given in dependence of photon energy E as $\alpha_{IVB} = 2550\ \mathrm{cm}^{-1} - 2420 \times E\ \mathrm{cm}^{-1}/\mathrm{eV}^{-1}$. The change in the real part of the refractive index is accounted for by the Drude model introduced in chapter 4.3. For the imaginary part of the refractive index, the interband absorption from Fig. 5.3 is added to the loss function α_{IVB}. The simulations are performed without carrier injection (grey, filled area) and for injected electron densities of 1×10^{17} cm^{-3}, 1×10^{18} cm^{-3} and 1×10^{19} cm^{-3}. The resulting electron densities at the Γ valley are given in the figures.

For a total electron density of 1×10^{17} cm^{-3}, the density is too small to induce a bleaching spanning from 0.5 - 0.6 eV. At a density of 1×10^{19} cm^{-3} injected electrons, the simulated bleaching and optical amplification is by far exceeding the experimentally observed values. The best description of the bleaching at $\Delta t = 200$ ps is obtained if a total electron density of 1×10^{18} cm^{-3} is assumed. While the observed gain and bleaching suggests an electron density in the order of 1×10^{18} cm^{-3}, this is not in accordance with either the excitation power density or the observed pump-induced absorption. From the excitation power of 10 MW/cm^2, a carrier density of the order of 10^{20} cm^{-3} is estimated to be injected at $\Delta t = 0$. After 200 ps, this carrier density decays to $\sim 1\times10^{19}$ cm^{-3} under the assumption of $\tau = 170$ ps. If we assume that the intervalence band absorption for GeSn is of the same order of magnitude as for Ge, the experimentally determined absorption loss of ~ 1400 cm^{-1} at 0.5 eV relates to a carrier density in the low 10^{19} cm^{-1} when the cross sections and energy disperson from [62] are used, which is in accordance with the density estimated based on the excitation density and non-radiative lifetime. This suggests that the electrons are not occupating the Γ states as predicted by the quasi-equilibrium approximation, but are rather distributed either into higher Γ states or into the high density of states at the L-valley. Furthermore, due to the strong excitation far above the band gap, a large phonon population is introduced during thermalization of the carriers into the band edges. This high phonon occupation might promote fast intervalley processes between the Γ and L-valleys, with the process L→ Γ being

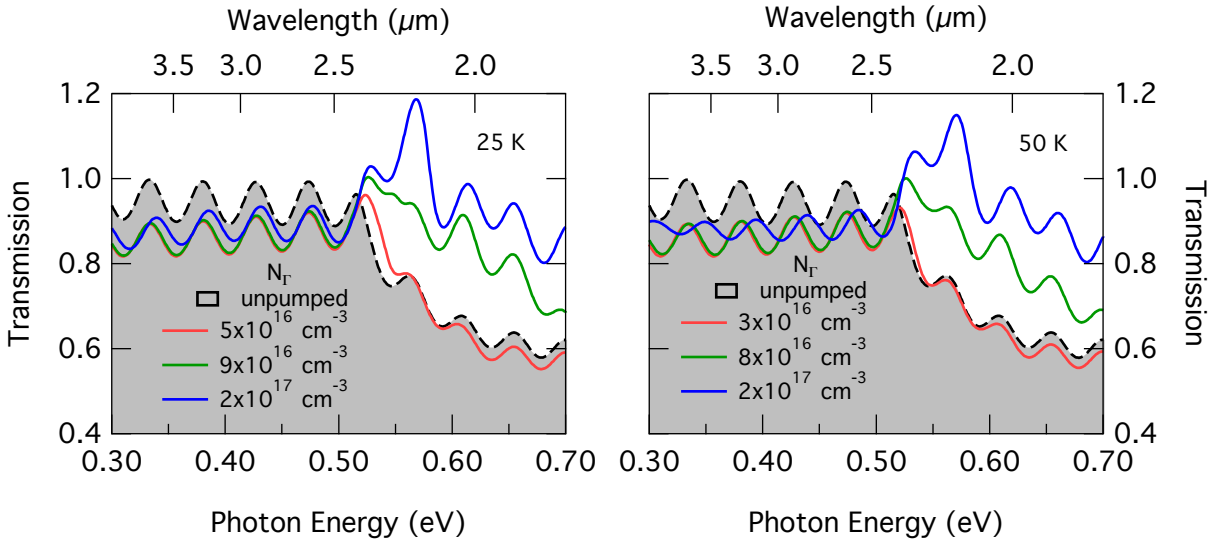

(a) Modelled transmission for different carrier densities N_Γ at 25 K.

(b) Modelled transmission for different carrier densities N_Γ at 50 K.

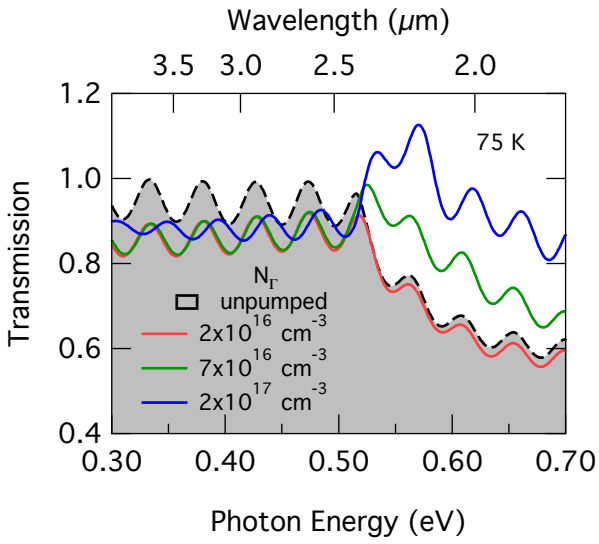

(c) Modelled transmission for different carrier densities N_Γ at 75 K.

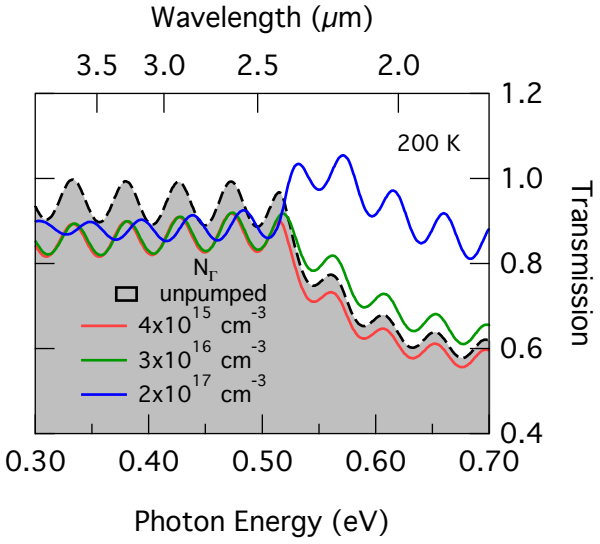

(d) Modelled transmission for different carrier densities N_Γ at 200 K.

Figure 5.18: Simulation of pump-probe transmission spectra for $Ge_{0.875}Sn_{0.125}$ at temperatures between 25 K and 200 K at $\Delta t = 200$ ps. The parasitic absorption is taken from the experimental spectra at $\Delta t = 200$ ps. The interband absorption is calculated for total electron densities of 1×10^{17} cm^{-3} (red), 1×10^{18} cm^{-3} (green), and 1×10^{19} cm^{-3} (blue). In the figures, the respective electron density at the Γ valley is given.

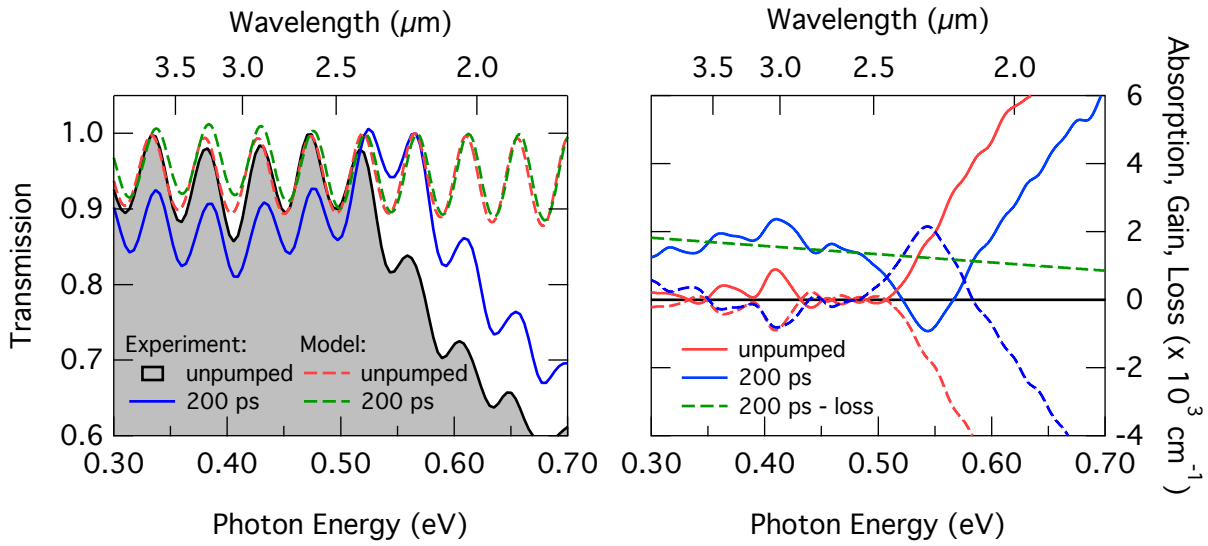

(a) Experimental transmission (solid lines) and model without absorption (dashed lines).

(b) Extracted total absorption (full lines), deduced material absorption (dashed red and blue lines) and linear pump-induced loss (dashed green line).

Figure 5.19: Procedure to extract material gain and parasitic absorption losses from transmission measurements. The routine is exemplarily shown at $\Delta t = 200$ ps and for the unpumped transmission. From the modelled transmission without absorption, the total absorption is extracted by a root-finding algorithm.

slow because of the small density of final states.

In order to quantify the difference for interband gain and absorption loss in function of temperature, the former are extracted for sample C (i.e. the material used for the first demonstration of lasing in GeSn in [77]) at 25 K. Generally, the best suitable measurement geometry is under the Brewster angle such that the interference effects can be suppressed [62]. However, due to the experimental constraints with sample cooling in a cryostat this was not possible here. Instead, a method is developed where the absorption is a free fitting parameter and is extracted by fitting the calculated transmission without absorption to the experimental data.

The procedure starts with the unpumped transmission, which is calculated based on the transfer-matrix-method with the thicknesses and dielectric constants as input parameters. At this step, no absorption is taken into account. In Fig. 5.19(a), the dashed, red line shows the modelled unpumped transmission at 25 K which yields a good agreement with the experimental data (grey, filled area) especially in the vicinity and below the direct band gap. Then, the total absorption is extracted by a root-finding algorithm, which yields the

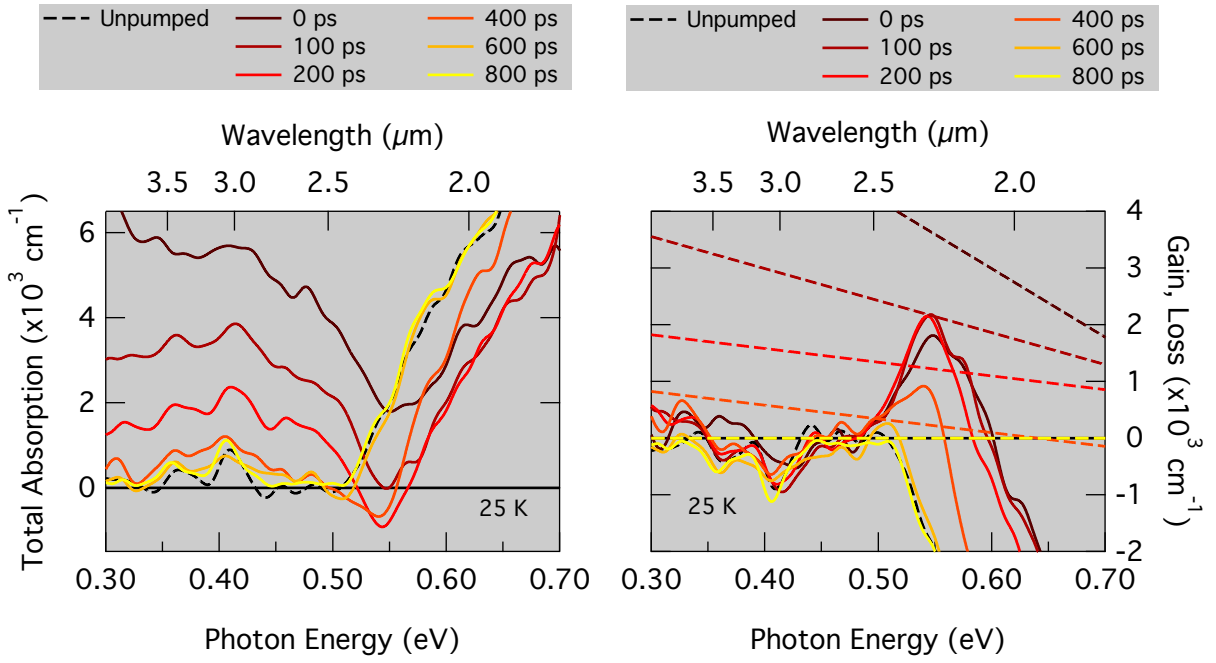

(a) Total absorption at 25 K. Negative absorption at $\Delta t = 200$ ps, 400 ps indicates a net gain.

(b) Material gain (solid lines) and parasitic loss (dashed lines) extracted from the spectra in (a).

Figure 5.20: Total absorption for $Ge_{0.875}Sn_{0.125}$ for varying pump-probe delay times. The absorption is obtained with the imaginary refractive index κ as free fitting parameter for modelling the transmission through the layer stack.

imaginary refractive index κ for which the model fits to the experimental data. To extract the absorption from pumped spectra, the initial transmission is calculated for an injected carrier density N_c, which is chosen to match the oscillation maxima and -minima of the experiment. An example is given in Fig. 5.19(a) for $\Delta t = 200$ ps with the experimental and modelled transmission as solid, blue and dashed, red line, respectively. For the transmission model at $\Delta t = 200$ ps, a carrier density of $7{\times}10^{18}$ cm^{-3} is assumed.

The resulting absorption spectra are plotted in Fig. 5.19(b) as solid red (unpumped) and blue ($\Delta t = 200$ ps) lines. The deviation of the oscillation depth between experiment and model results in an artificial increase in absorption at ~ 0.4 eV. Otherwise, the unpumped absorption shows the expected behavior with zero absorption below the direct band gap and a steep increase for photons with energy above the direct band gap at ~ 0.5 eV. The total absorption for the transmission with optically excited carrier injection can be separated into a linear absorption loss α_{loss} and the interband material gain $g_{IB} = -\alpha_{IB}$, which is defined as the negative interband absorption. The green, dotted line depicts the extracted linear loss function. After subtraction of α_{loss} from the total absorption and representation

as negative absorption, the interband gain is shown as broken, blue line. The negative absorption spectrum extracted from the unpumped spectrum is shown as broken, red line. Both spectra match well for energies below the band gap, including the mentioned artifacts, which indicates that the loss function is correctly determined. Above the band gap, gain with a peak of 2000 cm^{-1} builds up and exceeds the parasitic losses (dashed green line), which indicates optical amplification.

In Fig. 5.20(a), the analogously determined absorption spectra are shown for $Ge_{0.875}Sn_{0.125}$ at 25 K for delay times up to 800 ps, when the system has fully recovered. The unpumped absorption is depicted as broken, black line. After determination of the loss function for each of the spectra, the separated gain and loss functions are shown in Fig. 5.20(b). For $\Delta t = 0$ ps, a peak gain of ~ 2000 cm^{-1} is obtained. However, the loss significantly exceeds the interband gain, such that a net gain and, hence, optical amplification does not set in. Interestingly, there is a fast decay of the losses to less than 2000 cm^{-1} within 400 ps, while within the same time interval the interband gain does not decrease. On the contrary, the maximum peak gain is observed for $\Delta t = 100$ ps and 200 ps, while the loss at 0.55 eV decreases from ~ 3500 cm^{-1} to ~ 1000 cm^{-1}. Obviously, the density of electrons at the Γ valley, which determines the gain intensity, remains constant. Due to that non-simultaneous decrease of electrons at Γ and holes, a net gain can build up. In comparison, for the classical direct band gap system InGaAs, the interband gain was found to decrease by $\sim 30\%$ within 250 ps [198]. This observation of Γ states remaining filled over a time period of ~ 200 ps is another hint pointing towards a non-equilibrium condition for the conduction band.

With the new results gained from the pump-probe measurements, we revisit the high excitation threshold densities for the optically pumped GeSn lasers. At 200 kW/cm^2 excitation density and a lifetime of 170 ps, a threshold carrier density of $\sim 2{\times}10^{18}$ cm^{-3} is estimated from the lasing experiments for a 560 nm thick GeSn layer. To correct the expected threshold density according to the experimentally observed reduced Γ population, the interband absorption for a GeSn alloy with $\Delta E_{cb} = -25$ meV is calculated with taking only 10% of the injected electrons into account for the determination of the electron quasi-Fermi level. For the losses, all injected carriers are accounted for with the absorption cross-sections for Ge. According to the model, transparency is reached at an injected carrier density of $1{\times}10^{17}$ cm^{-3}, which is an order of magnitude lower compared to the experiments. The discrepancy might be ascribed to a combination of effects, which are not accounted for in the model. These effects include an increased carrier temperature due to the strong excitation, larger absorption losses for GeSn than for Ge, cavity losses due to scattering at the sidewall or the remaining Ge pillar, or carrier leakage and diffusion into the Ge.

5.5.3 Outlook

For future experiments to clarify the above presented results, certain adaptions in terms of material layout or experimental setup might be of profit, as well as additional experimental approaches:

As the electron population in the conduction band seems not to be distributed according to the quasi-equilibrium approximation, the investigation of the occuring processes is highly rewarding and essential to gain a deeper understanding of the limitations to reach room temperature lasing with GeSn. To investigate such fast processes like carrier thermalization and intervalley scattering, time-resolved spectroscopy with time resolution in the ps or fs range would be the right choice.

If the limitations were due to a non-equilibrium electron distribution caused by hot electron injection and the subsequent generation of a high density of phonons, the observed limitations should not prevail if the electrons are resonantly pumped into the Γ valley. For such an experiment, pump-probe measurements face difficulties as the pump- and probe energies are spectrally too close to each other. This might be solved by an off-axis excitation. Another approach would be the resonant excitation of Fabry-Perot waveguide cavities where the excitation beam and the detected emission are perpendicular to each other, such that scattered light from the laser into the detection path can be minimized.

Due to the small refractive index contrast between GeSn and Ge or Si, the Fabry-Perot oscillations are not strongly modulated. From the experience of investigating Ge layers grown on SOI or transferred onto an oxide, a strong modulation was found to be helpful to reach a high sensitivity for the determination of the carrier density. GeSn layers transferred onto an oxide or epitaxially grown on e.g. GeOI would offer the same sensitivity.

For the preceding experiments, charge carriers were optically injected into the GeSn and the Ge VS due to the excitation wavelength of 1064 nm. Performing similar pump-probe measurements on underetched structures would on the one hand help to only inject carriers into the GeSn layer and, therefore, investigate the GeSn properties without the losses ascribed to the Ge VS. On the other hand, if the experiments were to be performed on the free-standing part of a not fully underetched structure like the undercut waveguide cavities presented in the first part of this chapter, then a high refractive index contrast would be achieved as well. However, this proposal is only valid under the assumption that an underetching in the order of 20 - 30 μm can be achieved without a degradation of the material.

The extraction of the spectral gain and loss functions does not profit from the multiple interferences, but the oscillations rather add an unwanted complexity to the analysis. A better access to gain and loss is achieved if the measurements were done under the Brewster angle, such that the oscillations do not occur. However, this increases the complexity for

the measurement geometry if the measurements are to be performed at liquid helium temperatures in a cryostat.

A solution for carrier injection only into the GeSn without additional fabrication efforts would be to use an excitation source at a longer wavelength. An optical excitation at 1.5 μm would lead to the creation of virtually all charge carriers in the GeSn, such that losses due to absorption in the Ge VS can be suppressed. Similarly, for excitation at much shorter wavelengths such as e.g. 532 nm, the whole excitation power is absorbed in the GeSn layer due to the high absorption coeffient and the, thus, resulting penetration depth in the range of only a few tens of nm.

Due to the difference in wave propagation and modal overlap, the total absorption measured in normal incidence through the GeSn/Ge/Si layer stack does not correspond to the modal gain obtained for propagation along a Fabry-Perot waveguide cavity. For an investigation of the very same configuration, the single-mode transmission through the waveguide can be measured while the cavity is homogeneously excited over the full length as for the experiments for optically excited FP waveguide cavities. To that end, the synchrotron probe beam has to be coupled into the FP waveguide via the facet and is detected from the back facet of the waveguide. However, this is difficult to achieve with a high coupling efficiency which is needed to acquire spectra with a reasonable signal-to-noise ratio.

5.6 Summary

The impact of surface states was investigated by comparing a passivated GeSn FP laser with an unpassivated device from the same epilayer. While the temperature-dependent threshold density was changing with surface passivation, the threshold excitation at 20 K remained unaffected. Furthermore, the maximum lasing temperature could not be increased, such that it was concluded that unsaturated surface states do not play a prominent role in either the threshold density or the maximum operation temperature.

To study the impact of the conduction band alignment, Fabry-Perot waveguide cavities were fabricated from GeSn layers with Sn concentration between 8.5% and 14.0%. The selective removal of the underlying Ge virtual substrate was shown to reduce the lasing threshold and to increase the maximum lasing temperature. This is ascribed to an increased offset between the Γ- and L-valleys due to strain relaxation caused by the undercut, and an increased mode confinement factor. While the maximum lasing temperature could be increased, the difference between 8.5% and 12.5% Sn is only 55 K despite an increase in conduction band offset by > 50 meV. Furthermore, the analysis of the increase in threshold density in function of temperature revealed a similar exponential increase independent of Sn

concentration. The temperature range for this exponential increase, however, was found to differ. The regime of exponential increase ended with a rapid increase of threshold density above the accessible excitation power. The temperature where this limiting increase occured could be increased by higher Sn concentrations. With the underetched waveguide cavities, lasing could be achieved up to a maximum temperature of 135 K.

The non-radiative lifetimes were investigated by time-resolved transmission measurements. The decay time in Ge was found to decrease by one order of magnitude when GeSn was deposited on top. This decrease is attributed to the highly defective interface, which originates from plastic strain-relaxation in the GeSn layer.

While an indirect determination of the lifetime based on temperature-dependent PL measurements indicated an increased lifetime for low temperatures, the synchrotron-based measurements revealed no significant difference between 300 K and 20 K for 8.5% Sn concentration. For a higher Sn content of 12.5%, where an inferior interface quality is expected, there is a decrease in the decay time for low temperatures in contrast to the results from PL experiments. The lifetimes for GeSn were determined to be in the 200 ps to 400 ps range. The short lifetime at 20 K, which differs by approx. one order of magnitude compared to the PL measurements, is one aspect for the high threshold required to start lasing. However, the discrepancy between experiment and model cannot be fully attributed to the lifetime which is shorter than previously assumed.

The gain and loss was extracted from pump-probe transmission measurements for an epilayer with 12.5% Sn at 25 K. It was found that the electron density in the Γ valley does not seem to decrease over the first 200 ps, whereas the broadband absorption decreases by a factor of 3.5 within the same time. Furthermore, the electron density either inferred from the broadband absorption or from the excitation density is one order of magnitude larger than the electron density which is predicted form theory for the observed interband gain. Therefore, it seems that the electron distribution between Γ and L valleys is not in equilibrium.

5.7 Compendium

In this chapter, direct band gap GeSn waveguide lasers and unprocessed epilayers were investigated. The focus was directed towards the effect of unsaturated surface states, the conduction band offset and the non-radiative carrier lifetime on the high threshold for GeSn lasers and the limitation towards low temperature operation, whereas room temperature lasing is predicted by theory for the investigated alloys. Two of our observations give a strong indication that the theoretical model has to be adjusted: First, the lifetime at measured at

excitation densities similar to the lasing experiments are very short and, thus, the carrier concentration is one order of magnitude lower than previously anticipated from the analysis of temperature-dependent PL measurements under continuous-wave excitation. Second, the gain spectrum suggests that the electrons at Γ are not in thermal equilibrium with those at the L-states. Remarkably, this is similar to what was inferred from the analysis of the PL emission efficiency in highly-strained Ge.

6

Supplements and Outlook

Contents

During the course of this work, several technological challenges could be solved and scientific questions answered. Nevertheless, there remain open tasks and novel approaches to work on, from which some will briefly be presented in the following.

6.1 Covalent Bonding of Strained Ge Bridges onto Substrate

Bonding the strain-enhanced microbridge structures onto the underlying substrate offers distinct improvements compared to being suspended in air. On the one hand, heat can dissipate into the substrate such that the device temperature under optical or electrical injection can be reduced [145]. On the other hand, if a strong bond of the Ge layer with the substrate can be achieved, then new possibilities arise for device fabrication. The definition of an optical cavity could e.g. be performed by dry etching after an unpatterned constriction was attached to the substrate, and contacting the pads with metal electrodes is facilitated. Furthermore, the overall mechanical stability against vibrations etc. would increase. But the bonding does not only have advantages as it reduces the refractive index contrast between the gain material and its surroundings. This drawback can be mitigated by sophisticated substrate materials with two oxide layers (see chapter 3.2.4) or by using thicker Ge layers such that the optical mode is well confined within the Ge.

The first attempt to bond and post-process a strain-enhanced structure was reported

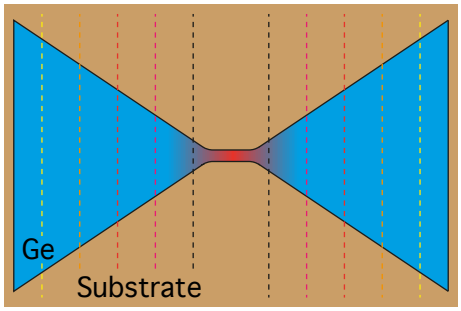

Figure 6.1: Schematic illustration of experimental determination of bond strength. After annealing of the Ge bridge which is brought into contact with the underlying substrate, the pads are removed via dry etching in varying distances d from the strained constriction as indicated by the dashed lines.

by Sukhdeo *et al.* where the pads of a biaxially strained constriction were removed by dry etching after attaching the Ge layer onto SiO_2 using capillary forces [157]. Subsequently, an anneal at 350°C was performed to increase the bonding strength. After post-patterning, a decrease in strain and an increased strain inhomogeneity was observed due to the introduced free surfaces. An experiment to determine and optimize the bond strength between Ge and the underlying substrate is proposed and schematically depicted in Fig. 6.1. After processing a uniaxially stressed microbridge, the structure is attached to the underlying substrate by van-der-Waals forces. Subsequently, the structure is annealed with given parameters to maximize the bond strength. After the annealing process, the pads are removed at varying distances d from the strained central constriction by dry etching. As an indicator for the achieved bond strength, the strain in the constriction is measured via Raman spectroscopy.

6.2 Tensile-Strained GeSn Quantum Well by Strain Redistribution

In chapter 5, it was shown that the material quality for GeSn alloys is significantly inferior compared to Ge layers on Si evidenced by the determination of the non-radiative lifetime. The reason is the high density of dislocations induced by plastic strain-relaxation. The relaxation of the compressive strain is required to reduce the conduction band offset ΔE_{cb}. Superior material quality is expected if GeSn is grown coherently on Ge such that defect creation due to strain-relaxation is avoided. Then, other techniques are required to reduce the large compressive strain. To achieve an improved strain distribution, the strain-enhancement technique discussed in chapter 3 can be employed for GeSn quantum wells (QW) embedded between Ge barriers.

As an example, we theoretically investigate GeSn QWs with 8% Sn coherently grown on Ge VS with Ge barriers. The Ge layer is under a biaxial tensile strain of 0.16%. Such structures have been investigated in optically [270] and electrically pumped devices [251]. The in-plane compressive strain for such QWs amounts to −1.0%. Following the approach described in chapter 5.3.3, this corresponds to $\Delta E_{cb} = 87$ meV. With this conduction band alignment, no lasing could be achieved under optical excitation at room temperature [270] for a single QW. This multilayer could be patterned into a microbrige structure and released from the substrate by selective underetching. The underetching could either be done via CF_4 chemistry utilizing a GeSn etch stop layer [268, 270], by removing the Si substrate in KOH [73]. If the Ge bridge reaches a strain of $\varepsilon_{xx} = 3.0\%$, the in-plane strain in the GeSn QW reaches $\varepsilon_{xx} = 1.7\%$ along the stress direction and $\varepsilon_{yy} = -2.0\%$ perpendicular to the stress. The strain in growth direction is calculated from [138] as

$$\varepsilon_{xx} = \frac{C_{11}\sigma_{xx} + C_{12}\sigma_{xx} - C_{12}\sigma_{yy} - C_{12}\sigma_{zz}}{C_{11}^2 + C_{11}C_{12} - 2C_{12}^2}, \tag{6.1}$$

$$\varepsilon_{yy} = \frac{C_{11}\sigma_{yy} + C_{12}\sigma_{yy} - C_{12}\sigma_{xx} - C_{12}\sigma_{zz}}{C_{11}^2 + C_{11}C_{12} - 2C_{12}^2}, \tag{6.2}$$

$$\varepsilon_{zz} = \frac{-C_{12}\sigma_{xx} - C_{12}\sigma_{yy}}{C_{11}^2 + C_{11}C_{12} - 2C_{12}^2}. \tag{6.3}$$

The stiffness constants C_{ij} for GeSn are linearly interpolated as described in chapter 5.3.3, there is no stress in growth direction as expressed by $\sigma_{zz} = 0$ and the in-plane strain components ε_{xx} and ε_{yy} are inserted as given above. This leads to a small tensile strain along the growth direction $\varepsilon_{zz} = 0.1\%$. For the conduction band alignment, this calculated strain tensor yields $\Delta E_{cb} = 27$ meV, such that the offset between Γ and L-states can be significantly reduced by 60 meV while maintaining highly crystalline material quality.

For uniaxial tensile stress as discussed above, the in-plane strain component perpendicular to the applied stress is negative which limits to reach a larger hydrostatic strain. A larger gain in hydrostatic strain can be achieved when a biaxial tensile stress is induced by strain-redistribution as shown in [140, 141]. If 1.5% biaxial tensile strain is induced in a Ge structure, the incorporated GeSn QW exhibits in-plane tensile strain of 0.25%. Therefore, the biaxial strain is converted from −1.0% compressive strain into a small tensile strain. The strain-component along the growth direction follows as −0.20%. This strain tensor translates into a conduction band offset of $\Delta E_{cb} = -3$ meV. Therefore, a combination of coherently grown GeSn QWs in Ge and strain redistribution offers the possibility to achieve direct band gap GeSn with a significantly increased material quality compared to partially strain-relaxed

layers. This approach can be extended to the use of SiGeSn barriers which allows for an increased confinement within the GeSn QW and an increased prestrain depending on the concentration of Si, Ge and Sn.

6.3 In-Plane Transmission Through Strained Ge Microbridge

Pump-probe transmission measurements are a powerful tool to investigate gain, loss and the carrier lifetime as shown in chapters 4 and 5. For the transmission measurements on strained Ge microbridges (see chapter 4.6), it was observed that the spectral features significantly differ from spectra on blanket layers due to a complicated coupling of the synchrotron probe beam to the small, suspended structure. While the carrier lifetimes could be extracted, an interpretation of the data to extract gain and losses was hampered. However, a deeper insight into the strain-dependent changes in gain and loss would be favorable to prepare the final steps for the realization of a laser based on tensile-strained Ge. To investigate the absorption of Ge microbriges, in-plane transmission measurements are proposed. These measurements could be realized by two different types of coupling strategies.

By etching trenches into the pad, a waveguide can be realized which does not alter the strain field in the constriction similar as for the cornercube cavity presented in chapter 3.5. Then, the probe beam can be coupled into the waveguide facet and is guided to the strained constriction. After the constriction, another symmetric waveguide collects the signal which can be detected from the end facet. Due to the reduced band gap in the strained constriction, the investigated wavelength range can propagate through the relaxed Ge without absorption losses as long as no charge carriers are generated.

A second approach is to measure the in-plane transmission through the constriction by utilizing grating couplers. Grating couplers offer a reduced experimental complexity as the measurements can be done in a normal-incidence configuration. However, the grating couplers lead to an additional wavelength dependence and can limit the accessible wavelength range depending on the design.

7

Summary and Conclusion

The overall topic of this thesis is devoted to gain insight about the physics of direct band gap Ge systems in form of tensile-strained Ge and GeSn alloys. Those systems are uttermost prospective candidates to realize an efficient, CMOS-compatible laser for monolithic integration on Si.

The electron distribution within the conduction band was calculated in function of strain from 8-band k·p theory and the generally applied deformation potential parameters. The same model was found to fail to reliably predict the intervalence band absorption strength, which is known to be the main loss factor for Ge-based lasing. Because of the lack of corresponding experimental data, the loss for the calculation of the net gain was extrapolated from the experimental absorption cross-sections of weakly biaxially strained Ge. Using this input, transparency was simulated as a function of the directness of the conduction band alignment. It was found that transparency can be reached for intrinsic Ge already before a direct band gap is achieved (4% strain) at injection densities larger than $1{\times}10^{19}$ cm^{-3}. The requirement can be relaxed by n-doping such that transparency can be reached for strain below 3.0% at 10× lower excitation densities. However, doping will have an impact on the non-radiative carrier lifetime and state broadening, as shown for the former by pump-probe experiments.

Ge microstructures with up to 3.6% uniaxially loaded strain in a 500 nm × 6 μm × 1 μm constriction were routinely obtained by applying our strain-redistribution technique to GeOI substrates developed by CEA-LETI. Photoluminescence spectroscopy revealed an increasing emission intensity for an increasing strain as expected by theory due to the enhanced population of the Γ valley. Furthermore, an efficient drift of carriers was observed from charge carriers which are excited in the non-strained volume and radiatively recombine in the highly strained volume.

It was demonstrated that cooling Ge below room temperature increases the tensile pre-strain up to 0.07% due to the difference in thermal expansion coefficients of Ge and

Si. Temperature-dependent PL measurements on Ge microbridges confirmed this behavior, which was substantiated by comparing the extracted direct gap energies with the emission energy calculated from mechanical FEM simulations and a tight-binding calculation of the strain-dependent band edges. Upon cooling, the electrons are redistributed between the conduction band valleys such that for indirect structures, the direct gap emission vanishes at low temperatures, whereas the emission intensity increases for fundamentally direct gap Ge. This characteristic behavior was observed in temperature-dependent PL on microbridges, such that the crossover from an indirect to a fundamentally direct band gap configuration is attributed to a strain along [100] between 4.0% and 4.5%.

Optical microcavities were incorporated into the microbridge geometry by dry-etching reflectors into the unstrained pad regions. The introduced mirrors did not alter the strain in the constriction. At 50 K, PL was measured on a cornercube cavity structure with a strain of 4.9%, i.e. direct band gap Ge integrated into a cavity. The signature of the cavity was observed in form of a strong modulation of the emitted signal yielding a maximum Q-factor of 530. However, no sign of stimulated emission could be observed neither under continuous-wave nor under pulsed excitation at 532 nm or 1064 nm, respectively. We characterized the PL intensity in absolute terms and found a deviation of $\sim 30\times$ from published recombination parameters and the experimentally determined non-radiative lifetime. This finding could become the key to understand the underperformance of the strained Ge system in terms of lasing under non-resonant pumping.

The material quality of the Ge epilayers and strained Ge microbridges was accessed via their carrier lifetimes as extracted from time-resolved pump-probe transmission measurements, which give direct insight about the carrier density dynamics. The defective Ge/Si interface was identified as the limiting factor for Ge epilayers directly grown on Si. The longest lifetimes of 5.0 ns for a 1 µm thick layer were found for GeOI, where the interface is removed. Doping was found to have detrimental effects on the lifetime with a decrease by a factor of 5 or more in the investigated cases, either due to agglomeration of dopant atoms along threading dislocations for in-situ doping, or due to crystal damage for doping by ion implantation.

Measurements on GeSOI and GeOI microbridges revealed that neither the strain nor the additionally introduced free surfaces seem to cause a negative effect on the lifetimes. The latter is also true for GeSn if the surface is properly passivated. However, the lifetimes in GeSn are in general ~ 1.5 orders of magnitude shorter than in Ge. This distinct difference in lifetime represents a crucial difference when comparing the performance of strained Ge with GeSn.

The short lifetime for GeSn observed in the pulsed excitation regime is identified as an

essential ingredient for the understanding of the high lasing threshold densities of the order of 200 - 400 kW/cm^2 and the limitation of lasing to low temperature. To that end, we also investigated Fabry-Perot waveguide cavities which were selectively underetched to decrease the compressive strain and to increase the optical mode confinement. Owing to the improved device properties, maximum lasing temperatures of $T_{max} = 135$ K and a low temperature lasing onset for a GeSn layer with only 8.5% of Sn could be demonstrated. Compared to the 8.5% Sn sample, T_{max} for a 12.5% Sn alloy was found to increase by 55 K, even though the increase in directness, i.e. the separation between Γ and L-states, is larger than 50 meV. This rather vain dependence of T_{max} on the directness together with the only slight variation of the low temperature lasing threshold for GeSn layers with alloy concentrations between 8.5% and 12.5% is another puzzling observation. Furthermore, we showed that unsaturated surface states are to exclude as reason for the so far insufficiently high T_{max}.

As mentioned above, the carrier lifetimes for GeSn epilayers determined by the same time-resolved pump-probe spectroscopy as used for the Ge revealed lifetimes as short as 200 ps, which indicates the adverse effects of the introduced defects on the carrier dynamics. A slightly longer lifetime was found for alloys with lower Sn concentration, which is ascribed to the reduced amount of dislocations introduced by strain relaxation. No increase in lifetime was found at low temperatures in contrast to the analysis of temperature-dependent PL measurements, which might be connected to the different carrier densities in pulsed and continuous-wave excitation mode.

The pump-probe measurements also allowed to extract the time-dependent gain and loss for GeSn alloys in dependence of carrier density. A large discrepancy was found between the carrier density related to the observed loss and the observed material gain. This experimental finding indicates that the electron distribution in the conduction band is not in quasi-equilibrium. This hypothesis is furthermore strengthened by the fact that the absorption loss, which is mainly caused by intervalence band absorption, decreases by 3.5× within the first 200 ps while the material gain stays virtually constant for almost 400 ps. While the first quantity relates to the number of holes and, thus, to the total number of excited carriers, the gain relates to the apparently not in equilibrium population of electrons in Γ. This is strikingly similar to what we have shown for the case of strained Ge from the quantitative analysis of the PL efficiency. Like for GeSn, the electron population of the Γ valley is significantly lower than estimated under the assumption of a quasi-equilibrium distribution. Therefore, the observed effects might be characteristic for direct band gap Ge systems under optical pumping where the excitation energy is much larger than the band gap.

In perspective, several substantial steps could be made within the course of this work to-

wards a better understanding on how to realize an efficient group IV laser. Main contributions include the first experimental demonstration of uniaxially stressed Ge with a fundamental direct band gap, the realization of direct band gap Ge incorporated in an optical microcavity, systematic investigations of the carrier lifetime in Ge layers on Si, and the detailed investigation of lasing characteristics, lifetimes and gain in direct band gap GeSn alloys. With the recent first demonstration of lasing in direct gap GeSn, and the demonstration of cavity modes in direct gap strained Ge, we are just at the beginning of an exciting journey which may bring us a new class of lasers for monolithic integration compatible with Si CMOS technology.

In conclusion, the proof-of-concept for direct band gap Ge could be presented in form of strained Ge and GeSn alloys. First success like lasing in GeSn or a tensile-strained direct gap Ge microcavity show the potential of this approach. However, fundamental physical questions have to be answered to exploit the full potential of these promising material systems. This thesis, moreover, demonstrates powerful experimental methods to investigate the remaining open questions.

A

Appendix

Contents

A.1 NextNano^3 k·p Simulations

The band structure parameters which enter the gain simulations in chapter 2 are determined with the 8-band k·p approach implemented in the simulation tool nextnano^3 [78]. Here, a brief introduction into the basics of k·p theory is recited, followed by the list of material parameters used for the simulations concerning strained Ge. For more details on the implemented approach, the reader may refer to [278, 279]. The following summary is based on the execution in [279].

The many-particle Hamiltonian describing the electronic band structure of a bulk semiconductor can be reduced using a mean field approximation to a single-particle Schrödinger equation as

$$\hat{H}\psi_n(\mathbf{x}) = \left[\frac{\mathbf{p}^2}{2m_0} + V(\mathbf{x})\right]\psi_n(\mathbf{x}) = E_n\psi_n(\mathbf{x}), \tag{A.1}$$

with the lattice periodic potential $V(\mathbf{x}) = V(\mathbf{x}+\mathbf{R})$, where $\mathbf{R}$ is the Bravais lattice vector. The eigenfunctions $\psi_{n,\mathbf{k}}(x)$ of equation (A.1) are Bloch functions

$$\psi_{n,\mathbf{k}}(\mathbf{x}) = \exp(i\mathbf{k}\cdot\mathbf{x})\,u_{n,\mathbf{k}}(\mathbf{x}), \tag{A.2}$$

with the periodic Bloch factors $u_{n,\mathbf{k}}(\mathbf{x})$ and plane waves $\exp(i\mathbf{k}\cdot\mathbf{x})$. With the Bloch functions, equation (A.1) leads to

$$\hat{H}(\mathbf{k})\,u_{n,\mathbf{k}}(\mathbf{x}) = \left[\frac{(\mathbf{p}+\hbar\mathbf{k})^2}{2m_0} + V(\mathbf{x})\right]u_{n,\mathbf{k}}(\mathbf{x}) = E_n(\mathbf{k})\,u_{n,\mathbf{k}}(\mathbf{x}). \tag{A.3}$$

The solution of equation (A.3) for $E_n(\mathbf{k})$ delivers the dispersion of the electronic bands in k-space, but the computation requires simplifications and numerical methods. In k·p theory, we make use of the fact that the crucial part of the electronic band structure, which determines the electronic and optical properties of a material, is at the conduction- and valence band extrema. Therefore, the bandstructure is expanded around an extremum $\mathbf{k_0}$ with the $\mathbf{k}$-dependent part of the Hamiltonian as

$$\hat{H}(\mathbf{k}) = \hat{H}(\mathbf{k}_0) + \frac{\hbar(\mathbf{k}-\mathbf{k}_0)\cdot\mathbf{p}}{m_0} + \frac{\hbar^2\left(\mathbf{k}^2-\mathbf{k}_0^2\right)}{2m_0}, \tag{A.4}$$

where the extremum part $\hat{H}(\mathbf{k}_0)$ is solved as

$$\hat{H}(\mathbf{k}_0)\, u_{n,\mathbf{k}_0}(\mathbf{x}) = E_n(\mathbf{k}_0)\, u_{n,\mathbf{k}_0}(\mathbf{x}), \tag{A.5}$$

with the Bloch factors $u_{n,\mathbf{k}_0}(\mathbf{x})$ forming a complete and orthonormal basis set. This basis set can be used to express all unknown Bloch factors $u_{n,\mathbf{k}}(\mathbf{x})$ for any $\mathbf{k}$. By inserting the expansion in Bloch factors into equation (A.3), the following eigenvector problem can be defined for the expansion coefficeints $c_{n,\mu}$ as

$$\sum_{\mu} \hat{H}_{\nu\mu}(\mathbf{k})\, c_{n,\mu}(\mathbf{k}) = E_n(\mathbf{k})\, c_{n,\nu}(\mathbf{k}), \tag{A.6}$$

with the Hamiltonian given by the matrix

$$\hat{H}_{\nu\mu}(\mathbf{k}) = \left[E_\mu(\mathbf{k}_0) + \frac{\hbar^2}{2m_0}\left(\mathbf{k}^2-\mathbf{k}_0^2\right)\right]\delta_{\nu\mu} + \frac{\hbar}{m_0}(\mathbf{k}-\mathbf{k}_0)\cdot\mathbf{p}_{\nu\mu}, \tag{A.7}$$

where $\mathbf{p}_{\nu\mu}$ is the momentum matrix element which introduces a coupling between the electronic bands ν and μ.

For our simulations, an 8-band k·p approach is applied, where 8 basis functions are explicitly considered, while the other bands are treated as perturbation. Nextnano[3] thus iteratively solves equation (A.6), which becomes an 8×8 matrix.

The list of material parameters which are used used for the band structure parameters are given in table A.1. The 6-band Dresselhaus parameters L, M and N were calculated using the experimental Lüttinger parameters γ_1, γ_2 and γ_3 obtained by Hensel and Suzuki [280]. The 6-band parameters were scaled to the respective 8-band parameters using the dipole matrix element E_p and the direct band gap E_Γ.

Parameter	Value	Reference
$a_{c\Gamma}$ (eV)	−10.41	[274]
a_{cL} (eV)	−4.35	[274]
a_v (eV)	−0.35	[274]
b (eV)	−2.86	[281]
E_Γ (eV)	0.80	[162]
E_L (eV)	0.66	[162]
γ_1	13.38	[280]
γ_2	4.24	[280]
γ_3	5.69	[280]
E_p (eV)	26.3	[97]
Δ_{so} (eV)	0.289	[282]
L' $(\hbar^2/2m_0) = L + E_p/E_\Gamma$	1.16	[280]
M' $(\hbar^2/2m_0) = M$	−5.9	[280]
N' $(\hbar^2/2m_0) = N + E_p/E_\Gamma$	−1.64	[280]

Table A.1: List of material constants used for band structure calculations in nextnano[3].

A.2 Transfer-Matrix-Method for Multilayer Transmission Modelling

To calculate the reflection from or transmission through a multilayered material stack, the transfer-matrix-method (TMM) is used where the electric fields of forward- and backward traveling waves E^i_{for} and E^i_{back} at the first interface of a layer stack are related to the respective electric fields after the last interface E^f_{for} and E^f_{back} by the transfer matrix T_{tot} as follows:

$$\begin{pmatrix} E^i_{for} \\ E^i_{back} \end{pmatrix} = T_{tot} \begin{pmatrix} E^f_{for} \\ E^f_{back} \end{pmatrix} = \begin{pmatrix} T^{1,1}_{tot} & T^{1,2}_{tot} \\ T^{2,1}_{tot} & T^{2,2}_{tot} \end{pmatrix} \begin{pmatrix} E^f_{for} \\ E^f_{back} \end{pmatrix}. \tag{A.8}$$

For the transfer matrix of the full GeSOI system, the transmission and reflection at each interface as well as the transmission through each layer is accounted for as:

$$T_{tot} = T_{air,Ge}\ T_{Ge}\ T_{Ge,Si}\ T_{Si}\ T_{Si,air}\ T_{air}\ T_{air,Si}, \tag{A.9}$$

$$T_{i,j} = \frac{1}{t_{i,j}} \begin{pmatrix} 1 & r_{i,j} \\ r_{i,j} & 1 \end{pmatrix}, \quad T_i = \begin{pmatrix} e^{j\Phi_i} & 0 \\ 0 & e^{-j\Phi_i} \end{pmatrix}, \quad \Phi_i = \frac{2\pi}{\lambda} n_i d_i \cos\theta_i, \tag{A.10}$$

	Air	Ge	Si	Air	Si
n_{ref}	1.0	4.0	3.4	1.0	3.4
d (nm)	∞	1400	340	1000	∞

Table A.2: Input parameters for calculation of reflection at GeSOI surface via transfer-matrix-method.

where λ is the wavelength of the light, n_i and d_i are the refractive index and the thickness of layer i, respectively, and θ_i is the angle of incidence.

For transverse-electric (TE) and transverse-magnetic (TM) field polarizations, the respective transmission- and reflexion-coefficients $t_{i,j}$ and $r_{i,j}$ are calculated as:

$$\text{TE:} \qquad r_{i,j} = \frac{n_i \cos\theta_i - n_j \cos\theta_j}{n_i \cos\theta_i + n_j \cos\theta_j}, \qquad t_{i,j} = \frac{2n_i \cos\theta_i}{n_i \cos\theta_i + n_j \cos\theta_j}, \tag{A.11}$$

$$\text{TM:} \qquad r_{i,j} = \frac{n_j \cos\theta_i - n_i \cos\theta_j}{n_j \cos\theta_i + n_i \cos\theta_j}, \qquad t_{i,j} = \frac{2n_i \cos\theta_i}{n_j \cos\theta_j + n_i \cos\theta_j}. \tag{A.12}$$

From equation A.8, the reflection and transmission r and t can be obtained under the assumption $E^f_{back} = 0$ as

$$r = \frac{T^{2,1}_{tot}}{T^{1,1}_{tot}} \qquad t = \frac{1}{T^{1,1}_{tot}}. \tag{A.13}$$

For the modeled reflexion in Fig. 3.14(c), the input parameters for thicknesses d_i and refractive indices n_{ref} are given in table A.2. Absorption in Ge was neglected as well as the dispersion of the refractive indices.

Bibliography

[1] J. S. Kilby. Turning Potential into Realities: The invention of the integrated ciruit. *International Journal of Modern Physics B* **16(05)**, 699–710 (2002).

[2] J. S. Kilby. The integrated circuit's early history. *Proceedings of the IEEE* **88(1)**, 109 (2000).

[3] R. N. Noyce. Semiconductor device-and-lead structure. *US Patent* 2981877 (1961).

[4] G. E. Moore. Cramming more components onto integrated circuits. *Electronics* **38(8)**, 114–117 (1965).

[5] M. M. Waldrop. The chips are down for Moore's law. *Nature* **530(7589)**, 144–147 (2016).

[6] J. Gubbi, R. Buyya, S. Marusic and M. Palaniswami. Internet of Things (IoT): A vision, architectural elements, and future directions. *Future Generation Computer Systems* **29(7)**, 1645–1660 (2013).

[7] L. Wilson. International technology roadmap for semiconductors (ITRS). *Semiconductor Industry Association* (2013).

[8] V. Venkatachalam and M. Franz. Power reduction techniques for microprocessor systems. *ACM Computing Surveys* **37(3)**, 195–237 (2005).

[9] G. Chandra, P. Kapur and K. C. Saraswat. Scaling trends for the on chip power dissipation. *Proceedings of the IEEE International Interconnect Technology Conference 2002* 170–172 (2002).

[10] J. W. Goodman, F. J. Leonberger, S.-Y. Kung and R. A. Athale. Optical interconnections for VLSI systems. *Proceedings of the IEEE* **72(7)**, 850–866 (1984).

[11] G. Chen, H. Chen, M. Haurylau, N. Nelson, D. Albonesi, P. M. Fauchet and E. G. Friedman. Electrical and optical on-chip interconnects in scaled microprocessors. In *IEEE International Symposium on Circuits and Systems*, 2514–2517 Vol. 3 (2005).

[12] D. Miller. Physical reasons for optical interconnection. *International Journal of Optoelectronics* **11(3)**, 155–168 (1997).

[13] D. A. B. Miller. Rationale and challenges for optical interconnects to electronic chips. *Proceedings of the IEEE* **88(6)**, 728–749 (2000).

[14] D. A. B. Miller. Device Requirements for Optical Interconnects to Silicon Chips. *Proceedings of the IEEE* **97(7)**, 1166–1185 (2009).

[15] L. Vivien and L. Pavesi (Editors). *Handbook of Silicon Photonics*. CRC Press (2013).

[16] T. Tsuchizawa, K. Yamada, T. Watanabe, H. Fukuda and S. Itabashi. Ultrasmall Optical Devices using Silicon Wire Waveguides. In *32nd European Conference on Optical Communications*, 1–3 (2006).

[17] C. Qiu, Z. Sheng, H. Li, W. Liu, L. Li, A. Pang, A. Wu, X. Wang, S. Zou and F. Gan. Fabrication, Characterization and Loss Analysis of Silicon Nanowaveguides. *Journal of Lightwave Technology* **32(13)**, 2303–2307 (2014).

[18] B. G. Lee, J.-O. Plouchart, A. V. Rylyakov, J. H. Song, F. E. Doany and C. L. Schow. Passive Photonics in an Unmodified CMOS Technology With No Post-Processing Required. *IEEE Photonics Technology Letters* **25(4)**, 393–396 (2013).

[19] W. Bogaerts, R. Baets, P. Dumon, V. Wiaux, S. Beckx, D. Taillaert, B. Luyssaert, J. Van Campenhout, P. Bienstman and D. Van Thourhout. Nanophotonic waveguides in silicon-on-insulator fabricated with CMOS technology. *Journal of Lightwave Technology* **23(1)**, 401–412 (2005).

[20] D. Dai and J. E. Bowers. Silicon-based on-chip multiplexing technologies and devices for Peta-bit optical interconnects. *Nanophotonics* **3(4-5)**, 283–311 (2014).

[21] A. Liu, L. Liao, Y. Chetrit, J. Basak, H. Nguyen, D. Rubin and M. Paniccia. Wavelength Division Multiplexing Based Photonic Integrated Circuits on Silicon-on-Insulator Platform. *IEEE Journal of Selected Topics in Quantum Electronics* **16(1)**, 23–32.

[22] C. P. Chen, J. B. Driscoll, R. R. Grote, B. Souhan, R. M. Osgood and K. Bergman. Mode and Polarization Multiplexing in a Si Photonic Chip at 40Gb/s Aggregate Data Bandwidth. *IEEE Photonics Photonics Technology Letters* **27(1)**, 22–25.

[23] X. Zheng, I. Shubin, G. Li, T. Pinguet, A. Mekis and J. Yao. A tunable 1x4 silicon CMOS photonic wavelength multiplexer/demultiplexer for dense optical interconnects. *Optics Express* **18(5)**, 5151–5160 (2010).

[24] F. Y. Gardes, D. J. Thomson, N. G. Emerson and G. T. Reed. 40 Gb/s silicon photonics modulator for TE and TM polarisations. *Optics Express* **19(12)**, 11804–11814 (2011).

[25] Q. Xu, B. Schmidt, S. Pradhan and M. Lipson. Micrometre-scale silicon electro-optic modulator. *Nature* **435(7040)**, 325–327 (2005).

[26] S. Ren, Y. Rong, S. A. Claussen, R. K. Schaevitz, T. I. Kamins, J. S. Harris and D. A. B. Miller. Ge/SiGe Quantum Well Waveguide Modulator Monolithically Integrated With SOI Waveguides. *IEEE Photonics Technology Letters* **24(6)**, 461–463 (2012).

[27] G. T. Reed, G. Mashanovich, F. Y. Gardes and D. J. Thomson. Silicon optical modulators. *Nature Photonics* **4(8)**, 518–526 (2010).

[28] J. Michel, J. Liu and L. C. Kimerling. High-performance Ge-on-Si photodetectors. *Nature Photonics* **4(8)**, 527–534 (2010).

[29] S. J. Koester, J. D. Schaub and G. Dehlinger. Germanium-on-SOI infrared detectors for integrated photonic applications. *IEEE Journal of Selected Topics in Quantum Electronics* **12(6)**, 1489–1502 (2006).

[30] T. Yin, R. Cohen, M. M. Morse, G. Sarid, Y. Chetrit, D. Rubin and M. J. Paniccia. 31GHz Ge n-i-p waveguide photodetectors on Silicon-on-Insulator substrate. *Optics Express* **15(21)**, 13965–13971 (2007).

[31] Y. Kang, H.-D. Liu, M. Morse, M. J. Paniccia, M. Zadka, S. Litski, G. Sarid, A. Pauchard, Y.-H. Kuo, H.-W. Chen, W. S. Zaoui, J. E. Bowers, A. Beling, D. C. McIntosh, X. Zheng and J. C. Campbell. Monolithic germanium/silicon avalanche photodiodes with 340 GHz gain–bandwidth product. *Nature Photonics* **3(1)**, 59–63 (2008).

[32] L. Chen and M. Lipson. Ultra-low capacitance and high speed germanium photodetectors on silicon. *Optics Express* **17(10)**, 7901–7906 (2009).

[33] S. Adachi. *Physical Properties of III-V Semiconductor Compounds*. Wiley-VCH (1992).

[34] J. R. Chelikowsky and M. L. Cohen. Electronic structure of silicon. *Physical Review B* **10(12)**, 5095–5107 (1974).

[35] M. L. Cohen and J. R. Chelikowsky. *Electronic Structure and Optical Properties of Semiconductors*. Springer Series in Solid-State Sciences (1988).

[36] K. J. Kuhn, A. Murthy, R. Kotlyar and M. Kuhn. Past, Present and Future: SiGe and CMOS Transistor Scaling. *ECS Transactions* **33(6)**, 3–17 (2010).

[37] D. Liang and J. E. Bowers. Recent progress in lasers on silicon. *Nature Photonics* **4(8)**, 511–517 (2010).

[38] X. Luo, Y. Cao, J. Song, X. Hu, Y. Cheng, C. Li, C. Liu, T.-Y. Liow, M. Yu, H. Wang, Q. J. Wang and P. G.-Q. Lo. High-Throughput Multiple Dies-to-Wafer Bonding Technology and III/V-on-Si Hybrid Lasers for Heterogeneous Integration of Optoelectronic Integrated Circuits. *Frontiers in Materials* **2**, 153 (2015).

[39] J. Justice, C. Bower, M. Meitl, M. B. Mooney, M. A. Gubbins and B. Corbett. Wafer-scale integration of group III–V lasers on silicon using transfer printing of epitaxial layers. *Nature Photonics* **6(9)**, 612–616 (2012).

[40] A. W. Fang, H. Park, O. Cohen, R. Jones, M. J. Paniccia and J. E. Bowers. Electrically pumped hybrid AlGaInAs-silicon evanescent laser. *Optics Express* **14(20)**, 9203–9210 (2006).

[41] Z. Wang, B. Tian, M. Pantouvaki, W. Guo, P. Absil, J. Van Campenhout, C. Merckling and D. Van Thourhout. Room-temperature InP distributed feedback laser array directly grown on silicon. *Nature Photonics* **9(12)**, 837–842 (2015).

[42] R. Chen, T.-T. D. Tran, K. W. Ng, W. S. Ko, L. C. Chuang, F. G. Sedgwick and C. Chang-Hasnain. Nanolasers grown on silicon. *Nature Photonics* **5(3)**, 170–175 (2011).

[43] H. Liu, T. Wang, Q. Jiang, R. Hogg, F. Tutu, F. Pozzi and A. Seeds. Long-wavelength InAs/GaAs quantum-dot laser diode monolithically grown on Ge substrate. *Nature Photonics* **5(7)**, 416–419 (2011).

[44] A. Y. Liu, C. Zhang, J. Norman, A. Snyder, D. Lubyshev, J. M. Fastenau, A. W. K. Liu, A. C. Gossard and J. E. Bowers. High performance continuous wave 1.3 μm quantum dot lasers on silicon. *Applied Physics Letters* **104(4)**, 041104 (2014).

[45] M. E. Groenert, C. W. Leitz, A. J. Pitera, V. Yang, H. Lee, R. J. Ram and E. A. Fitzgerald. Monolithic integration of room-temperature cw GaAs/AlGaAs lasers on Si substrates via relaxed graded GeSi buffer layers. *Journal Of Applied Physics* **93(1)**, 362–367 (2003).

[46] J. Palm, F. Gan, B. Zheng, J. Michel and L. C. Kimerling. Electroluminescence of erbium-doped silicon. *Physical Review B* **54(24)**, 17603–17615 (1996).

[47] T. J. Kippenberg, J. Kalkman, A. Polman and K. J. Vahala. Demonstration of an erbium-doped microdisk laser on a silicon chip. *Physical Review A* **74(5)**, 051802 (2006).

[48] Purnawirman, J. Sun, T. N. Adam, G. Leake and D. Coolbaugh. C-and L-band erbium-doped waveguide lasers with wafer-scale silicon nitride cavities. *Optics Letters* **38(11)**, 1760–1762 (2013).

[49] L. Pavesi, L. Dal Negro, C. Mazzoleni, G. Franzò and F. Priolo. Optical gain in silicon nanocrystals. *Nature* **408(6811)**, 440–444 (2000).

[50] U. Gnutzmann and K. Clausecker. Theory of direct optical transitions in an optical indirect semiconductor with a superlattice structure. *Applied physics* **3(1)**, 9–14 (1974).

[51] U. Menczigar, J. Brunner, E. Friess, M. Gail, G. Abstreiter, H. Kibbel, H. Presting and E. Kasper. Photoluminescence Studies of $Si/Si_{1-X}Ge_x$ Quantum-Wells and Si_mGe_n Superlattices. *Thin Solid Films* **222(1-2)**, 227–233 (1992).

[52] C. Zeller and G. Abstreiter. Electric Subbands in Si/SiGe Strained Layer Superlattices. *Zeitschrift für Physik B - Condensed Matter* **64(2)**, 137–143 (1986).

[53] M. d'Avezac, J.-W. Luo, T. Chanier and A. Zunger. Genetic-Algorithm Discovery of a Direct-Gap and Optically Allowed Superstructure from Indirect-Gap Si and Ge Semiconductors. *Physical Review Letters* **108(2)**, 027401 (2012).

[54] T. Etzelstorfer, M. R. Ahmadpor Monazam, S. Cecchi, D. Kriegner, D. Chrastina, E. Gatti, E. Grilli, N. Rosemann, S. Chatterjee, V. Holý, F. Pezzoli, G. Isella and J. Stangl. Structural investigations of the α_{12} Si–Ge superstructure. *Journal of Applied Crystallography* **48(1)**, 262–268 (2015).

[55] H. Rong, A. Liu, R. Jones, O. Cohen, D. Hak, R. Nicolaescu, A. Fang and M. Paniccia. An all-silicon Raman laser. *Nature* **433(7023)**, 292–294 (2005).

[56] H. Rong, R. Jones, A. Liu, O. Cohen, D. Hak, A. Fang and M. Paniccia. A continuous-wave Raman silicon laser. *Nature* **433(7027)**, 725–728 (2005).

[57] H. Rong, S. Xu, Y.-H. Kuo, V. Sih, O. Cohen, O. Raday and M. Paniccia. Low-threshold continuous-wave Raman silicon laser. *Nature Photonics* **1(4)**, 232–237 (2007).

[58] Y. Takahashi, Y. Inui, M. Chihara, T. Asano, R. Terawaki and S. Noda. A micrometre-scale Raman silicon laser with a microwatt threshold. *Nature* **498(7455)**, 470–474 (2013).

[59] J. Liu, X. Sun, R. Camacho-Aguilera, L. C. Kimerling and J. Michel. Ge-on-Si laser operating at room temperature. *Optics Letters* **35(5)**, 679–681 (2010).

[60] R. E. Camacho-Aguilera, Y. Cai, N. Patel, J. T. Bessette, M. Romagnoli, L. C. Kimerling and J. Michel. An electrically pumped germanium laser. *Optics Express* **20(10)**, 11316–11320 (2012).

[61] R. Koerner, M. Oehme, M. Gollhofer, M. Schmid, K. Kostecki, S. Bechler, D. Widmann, E. Kasper and J. Schulze. Electrically pumped lasing from Ge Fabry-Perot resonators on Si. *Optics Express* **23(11)**, 14815 (2015).

[62] L. Carroll, P. Friedli, S. Neuenschwander, H. Sigg, S. Cecchi, F. Isa, D. Chrastina, G. Isella, Y. Fedoryshyn and J. Faist. Direct-Gap Gain and Optical Absorption in Germanium Correlated to the Density of Photoexcited Carriers, Doping, and Strain. *Physical Review Letters* **109(5)**, 057402 (2012).

[63] M. Virgilio, C. L. Manganelli, G. Grosso, G. Pizzi and G. Capellini. Radiative recombination and optical gain spectra in biaxially strained n-type germanium. *Physical Review B* **87(23)**, 235313 (2013).

[64] B. Dutt, D. S. Sukhdeo, D. Nam, B. M. Vulovic, Z. Yuan and K. C. Saraswat. Roadmap to an Efficient Germanium-on-Silicon Laser: Strain vs. n-Type Doping. *IEEE Photonics Journal* **4(5)**, 2002–2009 (2012).

[65] D. Peschka, M. Thomas, A. Glitzky, R. Nurnberg, K. Gartner, M. Virgilio, S. Guha, T. Schroeder, G. Capellini and T. Koprucki. Modeling of edge-emitting lasers based on tensile strained germanium microstrips. *IEEE Photonics Journal* **7(3)** (2015).

[66] R. Geiger, J. Frigerio, M. J. Süess, D. Chrastina, G. Isella, R. Spolenak, J. Faist and H. Sigg. Excess carrier lifetimes in Ge layers on Si. *Applied Physics Letters* **104(6)**, 062106 (2014).

[67] P. Vogl, M. M. Rieger, J. A. Majewski and G. Abstreiter. How to convert group-IV semiconductors into light emitters. *Physica Scripta* **1993(T49B)**, 476 (1993).

[68] Y. Ishikawa, K. Wada, D. Cannon, J. Liu, H. Luan and L. Kimerling. Strain-induced band gap shrinkage in Ge grown on Si substrate. *Applied Physics Letters* **82(13)**, 2044–2046 (2003).

[69] Y. Ishikawa, K. Wada, J. Liu, D. Cannon, H. Luan, J. Michel and L. Kimerling. Strain-induced enhancement of near-infrared absorption in Ge epitaxial layers grown on Si substrate. *Journal Of Applied Physics* **98(1)**, 013501 (2005).

[70] A. Ghrib, M. El Kurdi, M. Prost, S. Sauvage, X. Checoury, G. Beaudoin, M. Chaigneau, R. Ossikovski, I. Sagnes and P. Boucaud. All-Around SiN Stressor for High and Homogeneous Tensile Strain in Germanium Microdisk Cavities. *Advanced Optical Materials* **3(3)**, 353–358 (2015).

[71] G. Capellini, C. Reich, S. Guha, Y. Yamamoto, M. Lisker, M. Virgilio, A. Ghrib, M. El Kurdi, P. Boucaud, B. Tillack and T. Schroeder. Tensile Ge microstructures for lasing fabricated by means of a silicon complementary metal-oxide-semiconductor process. *Optics Express* **22(1)**, 399–410 (2014).

[72] R. W. Millar, K. Gallacher, A. Samarelli and J. Frigerio. Expanding the Ge emission wavelength to 2.25 μm with Si_xN_y strain engineering. *Thin Solid Films* **602**, 60–63 (2015).

[73] M. J. Süess, R. Geiger, R. A. Minamisawa, G. Schiefler, J. Frigerio, D. Chrastina, G. Isella, R. Spolenak, J. Faist and H. Sigg. Analysis of enhanced light emission from highly strained germanium microbridges. *Nature Photonics* **7**, 466–472 (2013).

[74] D. Nam, D. S. Sukhdeo, J.-H. Kang, J. Petykiewicz, J. H. Lee, W. S. Jung, J. Vuckovic, M. L. Brongersma and K. C. Saraswat. Strain-Induced Pseudoheterostructure Nanowires Confining Carriers at Room Temperature with Nanoscale-Tunable Band Profiles. *Nano Letters* **13(7)**, 3118–3123 (2013).

[75] D. S. Sukhdeo, D. Nam, J.-H. Kang, M. L. Brongersma and K. C. Saraswat. Direct bandgap germanium-on-silicon inferred from 5.7% <100> uniaxial tensile strain. *Photonics Research* **2(3)**, A8 (2014).

[76] C. H. L. Goodman. Direct-gap group IV semiconductors based on tin. *IEE Proceedings I - Solid State and Electron Devices* **129(5)**, 189–192 (1982).

[77] S. Wirths, R. Geiger, N. von den Driesch, G. Mussler, T. Stoica, S. Mantl, Z. Ikonic, M. Luysberg, S. Chiussi, J. M. Hartmann, H. Sigg, J. Faist, D. Buca and D. Grützmacher. Lasing in direct-bandgap GeSn alloy grown on Si. *Nature Photonics* **9(2)**, 88–92 (2015).

[78] S. Birner, T. Zibold, T. Andlauer, T. Kubis, M. Sabathil, A. Trellakis and P. Vogl. nextnano: General Purpose 3-D Simulations. *IEEE Transactions on Electron Devices* **54(9)**, 2137–2142.

[79] C. G. van de Walle. Band lineups and deformation potentials in the model-solid theory. *Physical Review B* **39(3)**, 1871–1883 (1989).

[80] J. J. Wortman and R. A. Evans. Young's Modulus, Shear Modulus, and Poisson's Ratio in Silicon and Germanium. *Journal Of Applied Physics* **36(1)**, 153–156 (1965).

[81] M. El Kurdi, G. Fishman, S. Sauvage and P. Boucaud. Band structure and optical gain of tensile-strained germanium based on a 30 band k·p formalism. *Journal Of Applied Physics* **107(1)**, 013710 (2010).

[82] M. Virgilio, C. L. Manganelli, G. Grosso, T. Schroeder and G. Capellini. Photoluminescence, recombination rate, and gain spectra in optically excited n-type and tensile strained germanium layers. *Journal Of Applied Physics* **114(24)**, 243102 (2013).

[83] H. Wen and E. Bellotti. Rigorous theory of the radiative and gain characteristics of silicon and germanium lasing media. *Physical Review B* **91(3)**, 035307 (2015).

[84] M. Cardona and F. Pollak. Energy-Band Structure of Germanium and Silicon: The k·p Method. *Physical Review* **142(2)**, 530–543 (1966).

[85] M. Rieger and P. Vogl. Electronic-band parameters in strained $Si_{1-x}Ge_x$ alloys on $Si_{1-y}Ge_y$ substrates. *Physical Review B* **48(19)**, 14276–14287 (1993).

[86] J. Liu, X. Sun, D. Pan, X. Wang, L. C. Kimerling, T. L. Koch and J. Michel. Tensile-strained, n-type Ge as a gain medium for monolithic laser integration on Si. *Optics Express* **15(18)**, 11272–11277 (2007).

[87] G.-E. Chang and H. H. Cheng. Optical gain of germanium infrared lasers on different crystal orientation. *Journal of physics D: Applied Physics* **46(6)**, 1–15 (2013).

[88] O. Aldaghri, Z. Ikonic and R. W. Kelsall. Optimum strain configurations for carrier injection in near infrared Ge lasers. *Journal Of Applied Physics* **111(5)**, 053106 (2012).

[89] H. Tahini, A. Chroneos, R. W. Grimes, U. Schwingenschlögl and A. Dimoulas. Strain-induced changes to the electronic structure of germanium. *Journal of Physics: Condensed Matter* **24(19)**, 195802 (2012).

[90] Y.-M. Niquet, D. Rideau, C. Tavernier, H. Jaouen and X. Blase. Onsite matrix elements of the tight-binding Hamiltonian of a strained crystal: Application to silicon, germanium, and their alloys. *Physical Review B* **79(24)**, 245201 (2009).

[91] D. S. Sukhdeo. Band-engineered germanium for CMOS-compatible light emission. Ph.D. thesis, Stanford University (2015).

[92] R. Geiger, T. Zabel and H. Sigg. Group IV direct band gap photonics: Methods, Challenges and Opportunities. *Frontiers in Materials* **2**, 52 (2015).

[93] S. L. Chuang. *Physics of Optoelectronic Devices*. Wiley (1995).

[94] Y. Yin, D. Yan, F. Pollak, M. S. Hybertsen, M. J. Vandenberg and J. C. Bean. Temperature-Dependence of the Fundamental Direct Transitions of Bulk Ge and two Ge/SiGe Multiple-Quantum-Well Structures. *Physical Review B* **52(12)**, 8951–8958 (1995).

[95] P. Y. Yu and M. Cardona. *Fundamentals of Semiconductors*. Graduate Texts in Physics. Springer (2010).

[96] E. Rosencher and B. Vinter. *Optoelectronics*. Cambridge University Press (2002).

[97] P. Lawaetz. Valence-Band Parameters in Cubic Semiconductors. *Physical Review B* **4(10)**, 3460–3467 (1971).

[98] G. Bastard. *Wave mechanics applied to semiconductor heterostructures*. Les Éditions de Physique (1988).

[99] M. Virgilio and G. Grosso. Strain-modulated Ge superlattices. *Journal of Physics: Condensed Matter* **27(48)**, 485305 (2015).

[100] H. B. Briggs and R. C. Fletcher. Absorption of infrared light by free carriers in germanium. *Physical Review* **91(6)**, 1342 (1953).

[101] H. Fan, W. Spitzer and R. Collins. Infrared Absorption in n-Type Germanium. *Physical Review* **101(2)**, 566–572 (1956).

[102] G. H. Li, A. R. Goñi, K. Syassen and M. Cardona. Intervalley scattering potentials of Ge from direct exciton absorption under pressure. *Physical Review B* **49(12)**, 8017–8023 (1994).

[103] H. Briggs and R. Fletcher. New Infrared Absorption Bands in p-Type Germanium. *Physical Review* **87(6)**, 1130–1131 (1952).

[104] W. Kaiser, R. Collins and H. Fan. Infrared Absorption in P-Type Germanium. *Physical Review* **91(6)**, 1380–1381 (1953).

[105] I. Balslev. Inter-Valence-Band Transitions in Uniaxially Stressed Ge and GaAs. *Physical Review* **177(3)**, 1173–1178 (1969).

[106] J. Pankove and P. Aigrain. Optical Absorption of Arsenic-Doped Degenerate Germanium. *Physical Review* **126(3)**, 956–962 (1962).

[107] S. Wirths, Z. Ikonic, A. T. Tiedemann, B. Holländer, T. Stoica, G. Mussler, U. Breuer, A. Benedetti, J. M. Hartmann, S. Chiussi, D. Grützmacher, S. Mantl and D. Buca. Tensely strained GeSn alloys as optical gain media. *Applied Physics Letters* **103**, 192110 (2013).

[108] Y.-F. Lao and A. G. Unil Perera. Dielectric function model for p-type semiconductor inter-valence band transitions. *Journal Of Applied Physics* **109(10)**, 103528–103528–9 (2011).

[109] A. Kahn. Theory of the Infrared Absorption of Carriers in Germanium and Silicon. *Physical Review* **97(6)**, 1647–1652 (1955).

[110] J. B. Arthur, A. C. Baynham, W. Fawcett and E. Paige. Optical absorption due to free holes in germanium: A comparison of theory and experiment. *Physical Review* **152(2)**, 740 (1966).

[111] T. Bahder. Eight-band k·p model of strained zinc-blende crystals. *Physical Review B* **41(17)**, 11992–12001 (1990).

[112] M. El Kurdi, G. Fishman, S. Sauvage and P. Boucaud. Comparison between 6-band and 14-band k·p formalisms in SiGe/Si heterostructures. *Physical Review B* **68(16)**, 165333 (2003).

[113] S. Richard, F. Aniel and G. Fishman. Energy-band structure of Ge, Si, and GaAs: A thirty-band k·p method. *Physical Review B* **70(23)**, 235204 (2004).

[114] J. Taylor and V. Tolstikhin. Intervalence band absorption in InP and related materials for optoelectronic device modeling. *Journal Of Applied Physics* **87(3)**, 1054–1059 (2000).

[115] M. Nedeljkovic, R. Soref and G. Z. Mashanovich. Predictions of Free-Carrier Electroabsorption and Electrorefraction in Germanium. *IEEE Photonics Journal* **7(3)**, 1–14 (2015).

[116] L. Via and M. Cardona. Optical properties of pure and ultraheavily doped germanium: Theory and experiment. *Physical Review B* **34(4)**, 2586–2597 (1986).

[117] J. M. Hartmann, V. Benevent, V. Reboud, A. Chelnokov, K. Guilloy, N. Pauc and V. Calvo. Structural and electronic properties of in-situ phosphorous-doped Ge layers grown by reduced pressure-chemical vapour deposition. *Thin Solid Films* **602**, 13–19 (2015).

[118] X. Sun, J. Liu, L. C. Kimerling and J. Michel. Direct gap photoluminescence of n-type tensile-strained Ge-on-Si. *Applied Physics Letters* **95(1)**, 011911 (2009).

[119] M. Oehme, M. Gollhofer, D. Widmann, M. Schmid, M. Kaschel, E. Kasper and J. Schulze. Direct bandgap narrowing in Ge LED's on Si substrates. *Optics Express* **21(2)**, 2206–2211 (2013).

[120] Y. Shimura, S. A. Srinivasan, D. Van Thourhout, R. Van Deun, M. Pantouvaki, J. Van Campenhout and R. Loo. Enhanced active P doping by using high order Ge precursors leading to intense photoluminescence. *Thin Solid Films* (2015).

[121] T. K. P. Luong, A. Ghrib, M. T. Dau, M. A. Zrir, M. Stoffel, V. Le Thanh, R. Daineche, T. G. Le, V. Heresanu, O. Abbes, M. Petit, M. El Kurdi, P. Boucaud, H. Rinnert and J. Murota. Molecular-beam epitaxial growth of tensile-strained and n-doped Ge/Si(001) films using a GaP decomposition source. *Thin Solid Films* **557**, 70–75 (2013).

[122] R. Geiger, M. J. Süess, R. A. Minamisawa, C. Bonzon, G. Schiefler, J. Frigerio, D. Chrastina, G. Isella, R. Spolenak, J. Faist and H. Sigg. Enhanced light emission from Ge micro bridges uniaxially strained beyond 3%. In *IEEE 10th International Conference on Group IV Photonics*, 93–94 (2013).

[123] A. Lee, Q. Jiang, M. Tang, A. Seeds and H. Liu. Continuous-wave InAs/GaAs quantum-dot laser diodes monolithically grown on Si substrate with low threshold current densities. *Optics Express* **20(20)**, 22181–22187 (2012).

[124] Y. Bai, K. E. Lee, C. Cheng, M. L. Lee and E. A. Fitzgerald. Growth of highly tensile-strained Ge on relaxed $In_xGa_{1-x}As$ by metal-organic chemical vapor deposition. *Journal Of Applied Physics* **104(8)**, 084518 (2008).

[125] Y. Huo, H. Lin, C. Robert, M. Makarova, Y. Rong, M. Li, T. I. Kamins, J. Vuckovic and J. S. Harris. Strong enhancement of direct transition photoluminescence with highly tensile-strained Ge grown by molecular beam epitaxy. *Applied Physics Letters* **98(1)**, 011111 (2011).

[126] R. Jakomin, M. de Kersauson, M. El Kurdi, L. Largeau, O. Mauguin, G. Beaudoin, S. Sauvage, R. Ossikovski, G. Ndong, M. Chaigneau, I. Sagnes and P. Boucaud. High quality tensile-strained n-doped germanium thin films grown on InGaAs buffer layers

by metal-organic chemical vapor deposition. *Applied Physics Letters* **98(9)**, 091901 (2011).

[127] M. de Kersauson, M. Prost, A. Ghrib, M. El Kurdi, S. Sauvage, G. Beaudoin, L. Largeau, O. Mauguin, R. Jakomin, I. Sagnes, G. Ndong, M. Chaigneau, R. Ossikovski and P. Boucaud. Effect of increasing thickness on tensile-strained germanium grown on InGaAs buffer layers. *Journal Of Applied Physics* **113(18)**, 183508 (2013).

[128] S. Wirths, A. T. Tiedemann, Z. Ikonic, P. Harrison, B. Holländer, T. Stoica, G. Mussler, M. Myronov, J. M. Hartmann, D. Grützmacher, D. Buca and S. Mantl. Band engineering and growth of tensile strained Ge/(Si)GeSn heterostructures for tunnel field effect transistors. *Applied Physics Letters* **102(19)**, 192103 (2013).

[129] A. Ghrib, M. de Kersauson, M. El Kurdi, R. Jakomin, G. Beaudoin, S. Sauvage, G. Fishman, G. Ndong, M. Chaigneau, R. Ossikovski, I. Sagnes and P. Boucaud. Control of tensile strain in germanium waveguides through silicon nitride layers. *Applied Physics Letters* **100(20)** (2012).

[130] A. Ghrib, M. El Kurdi, M. de Kersauson, M. Prost, S. Sauvage, X. Checoury, G. Beaudoin, I. Sagnes and P. Boucaud. Tensile-strained germanium microdisks. *Applied Physics Letters* **102(22)**, 221112 (2013).

[131] G. Capellini, G. Kozlowski, Y. Yamamoto, M. Lisker, T. Schroeder, A. Ghrib, M. de Kersauson, M. El Kurdi, P. Boucaud and B. Tillack. Tensile Strained Ge Layers Obtained via a Si-CMOS Compatible Approach. In *Silicon-Germanium Technology and Device Meeting*, 1–2 (2012).

[132] G. Capellini, G. Kozlowski, Y. Yamamoto, M. Lisker, C. Wenger, G. Niu, P. Zaumseil, B. Tillack, A. Ghrib, M. de Kersauson, M. El Kurdi, P. Boucaud and T. Schroeder. Strain analysis in SiN/Ge microstructures obtained via Si-complementary metal oxide semiconductor compatible approach. *Journal Of Applied Physics* **113(1)**, 013513 (2013).

[133] M. Bollani, D. Chrastina, L. Gagliano, L. Rossetto, D. Scopece, M. Barget, V. Mondiali, J. Frigerio, M. Lodari, F. Pezzoli, F. Montalenti and E. Bonera. Local uniaxial tensile strain in germanium of up to 4% induced by SiGe epitaxial nanostructures. *Applied Physics Letters* **107(8)**, 083101 (2015).

[134] J. R. Jain, A. Hryciw, T. M. Baer, Miller, David AB, M. L. Brongersma and R. T. Howe. A micromachining-based technology for enhancing germanium light emission via tensile strain. *Nature Photonics* **6(6)**, 398–405 (2012).

[135] P. Velha, D. C. Dumas, K. Gallacher, R. Millar, M. Myronov, D. R. Leadley and D. J. Paul. Strained germanium nanostructures on silicon emitting at >2.2 μm wavelength. In *IEEE 10th International Conference on Group IV Photonics*, 142–143 (2013).

[136] L. M. Nguyen, R. Kuroyanagi, T. Tsuchizawa, Y. Ishikawa, K. Yamada and K. Wada. Stress tuning of the fundamental absorption edge of pure germanium waveguides. *Optics Express* **23(14)**, 18487–18492 (2015).

[137] E. A. Fitzgerald. Dislocations in strained-layer epitaxy: theory, experiment, and applications. *Materials Science Reports* **7(3)**, 87–142 (1991).

[138] M. J. Süess. Highly strained Si and Ge micro- and nanobridges for micro- and optoelectronic applications. Ph.D. thesis, ETH Zürich (2014).

[139] R. A. Minamisawa, M. J. Süess, R. Spolenak, J. Faist, C. David, J. Gobrecht, K. K. Bourdelle and H. Sigg. Top-down fabricated silicon nanowires under tensile elastic strain up to 4.5%. *Nature Communications* **3**, 1096 (2012).

[140] D. S. Sukhdeo, D. Nam, J.-H. Kang, M. L. Brongersma and K. C. Saraswat. A Nanomembrane-Based Bandgap-Tunable Germanium Microdisk Using Lithographically-Customizable Biaxial Strain for Silicon-Compatible Optoelectronics. *Optics Express* **23(13)**, 16740–16749 (2014).

[141] A. Gassenq, K. Guilloy, G. Osvaldo Dias, N. Pauc, D. Rouchon, J. M. Hartmann, J. Widiez, S. Tardif, F. Rieutord, J. Escalante, I. Duchemin, Y. M. Niquet, R. Geiger, T. Zabel, H. Sigg, J. Faist, A. Chelnokov, V. Reboud and V. Calvo. 1.9% bi-axial tensile strain in thick germanium suspended membranes fabricated in optical germanium-on-insulator substrates for laser applications. *Applied Physics Letters* **107(19)**, 191904 (2015).

[142] D. S. Sukhdeo, J. Petykiewicz, S. Gupta, D. Kim, S. Woo, Y. Kim, J. Vuckovic, K. C. Saraswat and D. Nam. Ge microdisk with lithographically-tunable strain using CMOS-compatible process. *Optics Express* **23(26)**, 33249–33254 (2015).

[143] E. Marin, C. Bonzon, R. Geiger, T. Zabel, H. Sigg and J. Faist. High order transversal modes in corrugated DFB micro-cavities. *European Conference on Lasers and Electro-Optics* (2015).

[144] V. Reboud, J. Widiez, J.-M. Hartmann, G. Osvaldo Dias, D. Fowler, A. Chelnokov, A. Gassenq, K. Guilloy, N. Pauc, V. Calvo, R. Geiger, T. Zabel, J. Faist and H. Sigg. Structural and optical properties of 200 mm germanium-on-insulator (GeOI) substrates for

silicon photonics applications. In G. T. Reed and M. R. Watts (Editors), *SPIE OPTO*, 936714–936714–6 (2015).

[145] J. Petykiewicz, D. Nam, D. S. Sukhdeo, S. Gupta, S. Buckley, A. Y. Piggott, J. Vuckovic and K. C. Saraswat. Direct Bandgap Light Emission from Strained Ge Nanowires Coupled with High-Q Optical Cavities. *Nano Letters* **16(4)**, 2168–2173 (2016).

[146] J. M. Hartmann, A. Abbadie and A. M. Papon. Reduced pressure–chemical vapor deposition of Ge thick layers on Si (001) for 1.3–1.55-μm photodetection. *Journal of Applied* ... (2004).

[147] D. D. Cannon, J. Liu, Y. Ishikawa, K. Wada, D. T. Danielson, S. Jongthammanurak, J. Michel and L. C. Kimerling. Tensile strained epitaxial Ge films on Si(100) substrates with potential application in L-band telecommunications. *Applied Physics Letters* **84(6)**, 906–908 (2004).

[148] J. M. Hartmann, A. M. Papon, V. Destefanis and T. Billon. Reduced pressure chemical vapor deposition of Ge thick layers on Si(001), Si(011) and Si(111). *Journal of Crystal Growth* **310(24)**, 5287–5296 (2008).

[149] A. Rickman. The commercialization of silicon photonics. *Nature Photonics* **8(8)**, 579–582 (2014).

[150] X. Chen, C. Li and H. K. Tsang. Device engineering for silicon photonics. *NPG Asia Materials* **3(1)**, 34–40 (2011).

[151] G. Isella, D. Chrastina, B. Rössner, T. Hackbarth, H. J. Herzog, U. König and H. von Känel. Low-energy plasma-enhanced chemical vapor deposition for strained Si and Ge heterostructures and devices. *Solid-State Electronics* **48(8)**, 1317–1323 (2004).

[152] T. Akatsu, C. Deguet, L. Sanchez, F. Allibert, D. Rouchon, T. Signamarcheix, C. Richtarch, A. Boussagol, V. Loup, F. Mazen, J.-M. Hartmann, Y. Campidelli, L. Clavelier, F. Letertre, N. Kernevez and C. Mazure. Germanium-on-insulator (GeOI) substrates—A novel engineered substrate for future high performance devices. *Materials Science in Semiconductor Processing* **9(4-5)**, 444–448 (2006).

[153] E. Augendre, L. Sanchez, L. Benaissa, T. Signamarcheix, J.-M. Hartmann, C. Le Royer, M. Vinet, W. Van Den Daele, J.-F. Damlencourt, K. Romanjek, A. Pouydebasque, P. Batude, C. Tabone, F. Mazen, A. Tauzin, N. Blanc, M. Pellat, J. Dechamp, M. Zussy, P. Scheiblin, M.-A. Jaud, C. Drazek, C. Maurois, M. Piccin, A. Abbadie, F. Lallement, N. Daval, E. Guiot, A. Rigny, B. Ghyselen, K. Bourdelle, F. Boulanger, S. Cristoloveanu,

T. Billon, O. Faynot, C. Deguet and L. Clavelier. Challenges and Progress in Germanium-on-Insulator Materials and Device Development towards ULSI Integration. *ECS Transactions* **25(7)**, 351–362 (2009).

[154] K. H. Lee, S. Bao, G. Y. Chong, Y. H. Tan, E. A. Fitzgerald and C. S. Tan. Fabrication and characterization of germanium-on-insulator through epitaxy, bonding, and layer transfer. *Journal Of Applied Physics* **116(10)**, 103506 (2014).

[155] R. Soref. Mid-infrared photonics in silicon and germanium. *Nature Photonics* **4(8)**, 495–497 (2010).

[156] E. Marin. High-Q Cavities for Use with Tensile Strained Ge Microbridges. Master thesis–ETH Zürich (2015).

[157] D. S. Sukhdeo, J. Petykiewicz, S. Gupta, D. Kim, S. Woo, Y. Kim, J. Vuckovic, K. C. Saraswat and D. Nam. Ge microdisk with lithographically-tunable strain using CMOS-compatible process. *Optics Express* **23(26)**, 33249–33254 (2015).

[158] M. J. Süess, R. A. Minamisawa, R. Geiger, K. K. Bourdelle, H. Sigg and R. Spolenak. Power-Dependent Raman Analysis of Highly Strained Si Nanobridges. *Nano Letters* **14(3)**, 1249–1254 (2014).

[159] A. Gassenq, S. Tardif, K. Guilloy, I. Duchemin, G. Osvaldo Dias, N. Pauc, D. Rouchon, J.-M. Hartmann, J. Widiez, J. Escalante, Y.-M. Niquet, R. Geiger, T. Zabel, H. Sigg, J. Faist, A. Chelnokov, F. Rieutord, V. Reboud and V. Calvo. Accurate strain measurements in highly strained Ge microbridges. arXiv:1604.04391 (2016).

[160] D. Nam, D. S. Sukhdeo, S. Gupta, J.-H. Kang, M. L. Brongersma and K. C. Saraswat. Study of Carrier Statistics in Uniaxially Strained Ge for a Low-Threshold Ge Laser. *IEEE Journal of Selected Topics in Quantum Electronics* **20(4)**, 1500107 (2014).

[161] Y. P. Varshni. Band-to-band radiative recombination in groups IV, VI, and III-V semiconductors (I). *Physica Status Solidi (b)* **19(2)**, 459–514 (1967).

[162] F. Schäffler. High-mobility Si and Ge structures. *Semiconductor Science and Technology* **12**, 1515–1549 (1997).

[163] C. D. Thurmond. The standard thermodynamic functions for the formation of electrons and holes in Ge, Si, GaAs, and GaP. *Journal of the Electrochemical Society* **122(8)**, 1133–1141 (1975).

[164] J. R. Sánchez-Pérez, C. Boztug, F. Chen, F. F. Sudradjat, D. M. Paskiewicz, R. Jacobson, M. G. Lagally and R. Paiella. Direct-bandgap light-emitting germanium in tensilely strained nanomembranes. *Proceedings of the National Academy of Sciences* **108(47)**, 18893–18898 (2011).

[165] C. Boztug, J. R. Sanchez-Perez, F. F. Sudradjat, R. B. Jacobson, D. M. Paskiewicz, M. G. Lagally and R. Paiella. Tensilely Strained Germanium Nanomembranes as Infrared Optical Gain Media. *Small* **9(4)**, 622–630 (2012).

[166] C. Boztug, J. R. Sánchez-Pérez, J. Yin, M. G. Lagally and R. Paiella. Grating-coupled mid-infrared light emission from tensilely strained germanium nanomembranes. *Applied Physics Letters* **103(20)**, 201114 (2013).

[167] Y. Okada and Y. Tokumaru. Precise Determination of Lattice-Parameter and Thermal-Expansion Coefficient of Silicon Between 300 K and 1500 K. *Journal Of Applied Physics* **56(2)**, 314–320 (1984).

[168] S. I. Novikova. Thermal Expansion of Germanium at Low Temperatures. *Soviet Physics Solid State* **2(1)**, 37–38 (1960).

[169] H. J. McSkimin. Measurement of Elastic Constants at Low Temperatures by Means of Ultrasonic Waves–Data for Silicon and Germanium Single Crystals, and for Fused Silica. *Journal Of Applied Physics* **24(8)**, 988 (1953).

[170] E. F. Schubert. *Light-Emitting Diodes*. Cambridge University Press (2006).

[171] Y. P. Varshni. Temperature dependence of the energy gap in semiconductors. *Physica* **34(1)**, 149–154 (1967).

[172] R. Lawrance. The Temperature Dependence of Drift Mobility in Germanium. *Physical Review* **89(6)**, 1295–1295 (1953).

[173] F. J. Morin. Lattice-Scattering Mobility in Germanium. *Physical Review* **93(1)**, 62–63 (1954).

[174] M. A. Cavicchia, W. Wang and R. R. Alfano. Intervalley Scattering as a Function of Temperature in GaAs Using Time-Resolved Visible Pump - IR Probe Absorption Spectroscopy. In *Hot Carriers in Semiconductors*, 365–368. Springer (1996).

[175] G. Mak and H. M. van Driel. Femtosecond transmission spectroscopy at the direct band edge of germanium. *Physical Review B* **49(23)**, 16817 (1994).

[176] K. Tanaka, H. Ohtake and T. Suemoto. Determination of Intervalley Scattering Time in Germanium by Subpicosecond Time-Resolved Raman Spectroscopy. *Physical Review Letters* **71(12)**, 1935–1938 (1993).

[177] V. Aubry-Fortuna and P. Dollfus. Electron transport properties in high-purity Ge down to cryogenic temperatures. *Journal Of Applied Physics* **108(12)**, 123706 (2010).

[178] A. L. Ruoff. On the ultimate yield strength of solids. *Journal Of Applied Physics* **49(1)**, 197 (1978).

[179] L. B. Valdes. Measurement of minority carrier lifetime in germanium. *Proceedings of the IRE* **40(11)**, 1420–1423 (1952).

[180] J. A. Burton, G. W. Hull, F. J. Morin and J. C. Severiens. Effect of Nickel and Copper Impurities on the Recombination of Holes and Electrons in Germanium. *Journal of Physical Chemistry* **57(8)**, 853–859 (1953).

[181] S. R. Lederhandler and L. J. Giacoletto. Measurement of minority carrier lifetime and surface effects in junction devices. *Proceedings of the IRE* **43(4)**, 477–483 (1955).

[182] S. G. Kalashnikov. Studies on the Recombination of Electrons and Holes in Germanium. *Journal of Physics and Chemistry of Solids* **8**, 52–59 (1959).

[183] R. Conradt and J. Aengenheister. Minority Carrier Lifetime in Highly Doped Ge. *Solid State Communications* **10(3)**, 321–323 (1972).

[184] Y.-Y. Chen, H. C. Chang, Y. H. Chi, C. H. Huang and C. W. Liu. GeO_2 Passivation for Low Surface Recombination Velocity on Ge Surface. *IEEE Electron Device Letters* **34(3)**, 444–446 (2013).

[185] N. Derhacobian, P. Fine, J. T. Walton, Y. K. Wong, C. S. Rossington and P. N. Luke. Determination of surface recombination velocity and bulk lifetime in detector grade silicon and germanium crystals. *IEEE Transactions on Nuclear Science* **41(4)**, 1026–1030 (1994).

[186] E. Gaubas and J. Vanhellemont. Dependence of carrier lifetime in germanium on resisitivity and carrier injection level. *Applied Physics Letters* **89(14)**, 142106 (2006).

[187] D. Poelman, P. Clauws and B. Depuydt. Chemical surface passivation of low resistivity p-type Ge wafers for solar cell applications. *Solar Energy Materials and Solar Cells* **76(2)**, 167–173 (2003).

[188] E. A. Fitzgerald, S. B. Samavedam and Y. H. Xie. Influence of strain on semiconductor thin film epitaxy. *Journal of Vacuum Science & Technology A* **15(3)**, 1048–1056 (1997).

[189] G. Grzybowski, R. Roucka, J. Mathews, L. Jiang, R. T. Beeler, J. Kouvetakis and J. Menendez. Direct versus indirect optical recombination in Ge films grown on Si substrates. *Physical Review B* **84(20)**, 205307 (2011).

[190] J. Mathews. Investigation of light absorption and emission in germanium and germanium tin films grown on silicon substrates. Ph.D. thesis, Arizona State University (2011).

[191] S. Kako, K. Oda, T. Ido and Y. Arakawa. Excess carrier lifetime in epitaxially grown layers of germanium on silicon. In *IEEE 12*th *International Conference on Group IV Photonics*, 171–172 (2015).

[192] S. Saito, F. Y. Gardes, A. Z. Al-Attili, K. Tani, K. Oda, Y. Suwa, T. Ido, Y. Ishikawa, S. Kako, S. Iwamoto and Y. Arakawa. Group IV Light Sources to Enable the Convergence of Photonics and Electronics. *Frontiers in Materials* **1(15)** (2014).

[193] T. Okumura, K. Oda, Y. Suwa, S. Saito, T. Ido and Y. Arakawa. Time-Resolved Photoluminescence Study of Highly n-doped Germanium Grown on Silicon. In *IEEE* 9^{th} *International Conference on Group IV Photonics*, 1–3 (2012).

[194] D. Nam, J.-H. Kang, M. L. Brongersma and K. C. Saraswat. Observation of improved minority carrier lifetimes in high-quality Ge-on-insulator using time-resolved photoluminescence. *Optics Letters* **39(21)**, 6205 (2014).

[195] J. J. Sheng, D. Leonhardt, S. M. Han, S. W. Johnston, J. G. Cederberg and M. S. Carroll. Empirical correlation for minority carrier lifetime to defect density profile in germanium on silicon grown by nanoscale interfacial engineering. *Journal of Vacuum Science & Technology B* **31(5)**, 051201 (2013).

[196] S. A. Srinivasan, M. Pantouvaki, P. Verheyen, G. Lepaee, P. Absil, J. Van Campenhout and D. Van ThouAout. Carrier lifetime assessment in integrated Ge waveguide devices. In *IEEE 12*th *International Conference on Group IV Photonics*, 167–168 (2015).

[197] L. Carroll, P. Friedli, P. Lerch, J. Schneider, D. Treyer, S. Hunziker, S. Stutz and H. Sigg. Ultra-broadband infrared pump-probe spectroscopy using synchrotron radiation and a tuneable pump. *Review of Scientific Instruments* **82(6)**, 063101 (2011).

[198] P. Friedli. Linear and Non-Linear Spectroscopy of Semiconductors using Synchrotron Infrared. Ph.D. thesis, ETH Zürich (2013).

[199] J. Sá, P. Friedli, R. Geiger, P. Lerch, M. H. Rittmann-Frank, C. J. Milne, J. Szlachetko, F. G. Santomauro, J. A. van Bokhoven, M. Chergui, M. J. Rossi and H. Sigg. Transient mid-IR study of electron dynamics in TiO_2 conduction band. *The Analyst* **138(7)**, 1966 (2013).

[200] F. K. Reinhart. A heuristic approach to determine the modifications of electronic and optical properties of "intrinsic" GaAs under free-carrier injection. Part II. *Journal Of Applied Physics* **97(12)**, 123535 (2005).

[201] F. K. Reinhart. Direct determination of the free-carrier injection density, the free-carrier absorption, and the recombination factors in double heterostructure diodes by optical phase measurements. Part III. *Journal Of Applied Physics* **97(12)**, 123536 (2005).

[202] H. H. Li. Refractive index of silicon and germanium and its wavelength and temperature derivatives. *Journal of Physical and Chemical Reference Data* **9(3)**, 561–658 (1980).

[203] R. Gross and A. Marx. *Festkörperphysik*. Oldenbourg Wissenschaftsverlag (2012).

[204] J. D. Jackson. *Classical Electrodynamics*. John Wiley & Sons (1999).

[205] S. Marchionna, A. Virtuani, M. Acciarri, G. Isella and H. von Känel. Defect imaging of SiGe strain relaxed buffers grown by LEPECVD. *Materials Science in Semiconductor Processing* **9(4-5)**, 802–805 (2006).

[206] H.-C. Luan, D. R. Lim, K. K. Lee, K. M. Chen, J. G. Sandland, K. Wada and L. C. Kimerling. High-quality Ge epilayers on Si with low threading-dislocation densities. *Applied Physics Letters* **75(19)**, 2909–2911 (1999).

[207] J. F. Young and H. M. van Driel. Ambipolar diffusion of high-density electrons and holes in Ge, Si, and GaAs: Many-body effects. *Physical Review B* **26(4)**, 2147–2158 (1982).

[208] A. Uleckas, E. Gaubas, T. Ceponis, K. Zilinskas, R. Grigonis, V. Sirutkaitis and J. Vanhellemont. Analysis of Auger Recombination Characteristics in High Resistivity Si and Ge. *Solid State Phenomena* **178-179**, 427–432 (2011).

[209] Y. Cai, R. Camacho-Aguilera, J. T. Bessette, L. C. Kimerling and J. Michel. High phosphorous doped germanium: Dopant diffusion and modeling. *Journal Of Applied Physics* **112(3)**, 034509 (2012).

[210] A. B. Sproul. Dimensionless solution of the equation describing the effect of surface recombination on carrier decay in semiconductors. *Journal Of Applied Physics* **76(5)**, 2851 (1994).

[211] A. Kurtz, S. Kulin and B. Averbach. Effect of Dislocations on the Minority Carrier Lifetime in Semiconductors. *Physical Review* **101(4)**, 1285–1291 (1956).

[212] Y.-L. Chao, R. Scholz, M. Reiche, U. Gösele and J. Woo. Characteristics of germanium-on-insulators fabricated by wafer bonding and hydrogen-induced layer splitting. *Japanese Journal of Applied Physics* **45**, 8565 (2006).

[213] M. L. David, F. Pailloux, D. Babonneau, M. Drouet, J. F. Barbot, E. Simoen and C. Claeys. The effect of the substrate temperature on extended defects created by hydrogen implantation in germanium. *Journal Of Applied Physics* **102(9)**, 096101–3 (2007).

[214] Y. Cai, Z. Han, X. Wang, R. E. Camacho-Aguilera, L. C. Kimerling, J. Michel and J. Liu. Analysis of Threshold Current Behavior for Bulk and Quantum-Well Germanium Laser Structures. *IEEE Journal of Selected Topics in Quantum Electronics* **19(4)**, 1901009 (2013).

[215] W. W. Chow, J. Kabuss and A. Carmele. Analysis of Lasing From Direct Transition in Ge-on-Si. *IEEE Journal of Selected Topics in Quantum Electronics* **19(4)**, 1502309 (2013).

[216] W. W. Chowa. Model for direct-transition gain in a Ge-on-Si laser. *Applied Physics Letters* **100(19)**, 191113 (2012).

[217] E. Gaubas and J. Vanhellemont. A simple technique for the separation of bulk and surface recombination parameters in silicon. *Journal Of Applied Physics* **80(11)**, 6293–6297 (1996).

[218] S. Jiang, S. Butler, E. Bianco, O. D. Restrepo, W. Windl and J. E. Goldberger. Improving the stability and optical properties of germanane via one-step covalent methyl-termination. *Nature Communications* **5**, 3389 (2014).

[219] E. Yablonovitch, D. L. Allara, C. C. Chang, T. Gmitter and T. B. Bright. Unusually low surface-recombination velocity on silicon and germanium surfaces. *Physical Review Letters* **57(2)**, 249 (1986).

[220] B. P. Swain, H. Takato and I. Sakata. Wet Chemical Surface Passivation of Germanium Wafers by Quinhydrone–Methanol Treatment for Minority Carrier Lifetime Measurements. *Applied Physics Express* **2(10)**, 105501 (2009).

[221] C. Andersson. Passivation of Ge for high mobility CMOS transistors. Ph.D. thesis, ETH Zürich (2012).

[222] J. Kim, S. W. Bedell and D. K. Sadana. Multiple implantation and multiple annealing of phosphorus doped germanium to achieve n-type activation near the theoretical limit. *Applied Physics Letters* **101(11)**, 112107 (2012).

[223] A. R. Peaker, V. Markevich, J. Slotte, M. Rummukainen, I. Capan, B. Pivac, R. Gwilliam, C. Jeynes and L. Dobaczewski. Understanding Ion Implantation Defects in Germanium. *ECS Transactions* **3(2)**, 67–76 (2006).

[224] E. W. J. Mitchell. The effect of radiation damage on the electronic properties of solids. *British Journal of Applied Physics* **8(5)**, 179–189 (1957).

[225] J. Liu, R. Camacho-Aguilera, J. T. Bessette, X. Sun, X. Wang, Y. Cai, L. C. Kimerling and J. Michel. Ge-on-Si optoelectronics. *Thin Solid Films* **520(8)**, 3354–3360 (2012).

[226] G. Scappucci, G. Capellini, W. C. T. Lee and M. Y. Simmons. Ultradense phosphorus in germanium delta-doped layers. *Applied Physics Letters* **94(16)**, 162106 (2009).

[227] G. Capellini, W. M. Klesse, G. Mattoni, M. Y. Simmons and G. Scappucci. Alternative High n-Type Doping Techniques in Germanium. *ECS Transactions* **64(11)**, 163–171 (2014).

[228] A. R. Beattie and P. T. Landsberg. Auger Effect in Semiconductors. *Proceedings of the Royal Society A: Mathematical, Physical and Engineering Sciences* **249(1256)**, 16–29 (1959).

[229] L. Huldt. Band-to-band Auger recombination in indirect gap semiconductors. *Physica Status Solidi (a)* **8(1)**, 173–187 (1971).

[230] A. R. Adams, M. Asada, Y. Suematsu and S. Arai. The Temperature Dependence of the Efficiency and Threshold Current of $In_{1-x}Ga_xAs_yP_{1-y}$ Lasers Related to Intervalence Band Absorption. *Japanese Journal of Applied Physics* **19(10)**, L621–L624 (1980).

[231] S. Brotzmann and H. Bracht. Intrinsic and extrinsic diffusion of phosphorus, arsenic, and antimony in germanium. *Journal Of Applied Physics* **103(3)**, 033508 (2008).

[232] G. Mattoni, W. M. Klesse, G. Capellini, M. Y. Simmons and G. Scappucci. Phosphorus Molecules on Ge(001): A Playground for Controlled N-Doping of Germanium at High Densities. *ACS Nano* **7(12)**, 11310–11316 (2013).

[233] W. M. Klesse, G. Scappucci, G. Capellini, J. M. Hartmann and M. Y. Simmons. Atomic layer doping of strained Ge-on-insulator thin films with high electron densities. *Applied Physics Letters* **102(15)**, 151103 (2013).

[234] P. R. Pukite, A. Harwit and S. S. Iyer. Molecular beam epitaxy of metastable, diamond structure Sn_xGe_{1-x} alloys. *Applied Physics Letters* **54(21)**, 2142 (1989).

[235] J. Olajos, P. Vogl, W. Wegscheider and G. Abstreiter. Infrared Optical Properties and Band Structure of α-Sn/Ge Superlattices on Ge Substrates. *Physical Review Letters* **67(22)**, 3164–3167 (1991).

[236] W. Wegscheider, K. Eberl, U. Menczigar and G. Abstreiter. Single-crystal Sn/Ge superlattices on Ge substrates: Growth and structural properties. *Applied Physics Letters* **57(9)**, 875 (1990).

[237] A. Harwit, P. R. Pukite, J. Anginello and S. S. Iyer. Properties of Diamond Structure SnGe Films Grown by Molecular-Beam Epitaxy. *Thin Solid Films* **184(1-2)**, 395–401 (1990).

[238] G. He and H. A. Atwater. Interband Transitions in Sn_xGe_{1-x} Alloys. *Physical Review Letters* **79(10)**, 1937–1940 (1997).

[239] R. W. Olesinski and G. J. Abbaschian. The Ge—Sn (Germanium—Tin) system. *Bulletin of Alloy Phase Diagrams* **5(3)**, 265–271 (1984).

[240] M. R. Bauer, J. Tolle, C. Bungay, A. V. G. Chizmeshya, D. J. Smith, J. Menéndez and J. Kouvetakis. Tunable band structure in diamond–cubic tin–germanium alloys grown on silicon substrates. *Solid State Communications* **127(5)**, 355–359 (2003).

[241] R. Chen, H. Lin, Y. Huo, C. Hitzman, T. I. Kamins and J. S. Harris. Increased photoluminescence of strain-reduced, high-Sn composition Ge1—xSnx alloys grown by molecular beam epitaxy. *Applied Physics Letters* **99(18)**, 181125 (2011).

[242] N. Bhargava, M. Coppinger, J. P. Gupta, L. Wielunski and J. Kolodzey. Lattice constant and substitutional composition of GeSn alloys grown by molecular beam epitaxy. *Applied Physics Letters* **103(4)**, 041908 (2013).

[243] M. Oehme, D. Buca, K. Kostecki, S. Wirths, B. Holländer, E. Kasper and J. Schulze. Epitaxial growth of highly compressively strained GeSn alloys up to 12.5% Sn. *Journal of Crystal Growth* **384**, 71–76 (2013).

[244] B. Vincent, F. Gencarelli, H. Bender, C. Merckling, B. Douhard, D. H. Petersen, O. Hansen, H. H. Henrichsen, J. Meersschaut, W. Vandervorst, M. Heyns, R. Loo and M. Caymax. Undoped and in-situ B doped GeSn epitaxial growth on Ge by atmospheric pressure-chemical vapor deposition. *Applied Physics Letters* **99(15)**, 152103 (2011).

[245] R. Chen, Y.-C. Huang, S. Gupta, A. C. Lin, E. Sanchez, Y. Kim, K. C. Saraswat, T. I. Kamins and J. S. Harris. Material characterization of high Sn-content, compressively-strained GeSn epitaxial films after rapid thermal processing. *Journal of Crystal Growth* **365**, 29–34 (2013).

[246] S. Wirths, D. Buca, G. Mussler, A. T. Tiedemann, B. Holländer, P. Bernardy, T. Stoica, D. Grützmacher and S. Mantl. Reduced Pressure CVD Growth of Ge and $Ge_{1-x}Sn_x$ Alloys. *ECS Journal of Solid State Science and Technology* **2(5)**, N99–N102 (2013).

[247] C. Xu, R. T. Beeler, L. Jiang, G. Grzybowski, A. V. G. Chizmeshya, J. Menéndez and J. Kouvetakis. New strategies for Ge-on-Si materials and devices using non-conventional hydride chemistries: the tetragermane case. *Semiconductor Science and Technology* **28(10)**, 105001 (2013).

[248] W. Du, S. A. Ghetmiri, B. R. Conley, A. Mosleh, A. Nazzal, R. A. Soref, G. Sun, J. Tolle, J. Margetis, H. A. Naseem and S.-Q. Yu. Competition of optical transitions between direct and indirect bandgaps in $Ge_{1-x}Sn_x$. *Applied Physics Letters* **105(5)**, 051104 (2014).

[249] J. D. Gallagher, C. L. Senaratne, P. Sims, T. Aoki, J. Menendez and J. Kouvetakis. Electroluminescence from GeSn heterostructure pin diodes at the indirect to direct transition. *Applied Physics Letters* **106(9)**, 091103 (2015).

[250] J. P. Gupta, N. Bhargava, S. Kim, T. Adam and J. Kolodzey. Infrared electroluminescence from GeSn heterojunction diodes grown by molecular beam epitaxy. *Applied Physics Letters* **102(25)**, 251117 (2013).

[251] D. Stange, N. von den Driesch, D. Rainko, C. Schulte-Braucks, S. Wirths, G. Mussler, A. T. Tiedemann, T. Stoica, J. M. Hartmann, Z. Ikonic, S. Mantl, D. Grützmacher and D. Buca. Study of GeSn based heterostructures: towards optimized group IV MQW LEDs. *Optics Express* **24(2)**, 1358–1367 (2016).

[252] B. Schwartz, M. Oehme, K. Kostecki, D. Widmann, M. Gollhofer, R. Koerner, S. Bechler, I. A. Fischer, T. Wendav, E. Kasper, J. Schulze and M. Kittler. Electroluminescence of GeSn/Ge MQW LEDs on Si substrate. *Optics Letters* **40(13)**, 3209 (2015).

[253] B. R. Conley, J. Margetis, W. Du, H. Tran, A. Mosleh, S. A. Ghetmiri, J. Tolle, G. Sun, R. Soref, B. Li, H. A. Naseem and S.-Q. Yu. Si based GeSn photoconductors with a 1.63 A/W peak responsivity and a 2.4 μm long-wavelength cutoff. *Applied Physics Letters* **105(22)**, 221117 (2014).

[254] M. Oehme, K. Kostecki, K. Ye, S. Bechler, K. Ulbricht, M. Schmid, M. Kaschel, M. Gollhofer, R. Körner, W. Zhang, E. Kasper and J. Schulze. GeSn-on-Si normal incidence photodetectors with bandwidths more than 40 GHz. *Optics Express* **22(1)**, 839–846 (2014).

[255] H. H. Tseng, H. Li, V. Mashanov, Y. J. Yang, H. H. Cheng, G. E. Chang and R. A. Soref. GeSn-based p-i-n photodiodes with strained active layer on a Si wafer. *Applied Physics Letters* **103(23)**, 231907 (2013).

[256] S. Gupta, R. Chen, B. Vincent, D. Lin, B. Magyari-Kope, M. Caymax, J. Dekoster, J. S. Harris, Y. Nishi and K. C. Saraswat. (Invited) GeSn Channel n and p MOSFETs. *ECS Transactions* **50(9)**, 937–941 (2013).

[257] L. Wang, S. Su, W. Wang, X. Gong, Y. Yang, P. Guo, G. Zhang, C. Xue, B. Cheng, G. Han and Y.-C. Yeo. Strained germanium–tin (GeSn) p-channel metal-oxide-semiconductor field-effect-transistors (p-MOSFETs) with ammonium sulfide passivation. *Selected Papers from the 6th International SiGe Technology and Device Meeting (ISTDM 2012)* **83(0)**, 66–70 (2013).

[258] S. Wirths, D. Buca and S. Mantl. Si–Ge–Sn alloys: From growth to applications. *Progress in Crystal Growth and Characterization of Materials* **62(1)**, 1–39 (2016).

[259] S. Gupta, B. Magyari-Köpe, Y. Nishi and K. C. Saraswat. Achieving direct band gap in germanium through integration of Sn alloying and external strain. *Journal Of Applied Physics* **113(7)**, 073707 (2013).

[260] N. von den Driesch, D. Stange, S. Wirths, G. Mussler, B. Holländer, Z. Ikonic, J. M. Hartmann, T. Stoica, S. Mantl, D. Grützmacher and D. Buca. Direct Bandgap Group IV Epitaxy on Si for Laser Applications. *Chemistry of Materials* **27(13)**, 4693–4702 (2015).

[261] S. Takeuchi, A. Sakai, K. Yamamoto, O. Nakatsuka, M. Ogawa and S. Zaima. Growth and structure evaluation of strain-relaxed $Ge_{1-x}Sn_x$ buffer layers grown on various types of substrates. *Semiconductor Science and Technology* **22(1)**, S231–S235 (2006).

[262] C. L. Senaratne, J. D. Gallagher, L. Jiang, T. Aoki, D. J. Smith, J. Menendez and J. Kouvetakis. $Ge_{1-y}Sn_y$ (y = 0.01-0.10) alloys on Ge-buffered Si: Synthesis, microstructure, and optical properties. *Journal Of Applied Physics* **116(13)**, 133509 (2014).

[263] S. A. Ghetmiri, W. Du, J. Margetis, A. Mosleh, L. Cousar, B. R. Conley, L. Domulevicz, A. Nazzal, G. Sun, R. A. Soref, J. Tolle, B. Li, H. A. Naseem and S.-Q. Yu. Direct-bandgap GeSn grown on silicon with 2230 nm photoluminescence. *Applied Physics Letters* **105(15)**, 151109 (2014).

[264] S. Wirths. Group IV Epitaxy for Advanced Nano- and Optoelectronic Applications. Ph.D. thesis, RWTH Aachen University (2015).

[265] Kusumandari, N. Taoka, W. Takeuchi, M. Sakashita, O. Nakatsuka and S. Zaima. Defects Induced by Reactive Ion Etching in Ge Substrate. *Advanced Materials Research* **896**, 241–244 (2014).

[266] F. Bellenger, C. Merckling, J. Penaud, M. Houssa, M. Caymax, M. Meuris, K. De Meyer and M. M. Heyns. Interface Properties Improvement of Ge/Al_2O_3 and $Ge/GeO_2/Al_2O_3$ Gate Stacks using Molecular Beam Deposition. *ECS Transactions* **16(5)**, 411–422 (2008).

[267] S. Wirths, D. Stange, M.-A. Pampillón, A. T. Tiedemann, G. Mussler, A. Fox, U. Breuer, B. Baert, E. San Andrés, N. D. Nguyen, J.-M. Hartmann, Z. Ikonic, S. Mantl and D. Buca. High-k Gate Stacks on Low Bandgap Tensile Strained Ge and GeSn Alloys for Field-Effect Transistors. *ACS Applied Materials & Interfaces* **7(1)**, 62–67 (2014).

[268] S. Gupta, C. Robert, Y.-C. Huang, Y. Kim, E. Sanchez, J. S. Harris and K. C. Saraswat. Highly Selective Dry Etching of Germanium over Germanium—Tin ($Ge_{1-x}Sn_x$): A Novel Route for $Ge_{1-x}Sn_x$ Nanostructure Fabrication. *Nano Letters* **13(8)**, 3783–3790 (2013).

[269] H. W. Icenogle, B. C. Platt and W. L. Wolfe. Refractive indexes and temperature coefficients of germanium and silicon. *Applied Optics* **15(10)**, 2348–2351 (1976).

[270] R. Chen, S. Gupta, Y.-C. Huang, Y. Huo, C. W. Rudy, E. Sanchez, Y. Kim, T. I. Kamins, K. C. Saraswat and J. S. Harris. Demonstration of a Ge/GeSn/Ge Quantum-Well Microdisk Resonator on Silicon: Enabling High-Quality Ge(Sn) Materials for Micro- and Nanophotonics. *Nano Letters* **14(1)**, 37–43 (2013).

[271] U. T. Schwarz, M. Pindl, E. Sturm, M. Furitsch, A. Leber, S. Miller, A. Lell and V. Härle. Influence of ridge geometry on lateral mode stability of (Al,In)GaN laser diodes. *Physica Status Solidi (a)* **202(2)**, 261–270 (2005).

[272] U. T. Schwarz and B. Witzigmann. Optical properties of edge-emitting lasers: measurement and simulation. In *Nitride Semiconductor Devices: Principles and Simulation*. Wiley (2007).

[273] G.-E. Chang, S.-W. Chang and S. L. Chuang. Strain-Balanced Ge_zSn_{1-z}-$Si_xGe_ySn_{1-x-y}$ multiple-quantum-well lasers. *IEEE Journal of Quantum Electronics* **46(12)**, 1813–1820 (2010).

[274] S.-H. Wei and A. Zunger. Predicted band-gap pressure coefficients of all diamond and zinc-blende semiconductors: Chemical trends. *Physical Review B* **60(8)**, 5404–5411 (1999).

[275] J. R. Chelikowsky and M. L. Cohen. Nonlocal Pseudopotential Calculations for Electronic-Structure of 11 Diamond and Zincblende Semiconductors. *Physical Review B* **14(2)**, 556–582 (1976).

[276] M.-Y. Ryu, T. R. Harris, Y. K. Yeo, R. T. Beeler and J. Kouvetakis. Temperature-dependent photoluminescence of Ge/Si and $Ge_{1-y}Sn_y$/Si, indicating possible indirect-to-direct bandgap transition at lower Sn content. *Applied Physics Letters* **102(17)**, 171908 (2013).

[277] P. Moontragoon, Z. Ikonic and P. Harrison. Band structure calculations of Si–Ge–Sn alloys: achieving direct band gap materials. *Semiconductor Science and Technology* **22(7)**, 742–748 (2007).

[278] S. Birner. Modeling of Semiconductor Nanostructures and Semiconductor-electrolyte Interfaces. Ph.D. thesis, TU München (2011).

[279] T. Andlauer. Optoelectronic and spin-related properties of semiconductor nanostructures in magnetic fields. Ph.D. thesis, TU München (2009).

[280] J. C. Hensel and K. Suzuki. Quantum resonances in the valence bands of germanium. II. Cyclotron resonances in uniaxially stressed crystals. *Physical Review B* **9(10)**, 4219–4257 (1974).

[281] M. Chandrasekhar and F. H. Pollak. Effects of uniaxial stress on the electroreflectance spectrum of Ge and GaAs. *Physical Review B* **15(4)**, 2127–2144 (1977).

[282] O. Madelung. *Semiconductors: Group IV Elements and Group III-V Compounds*. Springer (1991).

"Great difficulties are felt at first [in research] and these cannot be overcome except by starting from experiments . . . and then by conceiving certain hypotheses . . . But even so, very much hard work remains to be done and one needs not only great perspicacity but often a degree of good fortune".

Christiaan Huygens

Acknowledgements

During the last four years, I had the good fortune to be surrounded by a group of great scientist. Without their support, the outcome presented in this thesis could not have been achieved. But also the friendships I could build contribute in a similar manner to all the fond memories, which I will always have about my time in Switzerland.

I would like to thank Prof. Dr. Jérôme Faist for the academic supervision of my thesis and his strong interest in this topic. His scientific advice and vision were essential for the progress of the project, and his concise and motivational nature helped to keep the focus on the next goals.

I would similarly like to thank my direct supervisor at the Paul Scherrer Institute, Dr. Hans Sigg, for his guidance and support within the last years. I enjoyed his open-door policy, our frequent discussions about all aspects of physics and the time together in the lab, where I could profit a lot from his vast experimental know-how and experience.

I thank Prof. Dr. Gerhard Abstreiter and Dr. Alexei Chelnokov for agreeing to serve as members of my examination committee.

In Dr. Martin J. Süess I had the best colleague I could have asked for. I want to thank him for all his key contributions and help concerning Raman spectroscopy, FEM modelling, x-ray experiments and materials science, for the awesome times in Switzerland, Germany and Korea, and for being a great friend.

I would like to thank Dr. Peter Friedli for introducing me to the magic of synchrotron-based pump-probe measurements, endless on- and off-site support even long after his time at PSI, and great dinners all around Aargau.

I want to thank Dr. Thomas Zabel for reviving the good WSI times by joining our group in Switzerland. It was great to have an old friend back by my side and he helped a great deal with the results that were achieved within the last year of this thesis - besides also being a key part in the cup-winning LMN football line-up!

I would like to thank Esteban Marín for the great work during his master's thesis and during the start of his PhD. I enjoyed our time together in- and outside of the lab, all the in-depth discussions ranging from physics to non-sense, and wish him all the best for the future with his IT company.

I want to thank our collaborators from Forschungszentrum Jülich, namely Dr. Dan Buca, Dr. Stephan Wirths and Daniela Stange, for the pleasant teamwork on GeSn. In particular, I would like to thank Stephan for all those days and nights doing spectroscopy at the synchrotron, which were much easier to go through with someone likeable as him around to discuss exciting new results, think about workarounds for things that keep failing - as well as for watching matches of the best club in the world.

I would like to thank the team at CEA LETI for the fruitful collaboration on strained Germanium and for providing outstanding GeOI material, in particular Dr. Alexei Chelnokov, Dr. Jean-Michel Hartmann, and the groups of Dr. Vincent Reboud and Dr. Vincent Calvo.

I thank Dr. Giovanni Isella, Dr. Jacopo Frigerio and Dr. Daniel Chrastina from L-NESS in Como for providing the epitaxial GeSOI material and for their active participation within the project.

I want to thank Christopher Bonzon from ETH Zürich for all his contributions to the project in terms of cavity design and optical simulations, and for always having an open ear and a few minutes when I was around at Hönggerberg.

I want to thank Prof. Dr. Ralph Spolenak from ETH Zürich for his contributions to the project regarding the mechanical design aspects.

I thank Prof. Dr. Jim Harris, Dr. Robert Chen and Colleen Shang from Stanford University for the collaboration on their GeSn material, and especially Robert for his hospitality in California.

I would like to thank Dr. Stefan Birner for his support concerning the band structure simulations with NextNano^3.

I am grateful to Dr. Philippe Lerch, Marolt Bor and Luka Debenjak for their support with the infrared beamline at the SLS. Furthermore, I want to thank all the people that supported us during x-ray-based synchrotron measurements at SLS, namely Dr. Ana Diaz, Dr. Carlos Vaz and Dr. Armin Kleibert.

I would like to thank Prof. Dr. Jens Gobrecht for the pleasant working conditions and the cooperative atmosphere he created at LMN, as well as for his support of our project.

I thank Edith Meisel for all her support in administrative questions and for always thinking of me and the gas tank of my car.

I want to thank all the people at LMN taking care that cleanroom, process lab and all tools stay in optimal working conditions, in particular Christopher Wild, Eugen Deckardt, Thomas Neiger, Dario Marty, Anja Weber, Christian Spreu, Rajko Resanovic, Dr. Martin Bednarzik, and Konrad Vogelsang.

I want to especially thank Stefan Stutz, who did a great job in dealing with all our wishes concerning improvements of our optical setups, sample polishing, and whatever else came into our minds. In addition, I am very grateful for all the insight he gave me into the Swiss culture and language and for all the Swiss mountain tops, which I would not have seen if it had not been for him.

I would like to thank Dr. Vitaliy Guzenko for the first-class support in e-beam questions and sample processing, and for all those shared stories about what can go wrong while building or renovating a house.

I would like to thank Ute Drechsler from IBM Zürich for her great support in the cleanroom in Rüschlikon whenever any machine failed us at last second before a deadline. Furthermore, I thank her for all the help with the HF vapor etch tool and for making this great gift to us.

I thank Dorde Masovic for his contributions during his bachelor's thesis and Elias Peraticos for his work during his internship.

I would like to thank Dr. Salvatore Bagiante for his help in the cleanroom and with Mac-related issues, for all the fun discussions about science, sports, technology and gadgets, the outdoor fun in the Swiss mountains or valleys, and for his efforts to make me understand how things work in Italy.

I want to thank Dr. Ismo Vartiainen for sharing his outstanding expertise in dry-etching and all other process-related questions, for the right amount of pressure to leave early enough on Wednesdays for badminton, and for generally being a fantastic office mate.

I would like to thank Dr. Renato Minamisawa for all the starting help during my first months both, in the cleanroom as well as on the streets of Zürich.

I am grateful for the time I had with Dr. Jeroen Bosgra working together in the cleanroom, discussing about simulations or enjoying a coffee in the sun. He will never be forgotten.

I would like to thank all the other people, who might not have been directly involved in my research, but still contributed to a pleasant time and enjoyable atmosphere. I want to thank Dr. Thomas Siegfried for all the fun during making PhD hats and for this unforgettable trip to Uzbekistan. I thank Phillip Wohlhüter for the fun whenever we managed to be at our

desks at the same time, the shared suffering time during writing our theses, and for all those sweets that magically appeared from his never-empty drawer. For the helpful Italian-German tandem, I would like to thank Dr. Massimo Camarda. I want to thank Judith Wörle for the fun in the office and in the lodges of Switzerland and Austria, and her entertaining stories. I would like to thank Dr. Johannes Haase for the inspiring discussions about spectroscopy, and the many culinary highlights we could enjoy in Ennetbaden. I would, furthermore, like to thank Erna Hug for the administrative support at ETH Zürich, and all the people in Jerome's group at ETH for their support in terms of equipment or expertise.

I want to thank all my friends for having coped with my unavailability without grumble throughout these times, especially Johannes Volk, Roman Fritsch, Johannes Erlwein and Christa Jetté.

Finally, I would like to thank my parents Ethel and Zoltán as well as my sister Ilona with Hans and Raphael and my brother Martin with Andrea for their unconditional support, appreciation and trust. Without them, I would not be who I am today.

At last, I want to thank Claudia for her never-ending support, understanding and love. I am grateful for her extensive traveling efforts to visit me, for her patience, when measurements extended into nights and weekends, and for the right amount of motivation and pushes when it was needed.

Curriculum Vitae

Personal Details

Name	Richard Geiger
Date of Birth	15 August 1986
Place of Birth	Coburg, Germany
Nationality	German
E-Mail	richard.geiger@alumni.ethz.ch

Work Experience

1/2012 – 3/2016 Graduate student researcher,
Laboratory for Micro- and Nanotechnology, PSI, Villigen.
Quantum Optoelectronics Group, ETH Zürich.

Investigation of direct band gap Ge systems as potential CMOS-compatible laser to enable the convergence of electronic and photonic circuits.

- Design, modelling, fabrication and characterization of highly strained Ge microstructures.
- Optical characterization and modelling of lasing properties in GeSn alloys.
- Experimentation and user support at the pump-probe branch of the infrared beamline at the Swiss Light Source synchrotron.

Supervisors: Prof. Dr. Jérôme Faist and Dr. Hans Sigg.

10/2010 – 11/2011 Undergraduate student researcher,
Walter Schottky Institute, TU München.

- Fabrication of silicon light-emitting-diodes with germanium quantum dots acting as active emitters within electrically-contacted photonic crystal nanocavities.

- Testing of the diodes in terms of their electrical properties.
- Investigation of the optical properties via electro- and photoluminescence spectroscopy.

Supervisors: Prof. Dr. Gerhard Abstreiter and Prof. Dr. Dominique Bougeard.

10/2009 – 12/2009 Research assistant,
Walther-Meissner-Institute, TU München.

- Design of a lithography mask for printed circuit boards for surface acoustic wave-generation.
- Fabrication of printed circuit boards via optical lithography and wet chemical etching.

Supervisor: Dr. Sebastian T. B. Gönnenwein.

2/2009 – 4/2009 Research assistant,
Max Planck Institute for Solid State Research, Stuttgart.

- Development, test and application of an improved mass spectrometry LabVIEW software for a modern time-to-digital converter to use in electrospray mass spectrometry.

Supervisor: Dr. Stephan Rauschenbach.

Education

1/2012 – 3/2016 Doctorate in Physics,
ETH Zürich, Zürich, Switzerland.
Thesis title: *Direct Band Gap Germanium for Si-compatible Lasing.*

1/2010 – 4/2010 Visiting Student in Engineering,
University of Alberta, Edmonton, Canada.

9/2006 – 11/2011 Diploma in Physics,
TU München, München, Germany.
Thesis title: *Towards an Efficient Silicon-based LED with Germanium Islands as Active Emitters.*

9/1997 – 6/2006 German High-School Diploma,
Regiomontanus-Gymnasium, Haßfurt, Germany.

List of Publications

Peer-reviewed journal publications

As primary author

1. **R. Geiger**, T. Zabel and H. Sigg. Group IV direct band gap photonics: Methods, challenges and opportunities. *Frontiers in Materials* **2**, 52 (2015).

2. S. Wirths*, **R. Geiger***, N. von den Driesch, G. Mussler, T. Stoica, S. Mantl, Z. Ikonic, M. Luysberg, S. Chiussi, J. M. Hartmann, H. Sigg, J. Faist, D. Buca and D. Grützmacher. Lasing in direct-bandgap GeSn alloy grown on Si. *Nature Photonics* **9(2)**, 88-92 (2015). *These authors contributed equally to this work.

3. **R. Geiger**, J. Frigerio, M. J. Süess, D. Chrastina, G. Isella, R. Spolenak, J. Faist and H. Sigg. Excess carrier lifetimes in Ge layers on Si. *Applied Physics Letters* **104(6)**, 062106 (2014).

4. M. J. Süess*, **R. Geiger***, R. A. Minamisawa, G. Schiefler, J. Frigerio, D. Chrastina, G. Isella, R. Spolenak, J. Faist and H. Sigg. Analysis of enhanced light emission from highly strained germanium microbridges. *Nature Photonics* **7(6)**, 466-472 (2013). *These authors contributed equally to this work.

As contributing author

1. A. Gassenq, K. Guilloy, G. Osvaldo Dias, N. Pauc, D. Rouchon, J.-M. Hartmann, J. Widiez, S. Tardif, F. Rieutord, J. Escalante, I. Duchemin, Y.-M. Niquet, **R. Geiger**, T. Zabel, H. Sigg, J. Faist, A. Chelnokov, V. Reboud and V. Calvo. 1.9% bi-axial tensile strain in thick Germanium suspended membranes fabricated in optical GeOI substrates for laser applications. *Applied Physics Letters* **107(19)**, 191904 (2015).

2. M. J. Süess, R. A. Minamisawa, **R. Geiger**, K. K. Bourdelle, H. Sigg and R. Spolenak. Power-Dependent Raman Analysis of Highly Strained Si Nanobridges. *Nano Letters* **14(3)**, 1249-1254 (2014).

3. M. Schmidt, M. J. Süess, A. D. Barros, **R. Geiger**, H. Sigg, R. Spolenak and R. A. Minamisawa. A Patterning-Based Strain Engineering for Sub-22 nm Node FinFETs. *IEEE Electron Device Letters* **35(3)**, 300-302 (2014).

4. J. Sá, P. Friedli, **R. Geiger**, Ph. Lerch, M. H. Rittmann-Frank, C. J. Milne, J. Szlachetko, F. G. Santomauro, J. A. van Bokhoven, M. Chergui, M. J. Rossi and H. Sigg. Transient mid-IR study of electron dynamics in TiO_2 conduction band. *Analyst* **138(7)**, 1966 (2013)

Oral presentations

1. **R. Geiger**, T. Zabel, V. Reboud, J. M. Hartmann, J. Widiez, V. Calvo, N. Pauc, A. Gassenq, K. Guiloy, A. Chelnokov, J. Faist and H. Sigg. Optical Spectroscopy on strained Ge microbridges at the transition to a direct band gap. *IEEE 12th International Conference on Group IV Photonics (GFP)*, Vancouver (Canada), August 2015.

2. **R. Geiger**, S. Wirths, N. von den Driesch, Z. Ikonic, J. M. Hartmann, J. Faist, S. Mantl, D. Grützmacher, D. Buca and H. Sigg. A Direct Band Gap GeSn Laser on Si. *Conference on Lasers and Electro-Optics (CLEO)*, San Jose (USA), May 2015.

3. **R. Geiger**, M. J. Süess, J. Frigerio, D. Chrastina, G. Isella, R. Spolenak, J. Faist and H. Sigg. Infrared synchrotron determination of excess carrier lifetimes in strained Ge micro bridges. *SLS Symposium on Interdisciplinary Research*, Villigen (Switzerland), September 2014.

4. **R. Geiger**, M. J. Süess, C. Bonzon, J. Frigerio, D. Chrastina, G. Isella, R. Spolenak, J. Faist and H. Sigg. Carrier lifetimes in uniaxially strained Ge micro bridges. *IEEE 11th International Conference on Group IV Photonics (GFP)*, Paris (France), August 2014.

5. **R. Geiger**, M. J. Süess, C. Bonzon, R. A. Minamisawa, R. Spolenak, J. Faist and H. Sigg. Ultra highly strained Si and Ge structures for device applications. *European Materials Research Society Fall Meeting (E-MRS)*, Warsaw (Poland), September 2013.

6. **R. Geiger**, J. Frigerio, M. J. Süess, R. A. Minamisawa, D. Chrastina, G. Isella, R. Spolenak, J. Faist and H. Sigg. Excess carrier lifetimes in Ge layers on Si. *IEEE 10th International Conference on Group IV Photonics (GFP)*, Seoul (South Korea), August 2013.

Poster presentation

1. M. J. Süess, **R. Geiger**, R. A. Minamisawa, H. Sigg, G. Schiefler, J. Frigerio, D. Chrastina, G. Isella, J. Faist and R. Spolenak. Towards direct bandgap Ge for lasing applications. *31st International Conference on the Physics of Semiconductors (ICPS)*, Zürich (Switzerland), July 2012.